

PRE-CLINICAL ASSESSMENT OF CARDIAC AND LUNG
FIBROSIS USING NEXT GENERATION IMAGING
MODALITIES



Dissertation

for the award of the degree

“Doctor rerum naturalium” (Dr. rer. nat.)

of the Georg-August-Universität Göttingen

within the doctoral program Molecular Medicine

of the Georg-August-Universität Göttingen

Submitted by

Amara Khan

From Islamabad, Pakistan

Göttingen, 2021

MEMBERS OF THE THESIS ADVISORY COMMITTEE:

Prof. Dr. med. Frauke Alves

Dept. of Translational Molecular Imaging
Max Planck Institute for Experimental Medicine, Göttingen,
Clinic for Hematology and Medical Oncology; Institute for Diagnostic and Interventional
Radiology, University Medical Center Göttingen, Göttingen

Prof. Dr. med. Elisabeth Zeisberg

Department of Cardiology and Pneumology
University Medical Center Göttingen, Göttingen

Prof. Dr. med. Ralf Dressel

Institute for Cellular and Molecular Immunology
University Medical Center Göttingen, Göttingen

MEMBERS OF THE EXAMINATION BOARD:

Prof. Dr. med. Frauke Alves (1st Reviewer)

Dept. of Translational Molecular Imaging
Max Planck Institute for Experimental Medicine, Göttingen,
Clinic for Hematology and Medical Oncology; Institute for Diagnostic and Interventional
Radiology, University Medical Center Göttingen, Göttingen

Prof. Dr. med. Elisabeth Zeisberg (2nd Reviewer)

Department of Cardiology and Pneumology
University Medical Center Göttingen, Göttingen

FURTHER MEMBERS OF EXAMINATION BOARD:

Prof. Dr. Tim Salditt

Institute for X-ray Physics,
Georg-August-Universität Göttingen, Göttingen

Prof. Dr. Hubertus Jarry

Department of Clinical and Experimental Endocrinology
University Medical Center Göttingen, Göttingen

Prof. Dr. med. Thomas Meyer

Department of Psychosomatic Medicine and Psychotherapy,
University Medical Center Göttingen, Göttingen

Date of the oral examination: 01.09.2021

Table of Contents

List of figures	iv
List of abbreviations	v
Publications	vii
Abstract	viii
1. Introduction	1
1.1. Fibrosis – Pathogenesis and tissue remodeling	1
1.2. Pathophysiology and types of cardiac fibrosis	3
1.3. Anatomical and functional imaging of cardiac fibrosis	4
1.4. Label-free imaging of cardiac fibrosis	9
1.5. Pre-clinical models of cardiac fibrosis.....	15
1.6. Pathophysiology of pulmonary fibrosis	16
1.7. Anatomical and functional imaging of lung fibrosis	16
1.8. Preclinical models of pulmonary fibrosis.....	22
Aims and hypothesis	24
Individual contribution to the manuscripts	26
Chapter 1 – X-ray diffraction and second harmonic imaging reveal new insights into structural alterations caused by pressure-overload in murine hearts	29
Introduction	30
Materials and Methods	32
Results	35
Discussion	49
Conclusion and future prospective.....	52
Supplementary material.....	54
Reference List.....	67
Chapter 2 – Label-free imaging of age-related cardiac structural modulations in non-human primates using multiphoton nonlinear microscopy	71
Introduction	72
Materials and Methods	74
Results	76
Discussion	86
Supplementary Material	90

Reference list	94
Chapter 3 – Simple low dose radiography allows precise lung volume assessment in mice	99
Introduction	100
Materials and Methods	102
Results	106
Discussion	116
Supplementary material.....	119
Reference list	126
Discussion/ Summary of Publications.....	131
Conclusion	145
Appendix	147
Bibliography	155
Acknowledgments	168

List of figures

Figure 1: Overview of shared and distinct mechanisms of fibrotic tissue remodeling at different stages	2
Figure 2: Histological and schematic depiction of pathophysiology and types of fibrosis.....	4
Figure 3: In-vivo evaluation of contrast enhancement by eXIA 160 overtime using x-ray based imaging in mouse models of MI and TAC.	6
Figure 4: Principle of two-photon microscopy	12
Figure 5: Schematic for x-ray diffraction of cardiac muscle	14
Figure 6: Breathing induced modulations in the x-ray transmission at the chest region over time.....	20
Figure 7: Schematic showing timeline and mechanism of the bleomycin induced mouse model of lung fibrosis	23
Figure 8: Experimental timeline of bleomycin induced lung fibrosis and treatment with nintedanib	149
Figure 9: Micro-CT, XLF and histological assessment of healthy, untreated fibrotic and nintedanib treated mice.....	151

List of abbreviations

AAI	Allergic airway inflammation
CMR	Cardiac magnetic resonance
CT	Computed tomography
CCT	Cardiac computed tomography
CMR	Cardiac magnetic resonance imaging
ECC	Excitation-contraction coupling
ECG	Electrocardiogram
ECM	Extracellular matrix
ECV	Extracellular matrix volume
EHM	Engineered heart muscle
EIV	End-inspiratory volume
EMB	Endomyocardial biopsy
FAD	Flavin adenine dinucleotide
FEV	Forced expiratory volume
FOV	Field of view
FVC	Forced vital capacity
GaAsp	Gallium arsenide phosphide
GRIN	Gradient-index
HCM	Hypertrophic cardiomyopathy
HE	Hematoxylin and eosin stain
HHG	Higher harmonic generation
HRCT	High-resolution computed tomography
ICD	Intercalated disk
ICG	Indocyanine green
IPF	Idiopathic pulmonary fibrosis
iPSC	Induced pluripotent stem cells
I/R	Ischemia-reperfusion
LAD	Left anterior descending artery
LGE	Late gadolinium enhancement
LV	Left ventricle
MF	Myofibroblast
MEMS	Microelectromechanical systems

MI	Myocardial fibrosis
MRT	Magnetic resonance tomography
MTS	Masson's trichrome stain
NADH	Nicotinamide adenine dinucleotide
NHP	Non-human primate
PET	Positron emission tomography
PMT	Photomultiplier tube
PTI	Perfusable tissue index
ROS	Reactive oxygen species
ROI	Region of interest
RyR	Ryanodine receptor
SAXS	Small angle x-ray scattering
SENCEFUL	Self-gated non-contrast-enhanced functional lung
SERCA2a	Sarco/endoplasmic reticulum Ca ²⁺ -ATPase
SHG	Second harmonic generation
SPECT	Single photon emission computed tomography
SR	Synchrotron radiation
STE	Speckle tracking-echocardiography
TAC	Transverse aortic constriction
THG	Third harmonic generation
Ti:Sa	Titanium:sapphire
TPEF	Two-photon excitation fluorescence
TPM	Two-photon microscopy
TRPV4	Transient Receptor Potential Vanilloid-4
TV	Tidal volume
UIP	Unusual interstitial pneumonia
UWBP	Unrestrained whole body plethysmography
XLF	X-ray based lung function

Publications

Peer-reviewed publications:

Nicolas JD*, **Khan A***, Markus A, Mohamed BA, Toischer K, Alves F, Salditt T. X-ray diffraction and second harmonic imaging reveal new insights into structural alterations caused by pressure-overload in murine hearts. *Sci Rep*. 2020 Nov 9;10(1):19317. doi: 10.1038/s41598-020-76163-6.

**Shared first authorship*

Khan A, Markus A, Rittmann T, Albers J, Alves F, Hülsmann S, Dullin C. Simple low dose radiography allows precise lung volume assessment in mice. *Sci Rep*. 2021 Feb 18;11(1):4163. doi: 10.1038/s41598-021-83319-5.

Khan A, Ramos-Gomes F, Markus A, Mietsch M, Hinkel R, Alves F. Label-free imaging of age-related cardiac structural modulations in non-human primates using multiphoton nonlinear microscopy. (Under revision)

Hülsmann S, **Khan A**, Hagos L, Hindermann M, Nägel T, Dullin C. Evaluation of a mechanical lung model to test small animal whole body plethysmography. *Sci Rep*. 2021 11;17099. doi: 10.1038/s41598-021-96355-y

Reichardt M, Frohn J, **Khan A**, Alves F, Salditt T. Multi-scale X-ray phase-contrast tomography of murine heart tissue. *Biomed Opt Express*. 2020 Apr 17;11(5):2633-2651. doi: 10.1364/BOE.386576.

Reichardt M, Töpperwien M, **Khan A**, Alves F, Salditt T. Fiber orientation in a whole mouse heart reconstructed by laboratory phase-contrast micro-CT. *J Med Imaging (Bellingham)*. 2020 Mar;7(2):023501. doi: 10.1117/1.JMI.7.2.023501.

Nicolas JD, Bernhardt M, Schlick SF, Tiburcy M, Zimmermann WH, **Khan A**, Markus A, Alves F, Toischer K, Salditt T. X-ray diffraction imaging of cardiac cells and tissue. *Prog Biophys Mol Biol*. 2019 Jul;144:151-165. doi: 10.1016/j.pbiomolbio.2018.05.012.

Abstract

Fibrosis, defined as an excessive deposition of connective tissue components causing disruption of the physiological architecture and organ malfunction, is commonly associated with high morbidity and mortality. The global incidence of fibrosis is increasing rapidly making fibrosis one of today's major health-care challenges. Despite this recognition, fibrotic diseases are underdiagnosed in clinical practice mainly due to a lack of diagnostic tools for organ-specific detailed characterization. To establish innovative and unique imaging techniques, I chose two organ systems, i.e. heart and lung for structural and functional assessment of fibrosis in pre-clinical animal models.

By performing high-resolution and label-free imaging of cardiac tissue of mouse and marmosets, we aimed to identify sub-cellular fibrosis induced structural remodeling which is not feasible by currently used histology and non-invasive methods. To this end, we implemented comparative second harmonic generation (SHG) and x-ray diffraction imaging to analyse myocardial tissue in a mouse model of cardiac pressure overload. SHG emission from myosin and collagen was differentiated in tissue sections based on their distinct morphology. Heterogeneously distributed fibrotic lesions and micro-level distortion of myofibrils were detected and quantified by SHG imaging. These findings were corroborated with x-ray diffraction data which presented spatial maps of cardiac tissue and revealed increased lattice spacing, low anisotropy and peak intensity at the site of tissue remodeling. Regions that lacked both SHG and x-ray diffraction signals were identified as sites of active fibrosis due to high-immune cell infiltration. These findings show that the combined use of these imaging modalities allows detecting the different stages during cardiac fibrosis progression.

Our label-free imaging approach was further augmented by acquiring SHG signals in combination with two-photon-excitation fluorescence (TPEF) in three-dimensions (3D) to investigate age-related structural modulation in non-human primate model which reflects a comparable life span as humans. The hearts were obtained from common marmoset monkeys (*Callithrix jacchus*) of three different age groups including neonatal, young adult and old/geriatric. By devising a unique strategy for segregating collagen and myosin emitted SHG signals, I performed a volumetric assessment of collagen and total scattering tissue (collagen + myosin). Aged marmoset hearts exhibited an increase in collagen and total scattering tissue volume at the sites of severe tissue remodeling indicating the presence of age-related cardiac fibrosis. Our finding of marked low tissue volume in neonatal marmoset hearts was attributed

to a lack of banding between the myofibrils in maturing cardiac tissue. By applying semi-automated analysis, significant differences were revealed in parameters such as total tissue volume, myofibril length, alignment, curvature and angulation between all three age groups. Overall, our imaging approach highlights the unrivalled potential of TPM for detailed evaluation and characterization of age-related cardiac structural remodeling in the marmoset heart that may provide insight into pathological processes.

Pre-clinical monitoring of the degree of lung fibrosis will mostly profit from a reliable and standardized method for functional imaging. Therefore, I improved the x-ray based lung function (XLF) which uses dramatically lower x-ray doses and acquisition times in comparison to micro-CT and has been previously reported to be more sensitive than whole-body plethysmography (WBP) in allergic airway inflammation mouse models. Because XLF so far was unable to relate its parameters to pulmonary air volume, we designed an experimental set-up to perform correlative lung function measurements using either XLF or micro-CT with WBP on healthy mice. Using micro-CT as a gold-standard, our results reveal a strong correlation of lung volumes obtained from radiographic XLF and micro-CT and demonstrate that XLF is superior to WBP in precision and sensitivity to assess lung volumes. We thus present XLF as a promising tool for future pre-clinical studies on longitudinal assessment of lung fibrosis during the course of the disease and in response to therapy. Furthermore, XLF as a biomedically relevant non-invasive technique has a high potential for clinical translation.

1. Introduction

1.1. Fibrosis – Pathogenesis and tissue remodeling

Fibrosis is an outcome of tissue repair processes that become dysregulated upon severe tissue injury. It plays a role in various pathologies and can virtually affect all organs. Fibrosis accounts for 45% of all deaths in developed countries and is increasingly becoming one of the major health-care challenges (Henderson et al., 2020; Rockey et al., 2015). Despite the high prevalence, fibrotic diseases are incurable (Montesi et al., 2019), not well understood, often underdiagnosed and if uncontrolled, can lead to various life-threatening conditions (Henderson et al., 2020; Rockey et al., 2015; Wynn and Ramalingam, 2012).

Fibrosis is defined by excessive deposition of extracellular matrix (ECM) components such as collagen, proteoglycans and fibronectin (Friedman et al., 2013). Under non-repetitive tissue injury, fibrosis serves as a vital wound healing and reparative process for maintaining functional architecture of the tissue (Wynn and Ramalingam, 2012). Disease progression involving severe tissue injury, chronic inflammation, genetic alterations and autoimmune reactions triggers activation of chronically persistent and uncontrolled fibrotic response (Thannickal et al., 2014). The initial profibrotic cascade involves an early inflammation response which leads to infiltration, activation and accumulation of various immune cells (Figure 1). This persistent profibrotic milieu activates phenotypical transformation of fibroblasts and various other cell-types into myofibroblasts (MF) (Horowitz and Thannickal, 2018; Zeisberg and Kalluri, 2013). Activated MFs are the main effector cells that contribute to release of ECM components and secrete extracellular pro-collagen chains that assemble into collagen fibrils which become highly cross-linked to form the final fibers. Collagen cross-linking is a crucial post-translational modification which increases tensile strength of the tissue and the resistance of ECM for degradation by matrix metalloproteinases leading to MFs persistence. Late-stage fibrosis development retains the pathological ECM turnover whereby increased synthesis predominates over unchanged or decreased degradation of ECM proteins (Darby and Hewitson, 2007; Wynn, 2008; Karsdal et al., 2017; Distler et al., 2019). This progressive pathological tissue remodeling results in permanent tissue damage, organ dysfunction and ultimately organ failure. Although, the fundamental pathophysiological mechanisms contributing to fibrosis are shared amongst most of the organ systems, the risk

factors and the impact of fibrosis on structural and functional integrity is unique to each fibrotic entity (Distler et al., 2019). Figure 1 summarizes the shared and distinct mechanisms that govern fibrosis progression.

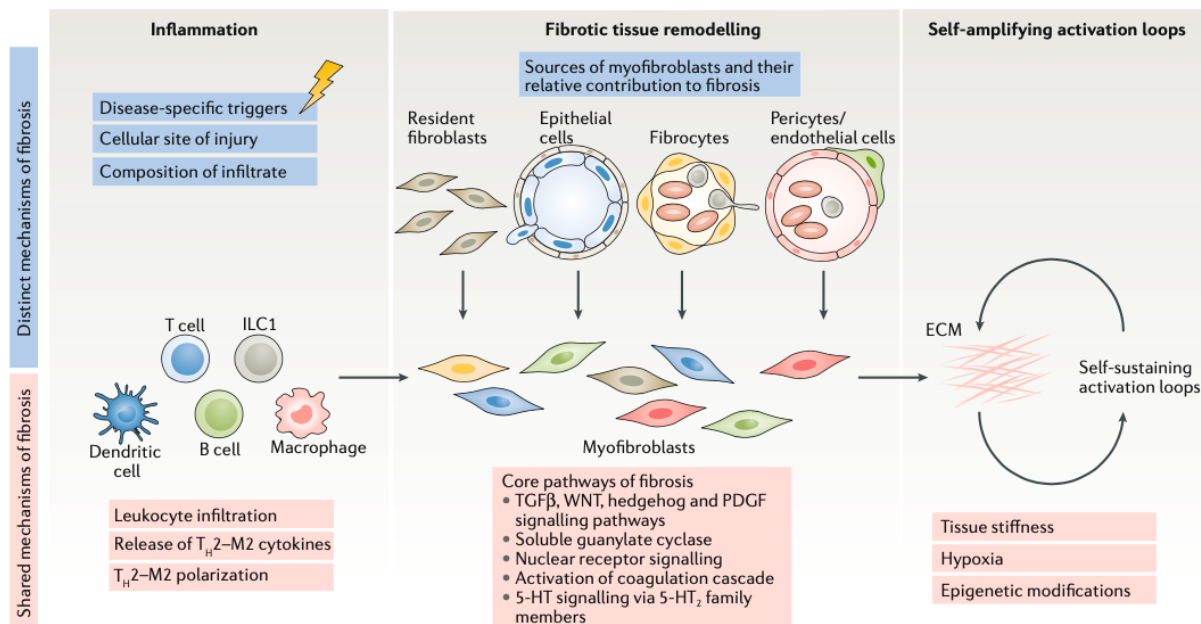


Figure 1: Overview of shared and distinct mechanisms of fibrotic tissue remodeling at different stages. Fibrosis progression at early phase involves an early inflammatory response triggering infiltration and activation of leukocyte, T_H2 cell–M2 macrophage polarization as well as secretion of profibrotic cytokines at the site of disease and cell injury. A disease-specific composition of infiltrates creates a profibrotic environment which induces activation and transdifferentiation of resident fibroblasts, epithelial cells, fibrocytes, pericytes and endothelial cells into MFs. Various core-signaling pathways activate the MFs including TGF β , WNT, hedgehog signaling which are influenced by regulatory pathways including sGC, nuclear receptor signaling, coagulation cascade activation and 5-HT signaling via 5-HT $_2$ receptor family. Progressive profibrotic activation induces self-amplifying activation loops resulting in ECM accumulation, tissue stiffness and hypoxia at the site of fibrosis leading to MFs persistence and epigenetic modifications. T_H2 (T helper 2 cell); MF, (Myofibroblast); 5-HT [5-hydroxytryptamine (serotonin)]; 5-HT $_2$ (5-HT receptor 2); ILC1 (group 1 innate lymphoid cell); PDGF (platelet-derived growth factor); TGF β (transforming growth factor- β); sGC (soluble guanylate cyclase signaling); ECM (extracellular matrix). Figure modified from Distler et al. 2019.

Despite a relatively advanced understanding of molecular and genetic pathway contributing to fibrosis, little is known about molecular level structural impairments and their impact on functional efficiency in different organs specifically during active fibrosis. This is largely due to a lack of organ-specific detailed characterization of fibrosis. Furthermore, molecular heterogeneity of tissue remodeling adds to the complexity of early detection of fibrosis (Baues et al., 2017; Gyöngyösi et al., 2017; Montesi et al., n.d.). This indicates a dire need for developing functional and molecular imaging in pre-clinical models of fibrosis to provide

substantial integrative knowledge required for early diagnostics, staging, advanced prognostics as well as to monitor the efficacy of novel therapeutics in different organs. To establish high-resolution imaging techniques for preclinical assessment of fibrosis I chose two organ systems – heart and lung.

1.2. Pathophysiology and types of cardiac fibrosis

Nearly all etiologies of cardiovascular disease involve pathological myocardial remodeling resulting in fibrosis, which reduces tissue compliance and accelerates the progression to heart failure. It is associated with adverse functional outcomes including arrhythmias, systolic and diastolic dysfunction (Ma et al., 2018).

Two main forms of cardiac fibrosis have been identified i) replacement and ii) interstitial fibrosis or perivascular fibrosis (Figure 2).

- i) Replacement fibrosis occurs in response to cardiac injury causing myocyte necrosis. After cardiac injury, a reparative response is activated in the heart, causing replacement of apoptotic cells and formation of a fibrous scar. Following this transmural infarction, a fibrous scar protects the heart from rupture by maintaining the structural integrity of the ventricle and also prevents dilative remodeling. Conditions associated with replacement fibrosis include myocardial infarction (MI), toxic cardiomyopathies and myocarditis.
- ii) Interstitial or perivascular fibrosis involves expansion of interstitial space without a significant loss of cardiomyocytes. This chronic diffuse or focal reactive fibrosis is a consequence of either pressure or volume overload due to persisting hypertension, valvular heart diseases, metabolic disorders, or aging (Frangogiannis, 2019; Travers et al., 2016).

Regardless of its type, myocardial fibrosis is a complicated process resulting in the abnormal deposition of ECM proteins.

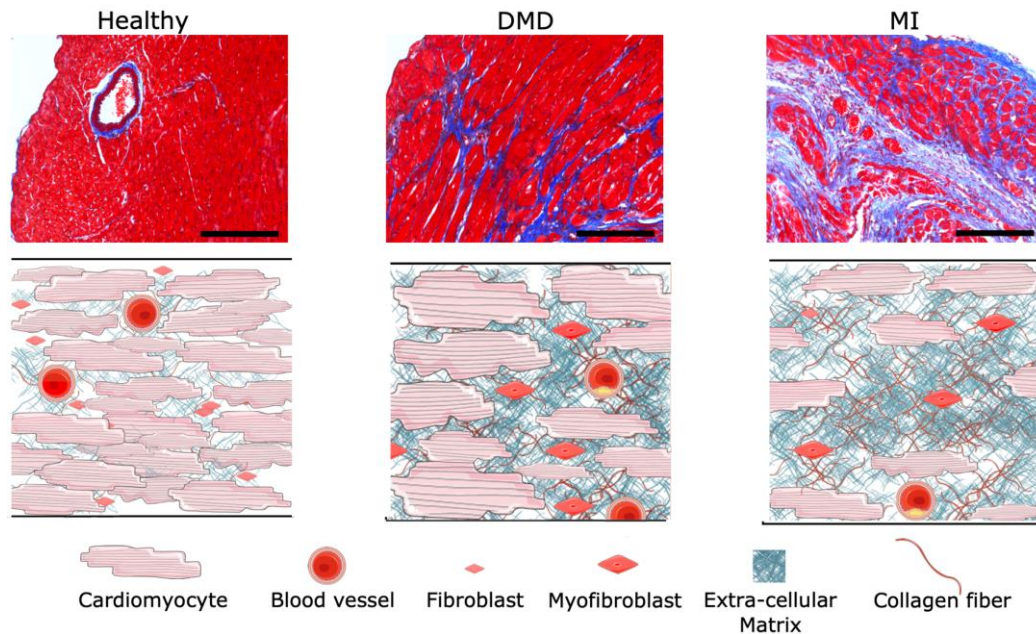


Figure 2: Histological and schematic depiction of pathophysiology and types of fibrosis. Masson trichrome (MTS) stained murine cardiac tissue slices (top panel) are shown for healthy, Duchenne muscular dystrophy (DMD) cardiomyopathy with interstitial fibrosis and myocardial infarction (MI) with replacement fibrosis. Cardiac muscle is stained red while collagen aniline blue. Schematic representation (lower panel) showing cardiomyocytes (CM) of normal size and arrangement surrounded by ECM and fibroblasts in healthy heart. The illustration for DMD heart (lower panel) displays hypertrophic CM with higher spacing and presences of activated myofibroblasts that contribute to excessive ECM deposition in the interstitial spaces and around the blood vessels. The schematic for MI heart exhibits a region with CM necrosis which is predominantly replaced with a fibrous scar with myofibroblast persistence. Scale bar: 100 μ m for all images. [All histological images were acquired using Axiovert 200 M inverted microscope (Carl Zeiss Microscopy GmbH) and schematic images were prepared using <https://smart.servier.com> and inkscape]. Unpublished data.

1.3. Anatomical and functional imaging of cardiac fibrosis

Various non-invasive and invasive imaging modalities have been used for pre-clinical and clinical assessment of cardiac fibrosis. A brief description for each technique is provided below to highlight the current status of anatomical and functional imaging of cardiac fibrosis.

1.3.1 X-ray based imaging

Traditionally, x-ray based luminography has been used as a standard for detecting peripheral and coronary arterial disease particularly in humans and large animal models (Patel et al., 2015; Suzuki et al., 2009). This minimally invasive angiography approach is usually performed by intravenous injection of radiopaque contrast agent through a catheter in combination with x-ray radiography to identify occlusions causing ischemic cardiomyopathy. While the

localization of obstruction is detected by this method, no information is extracted regarding cardiac dysfunction and extent of fibrosis from this data which makes further assessment inevitable (Patel et al., 2015).

In clinical research, cardiac computed tomography (CCT) has recently gained popularity due to its ability to quantify extracellular matrix volume (ECV) using iodine-based contrast agent distribution at higher resolution as compared to cardiac magnetic resonance imaging (CMR, discussed in the later section). The accumulation of contrast agent in the expanded ECM space and subsequent delayed clearance from this region depicts the infarct size and location (Yamada et al., 2020). In preclinical small animal models, 4D micro-CT is performed in combination with contrast agents that can diffuse from blood pool into the myocardial muscle overtime enabling assessment of cardiac function and site of the fibrotic lesion. One example of such contrast agent is eXIA 160, an aqueous colloidal poly-disperse contrast agent with a high concentration of iodine (Ashton et al., 2014). It provides initial blood enhancement and is taken up by tissues overtime with high metabolic activity including healthy myocardium with little or no uptake at the fibrotic scar in the MI and transverse aortic constriction (TAC) mouse model as shown in Figure 3. Due to high spatial resolution of micro-CT imaging particularly using synchrotron radiation, this technique holds promise to define fibrotic lesions at micrometer scale in three-dimension (3D) and/or 4D. Nonetheless, clinical CCT or preclinical micro-CT is not recommended to be applied for detecting and monitoring fibrosis progression mainly due to radiation exposure, inability to delineate diffused fibrotic lesions and poor sensitivity (Figure 3).

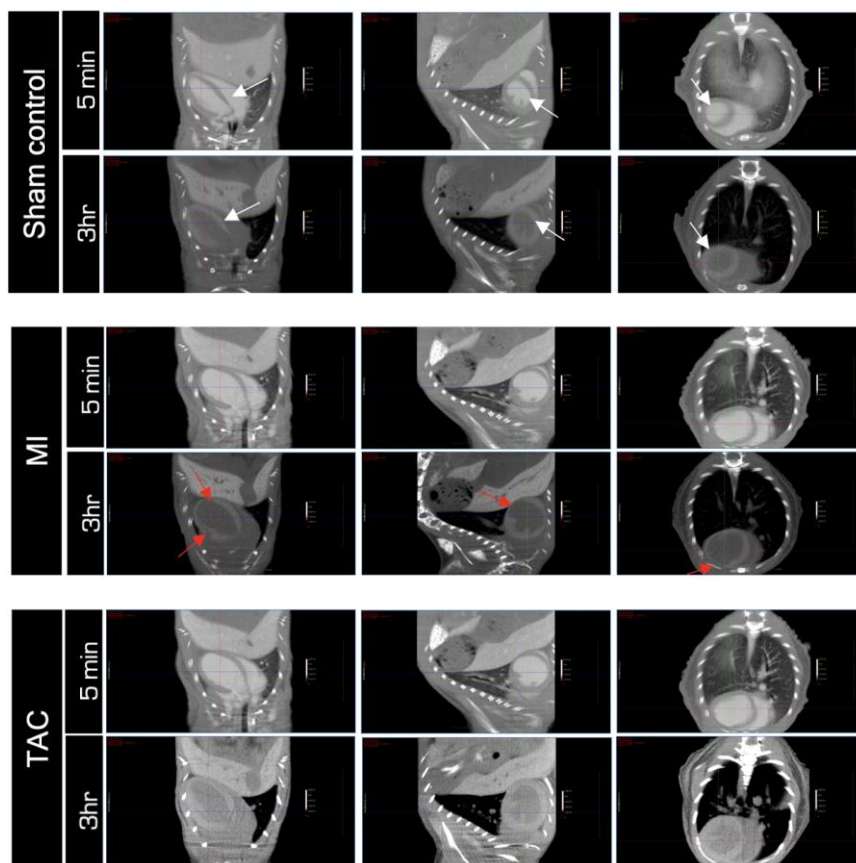


Figure 3: In-vivo evaluation of contrast enhancement by eXIA 160 overtime using x-ray based imaging in mouse models of MI and TAC. The contrast enhancement 5 min after the intravenous injection of eXIA 160 is observed in the blood pool. After ~3 hrs the contrast agent diffuses into the myocardium (white arrows) in all three groups including sham, MI, and TAC. In MI hearts, the infarcted region is detected by lack of contrast enhancement (red arrows) and overall thin myocardial wall with larger ventricular lumen can also be observed (red arrows). However, in TAC hearts diffused fibrotic lesions are not detected while cardiac hypertrophy is evident by an overall higher degree of wall-thickness. All images are shown in coronal, sagittal and transverse plane and were acquired using in-vivo micro-CT (QuantumFX, PerkinElmer) with 20 x 20 mm² field of view, 90 kVp x-ray tube voltage and 200 μ A tube current. (Unpublished data).

1.3.2 Echocardiography

Echocardiography is the most common and routinely used cardiac imaging technique in both clinical and pre-clinical assessment of cardiac function with a wide range of parameters such as wall thickness, left ventricle (LV) volume and mass and LV ejection fraction which are highly suitable for detecting global cardiac dilation and dysfunction. Further, Doppler echocardiography allows measuring velocity of cardiac motion and direction of blood flow. However, echocardiography is not recognized for tissue characterization due to poor image quality and resolution (Dewey et al., 2020). Advanced echocardiography methods including

speckle tracking-echocardiography (STE) uses tissue texture analysis for identifying fibrotic lesions. This technique tracks and identifies intrinsically occurring acoustic reflections or speckles. The pattern of speckles provides a fingerprint that is traced in each frame acquired, independent of motion and angulation. STE deformation parameters evaluate the effects of excessive ECM deposition on the myocardial mechanics by quantifying elastic stiffness and strain rate (Moharram et al., 2019). Despite the advantage of STE as a non-invasive, low cost and patient friendly technique with no side effects, it suffers various drawbacks for detecting and characterizing fibrosis at present, due to the lack of sensitivity, reproducibility and indirect assessment of the fibrotic regions. Importantly, such an approach cannot distinguish other underlying causes of impaired tissue texture, e.g. it is unable to differentiate amyloid infiltration from fibrosis. Another emerging pre-clinical tool for assessment of cardiac fibrosis is optoacoustic imaging which detects ultrasound waves emitted by thermoelastic expansion of tissue moieties following absorption of light with transient energy. Volumetric optoacoustic tomography using indocyanine green (ICG) successfully detected infarcted regions in a mouse model of MI by assessing pulmonary transit time and cardiac perfusion in ischemia-reperfusion (I/R) models (Ivankovic et al., 2020). Nonetheless, this approach is so far limited by low penetration depth and highly complex data processing and analysis. Additionally, molecular imaging probes for detecting fibrosis using optoacoustic imaging are by far lacking (Ivankovic et al., 2020; Karlas et al., 2019).

1.3.3. Cardiac magnetic resonance tomography

Similar to CCT, CMR or magnetic resonance tomography (MRT) is based on the use of contrast agent such as gadolinium for visualizing and quantifying ECV. Late gadolinium enhancement (LGE) relies on the accumulation of gadolinium chelates in the expanded ECM, as these cannot penetrate the cell membrane. This accumulation results in extremely shortened T1 relaxation times. The signal-to-noise ratio is further enhanced by either using phase sensitive inversion recovery or pulse inversion (Kellman et al., 2002). This procedure has previously shown close correlation between CMR determined ECV and histological collagen volume for ischemic scars in patients with heart failure and aortic stenosis (Sibley et al., 2012). However, the ECV readout require comparison with unaffected myocardium which reduces the standardization and routine application of this approach in both pre-clinical and clinical level (Everett et al., 2016). Other challenges involving CMR include gadolinium toxicity, relatively long acquisition time and highly skilled handling. Functional assessment of cardiac

fibrosis using CMR are performed in humans and animal models without using contrast agents, however, diffused fibrotic lesions are not detectable (Haaf et al., 2016; Moussavi et al., 2020).

1.3.4 PET and SPECT imaging

Positron emission tomography (PET) and single-photon emission computed tomography (SPECT) allow molecular and cellular level non-invasive assessment of cardiac fibrosis. PET is usually performed in combination with CMR or CT to mainly quantify the degree of inflammation and fibrosis. Isotopes with short half-life are used as PET tracers. Cardiac perfusion is monitored by using H_2^{15}O and C^{15}O tracers which indicates cardiac fibrosis by determining perfusable tissue index (PTI). A low PTI index represents reduction in exchange of water molecules at fibrotic regions serving as an indicator of fibrosis (Sado et al., 2011). Other PET probes that are used for assessing inflammatory response include i) ^{18}F -FCH and ^{11}C -cholin which act as reporter for lipid metabolism and membrane formation, ii) ^{68}Ga -DOTATATE which targets somatostatin receptor and iii) ^{11}C -PK11195 which is a selective ligand of a translocator protein expressed in activated macrophages (Baues et al., 2017). For sensitive assessment of cardiac ischemia, Ziegler *et al.*, tested the platelet targeting probe $\text{scFv}_{\text{anti-GP2b/3a-64CuMeCOSar}}$ since it is known that activated platelets undergo a conformational change in the integrin glycoprotein GP2b/3a receptor which triggers early phase of fibrosis. PET-CT scans in a mouse model of left anterior descending artery (LAD) ligation showed a significantly high uptake of $\text{scFv}_{\text{anti-GP2b/3a-64CuMeCOSar}}$ in the ischemic myocardium in contrast to sham hearts with no probe accumulation (Ziegler et al., 2016). These PET probes have a high potential in detection and imaging of relatively low degree of ischemia, however, PET lacks the resolution for delineating heterogeneously distributed diffused fibrotic lesions.

1.3.5 Endomyocardial biopsy

Histological and immunohistochemical staining of endomyocardial biopsy (EMB) is still the gold standard technique which is only performed when accurate detection of both early and late-stage fibrosis cannot be performed by any other techniques (Ahmed and Goyal, 2021). EMB is collected using a biptome which is usually inserted into the femoral or the right internal jugular vein and advanced to the right ventricle, where samples are taken from the ventricular septum (Ahmed and Goyal, 2021). While this procedure does play an important role in fibrosis detection, at the same time it is highly invasive involving procedures that may

lead to serious complications. It also suffers from sampling errors, non-representation of pathological tissue, laborious staining procedures and discrepancies in interpretation (Ahmed and Goyal, 2021; Baues et al., 2017; Montesi et al., n.d.).

Limitations of in-vivo imaging tools

Non-invasive imaging techniques such as echocardiography, CT and MRI provide multiple parameters that offer assessment of cardiac fibrosis in humans and animal models. Although, most of the imaging techniques described earlier are anatomically able to detect late-stage and established fibrotic lesion(s) in the heart, they are not sensitive to distinguish active fibrogenesis from a stable scar. So far, the routinely used clinical and pre-clinical imaging modalities are also hampered by contrast agent administration, error-prone diagnostic and lack of standardization. They also do not possess the resolution and sensitivity to detect diffused fibrosis, especially at sub-cellular level. Further, the micro- and macro-scale identification of fibrotic hallmarks could help refining and enhancing non-invasive or invasive in-vivo imaging of cardiac fibrosis for early diagnostics and treatment.

1.4. Label-free imaging of cardiac fibrosis

None of the techniques discussed in the previous section can directly examine myocardial regulation at the sarcomeric level and the effect of fibrosis progression on myofilaments in the healthy and fibrotic heart. Ex-vivo high-resolution visualization of structural changes in myofilament and accessory proteins using label-free imaging is vital to add new dimensions beyond fibrotic lesion to surrounding myocardium to potentially diagnose cardiac fibrosis at early stage. We established and applied non-linear optical microscopy in combination with x-ray diffraction and histology for assessment of cardiac fibrosis in heart samples obtained from pre-clinical models which are explained in detail in the following sections.

1.4.1 Multiphoton nonlinear optical microscopy for label-free imaging

Ex-vivo histological examination is a gold-standard for morphological assessment of the heart, but it lacks adequate resolution and specificity. Alternatively, high-resolution microscopy techniques offer detailed visualization on the cellular and sub-cellular level such as confocal microscopy and super-resolution microscopy techniques (Kohl et al., 2013; Mollova et al., 2013), however, they require intensive sample preparation and labeling of target proteins using fluorescent labeled antibodies often resulting in unspecific binding, overstaining and photobleaching of the fluorophore that can hinder repetitive imaging and quantitative analysis (Wang et al., 2018).

In recent years, multiphoton excitation using nonlinear optical microscopy has become an increasingly popular approach that combines a wide range of excitation/emission wavelengths for high-resolution 3D imaging of biological materials. The concept of two-photon excitation was first introduced by Maria Goppert-Mayer in 1931, as a principle of quantum mechanism (Perry et al., 2012). Initially applied in material sciences, two-photon excitation with further optimization of high-power lasers, objective design and high-sensitivity detectors was established in biological materials (Denk et al., 1990; Weigelin et al., 2016). Two-photon microscopy (TPM) generally utilizes femto-picosecond pulse width, near-infrared (usually ~ 670-1080 nm) Titanium:Sapphire (Ti:Sa) lasers and the emitted signals are detected at ultrasensitive photomultiplier tube (PMT) or gallium arsenite phosphide (GaAsp) detectors. In contrast to single photon or linear microscopy such as confocal microscopy, two photon excitation uses infrared wavelength and enables focal volume excitation which results in minimal scattering and phototoxicity, deep-tissue penetration and long-term time-lapse imaging (Figure, 4). Further, TPM also offers advanced optical detection efficiency since a pinhole is not required to remove out of focus imaging as is the case in confocal microscopy (Wu et al., 2017). These advantage makes a wide range of biological specimens amenable to TPM including thin or thick live, fresh and fixed samples as well as anesthetized animals for intravital microscopy (Perry et al., 2012).

TPM offers a broad excitation range allowing multicolor imaging at the same excitation wavelength. To attain TPM based label-free imaging, intrinsic signals in form of i) two-photon excitation fluorescence (TPEF) and ii) higher harmonic generation (HHG) including second harmonic generation (SHG) and third harmonic generation (THG) are detected from naïve, unstained structures (Friedl et al., 2007). Both TPEF and HHG depends on simultaneous

interaction of multiple photons with the target endogenous molecule/protein. In TPEF, two photons of incident wavelength and frequency are absorbed by the target fluorophore, to produce a single photon with loss of net energy (Figure 4). Intracellular TPEF mainly arises from the mitochondrial matrix proteins nicotinamide adenine dinucleotide (NADH), flavin adenine dinucleotide (FAD), and lipoamide dehydrogenase while extracellular autofluorescence occurs from the structural proteins such as elastin, collagen and also blood cells. The fluorescence in these molecules usually originates from smaller fluorophores within their structures such as amino acids including tyrosine, tryptophan, and phenylalanine and vitamins or vitamin derivatives such as retinol (vitamin A), riboflavin (vitamin B2), and folic acid (vitamin B9), pyridoxine (vitamin B6) and cholecalciferol (vitamin D3) (Wang et al., 2010; Zipfel et al., 2003).

Contrarily, HHG is a nonlinear coherent scattering process that occurs from phase matching and summation of light waves. Unlike TPEF, HHG does not involve photon absorption and energy decimation. HHG is induced by organic or inorganic structures possessing specific molecular order and physical properties. SHG results from conversion of two interacting photons with a non-centrosymmetric target into a single emitted photon, which has twice the energy and half the wavelength of the incident photons (Perry et al., 2012; Friedl et al., 2007). Myosin and collagen, both of which are integral components of cardiac tissue facilitate SHG emission (Green et al., 2017; Plotnikov et al., 2006). THG, as the name suggests, results from converting combined energy from three photons into one emitted photon with one third of the excitation wavelength and tripled frequency. THG, as opposed to SHG, is not dependent on asymmetry of the structures but relies on the structural interfaces such as the aqueous interstitial fluids and lipid-rich structures in cell-membranes (Weigelin et al., 2016). SHG imaging has been previously applied in cardiomyocytes to investigate myofibrillogenesis (Liu et al., 2011) and in embryonic hearts to examine heart development (Lopez and Larina, 2019).

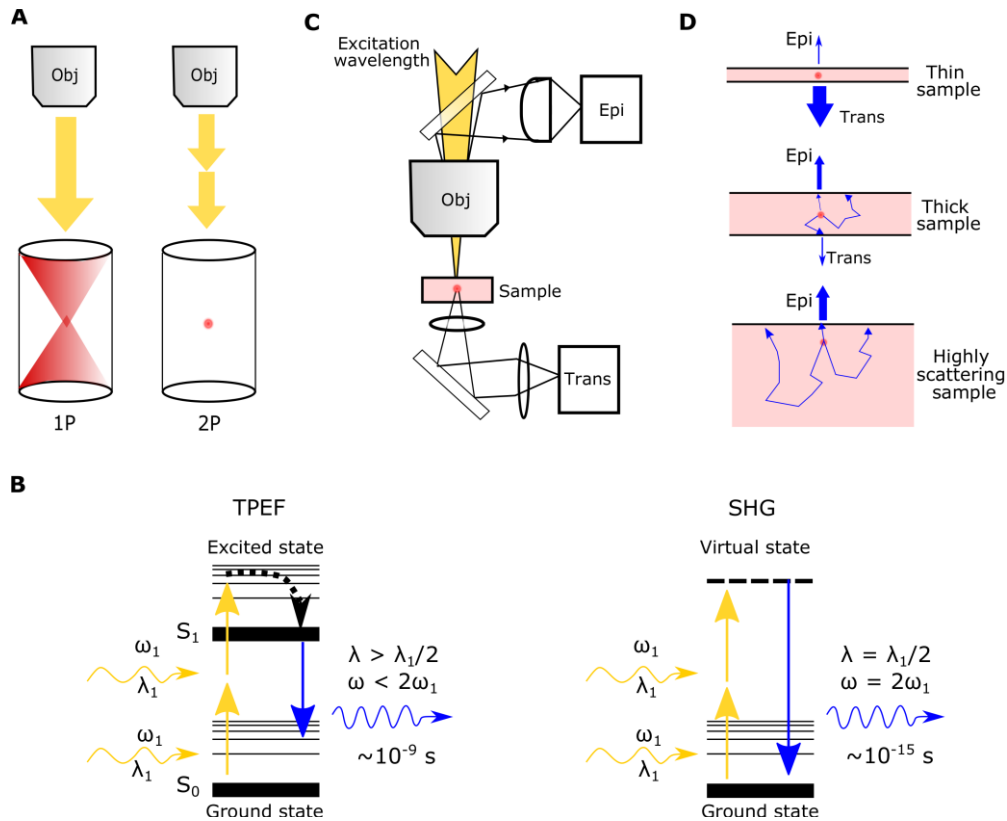


Figure 4: Principle of two-photon microscopy. A) The excitation volume of TPM (right) is confined within the focal plane (red dot), while single photon excitation (left) involves out-of-focus illumination. B) Simplified Perrin–Jablonski fluorescence diagram is shown for TPEF (left), and the energy-level diagram presents SHG signal emission (right). In TPEF, two photons (yellow arrows) of incident frequency (ω_1) and wavelength (λ_1) are simultaneously absorbed by the target fluorophore, resulting in emission of a single photon (blue arrow) with a wavelength ($\lambda > \lambda_1/2$) greater than one-half of the incident wavelength (λ_1) with some loss in net energy. Whereas in SHG, two photons of frequency (ω_1) and wavelength (λ_1) interacting simultaneously with a non-centrosymmetric structure, combine to produce a single photon (blue arrow) whose wavelength is exactly half ($\lambda = \lambda_1/2$) that of the irradiating wavelength (λ_1) with no net energy loss. C) Schematic of the experimental setup is shown for a multiphoton microscope equipped to detect epi (backward) and trans (forward) signals. The excitation light is focused on the sample through the objective (Obj) lens and the backward epi-signal is collected via the objective, reflected by a dichroic mirror and detected by an ultrasensitive photomultiplier tube (PMT). The forward transmitted (trans) signal is picked up by a condenser lens below the sample and subsequently focused onto a PMT. D) The relative intensity of epi versus trans SHG signals (blue arrows) is determined by sample thickness. In thin samples, SHG is ideally detected in the trans direction due to the lack of scattering. With the increase in sample thickness and scattering, the photon frequency below the samples weakens, however, it increases in the epi direction. [Schematic prepared using Inkscape (Inkscape Project, 2020. Available at: <https://inkscape.org>)]

The intensity of SHG from myosin (striated muscle) and collagen is crucially dependent on i) the organization and size of these signal-eliciting structures, ii) the excitation/detection approach, and iii) the power and polarization of the incident light (Friedl et al., 2007; Perry et al., 2012; Rubart Michael, 2004). In order to acquire images to achieve reliable data for 2D and

3D visualization and quantification of both cardiac harmonophores (i.e., myosin and collagen), these aspects of SHG imaging were extensively optimized in our work which is shown in chapter 1 and 2.

1.4.2 X-ray diffraction of cardiac muscle

Due to their high frequency and short wavelength, x-rays offer a large array of applications from medical diagnosis to investigating structures at atomic level. Combined, these advantages of x-rays facilitate examining interactions between contractile proteins of the muscle. The x-rays scattering away from the transmitted beam by large molecules, such as proteins, generate small-angle x-ray scattering (SAXS) which was first recognized in skeletal muscle by Huxley (Haselgrove and Huxley, 1973; Huxley et al., 1965) and then subsequently applied on heart muscle by Matsubara (Matsubara et al., 1977). The myosin and actin filaments in sarcomeres are aligned in parallel and arranged in a hexagonal lattice (Figure 5A). This arrangement of filaments acts as a 3D grating, which changes the traveling direction of x-rays and diffracts them when a finely collimated x-ray beam passes through the muscle. This hexagonal arrangement predominantly generates two diffraction peaks, the (1,0) and (1,1) equatorial reflections (Figure 5B). The distance between the filaments determines the position of the peaks while the intensity is dependent on the distribution of electron mass around the filaments. When myosin heads are attached to actin, the intensity of (1,1) reflection is high while the intensity of (1,0) reflection decreases. Hence, the intensity ratio of both equatorial reflections ($I_{1,0}/I_{1,1}$) relies upon the relative number of myosin heads attached to actin filaments and provides information regarding the cyclic changes of myosin mass transfer during muscle contraction. The interpolation of $I_{1,0}/I_{1,1}$ value can determine the quiescent muscle with no myosin motor attachments (relaxed state) and muscle with completely occupied actin binding sites (rigor state) (Haselgrove and Huxley, 1973; Shirai Mikiyasu et al., 2013).

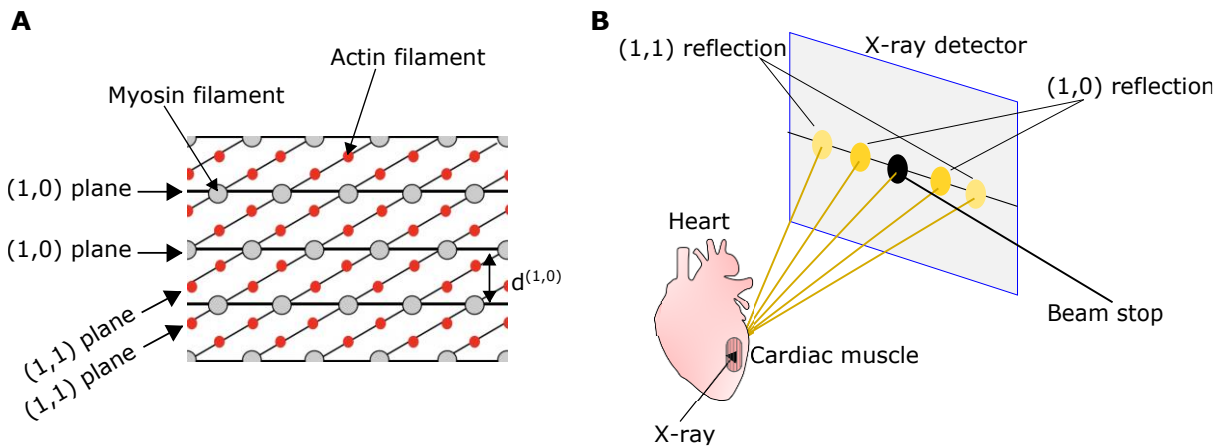


Figure 5: Schematic for x-ray diffraction of cardiac muscle. A) 2D hexagonal filament lattice of cardiac muscle is shown. The thick myosin filaments are on the (1,0) lattice plane and the thin actin filaments are aligned along the (1,1) plane with the myosin filaments. The interfilament spacing $d^{(1,0)}$ typically ranges between 35.0 nm and 38.3 nm for rodents and in humans it is approximately 40 nm. B) The acto-myosin lattice planes in (A) act as a 3D diffraction grating when x-ray passes through them whereas the undiffracted beam is blocked by the beam stopper. At the detector, four diffraction peaks are detected which are symmetrically at 90° angle to the myofilaments. The peak for (1,0) reflection appears closer to the center while the (1,1) reflection is further away from the center. [Schematic prepared using Inkscape (Inkscape Project, 2020. Available at: <https://inkscape.org>)]

Matsubara *et al.* provided initial evidence for the force–frequency relation in heart by recording x-ray intensity in real-time on an isolated papillary muscle (Matsubara *et al.*, 1978). They observed that during diastole a limited number of myosin heads remain attached to actin filaments without generating force of contraction. However, to generate force of contraction during systole, the myosin heads binding to actin filaments increase dramatically which tends to intensify with increasing heart rates (Matsubara *et al.*, 1978). Further studies on isolated and skinned (demembrated) cardiac muscle provided evidence to the length-dependent activation which is the Frank-Starling law of the heart (Matsubara *et al.*, 1989; Cazorla *et al.*, 2001; Konhilas *et al.*, 2002). Beyond isolated muscle, x-ray diffraction has been performed on cardiac tissue and whole beating hearts under ex-vivo, in-situ conditions as well as in-vivo conditions, however, in-vivo experiments face multiple complications such as diffraction signals from skeletal muscle (J. D. Nicolas *et al.*, 2019; J.-D. Nicolas *et al.*, 2019; Nicolas *et al.*, 2017; Toh *et al.*, 2006; Yagi *et al.*, 2004). Data from these experiments particularly ex-vivo and in-situ, contributed to our understanding of orientation of cardiomyocyte chains (fiber orientation), interfilament spacing and cross-bridge dynamics on whole hearts.

1.5. Pre-clinical models of cardiac fibrosis

Animal models are essential to decipher aetiologies and pathomechanisms contributing to cardiac fibrosis as well as for developing new diagnostics techniques for monitoring fibrosis progression and response to anti-fibrotic treatments. Small animals such as mice and rats are most commonly used pre-clinical models as they possess ~30,000 protein-coding genes that are homologue to human genome (Chinwalla et al., 2002). Relatively short breeding time, minimal housing and maintenance costs of small animals as compared to large ones increase the number of animals per experiment improving statistical power. These factors add to the value of utilizing rodents for producing genetically modified, pharmaceutical or surgical based models of cardiac fibrosis (Patten and Hall-Porter, 2009). To establish novel imaging techniques for detecting diffuse fibrosis which cannot be achieved with methods discussed in the previous section 1.3, a mouse of pressure overload such as the mouse model of transverse aortic constriction (TAC) is ideal. TAC mimics the clinical manifestation of hypertensive disease including cardiac hypertrophy and interstitial fibrosis with an increased ventricular mass (Patten and Hall-Porter, 2009). Another model of heterogeneously distributed interstitial and perivascular fibrosis is ageing. An aged heart exhibits development of left ventricular (LV) hypertrophy, ECM deposition and cardiomyocyte senescence even in absence of underlying pathology. Progressive collagen deposition at interstitial and perivascular spaces possesses adverse effects on cardiac functioning in aged hearts due to myocardial stiffness (Lima, 2017; Meschiari et al., 2017; Obas and Vasan, 2018). Early diagnostics and interventions can help to rescue an aged heart from developing heart failure. In comparison to rodents, imaging cardiac aging-associated fibrosis in non-human primates (NHPs) can provide highly clinically relevant data, as their genetic, metabolic, and physiologic regulation is similar to humans and equally important is the ability to control diet, environment, and breeding. Most importantly, other laboratory species, such as rodents or even large animal models (pigs or sheep) are unable reflect a comparable life span as humans (Moussavi et al., 2020; Velayutham et al., 2019). Among NHPs, using common marmoset monkeys (*Callithrix jacchus*) model in aging research provides various advantages such as a relatively small body size, short generation time and availability of transgenic models (Moussavi et al., 2020). With maximum life expectancy of about 16 years, marmoset have shortest lifespan as compared to other anthropoid primates. Pathologies concurring due to old age in marmosets usually occur at the age of 7 years or older (Tardif et al., 2011).

1.6. Pathophysiology of pulmonary fibrosis

Apart from the detrimental role of fibrosis in cardiac diseases, interstitial lung diseases are also often associated with development of fibrosis which is caused by a multitude of factors including genetic, autoimmune, drug-induced, infections and environmental factors. If lung fibrosis is due to known etiology, removal of initial insult may result in spontaneous resolution of fibrosis and/or applying a short course of steroids can also help prevent fibrosis progression (Thannickal et al., 2004). On the other hand, idiopathic pulmonary fibrosis (IPF) possesses a serious healthcare challenge because it is a chronic disease of unknown etiology which affects about three million people worldwide with a median survival of 3-5 years post diagnosis. Historically, IPF was regarded as chronic inflammatory disorder, which progressed to established fibrosis overtime. Recent studies, however, reveal that anti-inflammatory therapies do not improve the disease prognosis and immunosuppressive therapeutic strategy incorporating azathioprine and prednisolone was shown to increase mortality. IPF is now defined as a complex interaction of multiple environmental and genetic risk factors with repetitive micro-injuries to ageing pulmonary epithelium. These micro-injuries trigger aberrant epithelial–fibroblast communication, the induction of ECM producing myofibroblasts and remodeling of the lung interstitium (Richeldi et al., 2017; Sgalla et al., 2018).

1.7. Anatomical and functional imaging of lung fibrosis

1.7.1 X-ray imaging of lung fibrosis

As oppose to heart, which requires contrast agent administration for in-vivo visualization of soft tissue (muscle), radiographic x-ray imaging and CT of lungs are based on the visualization of air versus electron dense tissue contrast, that enables typical characterization of the diseased lung, such as interstitial patterns, pleural effusion, bronchial thickness, opacification and calcification (Mathieson et al., 1989). In humans, the current diagnosis of IPF manifests unusual interstitial pneumonia (UIP) histopathologically and also a subpleural and basal predominant reticulation with honeycombing on high-resolution computed tomography (HRCT) of the chest. Other diagnostic methods including bronchoalveolar lavage fluid and pulmonary function testing cannot detect early stage IPF. HRCT is regarded as a standard clinical practice for identifying IPF. However, it identifies only 37 to 67% of patients with histological UIP; therefore, a surgical lung biopsy is recommended for confirmation of IPF

(Lynch and Belperio, 2011; Richeldi et al., 2017). Surgical lung biopsies similar to cardiac biopsies involve risk posing invasive procedures and even worse these biopsies are not representative for the entire organ. Recently, micro-CT has become a promising tool for imaging the lung at micro-level not only ex-vivo or in-situ but also in-vivo in pre-clinical models. Lovric *et al.* studied lung inflation and deflation patterns in mice at a spatial resolution down to $1.1 \times 1.1 \mu\text{m}^2$ in-vivo (Lovric et al., 2017). These findings highlight the potential of micro-CT based imaging for morphological as well as functional evaluation of lung fibrosis progression in live animals.

1.7.2 Pulmonary magnetic resonance imaging

In humans, anatomical imaging using MRI enables 3D pulmonary angiography and distinguishes between healthy and fibrotic lung by characterizing vessel blockage in fibrotic due to enlarged, inflamed and mucus lined airways, whereas the healthy lung displays well-defined blood vessels with smooth lining (Miller et al., 2014). This MRI based morphological assessment is possible in both clinical and non-clinical models (Lonzetti et al., 2019; Velde et al., 2014).

In the context of functional imaging, traditional proton MRI involves various challenges due to respiratory motion, low $T2^*$ values and a relatively small water density (Theilmann et al., 2009). Efforts to enhance MRI functional imaging ability involves the use of inhaled contrast agents, such as molecular oxygen and hyperpolarized noble gases. However, the use of a ventilation MRI approach, due to the high cost of the procedure and poor availability of inhalation-based contrast agents, is limited to a few expert centers only (Baues et al., 2017; Kruger et al., 2016). To overcome these drawbacks, a mode of MRI called as the self-gated non-contrast-enhanced functional lung (SENCEFUL) has been developed which allows site-specific ventilation imaging (Veldhoen et al., 2017). So far it has been performed on patients with cystic fibrosis. However, this approach is susceptible to motion induced artefacts and require further longitudinal evaluation for standardization (Veldhoen et al., 2017). In pre-clinical studies, particularly small animals and rodents MRI is prone to scattering which results in relatively poor resolution for functional and anatomical pulmonary imaging (Adamson et al., 2017; Gammon et al., 2014; Zhou et al., 2015).

1.7.3 PET imaging

Early detection of lung fibrosis is possible by molecular imaging using PET probes such as ^{18}F -Fluciclatide against integrins and ^{68}Ga -CBP8 that targets collagen. These probes have shown promising results in mouse models of lung fibrosis; however, clinical application requires further testing (Chen et al., 2017). Nonetheless, PET imaging alone is unable to assess pulmonary function, hence, has to be performed in combination with CT or MRI.

1.7.4 Spirometry and Plethysmography for functional assessment

The clinical pulmonary function test known as spirometry is a routine medical procedure for monitoring functional capacity and compliance of the lungs in IPF patients. Impaired survival in IPF patients has been associated with an increased ratio of forced expiratory volume in 1 s and forced vital capacity (FEV1/FVC ratio), change in FVC/carbon monoxide transfer factor and reduced total lung capacity. However, there is a lack of consensus for interpreting lung function testing in IPF due to variability in data published on the subject. Further, such functional assessment cannot differentiate IPF from other pulmonary anomalies and require further diagnostic procedure using HRCT or histological classification (Casan Clarà et al., 2016). The preclinical barometric or chamber-based plethysmography is the most common method for performing lung function test (Lim et al., 2014). Other preclinical methods such as forced oscillation technique require invasive intubation procedures some of which tend to be terminal (McGovern et al., 2013). The main limitation of non-invasive plethysmography techniques is that the functional alterations are dependent on the pressure changes, and the relationship between chamber pressure and the lung mechanics might be non-linear (Adler et al., 2004; Zhang et al., 2009). In a recent study, Hülsmann *et al.* defined various factors that compromise the precision of plethysmography measured lung volume including the conditioning of air within the residual volume and death space that is recruited during inspiration. They further reported that the “enhanced pause” (Penh) parameter is a consequence of active expiration by the animal to overcome airway resistance rather than direct measure of airway resistance (Hülsmann et al., 2021). These findings raise concerns over the standardization and validity of the plethysmography acquired parameters to assess lung function particularly in diseased mice.

X-ray based lung function

Unlike in cardiac research, the current methods for measuring lung function in pre-clinical studies are not reliable. Plethysmography is the most commonly used method for pre-clinical lung function assessment, which may involve intrinsic problems in mouse models such as intubation or restraining. Alternatively, the use of unrestrained whole-body plethysmography (UWBP) does overcome these limitations, however, the reliability and standardization of the plethysmography parameters is debatable as discussed in previous section 1.7.4. Hence, the development of novel and sophisticated non-invasive techniques is fundamentally required in pre-clinical and clinical settings for advanced lung function measurements in combination with morphological assessments for early and reliable detection of pulmonary fibrosis and for monitoring disease progression and response to therapeutics.

Recently Dullin *et al.*, developed a non-invasive lung function method based on planar cinematic X-ray imaging of the chest known as the x-ray-based lung function (XLF). XLF has been previously applied to assess the lung function in isoflurane-anesthetized mice with allergic airway inflammation (AAI) (Figure 6). XLF measurements provide various quantitative parameters that can reflect upon acute inflammatory response, airway resistance and lung compliance (Dullin et al., 2016). These parameters are summarized in table 1.

Using minimal radiation dose and short exposure time, XLF previously showed significantly higher sensitivity than WBP for reliable assessment of lung function in AAI mice and mice treated with dexamethasone (Dullin et al., 2016) (Figure 6). Commonly, precise lung function assessment in pre-clinical models particularly in response to treatment is performed using terminal and invasive forced oscillation technique. XLF, on the contrary, is a non-invasive approach that enables longitudinal application which dramatically reduces the numbers of animals required and enhances the predictive value of the data obtained due to the absence of inter-subject variations (Dullin et al., 2016; Markus et al., 2017). However, the functional parameters of XLF are not exactly relatable to commonly used lung function techniques including WBP and micro-CT and none of the XLF parameters represented the lung volume.

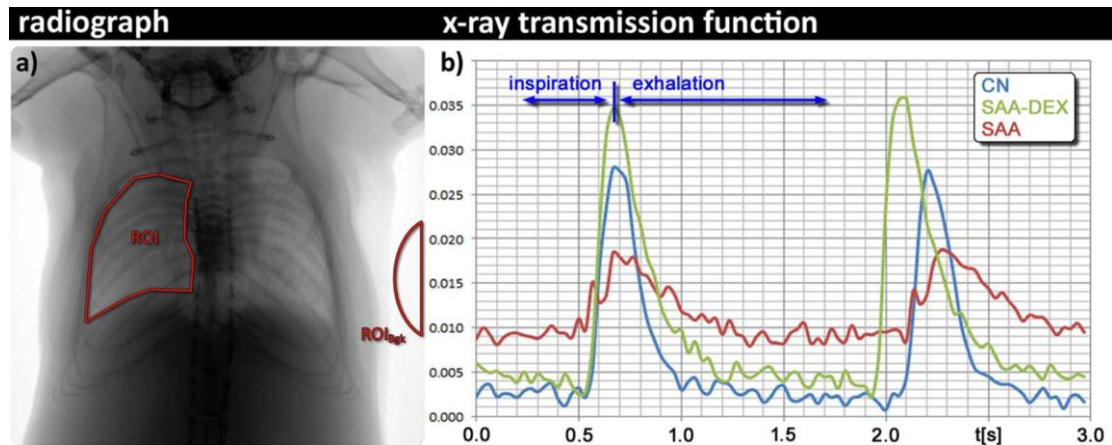


Figure 6: Breathing induced modulations in the x-ray transmission at the chest region over time.

a) Exemplary radiograph showing the average x-ray transmission function over time which is measured at a region of interest (ROI) of the lung and normalized by the background intensity (ROIBgk). b) Exemplary two breathing cycles of a healthy control animal CN (blue curve); a mouse with the severe acute airway inflammation model (SAA) (red curve) and mouse from the same model that had been treated with dexamethasone before each challenging step (SAA-DEX, green curve). The SAA mouse presents a strong reduction in the area under the curve owing to the lower air content in the lung at the peak inspiration and an asymmetric shape of the breathing event with a shorter time to peak. The treated mouse (SAA-DEX) demonstrates XTF properties comparable to the healthy control mouse CN. Image modified from Dullin et al., 2016.

Table 1: Functional parameters of X-ray based lung function

Parameter	Relates to/is influenced by:
b_1	Shift of the curve/time of inhalation
b_2	Asymmetry of the curve
b_3	Speed of air exchange
b_4	Asymmetry of the curve
b_5	Air volume/inflammation/air trapping
L, s	Breath length
AuC	Total air volume/inflammation
$AnIso$	Anisotropy index (time of inhalation/exhalation)
BP	Periodicity of the breathing events
T_{peak}, s	Time to reach maximum inhalation volume
$T_{in}, \%$	Relative time of inhalation (t_{peak}/l)
$ATrp$	Air trapping

XTF, X-ray transmission function; L, length; AuC, area under the curve of the breathing peak; AnIso, anisotropy index; BP, breath periodicity; ATrp, air trapping

Limitations of current diagnostics tools

The current diagnostic can only reliably detect IPF at late stage of disease progression implying an urgent need for new and advanced diagnostic strategies for an early assessment of IPF for effective earlier interventions. Pre-clinical studies are a vital tool to establish and understand suitable diagnostic techniques and therapies for IPF, despite their limitation to mimic the irreversible nature of human pulmonary fibrosis. However, techniques for longitudinal, non-invasive and clinically relevant lung function measurement in animal models of lung fibrosis are lacking. We developed advanced XLF approach to overcome the address these limitations which is presented in chapter 3.

1.8. Preclinical models of pulmonary fibrosis

Various genetic and environmental models of pulmonary fibrosis help understand development of fibrosis by known causes and in case of IPF they offer insights into pathogenesis of intractable factors contributing to fibrosis. Bleomycin induced mouse model of lung fibrosis is one of the most common model to develop and investigate diagnostic tools, pathophysiology of fibrosis and response to anti-fibrotic treatments since past four decades (B. Moore et al., 2013) (Figure 7). This mainly because in comparison to silica, asbestosis and ageing model, bleomycin induced lung fibrosis is developed at much faster rate (B. Moore et al., 2013). Bleomycin is an antibiotic isolated from *Streptomyces verticillatus*, which is used as a chemotherapeutic agent to treat germinative tumors and lymphomas in humans. However, the use of bleomycin therapy is limited due to its pro-fibrotic properties, leading to the development of pulmonary fibrosis in 5-10 percent of patients receiving it (Ruscitti et al., 2017). In rodents, it acts as a strong oxidative agent which causes lung injury by DNA breakage and production of reactive oxygen species (ROS). The initial inflammatory phase is followed by a peak fibrotic response which is resolved over-time (B. Moore et al., 2013; Ruscitti et al., 2017) (Figure 7).

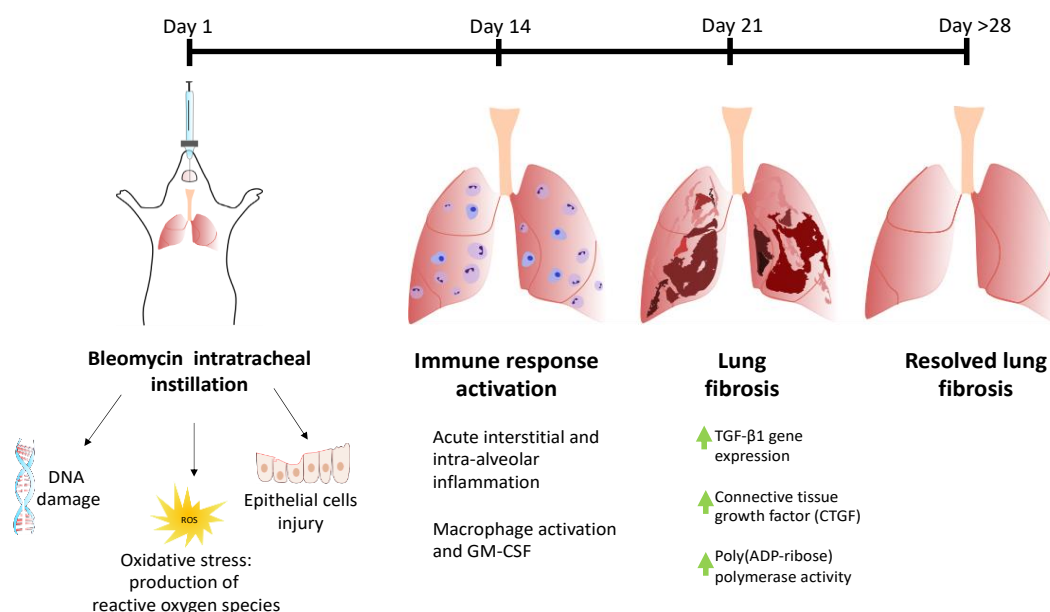


Figure 7: Schematic showing timeline and mechanism of the bleomycin induced mouse model of lung fibrosis. Bleomycin is able to break DNA in the presence of iron and oxygen with a high production of reactive oxygen species (ROS) and reactive nitrogen species (RNS), consequently leading to epithelial cell damage and injury. Intra-tracheal instillation of bleomycin induces bronchiolocentric accentuated fibrotic changes triggering acute interstitial and intra-alveolar inflammation, macrophage activation and expression of granulocyte-macrophage colony stimulating factor (GM-CSF) and some interleukins around day 14. Following the acute inflammatory event, other cytokines such as transforming growth factor beta (TGF- β) and connective tissue growth factor (CTGF) are up-regulated during the fibrotic stage at ~21 days. Without further administration of bleomycin, the mice spontaneously resolve fibrosis after ~28 days. [Schematic prepared using Inkscape (Inkscape Project, 2020. Inkscape, Available at: <https://inkscape.org>)].

Aims and hypothesis

The inadequacies of current imaging techniques for detecting fibrosis require novel next generation imaging tools for i) label-free, high-resolution, multiscale and multimodal imaging of cardiac structural remodeling in fibrotic hearts and ii) advanced non-invasive x-ray based lung functional assessment with biomedically relatable parameters in progression of lung fibrosis and in response to therapy.

Label-free imaging of cardiac fibrosis

We hypothesized that post-fibrosis, cardiac tissue remodeling is not restricted to localized regions of fibrotic lesions, but it also alters the structural architecture of the surrounding cardiac tissue. We further postulated that various types of fibrosis due to distinct underlying causes result in common modulations of the overall cardiac structures which in future can add more dimensions for detecting fibrosis and also provide new therapeutic targets. To address our hypothesis, the aim of my thesis is to evaluate and characterize the structural alterations following fibrosis within the diseased and aged heart using a label-free imaging approach in mice and non-human primates.

For this purpose, the following objectives were addressed:

- i) Assessment of structural changes in fibrotic and hypertrophic hearts obtained from wild-type mice subjected to TAC by establishing SHG imaging in combination with spatially-resolved x-ray diffraction.
- ii) Comprehensive assessment of collagen deposition and myofibril morphology using SHG imaging in a mouse model of TAC and NHP model of aging.
- iii) Volumetric quantification of collagen and myosin emitted SHG in different age groups of NHP.
- iv) Validation of the imaging data obtained using standard diagnostic methods including echocardiography, histology and/or immunohistochemistry.

Advanced X-ray based lung function

Owing to extensive discrepancies in current diagnosis of lung fibrosis in mouse models using functional assessment, we aim to improve the XLF approach to provide parameters that can be applied for direct and reliable assessment of lung fibrosis in pre-clinical models and also possess a high translational value. Since the functional parameters of XLF are currently not

exactly relatable to commonly used preclinical lung function techniques including UWBP and micro-CT, the aim of this part of my thesis is to redefine the XLF algorithm as a biomedically relevant preclinical non-invasive technique by addressing the following objectives:

- i) Establishing a correlative set-up for simultaneous lung function assessment using XLF, micro-CT and UWBP.
- ii) Acquiring lung volumes from simple low dose radiographic XLF measurements.
- iii) Correlating the lung volumes obtained from XLF with micro-CT and UWBP.

Individual contribution to the manuscripts

Two peer-reviewed articles and one submitted manuscript are considered for this cumulative thesis to fulfill the rules and regulations of the PhD program Molecular Medicine (MolMed) of the Göttingen Graduate Center for Neurosciences, Biophysics, and Molecular Biosciences (GGNB) that is part of the Georg-August University School of Science (GAUSS):

Peer-reviewed publications:

1. Nicolas JD, **Khan A**, Markus A, Mohamed BA, Toischer K, Alves F, Salditt T. X-ray diffraction and second harmonic imaging reveal new insights into structural alterations caused by pressure-overload in murine hearts. *Sci Rep.* 2020 Nov 9;10(1):19317. doi: 10.1038/s41598-020-76163-6.

Shared first and last authorship

JDN, AK, FA, AM and TS designed research. AK performed second harmonic imaging with help from AM and supervision by FA. AK performed analysis of second harmonic data, with input from JDN and TS. JDN and TS performed synchrotron measurements. JDN analyzed synchrotron data, with input from TS. JDN and AK prepared the figures. BAM and KT contributed expertise in mouse models, sample preparation and performed the in-vivo echocardiography experiments. AK and AM performed histological analysis. FA supervised the cardiovascular research program. All authors discussed the results. AK, JDN, AM, TS and FA wrote the manuscript.

2. **Khan A**, Markus A, Rittmann T, Albers J, Alves F, Hülsmann S, Dullin C. Simple low dose radiography allows precise lung volume assessment in mice. *Sci Rep.* 2021 Feb 18;11(1):4163. doi: 10.1038/s41598-021-83319-5.

AK, CD, FA and SH designed the research. AK, AM, CD, and SH performed the experiments with the help from JA. TR designed the software for micro-CT lung volume measurements (RetrospeCT) with assistance from CD. CD designed the XLF software (XLFfinal). SH performed data analysis for plethysmography data. AK and CD performed data analysis for XLF and micro-CT data. AK prepared the figures and wrote the manuscript with the input from CD and SH. All authors discussed the results and proofread the manuscript.

Submitted manuscript:

3. **Khan A**, Ramos-Gomes F, Markus A, Mietsch M, Hinkel R, Alves F. 2021. Label-free imaging of age-related cardiac structural modulations in non-human primates using multiphoton nonlinear microscopy. (Submitted to *Biomedical Optics Express*).

AK, FA and RH designed the research. AK performed the experiments with the input from FRG and AM. AK acquired the data. The samples and animal data were provided by MM and RH. AK analyzed the 3D data and 2D images were analyzed by AK and FRG. AK prepared the figures and wrote the manuscript. All authors discussed the results and proofread the manuscript.

Chapter 1 – X-ray diffraction and second harmonic imaging reveal new insights into structural alterations caused by pressure- overload in murine hearts

Jan-David Nicolas, Amara Khan*, Andrea Markus, Belal A. Mohamed, Karl Toischer, Frauke Alves, & Tim Salditt*

Reproduced from Scientific Reports 10, 19317 (2020).

Shared first authorship*

We demonstrate a label-free imaging approach to study cardiac remodeling of fibrotic and hypertrophic hearts, bridging scales from the whole organ down to the molecular level. To this end, we have used mice subjected to transverse aortic constriction and imaged adjacent cardiac tissue sections by microfocus X-ray diffraction and second harmonic generation (SHG) imaging. In this way, the acto-myosin structure was probed in a spatially resolved manner for entire heart sections. From the recorded diffraction data, spatial maps of diffraction intensity, anisotropy and orientation were obtained, and fully automated analysis depicted the acto-myosin filament spacing and direction. X-ray diffraction presented an overview of entire heart sections and revealed that in regions of severe cardiac remodeling the muscle mass is partly replaced by connective tissue and the acto-myosin lattice spacing is increased at these regions. SHG imaging revealed sub-cellular structure of cardiac tissue and complemented the findings from X-ray diffraction by revealing micro-level distortion of myofibrils, immune cell infiltration at regions of cardiac remodeling and the development of fibrosis down to the scale of a single collagen fibril. Overall, our results show that both X-ray diffraction and SHG imaging can be used for label-free and high-resolution visualization of cardiac remodeling and fibrosis progression at different stages in a cardiac pressure-overload mouse model that cannot be achieved by conventional histology.

Introduction

Heart failure is a common disease amongst the elderly population entailing a high mortality rate. Both structural and functional changes contribute to heart failure. The deposition of extracellular matrix (ECM) either within the interstitial space or by replacement of the cardiac muscle is a common histopathological finding accompanying heart failure^{1,2,3,4}. Progression of fibrosis involves inflammatory stimuli, which in turn initiate pro-fibrotic signaling. ECM remodeling and impaired cardiac muscle function are hallmarks of cardiac fibrosis which consequently lead to increased stiffness of left ventricle and impairment of mechano-electric coupling, thus causing arrhythmias. Cardiac fibrosis can occur due to aging and other heart-related pathophysiology such as hypertensive heart disease^{2,5}. Transverse aortic constriction (TAC) is a well-established animal model of pressure-overload induced cardiac hypertrophy and failure. TAC mimics hypertensive heart disease in patients correlating to the clinical manifestation of pressure overload. Consequently, it causes cardiac hypertrophy and interstitial fibrosis in mice with an enlarged ventricular mass^{6,7}.

While the importance of cardiac remodeling in heart failure is undisputed, the molecular structural changes involved in the progression of cardiac hypertrophy and fibrosis have so far not been at the focus of medical research. Moreover, there is a lack of understanding of the molecular mechanisms that underlie the interaction of cardiomyocytes with surrounding extracellular components in the healthy and fibrotic myocardium. For this purpose, imaging techniques are required to visualize cardiac remodeling of fibrotic and hypertrophic hearts. So far only histology and immunohistochemistry (IHC) are used as standard techniques for assessing the structural composition of the myocardium but these methods lack adequate resolution and specificity to visualize sub-cellular structures. Ideally, the imaging techniques should be able to probe the molecular structure and alterations thereof associated with pathologies, and at the same time also cover the entire cross section of a heart at sub-molecular level to find and to quantify the affected regions.

Alterations in heart muscle at the molecular level can be studied by using X-ray diffraction. For example, X-ray diffraction can be used to assess kinetics of myosin binding in actively contracting muscles^{8,9,10,11}. One main disadvantage of the classical muscle diffraction technique is the requirement to extract intact muscle fibers from the heart. Contrarily, recent progress in X-ray optics has made it possible to focus the beam down to a few micrometers and even nanometers¹². By sacrificing resolution in reciprocal space, millions of X-ray diffraction

experiments can be performed sequentially by raster-scanning the X-ray beam over the sample and collecting a diffraction pattern in each spot¹³. Such an experiment offers real-space resolution and structural information, most importantly filament lattice spacing, filament orientation and degree of filament alignment. Spatially-resolved X-ray diffraction has been used for single cardiomyocyte imaging, where it was combined with STED microscopy to obtain a multiscale overview of cardiac sub-micron structures¹⁴. Most recently, these cells could even be imaged alive in a hydrated environment¹⁵. The overall tissue structure was so far only imaged in a proof-of-concept study¹² on a single tissue section of a non-pathological heart and later on a thin section of engineered cardiac tissue^{16,17}.

For the present analysis more than 17.8 million diffraction patterns each with a size greater than 4 megapixels were analyzed, which requires a fast detection scheme coupled with a fast and robust data analysis. This is to date the largest screening of cardiac and more generally hydrated soft biological tissue by means of spatially-resolved X-ray diffraction.

A second powerful label-free imaging method for cellular scale visualization of biological tissue is second harmonic generation (SHG) imaging¹⁸. In contrast to X-ray diffraction, it does not depend on or require long-range or medium-range molecular order, but only relies on molecular inversion symmetry. It is based on the non-linear optical effect of SHG in non-centrosymmetric polarizable medium. Accordingly, in a coherent optical process the combined absorption of two excitation photons results in the generation of a single photon of exactly twice the energy and half the wavelength of the original excitation wavelength¹⁹. Interestingly, both collagen and myosin fibers generate intrinsic SHG, making this imaging approach ideal for investigating ECM remodeling and muscle integrity following fibrosis and hypertrophy in cardiac tissue^{20,21}. Despite the remarkable advantages of SHG imaging over conventional histology such as high resolution, specificity and reproducibility, the use of this approach for investigating cardiac remodeling in diseased tissue is still in its infancy. SHG imaging of diseased cardiac tissue has so far focused almost exclusively on the detection of collagen as an indicator of ECM remodeling but has not studied the myosin fibers and overall tissue architecture²². In fact, studies targeting the pathological alteration in myosin filaments have been performed at cellular level only²³.

In this study, our primary aim was to establish spatially-resolved X-ray diffraction and SHG imaging for assessing structural changes in fibrotic and hypertrophic hearts obtained from wild-type mice subjected to TAC. Using X-ray diffraction, we demonstrated that the acto-myosin

lattice spacing in the areas of severe pathological remodeling of TAC hearts is higher compared to controls and more heterogeneously distributed, and that the semi-crystalline order in damaged regions is slightly reduced. The evaluation of lattice spacing could also reveal structural features, such as a ring-type structure in the myocardium, that would not be observable in classical X-ray diffraction. These findings were further complemented by SHG imaging which revealed sub-cellular deterioration of myofibrils and surrounding tissue due to underlying ECM remodeling and collagen deposition.

Materials and Methods

Animal model

For the pressure-overload model, eight weeks old C57Bl/6N mice were operated with transverse aortic constriction as described previously^{7,38}. Sham animals underwent the same procedure except the banding of the aorta. Mice were euthanized 16 weeks post TAC surgery and whole hearts were excised. All animal in-vivo procedures were performed in compliance with the guidelines of the European Directive (2010/63/EU) and the German ethical laws and were approved by the administration of Lower Saxony, Germany (No. 33.8-42502-04-17/2585). Sample preparation

Sample preparation

Freshly explanted hearts were weighed, briefly washed in phosphate buffer saline (PBS) and then fixed in 4% formaldehyde solution (FA) overnight at room temperature (RT). Hearts were then cut into transverse tissue sections of varying sizes such that adjacent tissue sections from the same heart sample were used for X-ray diffraction, SHG imaging and histology (Fig. 1A). Briefly, for sectioning, hearts were embedded in 5% agarose and were cut into 30 μ m and 1 mm sections using a vibratome (VT1000 S; Leica Biosystems). The 30 μ m thick tissue sections were used for X-ray diffraction and 2P-LSM and were stored in PBS containing 0.04% sodium azide until the day of the experiment. The 1 mm sections were embedded in paraffin for histology.

Scanning X-ray diffraction

The spatially-resolved X-ray diffraction experiments were carried out on 30 μ m cardiac tissue slices, which were mounted between two polypropylene foils as described before in Nicolas et

al. 2017 at the microfocus endstation of the beamline ID13 at the European Synchrotron Radiation Facility (ESRF)¹². The undulator gap was adjusted to generate an X-ray beam with a mean energy of $E = 13.0$ keV and bandwidth of $\Delta E = 10^{-4} E$, as defined by a channel-cut Si(111) monochromator. The beam was focused by a combination of compound refractive lenses (CRL) inside a transfocator. The beam size in the focus was estimated from vertical and horizontal scans across the edges of two gold wires and was determined at $2.9 \mu\text{m}$ (horizontal) \times $1.4 \mu\text{m}$ (vertical). A helium-filled tube was placed directly behind the focus of the beam to suppress air scattering along the beam path until approximately 10 cm behind the focus position where a lead wire with a diameter of 1 mm was used to block the primary beam. A calibrated diode was used to determine the total photon flux $I_0 = 1.57 \times 10^{12}$ photons s^{-1} . Given E , I_0 and an exposure time of 10 ms, one can estimate the dose D at $D = I_0 \tau E \mu/(\rho \Delta x \Delta y) = 2.54$ MGy, where $\mu/\rho = 3.1582 \text{ cm}^2 \text{ g}^{-1}$ is the mass absorption coefficient estimated for skeletal muscle and $\Delta x \times \Delta y$ the focal size of the beam (FWHM).

Immunofluorescence staining

Agarose embedded $30 \mu\text{m}$ vibratome sections were washed three times in TBS-T solution (20 mM Tris, 150 mM NaCl, 0.1% Tween 20). The tissue sections were incubated free-floating in 500 μL of DRAQ5 (Biostatus, 1:1000) for nuclear staining and were mounted on a glass slide using Immu-mount (Thermo Fisher Scientific).

Second harmonic generation imaging

SHG imaging was performed for label-free imaging of myosin and collagen on $30 \mu\text{m}$ sections stained with the nuclear dye DRAQ5. Images were acquired with a two photon laser scanning microscopy (2P-LSM) setup (TriM Scope II, LaVision BioTec) equipped with a femtosecond-pulsed titanium-sapphire (Ti:Sa) laser (Chameleon Ultra II; Coherent). A Zeiss W Plan-Apochromat 20x (NA 1.0) water immersion objective was used for image acquisition. Multi-photon signals from tissue sections were detected in the backward and forward direction. For excitation of the SHG from the cardiac tissue, the Ti:Sa laser was set at 810 ± 5 nm and the nuclei stain DRAQ5 was excited at 720 ± 5 nm. The emitted light was split by a 495 nm and T560 nm long pass dichroic mirror (Semrock). The SHG signal was collected through a 405 ± 5 nm (FF01-405/10; Semrock) bandpass filter at photomultiplier (PMT) detectors (Hamamatsu) in the forward direction. The emitted fluorescent signal from nuclear stain was detected at a GaAsP PMT detector (Hamamatsu) in backward direction. All images were collected and

processed with ImSpector (LaVision BioTec) and Fiji³⁹. For the overview images an image size of $336 \times 336 \mu\text{m}$ with 1024×1024 pixels and a pixel dwell time of $2.1 \mu\text{s}$ was used. Magnified images at the region of interest (ROI) were acquired using $100 \times 100 \mu\text{m}$ image size, 916×916 pixels and $5.5 \mu\text{s}$ pixel dwell time.

Histology and immunohistochemistry

The paraffin-embedded 1 mm cardiac tissue slices from regions adjacent to tissue sections used for X-ray diffraction and SHG imaging were cut into $2 \mu\text{m}$ sections (Fig. 1A). The sections were deparaffinized and dehydrated followed by haematoxylin & eosin (H&E) and Masson's Trichrome staining (MTS) was performed as described before^{40,41}.

For immunohistochemistry (IHC), deparaffinized sections were boiled for 20 min in Target Retrieval Solution (Dako) to perform the antibody staining with: anti α -SMA (clone 5694, abcam, 1:1000, overnight at 4°C); anti CD68 (ab125212, abcam, 1:500, 1 h at 37°C) and anti CD45 (clone 30-F11, 1:250, overnight at 4°C) to identify the presence of activated fibroblasts, macrophages and leukocytes, respectively. After washing, the secondary antibody (anti-rabbit-horseradish-peroxidase, undiluted, Histofine) was added for 30 min at RT. Sections were counterstained with haematoxylin.

The images were acquired with an Axiovert 200 M inverted microscope (Carl Zeiss Microscopy GmbH). Image generation and processing were performed with the software AxioVision Rel.4.6 (<https://carl-zeissaxiovisionrel.software.informer.com/4.6/>) and Fiji³⁹, respectively.

Statistical analysis

Maps of structural parameters obtained from the X-ray diffraction data and presented in Fig. 2 were segmented semi-automatically using k-means clustering. A five-dimensional dataset consisting of five parameters used in least-square fitting of the one-dimensional structure factors was used for the analysis and three clusters were isolated. Numerically, the k-means implementation of the open source library VLFeat 42 was used for this task. Histograms of lattice spacing shown in Figure S5 were modeled using a pseudo-Voigt profile, while the mode of the distribution was obtained from a kernel density estimation using the function `ksdensity` available in Matlab 2018b (MATLAB, Mathworks Inc). A two-tailed paired Student's t-test

implemented in MATLAB with a p-value of 0.05 (*) as margin for statistical significance was used for the statistical analysis of the data.

Results

Comparative imaging of cardiac tissue using X-ray diffraction, SHG imaging, and histology

Mice subjected to TAC-operation developed cardiac hypertrophy within 16 weeks post TAC surgery depicted by significantly higher weights of the TAC hearts ($350 \text{ mg} \pm 25 \text{ mg}$; p-value = 0.002) as compared to healthy hearts ($150 \text{ mg} \pm 25 \text{ mg}$) (Supp. Section 1, Table S1). Heart failure with impairment of cardiac function was also evident by echocardiography (Supp. Section 1, Table S2). TAC hearts presented different severity of cardiac remodeling and were composed of enlarged cardiomyocytes with an overall increase in ECM content (Fig. S1 and Fig. S2). To perform X-ray diffraction, SHG imaging, histology and IHC on adjacent sections, excised hearts were sectioned according to the protocol sketched in Fig. 1A. Note that the sectioning scheme was adapted to obtain tissue sections from similar regions from TAC and sham hearts. Tissue sections of $30 \text{ }\mu\text{m}$ for X-ray diffraction and SHG imaging (in red) were cut at approximately one-third and two-third distance from base to the apex (denoted as region 1 and region 2, respectively), while 1 mm neighboring blocks (in blue) were used for histology. Figure 1 exemplifies the combined use of the complete set of available modalities depicting the analysis of neighboring transverse tissue cross sections obtained from the same TAC heart (TAC 2, see Supp. Section 4–5). The differences in the overall shape of the neighboring heart tissue sections occurred due to serial cutting of tissue sections of varying thicknesses from whole heart and subsequent differences in the mounting of tissue sections for each imaging modality. The paraffin embedding procedure furthermore causes a slight shrinkage of the tissue, which may influence the appearance of the histological slice.

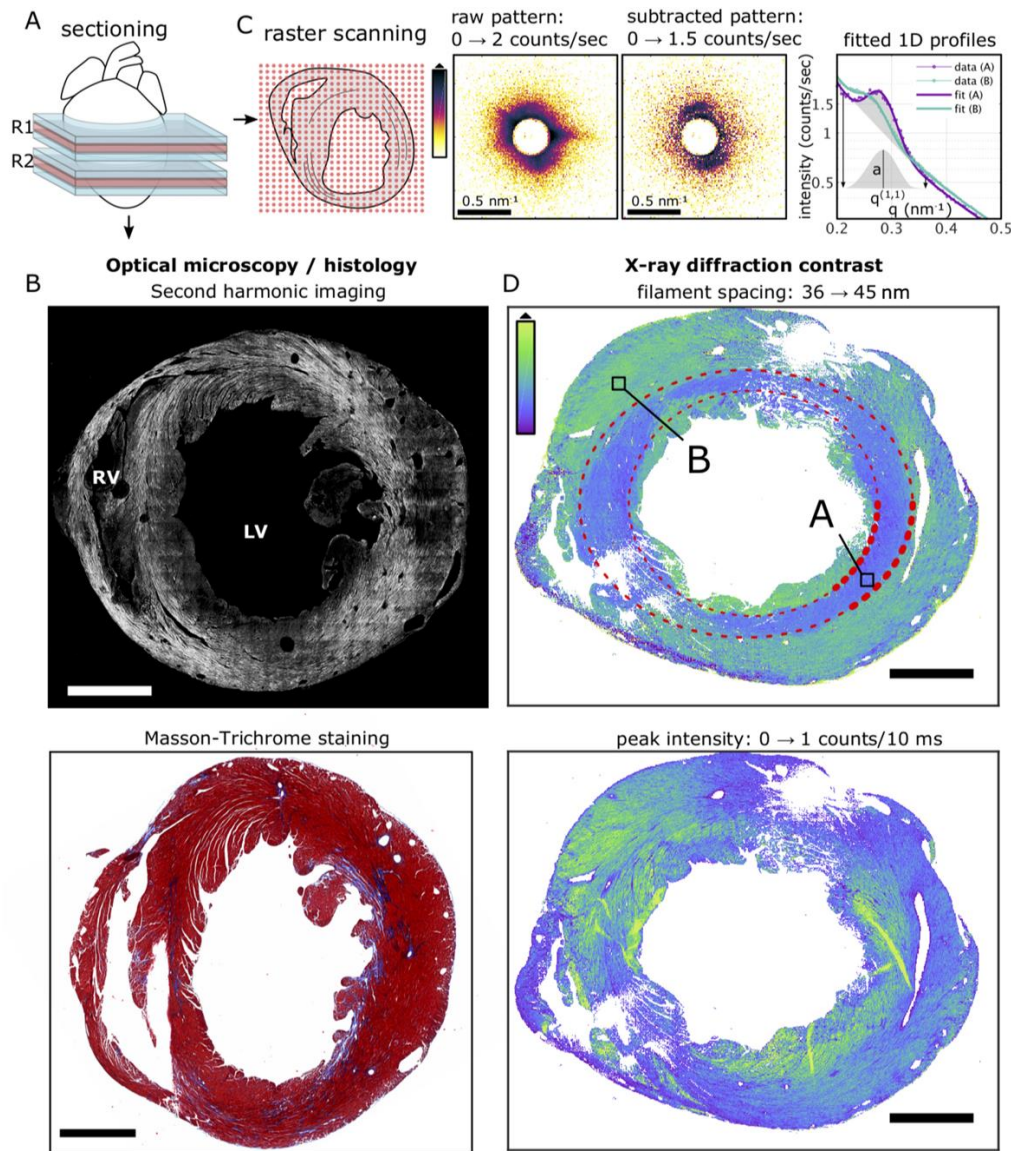


Figure 1: Comparative multi-imaging approach using SHG imaging, histological analysis and X-ray diffraction. (A) Hearts were sectioned in a pre-defined order. Tissue sections for X-ray diffraction and SHG imaging (in red) were cut at approximately 1/3 and 2/3 distance from base to apex, namely region 1 (R1) and region 2 (R2), respectively, while 1 mm neighboring blocks (in blue) were used for histology and IHC. (B) SHG (top) from myosin and collagen are shown in white and MT stained neighboring tissue section (bottom) depicts hypertrophy and interstitial fibrosis in which muscle is stained red and collagen deposition in blue. (C) Data taken by X-ray diffraction were first background-subtracted, angularly averaged and fitted by a model function before a map of a fit parameter such as filament spacing, and peak intensity could be created. (D) Filament spacing in the bulk tissue (top) is around 42 nm except for an inner ring marked between the red dotted lines, where 39 nm were measured. Peak intensity (bottom) is highest around the ventricle. All images were recorded on adjacent tissue sections obtained from the same TAC heart at region 2. Scale bar: 1 mm. RV right ventricle, LV left ventricle.

For SHG imaging, two-dimensional (2D) micrographs of 30 μm cardiac tissue slices were acquired using an average power of 40 to 50 mW at a wavelength of 810 nm for SHG emission (Fig. S7). A

stitched image of a tissue section is shown in Fig. 1B (upper panel) where the SH emission from the two cardiac harmonophores, i.e. myosin and collagen, are represented in white. Note that the stitched image presents an overview of the SH emission from an entire cardiac section, at a scale where SHG derived from myosin cannot be distinguished from the collagen originated SHG. The histological image (Fig. 1B, lower panel) represents a stitched image of a Masson's Trichrome (MTS)-stained adjacent heart tissue section from the same heart sample and shows the muscle stained in red while collagen in blue highlights regions of interstitial fibrosis.

X-ray diffraction data acquisition required three pre-processing steps, illustrated in Fig. 1C. The acto-myosin scattering signal was superimposed by intense scattering from the 1 mm thin lead beamstop wire. To perform accurate background subtraction, 20 empty frames in each line were averaged and used to subtract from the raw data in the respective line. The subtracted pattern now clearly shows the (1,1) reflection from the acto-myosin lattice while the (1,0) reflection was absorbed by the beamstop. Subtracted data were then angularly averaged to obtain one-dimensional (1D) profiles of the scattering signal as a function of the scattering angle θ , encoded in the wavevector transfer $q = 4\pi/\lambda \sin(\theta/2)$. The resulting intensity profiles $I(q)$ were then fitted using a model function comprised of a power-law decay and a Gaussian,

$$I(q) = S q^{-d} + I_p \exp(-(q - q_0)^2 / \sigma^2) + I_{bgr},$$

where the width σ of the Gaussian were fixed to 0.034 nm^{-1} , while the parameter S , the decay exponent d , the uniform background intensity I_{bgr} as well as the intensity I_p and lateral position q_0 of the Gaussian component, referred to here as peak intensity and peak position, were obtained from non-linear least square fitting. The lateral peak position q_0 was then converted to the filament spacing $a = 4\pi/q_0$ of the acto-myosin lattice. All processing steps were performed in MATLAB (MathWorks) using the nano-diffraction toolbox¹². From the fitted profiles it is already evident that the filament spacing can vary significantly. Figure 1D indicates that data was averaged within regions A and B.

Figure 1D shows how the filament spacing and the peak intensity, both structural parameters which can uniquely be assessed by scanning X-ray diffraction, vary throughout the cardiac tissue of the TAC heart. In this example, the filament spacing map reveals a central ring (highlighted in red) with lower filament spacing within the bulk of the tissue as compared to the remaining tissue. Three samples were found that exhibited this particular structural feature. The lattice spacing difference between the outer and inner ring was 1.7 nm, 2.2 nm and 2.4 nm, as detailed in Supp. Section 2.

X-ray diffraction imaging of sham heart tissue

Healthy tissue sections obtained from sham-operated hearts served as a control group. Figure 2 shows one example of two sections taken at region 1 and 2. In both regions, the peak intensity was, with more

than 1 counts/10 ms, significantly higher around the left ventricle than the bulk tissue with 0.22 counts/10 ms, estimated from the mode of the intensity distribution. The mode of the filament spacing distribution was determined at 38.6 nm and 38.9 nm in region 1 and 2, respectively, which is consistent with a previous observation by Nicolas et al. 2017¹², where the mode was found at 38.9 nm.

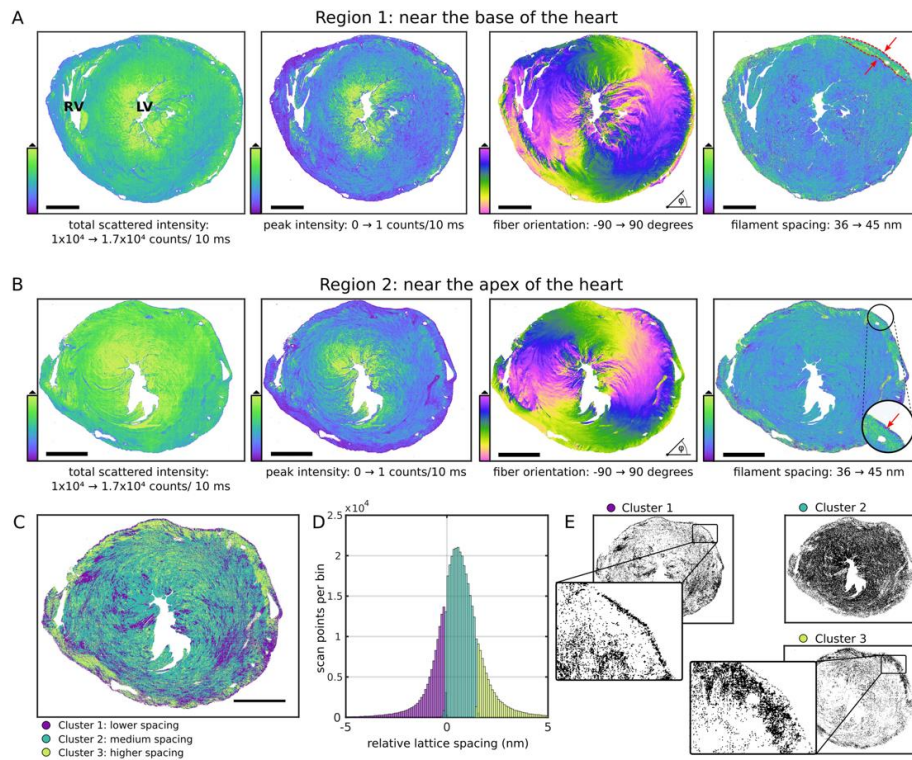


Figure 2: Comparison of structural parameters in region 1 (near the base of the heart) and region 2 (near to the apex of the heart) of a sham heart. (A) In region 1, the filament spacing is homogeneous, with the sole exception of a small layer in the outer myocardium where the filament spacing is increased, indicated by red arrows. (B) The filament spacing in region 2 resembles the distribution in region 1. In contrast to (A), the thin epicardial layer, indicated by a red arrow in a zoom inset, is now clearly visible. Note that in this layer the filament spacing is reduced. Sections from both regions appear very similar in shape and size. Total scattered intensity and peak intensity is increased around the left ventricle and filaments circulate smoothly around the left ventricle. (C) K-means clustering based on the five-dimensional dataset of fit parameters was used to identify three distinct clusters which are color-coded in (C). (D) Histograms of lattice spacings corresponding to the three clusters identified in (C). (E) Logical maps of the three clusters demonstrate more clearly, that cluster 1 with lattice spacings below 38.9 nm accounts well for the thin epicardial layer while cluster 2 represents the myocardium, with the exception of cluster 3 that highlights the outer myocardial layer with lattice spacings above 40.4 nm. Scale bar: 1 mm. *RV* right ventricle; *LV* left ventricle.

The outer layer of the myocardium, highlighted in red in Fig. 2A, has a higher filament spacing. This can be explained by the fact that these muscle fibers only support the structure of the heart while the inner myocardium generates the force of contraction. The lattice spacing is reduced at the outermost epicardial layer which is about 4–5 μm thick. A reduced lattice spacing, as

highlighted in red in Fig. 2B, reflects a stiffer matrix, which is primarily composed of connective tissue. In this region, the peak intensity is well below the mode of the distribution (Fig. 2B). It is even discernible that the epicardial layer in region 2 was slightly more prominent. This follows the intuition that region 2, i.e. the region closer to the apex of the heart, more strongly generates the force of contraction to pump blood into systemic circulation.

In fact, a segmentation of the data obtained in region 2 based on k-means clustering with three clusters could be used to identify the outermost epicardial layer with a lower lattice spacing and the outer myocardial layer with a higher lattice spacing, respectively. For discrimination of the three clusters, all five fit parameters, namely S , d , I_p , q_0 and I_{bgr} , were used. The map of clusters is shown in Fig. 2C together with a histogram of lattice spacings (Fig. 2D) that resulted from the clusters. Maps of all scan points belonging to one of the three clusters are shown in Fig. 2E. The outermost epicardial layer can be clearly seen in cluster 1, relating to a cluster with lower lattice spacings (below 38.9 nm). Lattice spacing corresponding to cluster 1 is also heterogeneously distributed within the myocardium which provides additional information about network of tightly packed tissue that might play a role in maintaining the overall structural integrity of the heart. The bulk of the tissue is composed of lattice spacings between 38.9 nm and 40.4 nm. The third cluster clearly highlights the outer myocardial layer with lattice spacings above 40.4 nm. The arrangement of the layers of the cardiac wall relative to filament spacing can provide additional cues about the mechanisms governing the cardiac contractility in healthy and diseased hearts.

X-ray diffraction, SHG imaging and histology of sham and TAC heart

Based on the 2D scattering patterns, the total scattered intensity and cardiomyocyte chain orientation or fiber orientation can be inferred. To calculate the former, it is sufficient to integrate the scattered intensity, while determining the cardiomyocyte chain orientation requires radial averaging of the 2D patterns within $0.2 - 0.5 \text{ nm}^{-1}$, yielding the 1D azimuthal intensity profile $I(\varphi)$. $I(\varphi)$ was normalized

$$Inorm(\varphi) = I(\varphi) - \min(I(\varphi)) / \sum_{\varphi} I(\varphi)$$

and the circular mean and circular variance (Var) were calculated. The circular mean angle φ_0 of the scattering is rotated 90° with respect to the cardiomyocyte chain orientation. Anisotropy can now be defined as $1 - \text{Var}(Inorm(\varphi))$, yielding values ranging between 0 and 1. Zero

anisotropy resembles no orientational order, while an anisotropy of 1, i.e. zero variance, would be indicating perfect orientational order.

In Fig. 3A, filament orientation, anisotropy, peak intensity and filament spacing are shown for one of the TAC hearts that represented severe cardiac remodeling at a localized region serving as an interesting example to present a comparison between X-ray diffraction and SHG imaging. The spatial maps from X-ray diffraction, reveal that a low anisotropy and peak intensity coincides with a larger filament spacing. In this example, the localized region of cardiac remodeling at R2 of the TAC heart can be found by thresholding the lattice spacing map at 46.0 nm, as shown in Supp. Section 3. The area is then characterized by an anisotropy of 0.12 and an intensity of 0.11 counts/s, i.e. most myocardium has been replaced by fibrotic, non-muscle tissue indicating replacement fibrosis at this region. In contrast, the entire sample is characterized by an anisotropy around 0.51 and an intensity of 0.27 counts/10 ms. This shows that, without the presence of intense reflections, there is only residual alignment and anisotropy reflects the orientational order of all scattering components of the tissue.

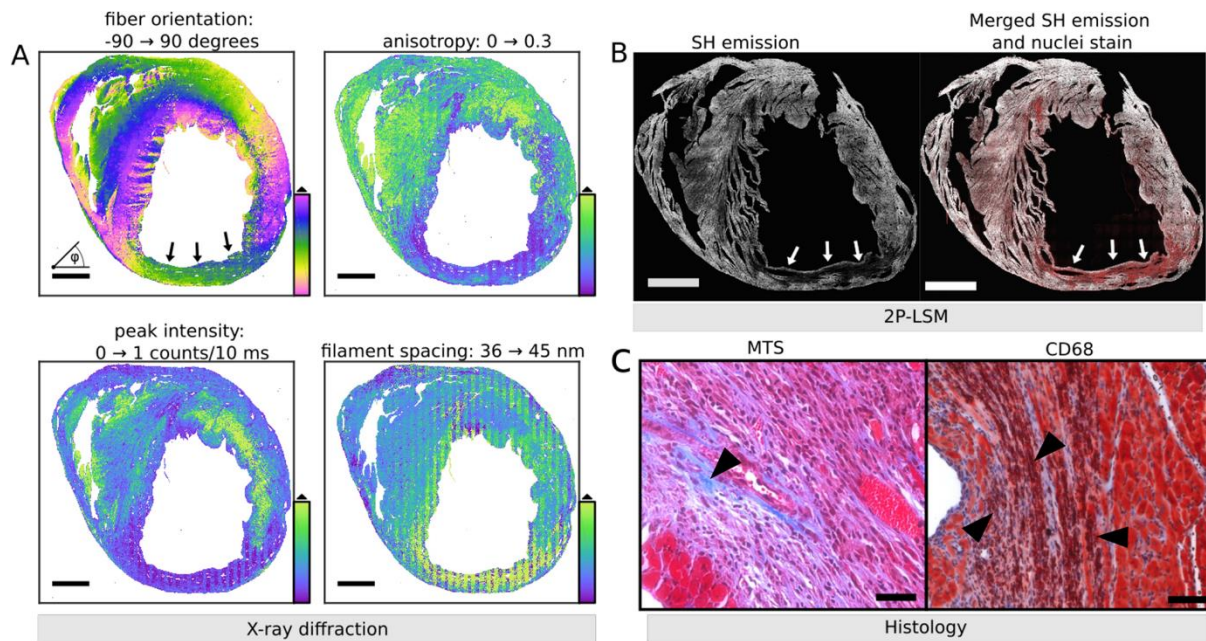


Figure 3: Images of tissue sections from the same TAC-operated heart with a region of severe pathological remodeling (pointed by arrows). (A) X-ray diffraction of this region (marked by black arrows) is distinguished by a lower anisotropy, a peak intensity close to zero and an increased filament spacing surrounding the affected tissue area while the primary orientation of the tissue components is maintained. For this reason, the fit diverges and the filament spacing reaches the fit boundary value of 45 nm. (B) SHG imaging shows negligible SH emission from myosin and collagen at this region and a higher signal from the DRAQ5 nuclear stain in red (marked by white arrows) which indicates a high cell infiltration. (C) Magnified histological images of this region reveal a limited deposition of collagen in blue as shown by the MTS (left image, marked by black arrowheads) and a high infiltration of positively stained macrophages shown by anti-CD68 IHC (right image, marked by black arrowheads). Scale bar in (A,B) 1 mm, scale bar in (C) 50 μ m. RV right ventricle; LV left ventricle.

The distribution of filament spacings together with maps of structural parameters for all 12 imaged sections are shown in Supp. Section 4. The average mode of all sham heart sections was 39.0 ± 0.3 nm and the lattice spacings in Figure S3 and Figure S6 are shown relative to this reference value to highlight any relative changes. The distribution of R2 of sample TAC 3, representative for a sample with a central ring, was bimodal with two modes at 38.7 nm and 40.3 nm.

Corresponding to these findings, Fig. 3B shows that the SH emission from both myosin and collagen is only sparsely present or even completely absent in this severely affected localized region of the TAC heart adding further evidence to the finding that this region had replacement fibrosis (Supp. Section 5, Fig. S7). Further, in this TAC heart the presence of high cell infiltration was also observed by DRAQ5 nuclear staining. An overall 78% increase in cell infiltration (Supp. Section 6, Fig. S8) in TAC 3 heart indicates an active immune response

which was confirmed by positive immunostaining of immune cells using antibodies against the leucocyte marker CD45 (Fig. S8A-B) and the macrophage marker CD68 (Fig. 3C and Fig. S8C-D). Furthermore, IHC also showed a 65% increase in the expression of alpha-smooth muscle actin within the myocardium of this TAC heart as compared to sham hearts, indicating the presence of active myofibroblasts (Fig. S8E-F).

SHG imaging of sham heart tissue

SHG imaging was performed to gain detailed information on the structural disruption of the cardiac tissue at sub-cellular level. A 2D image of a coronary blood vessel of a sham heart with representative images for DRAQ5 stained nuclei, SHG and the merged signal is shown in Fig. 4A. SH emission from myosin and collagen can be clearly distinguished as they present distinct structural morphology. The SHG from collagen fibers shows fibrous structures, which in healthy hearts were only visualized at localized regions such as around the large coronary blood vessels (Fig. 4B). Myofibrils are the main components of the cardiac muscle mass and hence myosin SHG signals were abundantly present throughout the heart. Within the sarcomere, the SHG signal originates from the A-band, which is the region primarily composed of thick myosin filaments. The A-band is separated by an isotropic region (I-band) composed of actin filaments which appear dark as they do not emit SH signal, resulting in the striated pattern of the myofibril (Fig. 4A). However, the efficiency of a myosin-specific SH signal was found to be strongly dependent on various factors including the orientation of the myofibrils, the focus of the imaging plane and the physical and virtual cut of the tissue. If the filament axis was lying in the imaging plane the characteristic striated pattern was resolved and had a high SHG signal intensity (Fig. 4B), which was weaker otherwise (Fig. 4C). On the other hand, the intensity of collagen specific SHG was less depended on the orientation but was mainly affected by the thickness and quantity of collagen fibers (Fig. 4B, C).

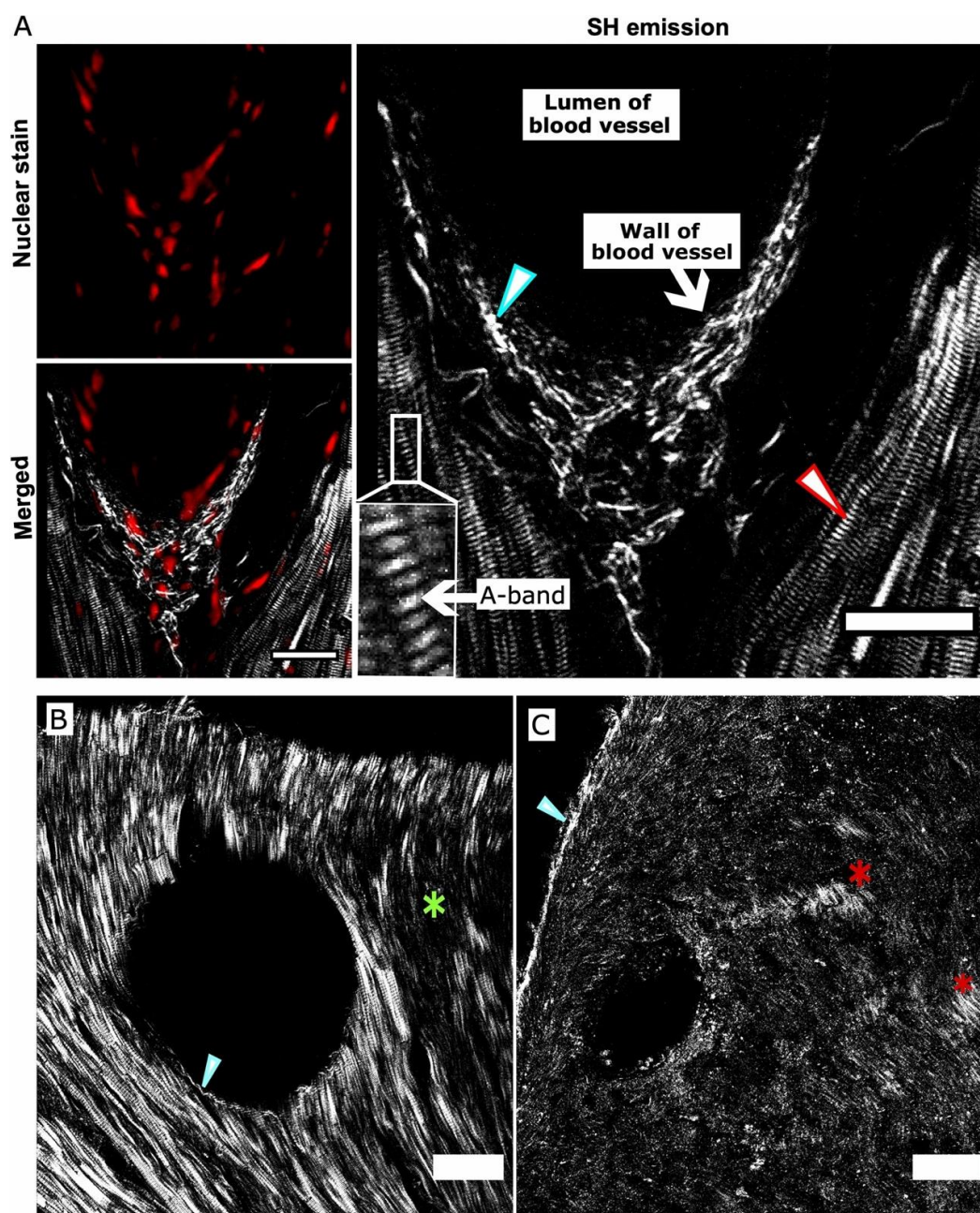


Figure 4: Representative 2D images of SH emission from myosin and collagen in a sham heart. (A) A region around a coronary blood vessel is shown including the images for DRAQ5 nuclear staining of cells, the merged image and an enlarged image for SH emission for clear visualization. The blue arrowhead marks the SH emission from collagen fibers localized around the blood vessel and the red arrowhead shows the SHG originating from myosin emitting a typical striated pattern. The Anisotropic band (A-band) is marked in the zoomed-in image of the myofibril. (B) SH emission from myosin fibers lying in the imaging plane except for the region marked with a green star. (C) SHG from myosin fibers which are not aligned in the imaging plane except for regions marked with red stars. Collagen-emitted SHG is marked by blue arrowheads which is present in (B) around the blood vessel and in (C) at the epicardium. Scale bar: 20 μm (A) and 50 μm (B, C).

Collagen-emitted SHG in sham and TAC heart tissue

Furthermore, the comparison of images of whole tissue sections from sham and TAC-operated hearts revealed the difference in the overall morphology and distribution of collagen and myosin represented by their SHG signal (Fig. 5). In sham hearts the collagen fibers were mainly visualized around the large coronary vessels and the epicardium (Fig. 5A). In comparison, the collagen emitted SHG intensity in TAC hearts was significantly higher (p-value = 0.015) (Supp. Section 7, Fig. S9A and C) around the coronary vessels signifying the development of perivascular fibrosis. This was further validated by histology which showed similar results (p-value = 0.039) (Supp. Section 7, Fig. S9B and D). SHG also revealed the presence of collagen fibers within the interstitial space at sub-micron scale in TAC hearts, allowing the visualization of the individual collagen fibrils surrounded by myofibers (Fig. 5B).

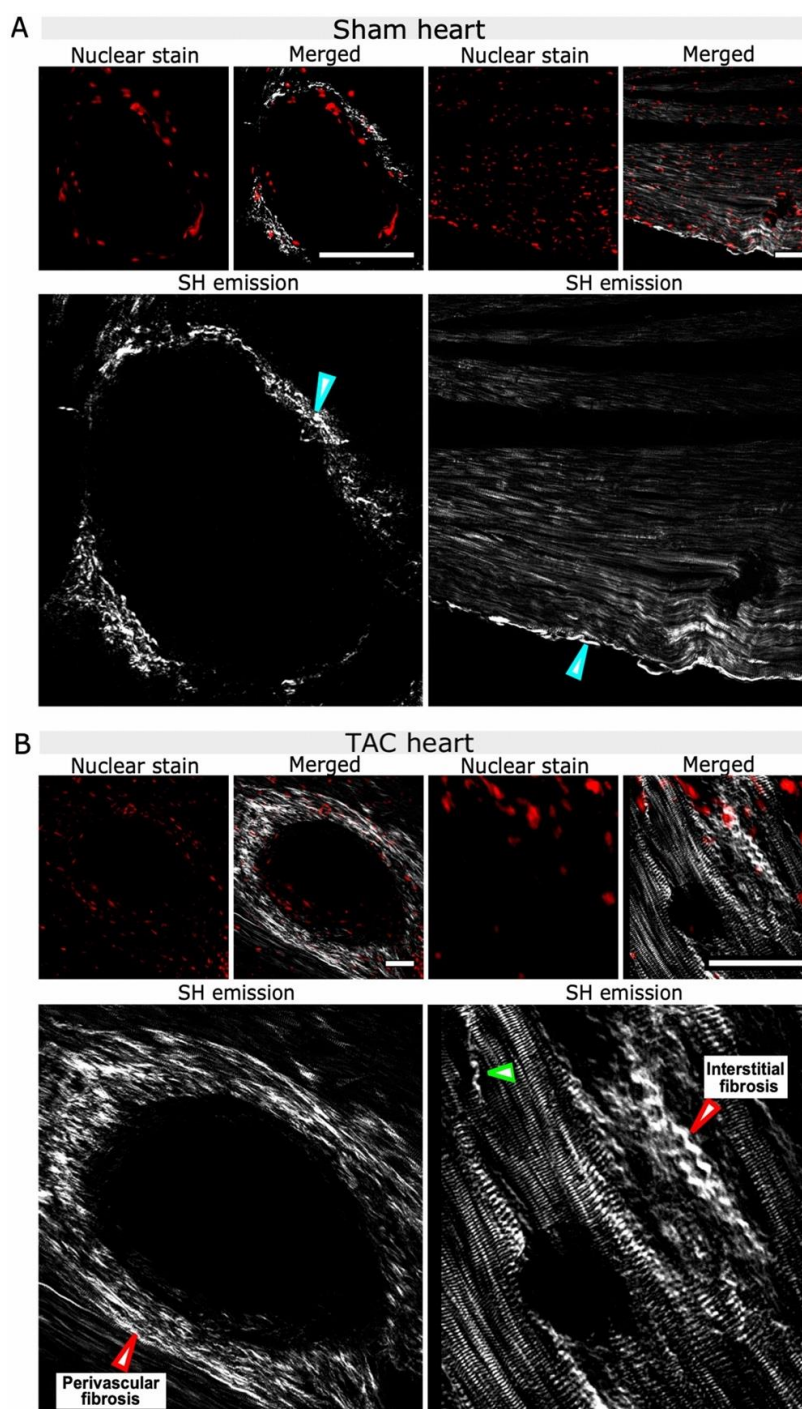


Figure 5: Representative images of the regions with collagen specific SHG in sham and TAC-operated hearts including DRAQ5 nuclear staining for visualization of cells, merged images for nuclear stain and SHG signal and enlarged images for SH emission for clear visualization. (A) Collagen-specific SHG signals in the sham heart were present around the coronary blood vessels and the epicardium (blue arrowheads). (B) SHG in the TAC hearts revealed the development of perivascular and interstitial fibrosis (red arrowheads). Individual collagen fibers were also visualized within the muscle mass in TAC hearts (green arrowhead). Scale bars: 50 μ m.

Myofibril morphology in sham and TAC hearts

SHG from myosin in sham heart tissue showed a linear arrangement of myofibrils. The intercalated disks between individual muscle fibers appear as dark regions owing to the fact that these areas do not generate SH signals (Fig. 6A). By contrast, areas with severe pathological tissue remodeling were found in TAC hearts, which contained distorted myosin fibers. These regions were comprised of abnormal and undulated myosin fibers that lacked periodicity and symmetry, features which were present in healthy hearts. Interestingly, the collagen fibers in these areas were sparsely present or completely absent (Fig. 6B). Such regions of abnormal myosin filaments were abundant at the wall of the left ventricle and within region 2, i.e. near the apex of TAC hearts.

SHG imaging also revealed that the deposition of collagen fibers has detrimental effects on myosin fiber morphology. An excess of collagen seemed to have caused the displacement of myofibrils which might also contribute to ruptures and changes in the arrangement of the surrounding myofibrils (Fig. 6C).

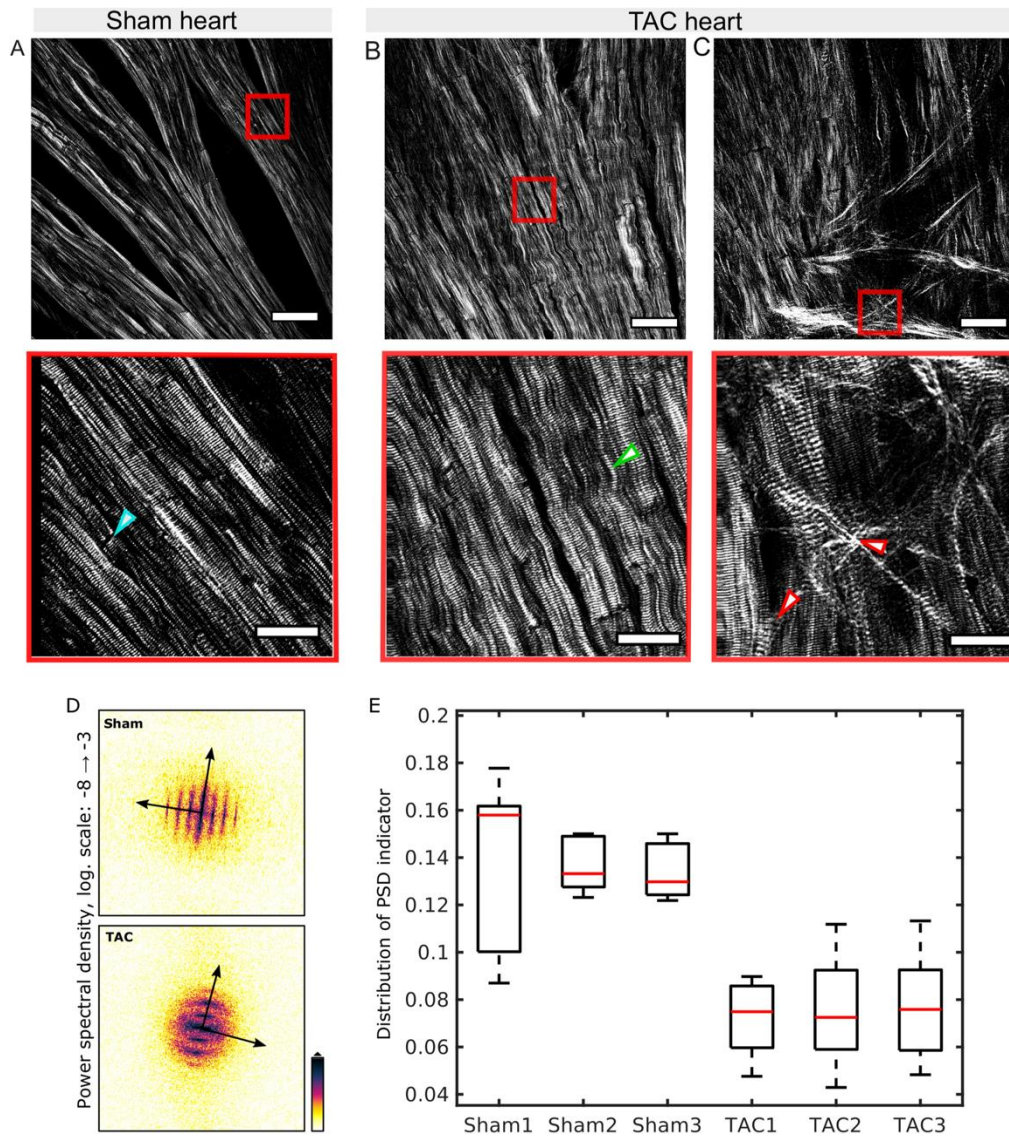


Figure 6: Representative images of SHG showing the arrangement of myosin fibers in sham and TAC-operated hearts with overview images (top) and magnified images at the ROI (bottom). (A) The myosin fibers show a linear and symmetric arrangement in the sham heart. The intercalated disks between myosin fibers do not emit SHG and appear dark which is pointed by a blue arrowhead. (B) In the TAC heart, undulated myosin fibers are located within the muscle mass as shown by a green arrowhead. (C) The cross-linked collagen fibers can be seen in the myocardium causing disruption and rupture of myosin fibers indicated by red arrowheads. Scale bars: 50 μm in overview images (top panel) and 20 μm in magnified ROI images (bottom panel). (D) Image analysis of myosin morphology in SHG micrographs of TAC and sham hearts. The power spectral density (PSD) was computed for each image, see the example of a TAC (bottom) and sham micrograph (top) by 2D fast Fourier transformation (FFT). The 2D PSD shows a pattern reflecting the orientation of myosin strands, the periodicity of the striation as well as the degree of undulation. (E) After azimuthal average, a single scalar indicator value can be computed from the 1D PSD, which differs between TAC and sham morphology with high statistical significance (see main text).

Next, we investigated whether the morphological changes in the myosin fibers described above for exemplary images, can be quantified by an automated image processing scheme and whether the group differences in morphology between TAC and sham stand up against statistical tests. To this end we designed a Fourier-based image processing workflow, starting with a 2D FFT operation for each micrograph. The resulting power spectral density (PSD) given by the squared modulus of the Fourier image was plotted which reflected the orientation of myofibril strand, the striation periodicity in terms of the corresponding lattice peaks, as well as the degree of undulation (Fig. 6D). The 2D PSD graphs were then analyzed with respect to their two main axes of symmetry determined by a principal component analysis (PCA)²⁴. Since the undulation was identified as the main characteristic feature of TAC morphology, a PSD-based indicator metric was computed as follows. Starting from the center of the PSD image, a cake integration was performed covering the two principal axes. The opening angle of this integration cone ('cake') was then varied between 5° and 20°. Division of a 1D PSD curve computed with larger angle by a curve computed with lower angle then yields an indicator curve. The larger the amount of (partial) rotational averaging by the undulations, the smaller the deviation of the indicator curve from a value of 1. This was finally captured by a simple root-mean-square analysis yielding a single scalar value for the PSD-indicator, as displayed in the box-whisker plot of (Fig. 6E). This was achieved by comparing a total of 20 TAC micrographs and 20 sham micrographs from 3 TAC and 3 sham hearts, respectively (Supp. Section 8). The distributions of the PSD-indicator for 3 TAC and 3 sham intra-group averages were then subjected to a two-tailed paired Student's t-test, indicating a p-value of $p = 0.0011$. In summary, these findings show that myofibrils in TAC hearts are irregular and distorted as compared to the very linear arrangement in sham hearts.

Discussion

In this proof of concept study, we demonstrated that spatially-resolved X-ray diffraction and SHG imaging enables an additive and comprehensive assessment of myosin filaments, revealing structural disruption of the myocardium due to fibrosis and hypertrophy in a mouse model of cardiac pressure-overload.

X-ray diffraction reveals the cardiomyocyte chain orientation throughout the whole myocardium (fiber orientation), the degree of chain alignment or anisotropy, the peak intensity reflecting the predominance and ordering of the acto-myosin structure, as well as the filament spacing as the most important structural parameter of the acto-myosin assembly. Together, the spatial maps of these parameters unveil the cardiac micro-architecture underlying its mechanical function. Importantly, this study shows how the scale-bridging ability of spatially-resolved X-ray diffraction arises from its intrinsic combination of information from real- and reciprocal space, enabled by automated analysis of millions of diffraction patterns. Compared to control (sham) hearts the diffraction signals in TAC hearts reveal structural abnormalities in the myocardium which exemplifies the ability of X-ray diffraction to elucidate pathological structure alterations. Based on 2D maps of filament spacing and peak intensity, we could identify fibrotic lesions and observe an increase in lattice spacing in the surrounding tissue. In sham hearts, only the outer myocardial layer coincides with an increased lattice spacing. This points to the fact that regions with a higher amount of connective tissue may be associated with a different structure of the acto-myosin assembly. Since at this point, we lack a model according to which the lattice spacing of thick and thin filaments can be put into direct relation to mechanical properties, the increased values are difficult to interpret, but may speculatively be attributed to a softer muscle structure. In this simplified picture, the outer myocardium, which is also characterized by an increased lattice spacing could potentially also accommodate a relaxed filament packing, in contrast to the inner myocardium which generates the contractile force.

Fibrotic tissue was found to also yield a low anisotropy, i.e. orientational order. This indicates that the replacing tissue components, although maintaining the original orientation of the tissue, do only pertain a residual degree of alignment. Mapping the filament spacing can also reveal ‘hidden features’ of the cardiac architecture. For example, we have found very distinct regions in the bulk of the tissue where the filament spacing was significantly lower than in the remaining tissue. We therefore hypothesize that sheets of myocardium that are required to

generate a larger force are composed of muscle fibers with denser filament packing. To this end, correlating the diffraction results to a full 3D vector field mapping of the cardiomyocyte chain orientation, as it can be obtained from X-ray tomography, could potentially show whether such sheets can be delineated and distinguished both in their radial and helical angles as well as actomyosin structure.

All TAC hearts presented different degrees of severity of cardiac remodeling which were successfully identified by using both techniques. For instance, one of the TAC hearts presented an active immune response and replacement fibrosis at the left ventricular wall. The regions of high cell infiltration in this TAC heart lacked the actomyosin diffraction signal, and also the SHG emission from myosin and collagen fibers, which signifies the presence of activated myofibroblasts and the transition of healthy cardiac tissue to a fibrotic subtype^{20,21}. By contrast, the two other TAC hearts did not show an active immune response but presented severe hypertrophy in the presence of either interstitial and/or perivascular fibrosis. Thus, the combined use of X-ray diffraction and SHG imaging corroborated the finding that two stages of fibrosis were observed: an active onset of fibrosis with immune response and an end-stage fibrosis with collagen deposition and ECM turnover accompanied by myofibril distortion^{3,5,25,26}.

Notwithstanding the unique capability of scanning X-ray diffraction, we must also briefly discuss the detrimental effect of radiation damage. As discussed in Nicolas et al. 2019¹⁶, the actomyosin reflection is sensitive to dose and dose rate, controlled by the various scan parameters. For this reason, we here chose a fixed exposure time of 10 ms, step sizes around 5 μm and a spacing of 5 μm between adjacent scan lines to avoid illumination of areas of the tissue which have already received a significant dose before and therefore do not reflect the undamaged structure. While the applied dose of 2.54 MGy still exceeds the tolerable dose of 0.5 MGy we can assume that by this ‘fresh spot’ illumination strategy, the sample is largely unaffected by radiation damage¹⁶. In particular, given this particularly careful choice of raster-scanning parameters, the structural parameters such as filament spacing are not affected as demonstrated in Nicolas et al. 2019¹⁶. The overall scan time required for one scan was, on average, approximately 8 h. This time will be significantly reduced in future experiments, given the brightness increase resulting from current and future synchrotron upgrades.

Complementing and extending these findings, features attributed to fibrosis and hypertrophy, starting from single collagen fibrils to deteriorated myofibrils, were also visualized by SHG

imaging. In particular our results demonstrate the ability of SHG imaging to visualize cardiac structure at sub-cellular scale which can be used to detect and distinguish SHG from the myosin and collagen fibers. Tiaho et al. 2007 showed that SHG from myosin and collagen can be distinguished in gastrocnemius muscle when excited using the same wavelength^{16,27}. Our results add to this finding by presenting SHG imaging in healthy hearts in comparison with hypertrophic and fibrotic hearts highlighting the possibility to visualize structural discrepancies in pathological heart tissue. This approach could be further exploited in future to study the detrimental effects of other pathologies on the most relevant structural and functional constituents of the heart, i.e. collagen and myosin^{28,29,30,31}. Previous work has further shown that changes in the SHG signal intensity can yield structural information on a crystallographic level, such as the semi-crystalline order of the A-band³² or the helical myosin filament angle¹⁶. Here, by scanning X-ray diffraction, we can now correlate a spatially varying SHG intensity to the changes in the crystallographic filament packing of acto-myosin.

We have also shown that morphological changes attributed to heart failure can be successfully identified at sub-micron scale using SHG imaging including reliable detection of interstitial and perivascular fibrosis and myofibril distortion at tissue level. Yuan et al. 2019 investigated the structure of cardiac myosin filaments in a pressure overload mouse model³³. They reported changes in the myosin structure in a cell stretch model but found no differences in morphology of the myocardium at tissue level. By contrast, we observed pronounced differences in the sub-cellular architecture of the myocardium in healthy and diseased hearts including collagen deposition and disruption of myosin fibrils at high-resolution (Fig. 6). The discrepancy in these findings is attributed to the fundamental differences in the methodology including the imaging approach. For instance, in the previous study polarized SHG imaging was performed to image cryofrozen tissue sections in relatively small fields of view (FOV)³³. While we performed non-polarized SHG imaging on fixed 30 μm vibratome tissue sections obtained from different regions of the hearts which were not frozen. Further, we also acquired overview scans for probing entire tissue sections and then performed subsequent high-resolution imaging at an ROI. Most importantly, in our study SHG imaging was performed on relatively severely affected hearts that were obtained 16 weeks post TAC operation, while in the previous study hearts were imaged 4 weeks after TAC which had early onset of cardiac remodeling only at single-cell level³³.

The observed disruption of myofibrils that may occur due to the cross-linking of collagen fibers as a result of ECM remodeling has not been reported before. This might be due to the fact that histology is the most commonly used conventional diagnostic tool for accessing cardiac pathology which is not able to visualize the micro-abrasions and cannot resolve composition and interaction of individual myofibrils and collagen fibers within the heart tissue. Moreover, unlike histology, SHG imaging is a label-free imaging approach which has high specificity and hence avoids complications like unspecific binding and overstaining of tissue slices and therefore saves a significant amount of time that is usually needed for the staining process.

In healthy cardiac tissue the myofibrils exhibited a regular and periodic organization while in the diseased hearts the myofibrils had irregularities in the periodicity. In certain myopathies inclusion of non-sarcomeric structures can cause damage to microarchitecture of the muscle³⁴. In TAC mouse model, the pressure-overload induced hypertrophy and fibrosis may have resulted in undulated and twisted and/or ruptured myofibrils. Since this phenomenon was not observed in sham hearts, it was not an artefact from sample preparation. We postulate that in fibrotic hearts, underlying ECM remodeling and collagen deposition in surrounding regions may cause undulation by displacing the myosin filaments within the cardiac muscle mass. However, further testing would be necessary to confirm this claim by analyzing thicker tissue samples in 3D obtained at different time points after TAC operation and also by looking into different cardiac pathologies. Since the sarcomere is the fundamental element of cardiac contractility, the reported micro-modulations of myofibrils can also help explain the contractile dysfunction and arrhythmias known to occur due to cardiac failure.

Conclusion and future prospective

Combined results from the two imaging modalities contribute to the understanding of the pathology of cardiac pressure-overload by providing unprecedented visualizations of pathological alterations in heart tissue samples. These findings are beyond the scope of conventional histology and IHC which cannot provide information on the crystallographic structure of acto-myosin filament lattice. Further, histology also lacks the resolution and specificity of SH intrinsic signal. Importantly, the recorded signals lend themselves to ample quantification, which in future can be extended well beyond the current level. The present study already provides a blueprint for such future studies, by comparing the structure of healthy and pathogenic hearts. The characteristic alterations of the micro-architecture in the diseased heart such as disarrayed myocardium, deterioration and rupture of myofibrils and interaction of ECM

with surrounding tissue may possibly also serve as “imaging biomarkers” in future diagnostic applications. Given prior combined and mutual corroboration of synchrotron X-ray and SHG imaging results for validation studies performed on cardiac biopsies, one would ultimately be able to base a diagnostic decision only on SHG imaging alone, since it is the clinically much more accessible technique^{35,36}. Finally, we hope that by revealing pathological alterations during different stages of cardiac remodeling, advanced imaging of cardiac structures using SHG as compared to histology will provide precise and reliable quantification of pathological alterations in cardiac tissue. This can consequently also facilitate the optimization of therapeutic strategies by allowing the visualization of the response to therapy at structural level in preclinical studies³⁷.

Supplementary material

S1. Echocardiography and histological data for sham and TAC hearts

Each TAC-operated mouse heart presented distinct severity of cardiac remodeling which is presented by the echocardiography functional analysis and histological data showing overview of cardiac morphology. All data for TAC hearts is presented in comparison to the sham hearts.

Table S2.1. Information on mice and hearts morphometry. Dates are given according to the international ISO 8601 standard, i.e. in the form yyyy-mm-dd.

ID	Sex	Date of birth	Operation	Date of operation	Date of sacrifice	Body weight at harvesting (g)	Heart weight (g)	Long. Length of heart (mm)	Trans-verse width of heart(mm)
Sham 1	F	2017-07-10	Sham	2017-09-04	2018-01-15	20.3	0.16	6	5
Sham 2	M	2017-07-10	Sham	2017-09-18	2018-01-15	28.0	0.15	7	5
Sham 3	M	2017-07-10	Sham	2017-09-18	2018-01-15	25.7	0.15	6	4
Sham 4*	-	-	-	-	-	-	-	-	-
TAC 1	F	2017-07-10	TAC	2017-09-04	2018-01-15	19.3	0.33	10	8
TAC 2	M	2017-07-10	TAC	2017-09-18	2018-01-15	26.7	0.36	11	9
TAC 3	M	2017-07-10	TAC	2017-09-18	2018-01-15	30.0	0.32	10	8

* Data published in Nicolas *et al.*, 2017.

Table S2. Echocardiographic parameters for sham and TAC mouse at 16 weeks after surgery

Mouse no.	HR (Bpm)	LVIDd (mm)	LVIDs (mm)	PWThd (mm)	PWThs (mm)	AWThd (mm)	AWThs (mm)	FS (%)	EF (%)	SV (μ l)	CO (mL/min)
Sham 1	437	4.0	2.9	0.6	0.9	0.8	1.1	27.5	52.4	41.8	18.3
Sham 2	559	4.2	3.4	0.6	1.2	0.8	1.1	27.9	51.7	61.9	34.6
Sham 3	470	4.0	2.5	0.8	1.5	0.9	1.0	38.7	66.3	56.9	26.8
Mean (n=3)	489	4.08	2.92	0.69	1.17	0.84	1.09	31.4	56.82	53.5	26.54
SEM (\pm)	36.4	0.07	0.27	0.07	0.18	0.04	0.02	3.67	4.75	6.05	4.72
TAC 1	445	4.4	3.8	1.0	1.1	1.1	1.3	11.7	31.2	33.8	15.0
TAC 2	553	4.9	3.7	0.8	1.2	1.0	1.2	23.9	46.8	67.6	37.4
TAC 3	468	4.7	4.0	1.0	1.1	1.1	1.5	15.2	39.3	52.0	24.3
Mean (n=3)	489	4.6*	3.9*	0.9	1.1	1.1*	1.4*	16.9*	39.1	51.1	25.6
SEM (\pm)	32.8	0.15	0.09	0.05	0.03	0.05	0.06	3.65	4.50	9.79	6.49

AWThd, left ventricle anterior wall thickness at diastole; AWThs, left ventricle anterior wall thickness at systole; bpm, beats per minute; Co, cardiac output; EF, ejection fraction; FS, fractional shortening; HR, heart rate; LVIDd, left ventricular internal diameter at diastole; LVIDs, left ventricular internal diameter at systole; PWThd, left ventricle posterior wall thickness at diastole; PWThs, left ventricle posterior wall thickness at systole; SV, stroke volume; TAC, transverse aortic constriction. *P < 0.05 vs. sham; two-tailed unpaired Student's t-test. Data are expressed as mean \pm SEM.

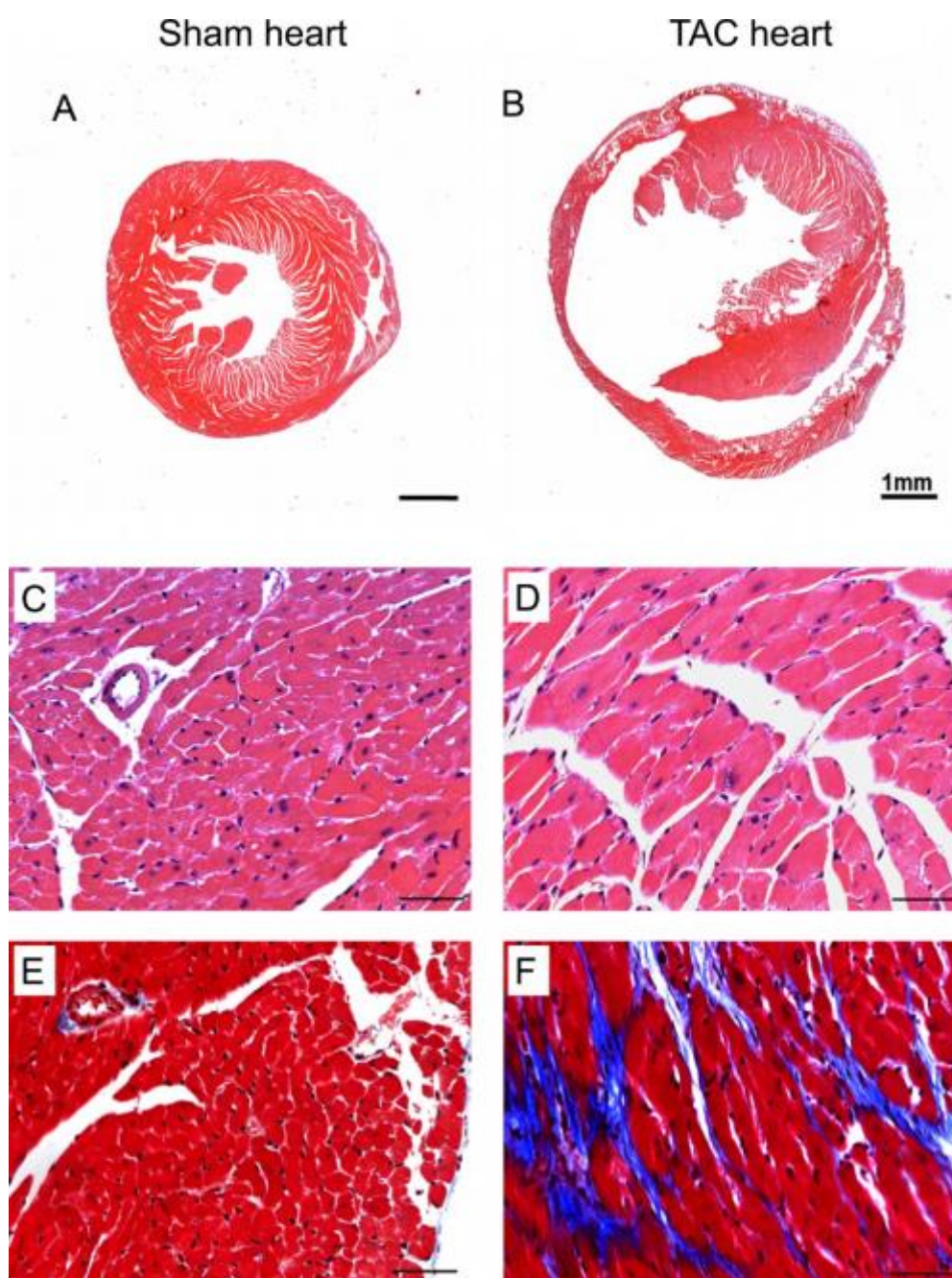


Figure S1: Histological representation of cardiac remodeling in transverse aortic constriction (TAC) heart. (A-B) Cardiac tissue sections stained with haematoxylin and eosin stain (H&E) shows increase in the overall size of a TAC heart in comparison to a sham heart. (C-D) Magnified images of H&E stained hearts showing the enlarged size of cardiomyocytes in the TAC heart as compared to the sham heart. (E-F) Representative magnified images of Masson's Trichrome stained (MTS) tissue from healthy sham heart with collagen (blue) deposition at the epicardium and in TAC heart MTS revealed development of interstitial fibrosis. Scale bar in A, B: 1 mm, scale bar in C-F: 50 μ m.

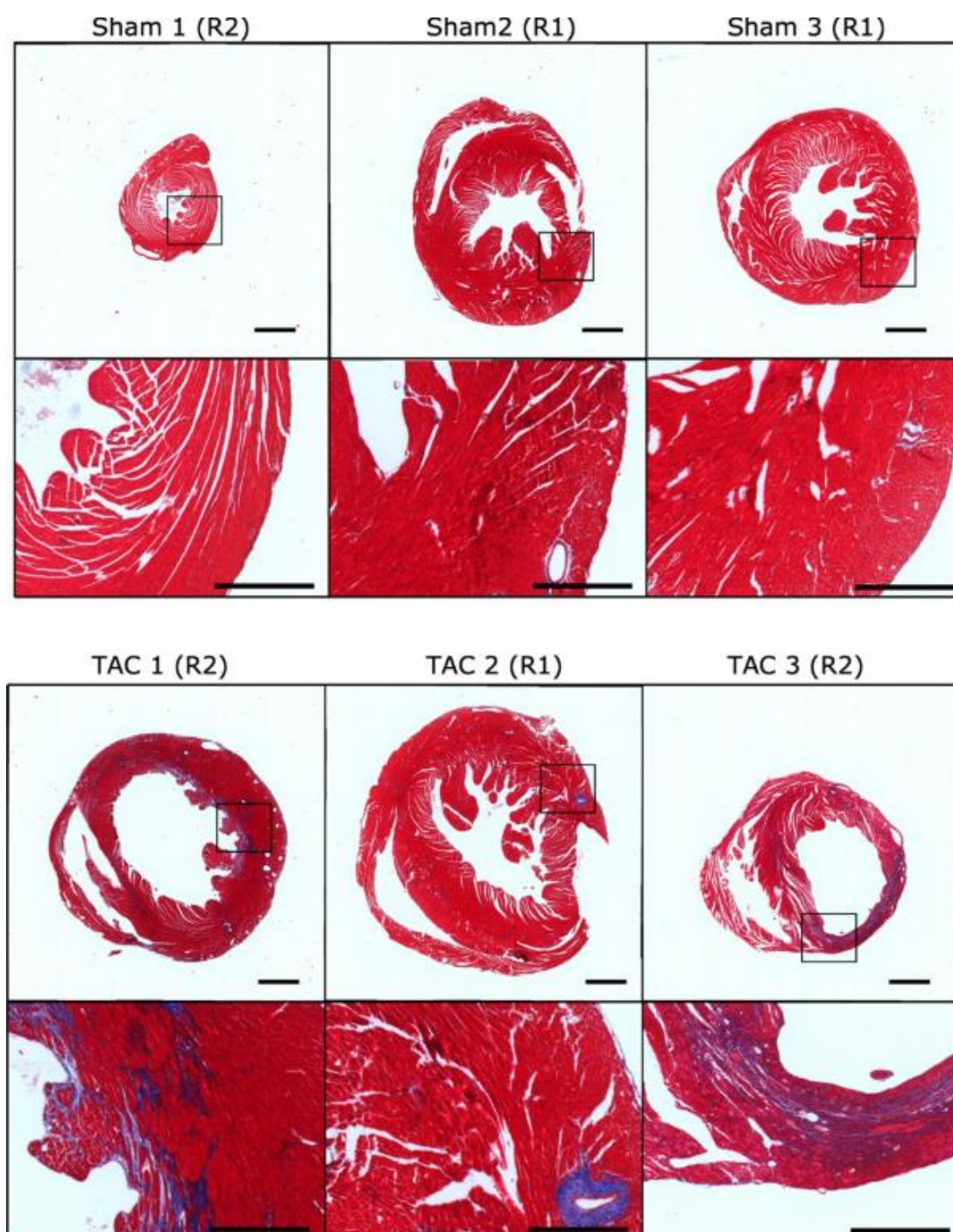


Figure S2: Overview and representative images at ROI of Masson Trichrome stained tissue sections from sham and TAC hearts. The muscle is stained pink while collagen is stained aniline blue.

S2. Quantification of lattice spacing difference in ring-like structural feature

Three samples show significant alterations in lattice spacing within two regions of the myocardium. The region with lower lattice spacing appears in a ring-like shape and was found in samples from both sham and TAC and in region 1 as well as region 2. In all three samples, two smaller regions of interest (labeled A and B in Fig. S2) were identified by eye and the mean lattice spacings were obtained. It was found, that the lattice spacing differed by 1.7, 2.2 and 2.4 nm in region 1 of Sham 1, region 2 of TAC 1 and region 1 of TAC 1, respectively. The lattice spacing map relative to a reference value of 39.0 nm is shown for all three samples in Fig. S2.

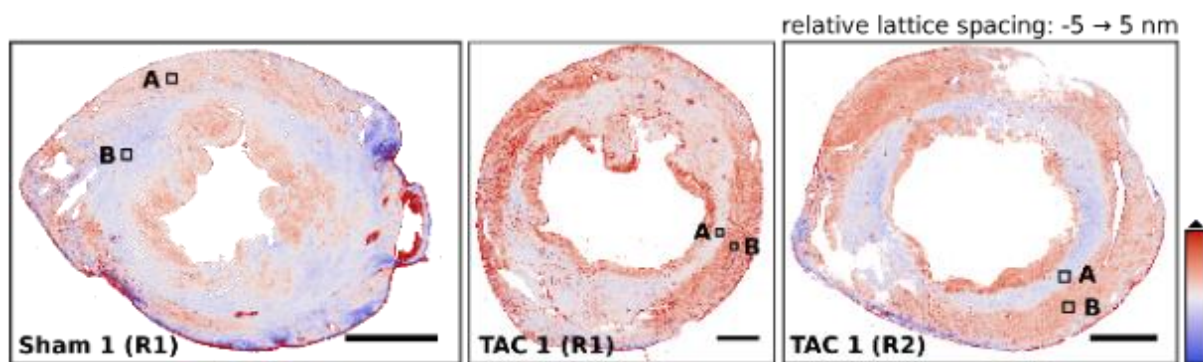


Figure S3: Three samples showed a reduction in lattice spacing within the myocardium with the shape of a ring. In region 1 of TAC 1 and region 2 of TAC 1, the boundary between these two regions appears sharp. The difference in lattice spacing was quantified by subtracting the mean lattice spacing obtained in region A from the mean lattice spacing of region B. Both regions are indicated by black boxes. Lattice spacing is given in nanometers, relative to a reference value of 39 nm.

S3. Quantification of anisotropy and lattice spacing in fibrotic lesion

Regions of low intensity and low anisotropy pointed out in region 2 of sample TAC 1 and discussed in Fig. 3 of the main text appear to correlate well with the region of intense cardiac remodeling. Based on the two-dimensional (2D) histograms (or: 2D density of scan points) of anisotropy against lattice spacing and intensity, the difference in intensity and anisotropy between the fibrotic lesion and the bulk tissue can be quantified. Fig. S3A shows the 2D histogram of anisotropy against lattice spacing. Clearly, the bulk of the tissue has a lattice spacing of 39.5 nm and an anisotropy of 0.57, as identified by the maximum of the histogram which is highlighted by a red circle in Fig. S3. The distribution of lattice spacing also broadens with decreasing anisotropy. A decrease in anisotropy is, however, also linked to a decrease in intensity, as shown in Fig. S3B. Here, the distribution is tailed towards lower intensity with

decreasing anisotropy. The maximum is now located at an anisotropy of 0.51 and an intensity of 0.27 counts/10 ms. To identify the region of cardiac remodeling, the lattice spacing serves as an accurate structural discriminator. Selecting only scan points with a lattice spacing greater than 45.0 nm yields the distribution shown in Fig. S3C, with a maximum at 0.12 and 0.11 counts/10 ms. Inspecting the logical map in (D) shows, that the affected region is indeed well localized by thresholding.

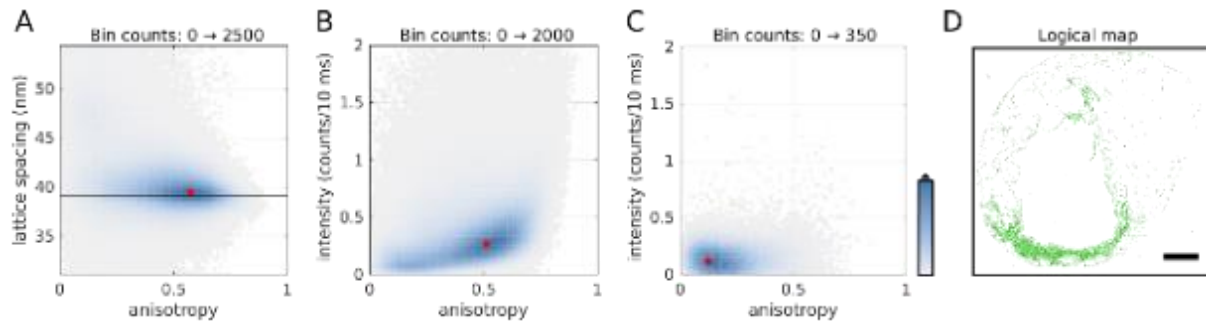


Figure S4: Estimation of intensity and anisotropy in the region of cardiac remodeling. (A) Density of scan points (excluding background) as a function of anisotropy and lattice spacing. The horizontal black line is located at a reference value of 39.0 nm obtained from six sham samples. A red dot marks the maximum of the density map. (B) Density of the same scan points shown in (A) plotted as a function of anisotropy and intensity, with a maximum at 0.51 and 0.27 counts/10 ms. (C) Selecting only scan points with a lattice spacing above 45 nm results in a distribution with a maximum at 0.12 in anisotropy and 0.11 counts/10 ms in diffraction intensity. Since the applied criterium coincides with the region of cardiac remodeling as seen in (D), it is the distribution of anisotropy and intensity within this region.

S4. Lattice spacing distributions and maps of structural parameters for all sample sections

The entire X-ray dataset processed within the period of two allocated beamtimes consisted of 12 samples. All samples were processed in the same fashion and five structural parameters were extracted per sample. The lattice spacing, encoding the packing density of myofibrils, is shown in violin and box plots in Fig. S4A. It is evident, that some distributions, e.g. for TAC 1 (R1) are asymmetric. Due to this skewness, we have quantified the mode of all distributions instead of the mean. The average mode for all 6 Sham samples was found to be 39.0 ± 0.3 nm, and is indicated by a solid black line in Fig. S4A. To obtain the lattice spacing mode, the data was binned into a histogram with a bin width of 0.1 nm and the histogram was modeled using kernel density estimation (as implemented by the function *ksdensity* in MATLAB). The peak of the model function was chosen as the mode of the distribution. An initial attempt to quantify

the distribution modeled the lattice spacing distribution as a sum of a Gaussian and Lorentz line shape with identical full width half maximum to include the longer tails of the distribution. The resulting pseudo-Voigt profile was fitted using a non-linear least-squares algorithm. In fact, in many samples the lattice spacing could be exactly modeled with this approach. It failed however for samples with significant skewness such as TAC 1 (R1) or Sham 1 (R1) or with more than one mode as in sample TAC 1 (R2) or, to a lesser extend, sample Sham 4. Data, kernel density estimate and model fit are shown in Fig. S4B. For completeness, the full dataset of all five structural parameters is on display in Fig. S5.

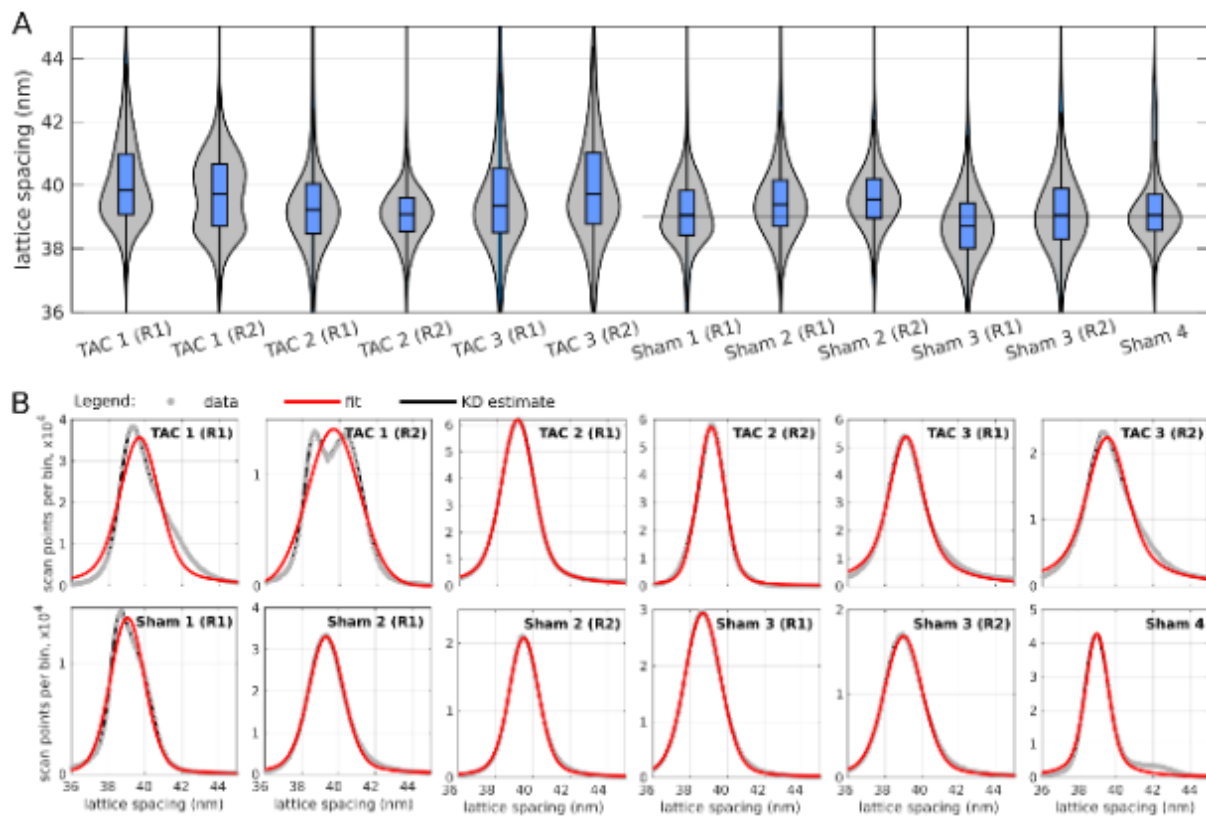


Figure S5: Analysis of the distribution of lattice spacings for all twelve imaged samples. (A) Violin and box plots of the lattice spacing distribution in 12 samples, out of which 6 samples were from three hearts of sham-operated mice, while 6 samples were from three murine hearts that showed hypertension and hypertrophy. Several samples showed an asymmetry in the lattice spacing distribution or even multimodality. The mean mode estimated from all Sham hearts was determined at 39.0 ± 0.3 nm. (B) The same distributions were modeled by a pseudo-Voigt profile using least-squares fitting and the mode was extracted from the maximum of the kernel density estimate.

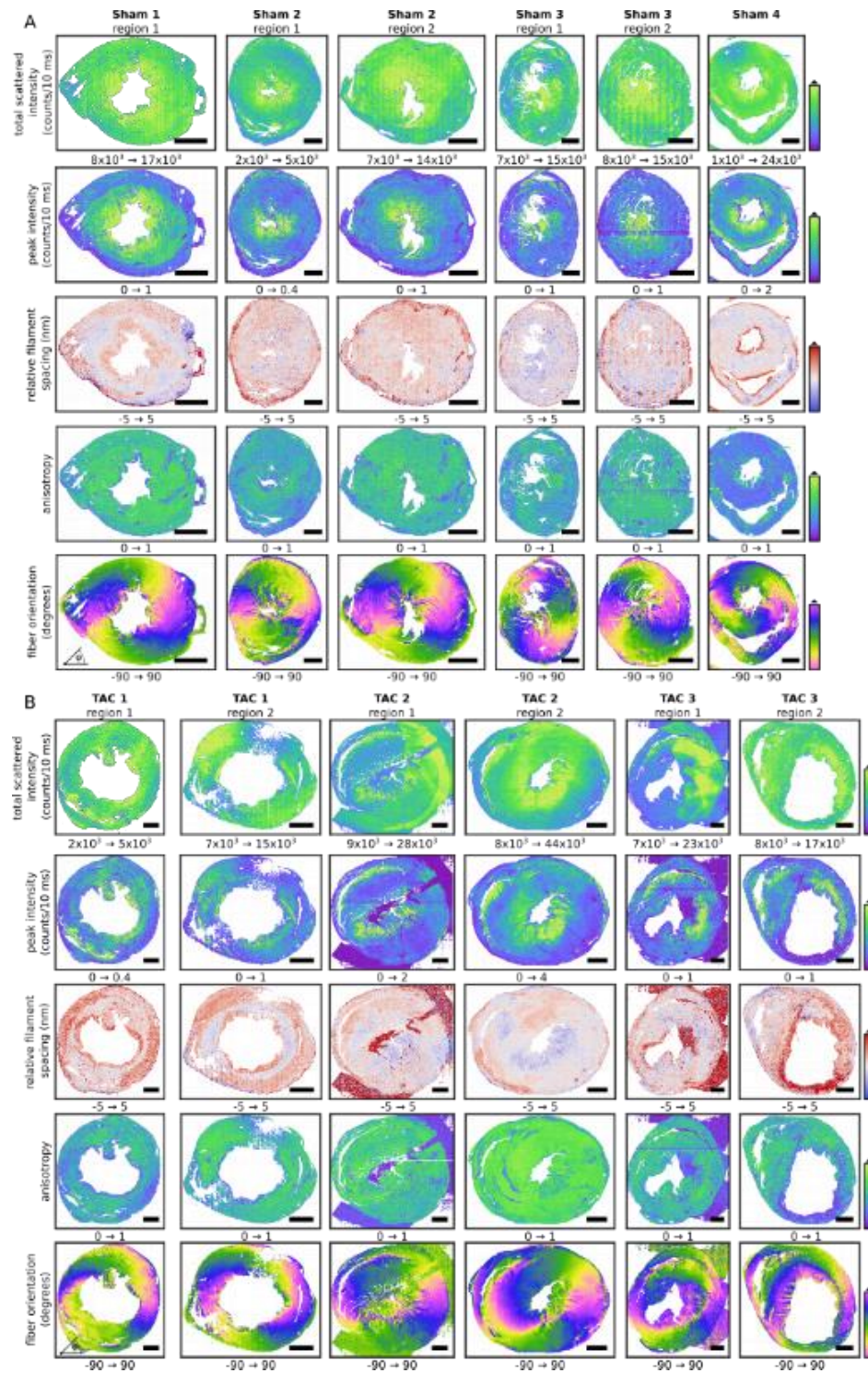


Figure S6: Maps of five structural parameters for all twelve imaged samples. (A) Sections from sham samples. (B) Sections from TAC samples.

S5. SHG micrographs for whole cardiac tissue sections

2D SHG micrographs of whole cardiac tissue sections were stitched to present an overview of the myocardium structure in sham and TAC hearts. Myofibrils in sham hearts showed a symmetrical and regular arrangement while in TAC hearts a clear disruption of the myocardium was observed.

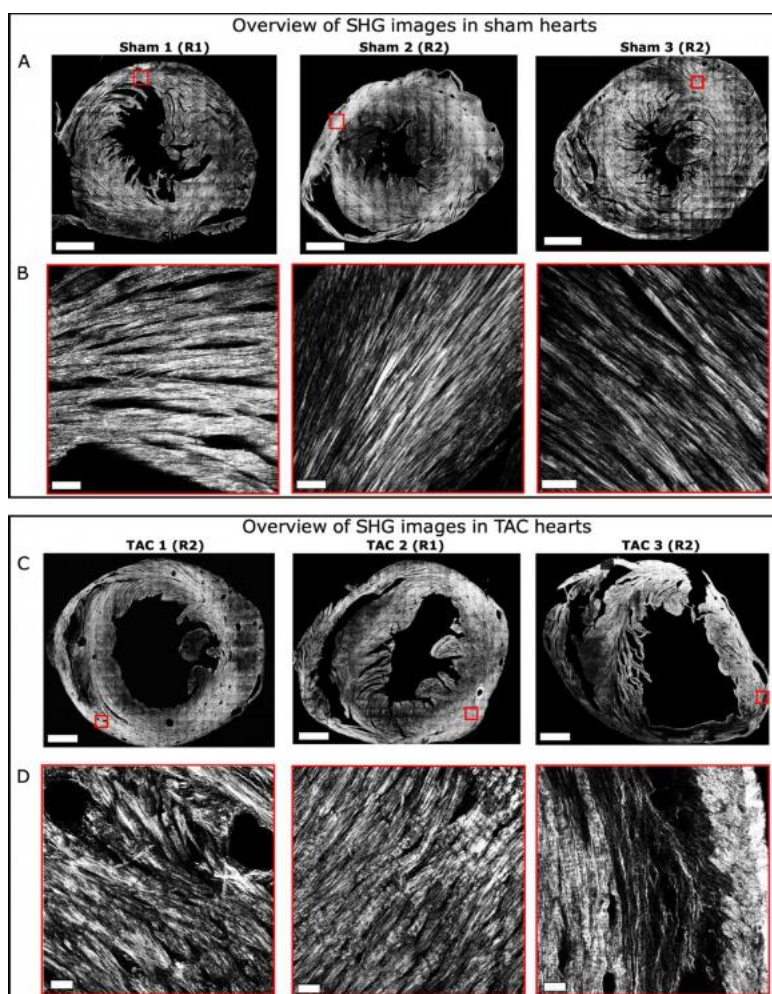


Figure S7: SHG imaging of sham and TAC hearts. Stitched 2D mosaic of whole cardiac tissue sections showing SHG in (A) sham and (C) TAC hearts. Representative images at ROI marked by a red box are shown for enhanced visualization of cardiac structures in (B) sham heart and (D) TAC heart. Scale bar in A and C: 1mm; scale bar in B and D: 100 μ m

S6. Quantification of immune cell infiltration and alpha-SMA expression in TAC 3

In order to quantify the cell infiltration in TAC 3 heart sample, the percentage increase in cell count was calculated at five ROI for both anti CD45 and anti CD68 stained tissue. An overall 78% increase in cell-infiltration was found in TAC 3 heart sample as compared to the sham hearts. The percentage area of positively labelled alpha-SMA was also measured for TAC 3 and sham hearts. The results showed a 65% increase in the expression of alpha-SMA in the myocardium of TAC 3 heart sample as compared to sham hearts.

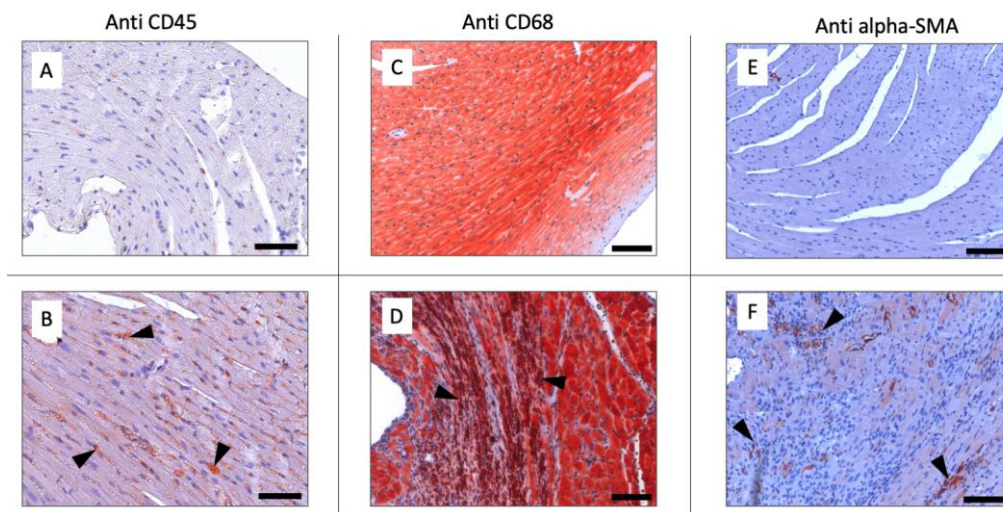


Figure S8: Representative images of IHC stained cardiac tissue sections a for sham hearts (top panel) and TAC hearts (bottom panel). (A-B) Image of anti-CD45 stained cardiac tissue revealing the infiltration of leucocytes in a representative TAC heart as compared to a sham heart. (C-D) Representative image of an anti-CD68 stained cardiac tissue shows an increased number of macrophages within the myocardium in a TAC heart as compared to sham heart. (E-F) Anti alpha-SMA staining shows cells positively labelled with alpha-smooth muscle actin in the myocardium of a TAC heart reflecting activated fibroblasts which are not present in the sham heart. The images represented are shown from sham 2 and 3, and TAC 3 heart samples. Scale bar: 100 μ m.

S7. Quantification of perivascular fibrosis

The quantification of perivascular fibrosis was performed on SHG and MTS images of sham and TAC heart using ImageJ software. Briefly, an ROI was selected around the blood vessels. A threshold was applied at the ROI to select the collagen emitted SHG and aniline blue stain for collagen in MTS images. The percentage area was then depicted which was used for statistical analysis. A two-tailed Student's t-test was applied which indicated significant

differences in collagen deposition between sham and TAC hearts for both SHG imaging ($p=0.015$) and MTS ($p=0.0391$).

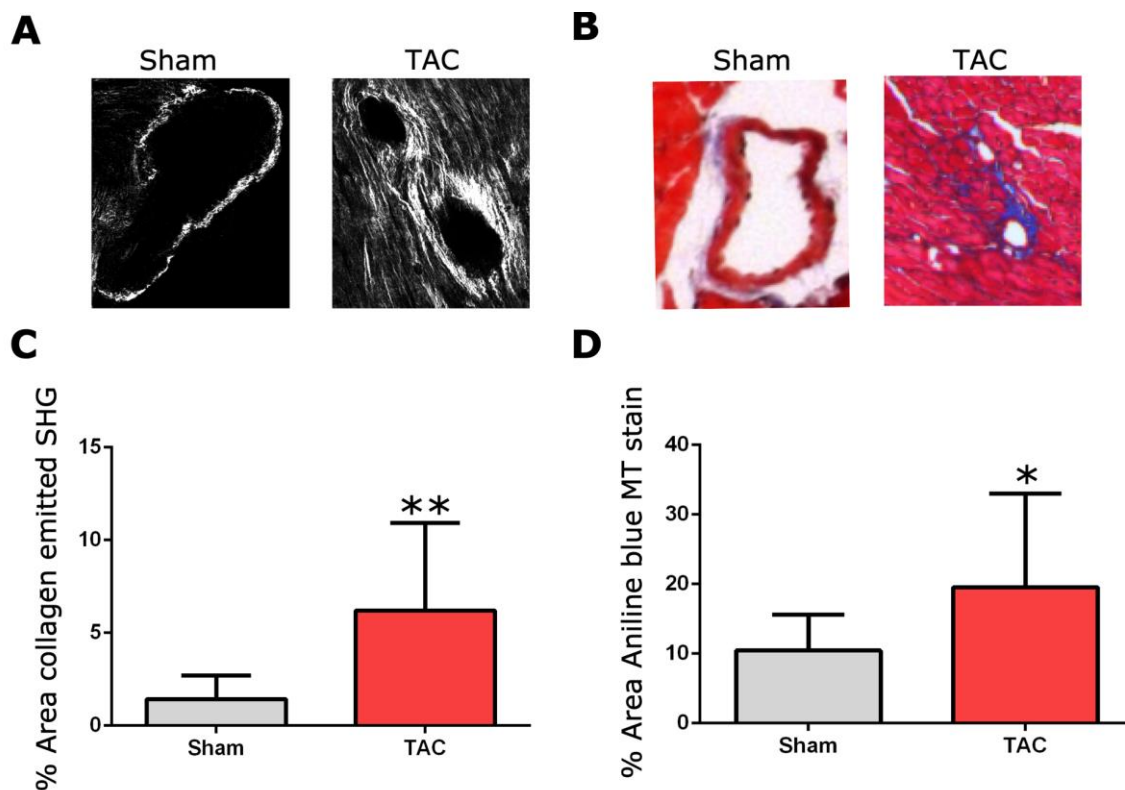


Figure S9: Quantification of perivascular fibrosis in sham and TAC hearts. A) Representative zoomed SHG images of coronary blood vessel in TAC and Sham heart. B) Representative zoomed images of MT stained blood vessel. C) Graph showing significantly higher percentage area of collagen emitted SHG in TAC heart as compared to the sham heart. D) Graph showing significantly higher percentage area for Aniline blue stain for collagen. The represented SHG and MTS images are from same sham and TAC sample. Data are the mean \pm SE. * $P<0.05$; $n = 3$ per group.

S8A. 2D micrographs used for quantification of myofibril periodicity in sham and TAC hearts

All images in section S8A and S8B were acquired with a two photon laser scanning microscopy (2P-LSM) setup (TriM Scope II, LaVision BioTec) equipped with a femtosecond-pulsed titanium-sapphire (Ti:Sa) laser (CRONUS laser; Coherent). A Zeiss W Plan-Apochromat 20x (NA 1.0) water immersion objective was used for image acquisition. All images were collected and processed with ImSpector (LaVision BioTec) and Fiji ³⁶. Images at the region of interest (ROI) were acquired using 112 x 112 μm image size, 1024 x 1024 pixels and 2.25 μs pixel dwell time.

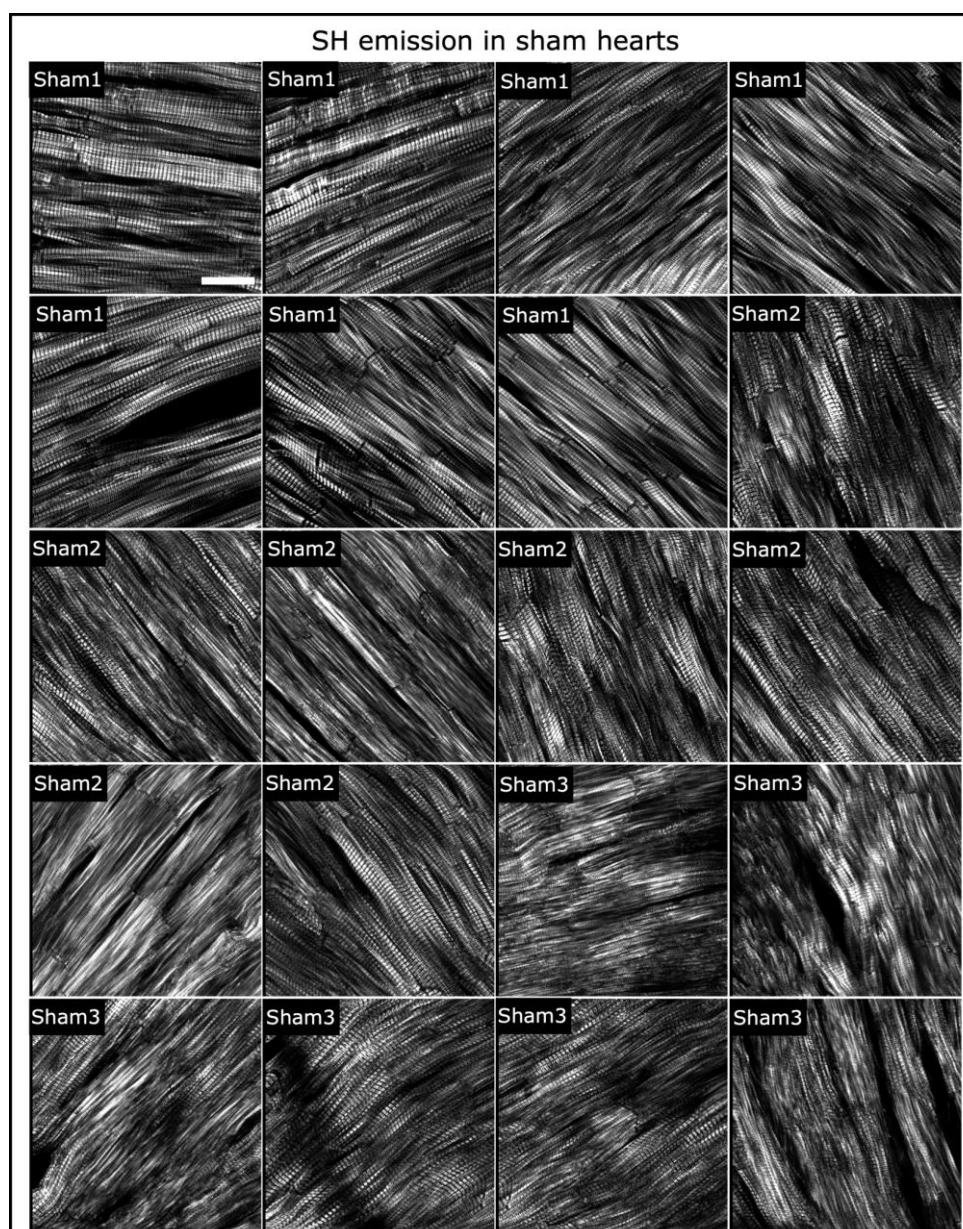


Figure S10: Twenty SHG micrographs showing the morphology of cardiac myofibrils in sham hearts ($n = 3$). All these images were used for quantitative and statistical assessment for determining the PSD indicator reflecting the orientation of strand, the striation periodicity in terms of the corresponding lattice peaks, as well as the degree of undulation in sham hearts. Scale bar: 25 μ m

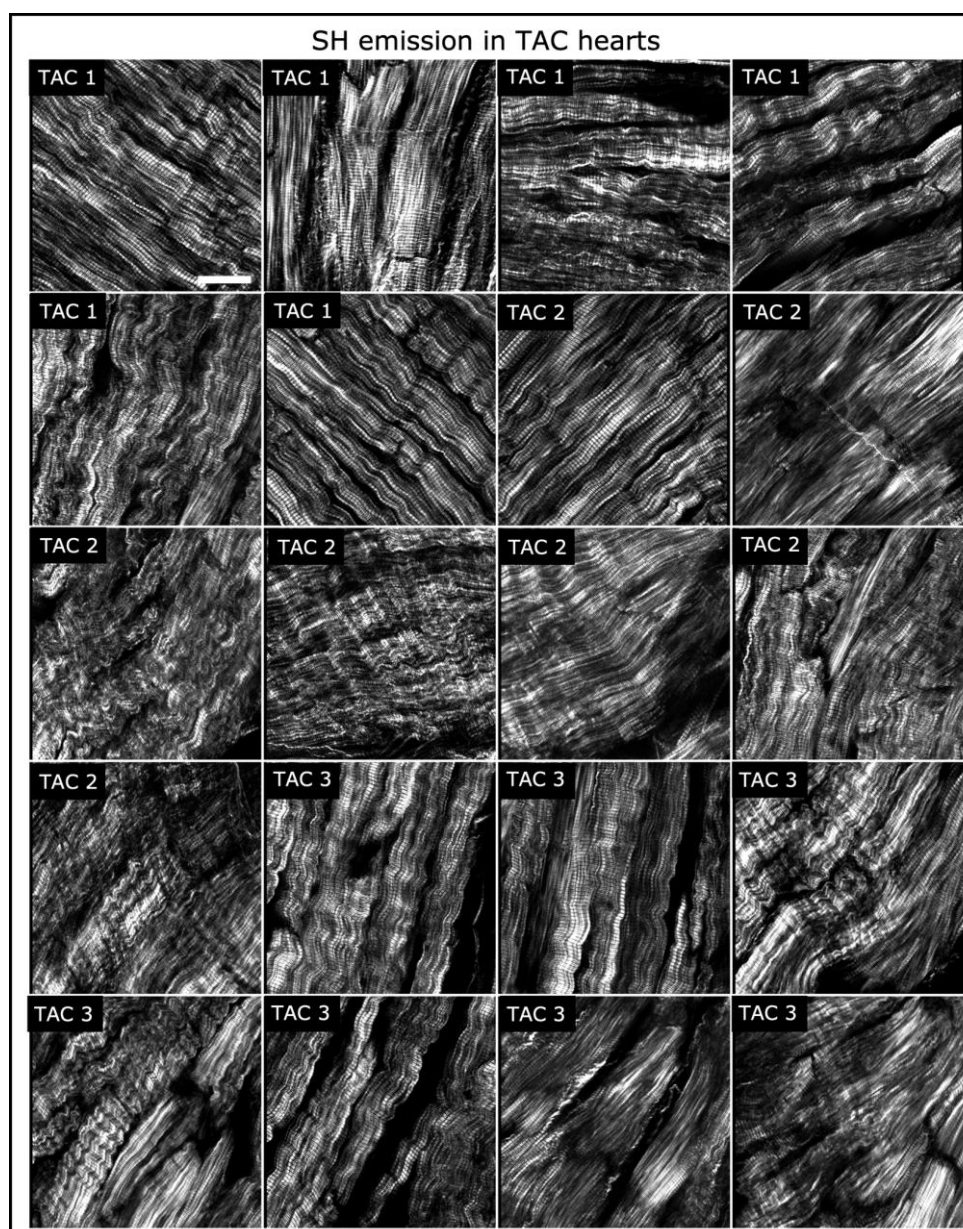


Figure S11: Twenty SHG micrographs showing the morphology of cardiac myofibrils in TAC hearts ($n = 3$). All these images were used for quantitative and statistical assessment for determining the PSD indicator reflecting the orientation of strand, the striation periodicity in terms of the corresponding lattice peaks, as well as the degree of undulation in TAC hearts. Scale bar: 25 μ m

Reference List

1. de Jong, S., van Veen, T. A. B., de Bakker, J. M. T. & Van Rijen, H. V. M. Monitoring cardiac fibrosis: A technical challenge. *Neth. Heart J.* 20, 44–48; 10.1007/s12471-011-0226-x (2012).
2. Hinderer, S. & Schenke-Layland, K. Cardiac fibrosis – A short review of causes and therapeutic strategies. *Adv. Drug Deliv. Rev.* 146; 10.1016/j.addr.2019.05.01177–82 (2019).
3. Liu, T. et al. Current Understanding of the Pathophysiology of Myocardial Fibrosis and Its Quantitative Assessment in Heart Failure. *Front. Physiol.* 8; 10.3389/fphys.2017.00238 (2017).
4. Ponikowski, P. et al. 2016 ESC Guidelines for the diagnosis and treatment of acute and chronic heart failure. *Eur. J. Heart Fail.* 18; 10.1002/ejhf.592 (2016).
5. Bacmeister, L. et al. Inflammation and fibrosis in murine models of heart failure. *Basic Res. Cardiol.* 114; 10.1007/s00395-019-0722-5 (2019).
6. DeAlmeida, A. C., van Oort, R. J. & Wehrens, X. H. T. Transverse aortic constriction in mice. *JOVE.* 38; 10.3791/1729 (2010).
7. Richards, D. A. et al. Distinct Phenotypes Induced by Three Degrees of Transverse Aortic Constriction in Mice. *Sci. Rep.* 9; 10.1038/s41598-019-42209-7 (2019).
8. Lombardi, V. et al. X-ray diffraction studies of the contractile mechanism in single muscle fibres. *Philos. Trans. R. Soc. Lond. B Biol. Sci.* 359; 10.1098/rstb.2004.1557 (2004).
9. Linari, M. et al. Force generation by skeletal muscle is controlled by mechanosensing in myosin filaments. *Nature* 528; 10.1038/nature15727 (2015).
10. Ait-Mou, Y. et al. Titin strain contributes to the frank-starling law of the heart by structural rearrangements of both thin- and thick-filament proteins. *PNAS* 113; 10.1073/pnas.1516732113 (2016).
11. Reconditi, M. et al. Myosin filament activation in the heart is tuned to the mechanical task. *PNAS* 114; 10.1073/pnas.1619484114 (2017).
12. Nicolas, J. D. et al. Scanning X-ray diffraction on cardiac tissue: Automatized data analysis and processing. *J. Synchrotron Radiat.* 24, 1163–1172; 10.1107/S1600577517011936 (2017).
13. Sakdinawat, A. & Attwood, D. Nanoscale X-ray imaging. *Nat. Photonics.* 4; 10.1038/nphoton.2010.267 (2010).
14. Bernhardt, M. et al. Correlative microscopy approach for biology using X-ray holography, X-ray scanning diffraction and STED microscopy. *Nat. Commun.* 9; 10.1038/s41467-018-05885-z (2018).
15. Reichardt, M. et al. X-Ray Structural Analysis of Single Adult Cardiomyocytes: Tomographic Imaging and Microdiffraction. *Biophys. J.* in press; 10.1016/j.bpj.2020.08.019 (2020).
16. Nicolas, J.-D., Aeffner, S. & Salditt, T. Radiation damage studies in cardiac muscle cells and tissue using microfocused X-ray beams: experiment and simulation. *J. Synchrotron Rad.* 26; 10.1107/S1600577519006817 (2019).
17. Freund, I. & Deutsch, M. Second-harmonic microscopy of biological tissue. *Opt. Lett.* 11, 94; 10.1364/ol.11.000094 (1986).
18. Mostaço-Guidolin, L. B. et al. Collagen morphology and texture analysis: From statistics to classification. *Sci. Rep.* 3; 10.3390/ijms18081772 (2013).

19. Green, N. H. et al. A new mode of contrast in biological second harmonic generation microscopy. *Sci. Rep.* 7; 10.1038/s41598-017-13752-y (2017).
20. Plotnikov, S. V., Millard, A. C., Campagnola, P. J. & Mohler, W. A. Characterization of the Myosin-Based Source for Second-Harmonic Generation from Muscle Sarcomeres. *Biophys. J.* 90; 10.1529/biophysj.105.071555 (2006).
21. Martin, T. P. et al. A novel approach for assessing cardiac fibrosis using label-free second harmonic generation. *Int J Cardiovasc Imaging.* 29; 10.1007/s10554-013-0270-2 (2013).
22. Varga, B. et al. Internal structure and remodeling in dystrophin-deficient cardiomyocytes using second harmonic generation. *NBM.* 30; 10.1016/j.nano.2020.102295 (2020).
23. Bernhardt, M. et al. X-Ray Micro- and Nanodiffraction Imaging on Human Mesenchymal Stem Cells and Differentiated Cells. *Biophys. J.* 110; 10.1016/j.bpj.2015.12.017 (2016).
24. Travers, J. G., Kamal, F. A., Robbins, J., Yutzey, K. E. & Blaxall, B. C. Cardiac Fibrosis: The Fibroblast Awakens. *Circ. Res* 118; 10.1161/CIRCRESAHA.115.306565 (2016).
25. Weber, K. T., Sun, Y., Bhattacharya, S. K., Ahokas, R. A. & Gerling, I. C. Myofibroblast-mediated mechanisms of pathological remodelling of the heart. *Nat. Rev. Cardiol.* 10; 10.1038/nrcardio.2012.158 (2013).
26. Nicolas, J.-D., Aeffer, S. & Salditt, T. Radiation damage studies in cardiac muscle cells and tissue using microfocused X-ray beams: experiment and simulation. *J. Synchrotron Rad.* 26; 10.1107/S1600577519006817 (2019).
27. Tiaho, F., Recher, G. & Rouède, D. Estimation of helical angles of myosin and collagen by second harmonic generation imaging microscopy. *Opt. Express* 15; 10.1364/oe.15.012286 (2007).
28. de Haas Hans J., Arbustini Eloisa, Fuster Valentin, Kramer Christopher M. & Narula Jagat. Molecular Imaging of the Cardiac Extracellular Matrix. *Circ. Res.* 114; 10.1161/CIRCRESAHA.113.302680 (2014).
29. Garcia-Canadilla, P. et al. Automated cardiac sarcomere analysis from second harmonic generation images. *J. Biomed. Opt.* 19; 10.1117/1.JBO.19.5.056010 (2014).
30. Igor Iruretagoyena, J. et al. Cardiac dysfunction is associated with altered sarcomere ultrastructure in intrauterine growth restriction. *Am. J. Obstet. Gynecol.* 210; 10.1016/j.ajog.2014.01.023 (2014).
31. Greenhalgh, C. et al. Influence of semicrystalline order on the second-harmonic generation efficiency in the anisotropic bands of myocytes. *Appl. Opt.* 46; 10.1364/AO.46.001852 (2007).
32. Rouède, D. et al. Determination of extracellular matrix collagen fibril architectures and pathological remodeling by polarization dependent second harmonic microscopy. *Sci. Rep.* 7; 10.1038/s41598-017-12398-0 (2017).
33. Yuan, C. et al. Changes in the crystallographic structures of cardiac myosin filaments detected by polarization-dependent second harmonic generation microscopy. *Biomed. Opt. Express* 10; 10.1364/BOE.10.003183 (2019).
34. Liu, W. Ralston, E. & Raben, N. Quantitative evaluation of skeletal muscle defects in second harmonic generation images. *J. Biomed. Opt.* 18; 10.1117/1.JBO.18.2.026005 (2013).
35. Llewellyn M. E. et al. Minimally invasive high-speed imaging of sarcomere contractile dynamics in mice and humans. *Nature* 454; 10.1038/nature07104 (2008).

36. Dejea, H. et al. Microstructural Analysis of Cardiac Endomyocardial Biopsies with Synchrotron Radiation-Based X-Ray Phase Contrast Imaging in Functional Imaging and Modelling of the Heart (eds. Pop, M. & Wright, G. A.) vol. 10263 23–31 Springer International Publishing (2017).
37. Zhang, Y. et al. FT011, a new anti-fibrotic drug, attenuates fibrosis and chronic heart failure in experimental diabetic cardiomyopathy. *Eur J Heart Fail.* 14; 10.1093/eurjhf/hfs011 549–562 (2012).
38. Toischer, K. et al. Differential Cardiac Remodeling in Preload Versus Afterload. *Circulation* 122; 10.1161/CIRCULATIONAHA.110.943431 (2010).
39. Schindelin, J. et al. Fiji: An open-source platform for biological-image analysis. *Nat. Methods* 9; 10.1038/nmeth.2019 (2012).
40. Cardiff, R. D., Miller, C. H. & Munn, R. J. Manual Hematoxylin and Eosin Staining of Mouse Tissue Sections. *Cold Spring Harb. Protoc.* 6; 10.1101/pdb.prot073411 (2014).
41. Foot, N. C. & Chandler, N. The Masson Trichrome Staining Methods in Routine Laboratory Use. *Stain Tech.* 8; 10.3109/10520293309116112 (1933).
42. Vedaldi, A. & Fulkerson, B. Vlfeat: an open and portable library of computer vision algorithms. *ICMR. MM'10*; 10.1145/1873951.1874249 (2008).

Acknowledgements

This work was supported by the Deutsche Forschungsgemeinschaft (DFG, German Research Foundation) under Germany's Excellence Strategy - EXC 2067/1- 39072994.

We thank Bärbel Heidrich and Regine Kurse for assistance in sample preparation and Sabine Wolfgramm and Bettina Jeep for providing great technical assistance for histology.

Funding

AK was supported by a seed grant of the Physics-to-Medicine Initiative Göttingen.

Competing interests

The authors declare that they have no competing interests.

Data availability

All data generated or analyzed during this study are included in this published article and its supplementary information files.

Chapter 2 – Label-free imaging of age-related cardiac structural modulations in non-human primates using multiphoton nonlinear microscopy

Amara Khan, Fernanda Ramos Gomes, Andrea Markus, Matthias Mietsch, Rabea Hinkel and Frauke Alves*

Submitted to 'Biomedical Optics Express' published by the Optical Society

Heart failure is one of the most common causes of morbidity and mortality. Both maturational abnormalities and age-associated cardiac pathologies contribute to heart failure. Imaging-based assessment to discern detailed cardiac structure at various maturational stages is imperative for understanding mechanisms behind cardiac growth and aging. Using two-photon microscopy (TPM) based label-free imaging, we investigated cardiac structural modulations in a human-relevant aging model, the common marmoset monkeys (*Callithrix jacchus*) divided into three different age groups including neonatal, young adult and old/geriatric. By devising a unique strategy for segregating collagen and myosin emitted second harmonic generation (SHG) signals, we performed volumetric assessment of collagen and total tissue (collagen + myosin). Aged marmoset hearts exhibited an increase in collagen and total tissue volume at the sites of severe tissue remodelling indicating age-related cardiac fibrosis. Significantly low tissue volume in neonatal marmoset hearts was attributed to a lack of banding between the myofibrils in maturing cardiac tissue. Comprehensive quantitative assessment of structural composition during maturation and aging of marmoset hearts revealed significant differences in myofibril length, alignment, curvature and angular distribution. In conclusion, label-free high-resolution TPM facilitates visualization and quantification of subcellular structural features for understanding vital age-related morphological alterations in the marmoset heart.

Introduction

Cardiac maturation and growth are dynamic processes that involve complex and well-orchestrated biochemical, physiological, and anatomical changes that define the cardiac function in different age groups. Our current understanding of postnatal cardiac development and aging is limited by an overall lack of reliable data about the cardiomyocyte (CM) growth and proliferation mechanisms in the heart from birth to early adulthood and old age [1–6].

Fundamental differences in cardiac structure and physiology exist between a neonatal and adult mammalian heart in several ways, mainly because the neonatal CM are not fully developed. Structural maturity and myocardial growth in humans are based on CM enlargement and proliferation at the early postnatal developmental stages [2,7–9]. Shortly after birth, numerous transitions are triggered in the neonatal heart that initiate complex remodeling from a fetal state into an adult heart. Radiocarbon birth dating has further shown that a small portion of CMs is replaced in humans older than 20 years [10]. Imaging-based assessment to discern detailed cardiac structural composition in neonatal hearts and its comparison at the cellular level with an adult heart and aged hearts is by far greatly lacking.

Over the span of cardiac growth and structural maturation, an aged heart begins to display pathophysiological remodeling which also makes aging one of the leading risk factors for heart failure related morbidity and mortality. Aged heart exhibits development of left ventricular (LV) hypertrophy, excessive extracellular matrix (ECM) deposition and CM senescence even in absence of underlying pathology [4,11–17]. Evolving evidence shows that inflammatory and fibrogenic pathways play a pivotal role in triggering CM as well as vascular aging [18–21]. Beside tissue remodeling, a myriad of additional cellular factors are associated with cardiac aging including age-related apoptosis and excitation-contraction coupling (ECC) disorder due to impaired Calcium (Ca^{2+}) handling [22,23].

Elucidating myocardial structure is imperative for investigating cardiac growth, maturation and age-related pathophysiological remodeling. Imaging cardiac aging in non-human primates (NHPs) can provide highly clinically relevant data, as they reflect a comparable life span as humans. Other laboratory species, such as rodents or even large animal models (pigs or sheep) are barely available as aged animals. Furthermore, reports on the influence of cardiac maturation and aging in NHPs is largely lacking [3,17]. Among NHPs, using common

marmoset monkeys (*Callithrix jacchus*) model in aging research provides various advantages such as a relatively small body size and short generation time [17].

Histological examination is a gold-standard for morphological assessment of the heart, but it lacks adequate resolution and specificity. Alternatively, high-resolution microscopy techniques offer detailed visualization on the cellular and sub-cellular level such as confocal microscopy and super-resolution microscopy techniques [9,25], however, they require labor intensive sample preparation and labeling of target proteins using fluorescent labeled antibodies often resulting in unspecific binding and overstaining. Furthermore, photobleaching of the fluorophore can hinder repetitive imaging and quantitative analysis [26]. Two-photon microscopy (TPM) provides a promising alternative as it can image intrinsic signals emitted in form of two-photon excitation fluorescence (TPEF) and second harmonic generation (SHG). Since in TPM an endogenous fluorescent molecule with specific physical properties and order is excited by pulsed near infra-red (IR) laser and the emitted signal is detected at ultrasensitive detectors, this allows increased imaging depth, high specificity and reproducibility [27,28].

Unlike TPEF, in which two photons are absorbed by the target structure to produce a fluorescent signal as a single photon with some loss of energy, SHG does not involve photon absorption and energy decimation. Instead, SHG as a non-linear coherent scattering process resulting in phase matching and summation of light waves and involves conversion of two excitation photons into a single emission photon with twice the energy and thus, half of the excitation wavelength. Biological materials with repetitive non-centrosymmetric units, including myosin within the striated muscle and fibrillar collagen which are both integral components of cardiac structure, facilitate the emission of SHG [27,29].

The intensity of SHG from myosin (striated muscle) and collagen is crucially dependent on i) the organization and size of these signal-eliciting structures, ii) the excitation/detection approach, and iii) the power and polarization of the incident light [27,29,30]. To this end, we recently established a comparative SHG and X-ray diffraction imaging approach for label-free and high-resolution visualization of cardiac remodeling and fibrosis progression at different stages in a cardiac pressure-overload mouse model. In this study the SHG emission from collagen and myosin was segregated based on structural morphology and was performed in two-dimension (2D) only [30].

Detailed analysis of subcellular structural components during maturation and aging was performed using TPM label-free imaging in common marmosets belonging to three different age groups including neonatal/newborn, young adult and old/geriatric without any additional disease or comorbidities. To achieve this, we harnessed the differences between collagen and myosin emitted SHG and devised a sophisticated label-free imaging strategy to enable signal segregation from the two harmonophores. This resulted in reliable volumetric assessment of connective tissue and total tissue (myosin + collagen) demonstrating cardiac fibrosis in old/geriatric marmosets and differences in morphological features of myofibril in all age groups.

Materials and Methods

Animal groups and organ collection

Experiments were conducted on nine common marmoset monkeys (*Callithrix jacchus*) with an age ranging from 6 days to 13 years (Table S1). The study cohort consisted of 1 female neonatal marmoset and 8 males belonging to different age groups (Table S1). The animals were divided into three groups – neonatal/newborn (<4 weeks, n = 3), young adult (1–4 years, n = 3), and old/geriatric (>10 years, n = 3) following general classifications according to literature [52].

All animals were raised and kept in accordance with the German Animal Welfare Act. All animal procedures were performed in compliance with the guidelines of the European Directive (2010/63/ EU) and the German ethical laws. Animals of this study were either euthanized due to animal welfare reasons (corresponding to humane endpoints) or they were euthanized for organ removal for other scientific purposes (according to §4 TierSchG).

To sacrifice, animals were deeply anaesthetized with either ketamine (intramuscular >15mg/kg, Ketamin 10%, WDT) or a combination of alphaxalone (i.m. 10mg/kg, Alfaxan 10mg/ml, Jurox) and diazepam (0.125mg/animal, Diazepam-ratiopharm 5mg/ml, ratiopharm GmbH) followed by an intraperitoneal or intravenous administration of pentobarbital (>150mg/kg). Heart was collected in addition to a broad spectrum of organs.

Sample preparation

Freshly explanted hearts were briefly washed in phosphate buffer saline (PBS) and then fixed in 4% formaldehyde solution (FA) overnight at room temperature (RT). Hearts were cut into transverse tissue sections for SHG imaging and adjacent tissue sections from the same heart sample were used for histology. Briefly, for sectioning, hearts were embedded in 5% agarose and were cut into 50 μm , 100 μm and 1 mm sections using a vibratome (VT1000 S; Leica Biosystems). The 50 and 100 μm thick tissue sections were used for TPM and were stored in PBS containing 0.04% sodium azide. The 1 mm sections were embedded in paraffin for histology (Fig. S1).

Two-photon microscopy

Label-free SHG and TPEF imaging were performed on an upright TriM Scope II multiphoton microscope (Mitenyi Biotech) equipped with a tuneable Ti:sapphire laser (Ti:Sa, 670–980 nm; Cronus, Mitenyi Biotech). Images were acquired using a Zeiss W Plan-Apochromat 20x (NA 1.0) water immersion objective. The emitted light was split by a 495 nm and T560 nm long pass dichroic mirror (Semrock) and signals were detected at 3 detectors with differential filter configuration (red 434/20, blue 434/20 and green 647 long pass, Semrock). Cardiac tissue sections were excited at 870 nm with 100 – 150 mW average power and simultaneous backscattered SHG and autofluorescence signals were detected through the objective lens at PMT detectors (Hamamatsu) and forward SHG signal was collected using a 1.4NA condenser lens at a third PMT detector (Hamamatsu). For the overview images, an image size of $336 \times 336 \mu\text{m}$ with 1024×1024 pixels and a pixel dwell time of 2.19 μs was used. Magnified images at the ROI were acquired using $112 \times 112 \mu\text{m}$ image size, 1024×1024 pixels, 2.25 μs pixel dwell time and $107 \times 107 \mu\text{m}$ size, 512×512 to achieve adequate image resolution for analysis.

Histology

The paraffin-embedded 1 mm cardiac tissue slices from regions adjacent to tissue sections used for TPM imaging were cut into 2 μm sections. The sections were deparaffinized and dehydrated followed by haematoxylin & eosin (H&E) and Masson's Trichrome staining (MTS), performed as described before [30].

The images were acquired with an Axiovert 200 M inverted microscope (Carl Zeiss Microscopy GmbH). Image generation and processing were performed with the software AxioVision Rel.4.6 (<https://carl-zeissaxiovisionrel.software.informer.com/4.6/>) and Fiji, respectively.

Image processing and statistical analysis

2D micrographs were processed with Fiji for assessing the histogram, intensity and length of the myofibrils. Myofibril curvature and alignment were quantified using the TWOMBLI plugin in Imagej [31]. 3D volumes, surface rendering of myofibril segments and angular distribution were processed and analysed using Imaris 9.6.0 (Bitplane) and Graph Pad Prism 9 (Graph Pad Software, Inc.). For statistical analysis, the t-test for the same mean implemented in Graph Pad Prism 9 was used with a p-value of 0.05 (*) as margin for statistical significance.

Results

Label-free imaging by TPM for distinction of myosin and collagen

The most common application of TPM involves excitation of exogenous or endogenous fluorescent molecules i.e., TPEF. For establishing a label-free imaging approach in marmoset cardiac tissue, we applied TPEF to detect only endogenous fluorescence signals emitted from intrinsic molecules in unstained tissue slices enabling repetitive and long-term imaging of the samples. Extracellular fluorescence in cardiac tissue arises from blood cells and elastin (Fig. 1, left panel) whereas the majority of intracellular fluorescence arises from the mitochondrial proteins nicotinamide adenine dinucleotide (NADH), flavin adenine dinucleotide (FAD) and other fluorescence emitting proteins. Nuclei, on the other hand, lack a fluorescent signal and hence appeared dark, and were detected easily due to their elongated morphology in the myocardium (Fig. 1, left panel).

Specimens amenable to bidirectional (forward and backward) detection include thin tissue slices or cleared tissue samples possessing high optical transparency while thick and highly opaque specimens are detected as backward scatter only. Since 50 μm cardiac tissue slices, which were relatively transparent, were used for TPM imaging, the SH emission signals were collected in both backscattered (epi-) and forward propagating direction (Fig. 1). SHG being a non-linear coherent process is strongly influenced by the harmonophores' spacing,

concentration, order and orientation hence these aspects were taken into account to enable segregation of SH emission from myosin and collagen. In our experimental design, collagen emitted SHG was detected in epi-direction while at the forward detector combined SH signals from myosin and collagen were visualized (Fig. 1 and 2).

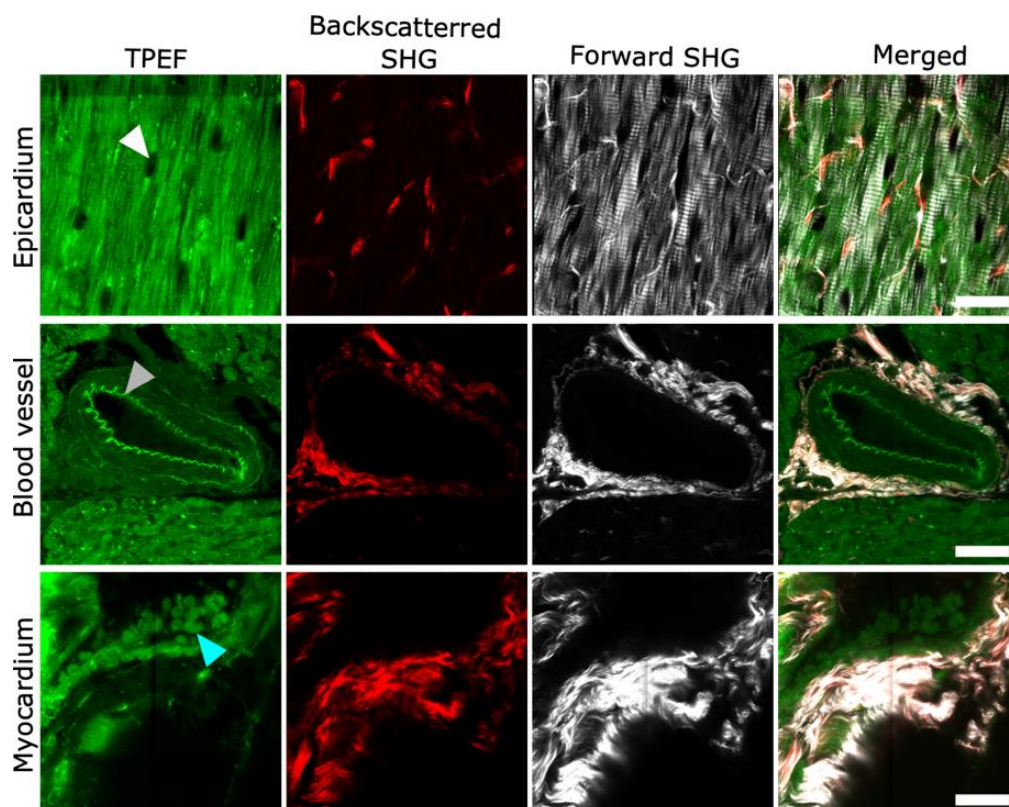


Figure 1: Label-free TPM images of old marmoset cardiac tissue. Representative TPEF, backscattered SHG, forward propagating SHG and merged images are shown for epicardial wall, coronary blood vessel and myocardium from the same heart. TPEF arises from endogenous fluorophores such as blood cells (marked by cyan arrowhead), elastin (marked by grey arrowhead) and other intracellular fluorescent proteins, while the nuclei appear dark (marked by white arrowhead). Backscattered SHG emission is detected mainly from collagen while the forward propagating SHG emission originates with high intensity from both collagen and myosin at the epicardium and myocardium and around blood vessel. Merged images show signal emission from all channels. Scale bar: 25 μm in all images.

Fig. 2 exhibits the detailed cross-correlation of SHG emission from the two harmonophores in adult cardiac tissue detected in both forward and backscattered direction. All images shown were acquired at the same regions simultaneously in both directions using the same illumination power, excitation (870 nm) and emission wavelengths (434 ± 20 nm) (Fig. 2). It is evident that in general the forward signals are stronger than the ones detected in the backward direction. Backward myosin SHG (mean intensity = 165.0) was considerably weaker than

forward myosin SHG signal with a poor signal-to-noise ratio (Fig. 2a and b). Contrarily, the backscattered collagen signal had optimum signal intensity (mean intensity = 1279.8), while it caused intense signal saturation at the forward detector (mean intensity = 6857.5) when acquired with identical image acquisition settings used for imaging myosin (Fig. 2c and d). These differences in the forward/backward SHG intensity ratios enabled us to further optimize image acquisition parameters to acquire SH emission mainly from collagen alone in backscattered direction and the combined signal from both collagen and myosin as the forward transmitted signal with minimal saturation from collagen (Fig. 2e and f). For quantification purposes, SHG signal in the forward channel from both harmonophores (mean intensity = 2572) was used for determining total volume while the signal intensities from collagen were ideal for quantification in backscattered direction (Fig. 2e and f). The discrepancy in amount of collagen detection at backscattered and forward detector was minimized by using thin tissue slices of 50 μm for the quantification of collagen.

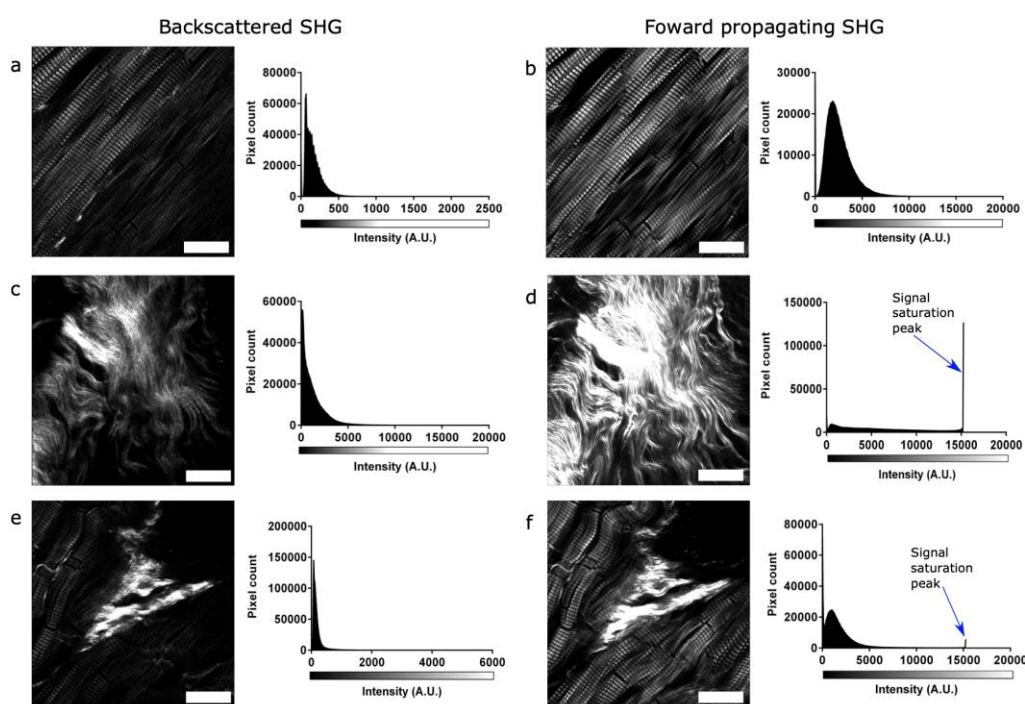


Figure 2: Cross-correlation of forward and backscattered SHG signal in adult marmoset cardiac tissue. Representative SHG images are shown for the same regions for backscattered (epi-) (left panel) and forward (right panel) detection with their respective histograms. Images and histograms are shown for SHG from different structures including (a-b) myosin (c-d) collagen and (e-f) both myosin and collagen. Scale bar: 25 μm in all images. All histograms are presented in a 16-bit image format.

Volumetric quantification of age-related differences in collagen and total tissue content

To investigate the overall tissue structural composition of collagen and myosin in different age groups, label-free imaging was performed on cardiac tissue sections obtained from neonatal/newborn ($n = 3$), young adult ($n = 3$) and old/geriatric ($n = 3$) marmosets (Fig. S2). Neonatal hearts were compared with the adult hearts for assessing cardiac maturation and growth. The age-associated cardiac remodeling was examined in old/geriatric hearts. 3D micrographs for volumetric assessment in $50\ \mu\text{m}$ tissue sections were acquired at randomly selected regions of interest (ROI) at the myocardium of the LV and the interventricular septum (IVS) wall for all three maturation stages shown in Fig. 3. The backscattered signal exhibited SHG exclusively emitted from collagen while the forward SH signal was generated from both myosin and collagen (referred to as the total tissue volume) (Fig. 3a). The data for average raw volumes of collagen and total tissue content showed an overall increase in tissue content with aging (Fig. 3b, Movie S1-S3). Compared to neonatal heart, the old hearts had significantly higher total tissue volume at the ROIs ($p\text{-value} = 0.0133$). Further, the percentage backscattered (collagen) and forward SHG (total tissue) volumes were compared to assess the relative tissue composition. The neonatal heart had an overall lowest total tissue volume and was mainly composed of muscle (Fig. 3b and c). The connective tissue (collagen) in the neonatal heart was found to be less than 1% of total tissue and was highest in the old marmosets (collagen = 17.2 %) (Fig. 3b and c). In contrast to the adult heart (collagen volume = 6.3%), the old heart had a high volume of connective tissue indicating the development of interstitial fibrosis causing an overall disruption of the surrounding muscle mass (Fig. 3a and b; MOVIE S1). Despite the overall high raw total tissue volume in the old hearts (Fig. 3b, $p\text{-value} = 0.0133$ as compared to neonatal hearts), the relative total tissue volume (forward/backward SHG) was slightly lower (82.8%) than in adult (93.7%) and neonatal (99%) hearts (Fig. 3c), revealing a high collagen-based tissue composition in the old/geriatric hearts (Movie S3).

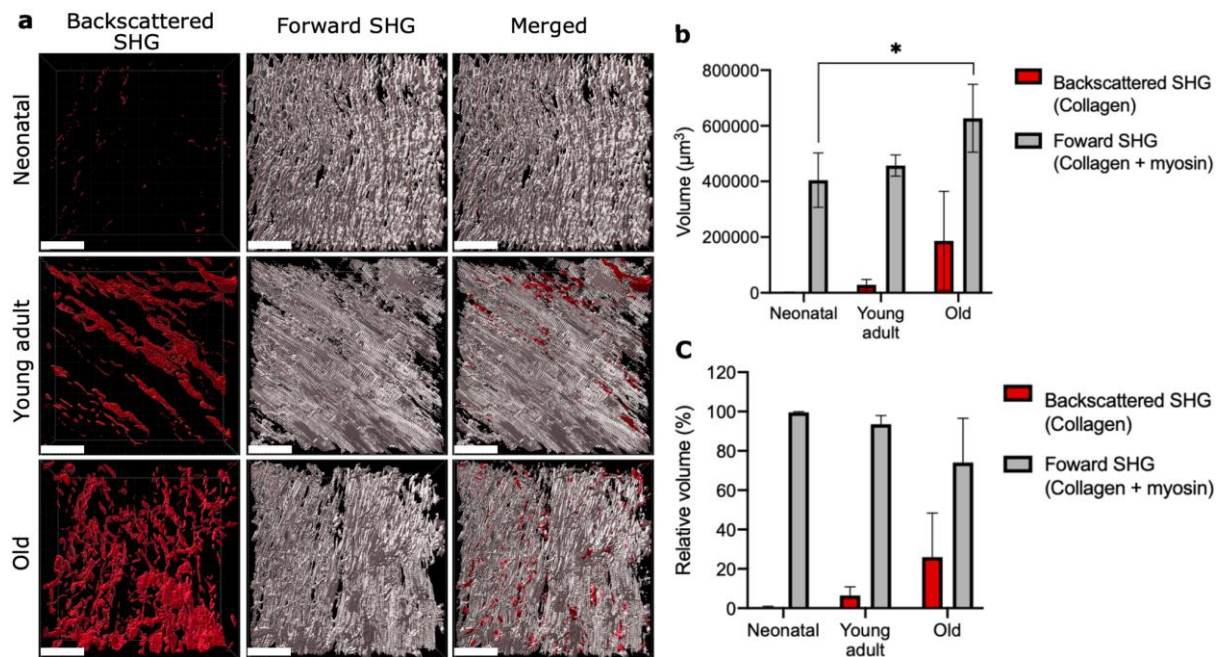


Figure 3: Quantification of collagen and myosin content at different cardiac developmental stages. a) 3D rendering of backscattered SHG emission from collagen, forward SHG emission from both myosin and collagen (total volume) and merged images are shown for neonatal, young adult and old marmoset cardiac tissue. b) Graph showing volume (μm^3) of backscattered SHG (collagen) and forward SHG (total volume). c) Percentage of relative tissue volumes detected at the backscattered and forward channels. Scale bars: 50 μm in all images.

Comprehensive analysis of age-related morphological changes in myofibrils

To further investigate the effects of tissue growth and maturation, the impact of the excess collagen deposition and overall increased total tissue volume on the muscle structure, 2D micrographs were obtained at randomly selected ROIs at the LV and IVS myocardial wall. These micrographs were used for examining the structure and spacing of myofibrils at the cellular level in the three age groups of marmosets. In the old hearts, the myocardium appeared compact with undulated myofibrils revealing a hypercontractile state (Fig. 4a). The muscle mass in adult hearts, similar to old hearts, was also dense with lower spacing between myofibrils, however, these were not hypercontracted (Fig. 4a). In comparison, the neonatal hearts displayed the highest degree of spacing between myofibrils which lacked overall organization and banding (Fig. 4a). The intercalated disks (ICDs) that bind the myofibrils were not visible at this stage in the neonatal/newborn indicating that these were not fully developed in cardiac tissue (Fig. 4a).

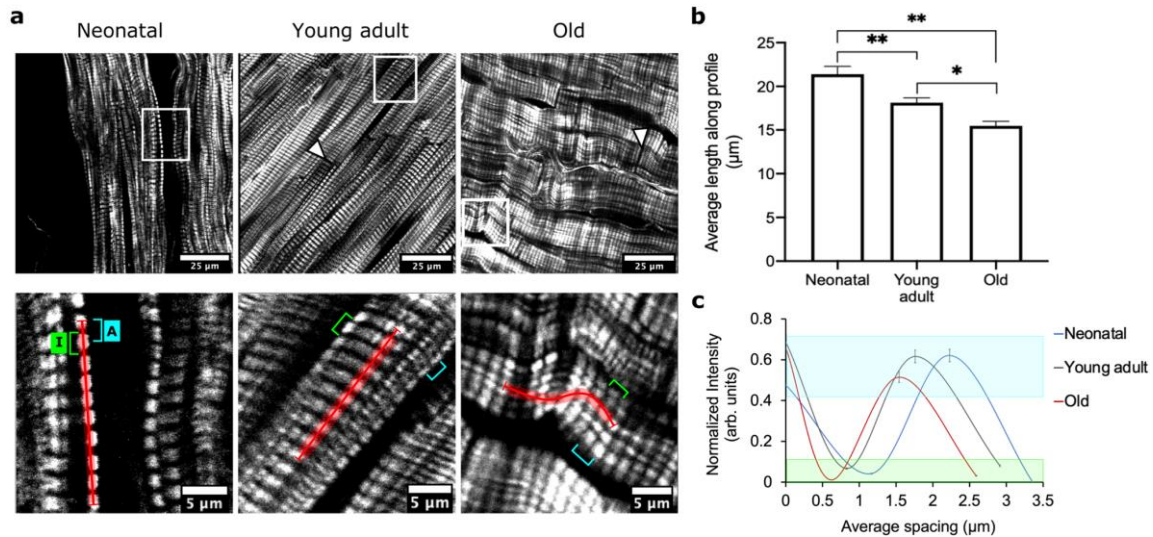


Figure 4: Myofibril morphology at different cardiac maturation stages. a) Representative images of TPM showing the arrangement of myosin fibers in neonatal (n = 3), adult (n = 3) and old (n = 3) marmoset hearts with overview images (top) and magnified images at the ROI marked by the white box (bottom). The white arrowheads mark the intercalated disks which were not visible in neonatal hearts. b) Graph for the average length of myofibril segment along the profile (marked by the red line in zoomed-in images). c) Normalized intensity and average spacing are shown for the distance between two SHG emitting anisotropic A-bands (cyan in a) and two non-SHG emitting isotropic I-bands (green in a); the distance profiles for A-bands lie within the shaded cyan box and for I-band within the green shaded box, respectively. Scale bars: 25 μm in overview images (top panel) and 5 μm in magnified ROI images (bottom panel).

The differences in spacing of myofibrils were quantified in zoomed-in images along ten SHG emitting myosin packed anisotropic (A) bands and nine non-SHG emitting isotropic (I) bands containing actin filaments (Fig. 4a, bottom). This micro-assessment of myofibrils for determining length was only possible on segments of myofibrils because ICDs could not be identified in immature neonatal, and the mature myocardium of adult and old/geriatric hearts comprised of overlapping myofibrils. The average length of these myofibril segments calculated along the ten A-bands was highest in neonatal hearts ($21.3 \mu\text{m} \pm 0.90$), reflecting an overall high-level of spacing which reduced significantly with cardiac tissue maturity in adult hearts ($18.3 \mu\text{m} \pm 0.56$, p-value = 0.01000) (Fig. 4b). In old/geriatric hearts, due to hypercontractility, the length of myofibrils was found to be significantly lower ($15.4 \mu\text{m} \pm 0.52$) as compared to adult (p-value = 0.0145) and neonatal (p-value = 0.0023) hearts (Fig. 4b). This significantly reduced spacing in old hearts can further be attributed to pathophysiological hypertrophy in addition to severe undulation which also contributes to high tissue volume in these hearts (Fig. 3b). Upon closer inspection, it was further revealed that the spacing between

two isolated A-bands and I-bands also followed a similar pattern (Fig. 4a and c). These results displayed the highest A-band to A-band spacing in neonatal hearts ($2.22 \mu\text{m} \pm 0.09$), followed by adult hearts ($1.76 \pm 0.20 \mu\text{m}$) and the lowest spacing was observed in the old hearts ($1.54 \mu\text{m} \pm 0.02$) (Fig. 4c). Similarly, the distance between two subsequent I-bands in neonatal tissues was highest ($2.19 \mu\text{m} \pm 0.06$) which was reduced in adult hearts ($2.10 \mu\text{m} \pm 0.21$) and old hearts ($1.99 \mu\text{m} \pm 0.17$) (Fig. 4c). The spacing profile in all age groups thus presents varying degrees of tissue maturation at the structural level.

Since myofibril assembly and arrangement presented diverse patterns in all three age groups, further assessment of myofibril morphology was performed on entire 2D micrographs obtained at random ROIs. Briefly, by using the TWOMBLI [31] (The Workflow Of Matrix BioLogY Informatics) plugin in Fiji, the spatial metrics for each group were derived and applied to the Ridge Detection tool for optimal masking of the images (Fig. 5a). Following, mask generation the patterning of myofibrils was defined by two metrics – alignment and curvature (Fig. 5b and c). The alignment parameter captured the extent of myofibril orientation in similar direction within the field of view where a high value (close to 1) present perfect alignment while a lower value (close to 0) presents isotropy. Our results demonstrated significant differences in myofibril alignment in neonatal (p-value = 0.0040) and old hearts (p-value = 0.024) as compared to adult hearts (Fig. 5b). The disassembly of neonatal myofibrils is attributed to the lack of banding, further supporting the observation that ICDs are not fully developed at this maturational stage (Fig. 4a). The significantly low alignment in old hearts suggests structure disruption that may occur due to excessive ECM deposition (Fig. 5b).

The curvature metric measures the average change in angle moving incrementally along the masked region. The adult hearts display high-level of straightness while the neonatal and old hearts revealed varying curvatures in the myofibril assembly (Fig. 5c). In neonatal hearts, the large range of curvature indicated an overall loose structure with undefined symmetry which was significantly different from the old hearts (p-value = 0.0242). The old/geriatric hearts also displayed a significantly different curvature as compared to the adult hearts (p-value = 0.0009). The tight curve radius in the old heart further substantiates the presence of hypercontractile myofibrils (Fig. 5c).

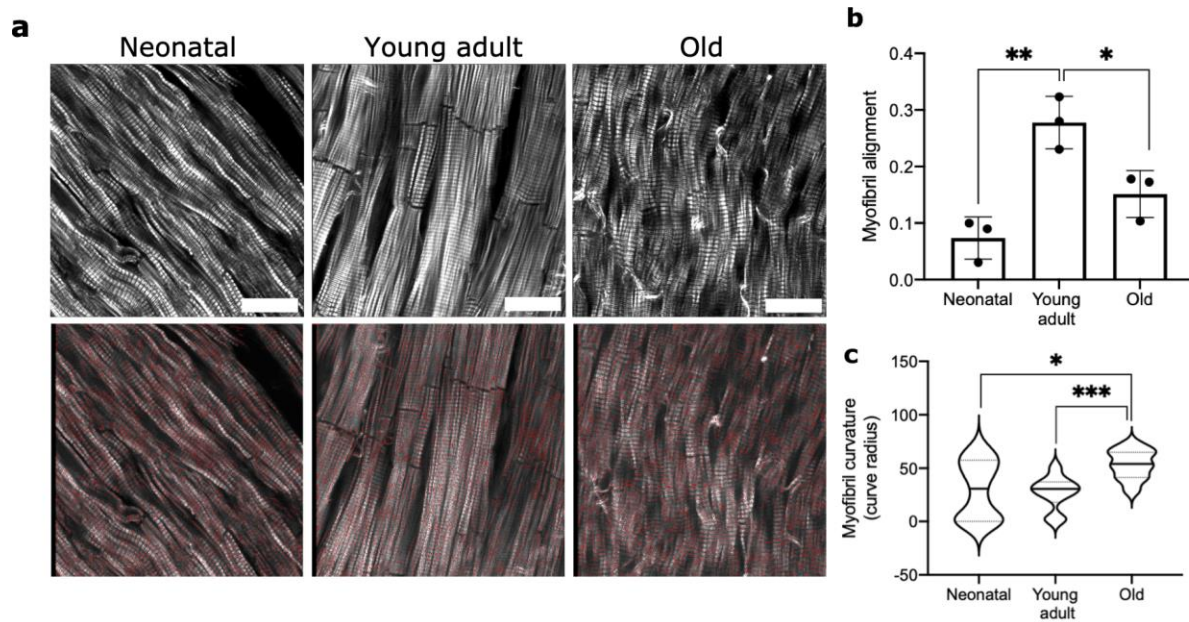


Figure 5: Assessment of myofibril organization in the myocardium. a) Representative TPM 2D micrographs (left panel) and respective masked images (right panel) showing myofibril organization in neonatal, young adult and old hearts. b-c) Graphs showing average myofibril alignment and myofibril curvature in all age groups. Scale bar: 25 μm for all images.

Micro-level 3D evaluation was performed to further confirm and evaluate the differences in myofibril morphology and assembly that orchestrates and contributes to complex structural composition of the entire cardiac tissue. To achieve this, fragments of myofibrils were cropped in 3D from entire tissue volume, containing ten A and nine I-bands (Fig. S3). 3D surface rendering of the isolated myofibril segments enabled marking measurement points at the center of the object i.e., at the individual A-band (Fig. 6a and Fig. S3). The angle between each measurement point exhibited the angular distribution at the micro-level. The adult heart presented the highest degree of straightness with an average angle of $177^\circ \pm 2.0$ which was significantly altered in neonatal hearts (p-value = 0.0108) with an average angle of $171^\circ \pm 3.7$ (Fig. 6b). The highest range of angular distribution was observed in the hypercontracted myofibrils of the old hearts with an average angle of $156^\circ \pm 16.6$ (p-value = 0.0256) (Fig. 6b). The changes in angular distribution reflect the overall structural integrity and organization at the micro-level in the different age groups of the marmoset model.

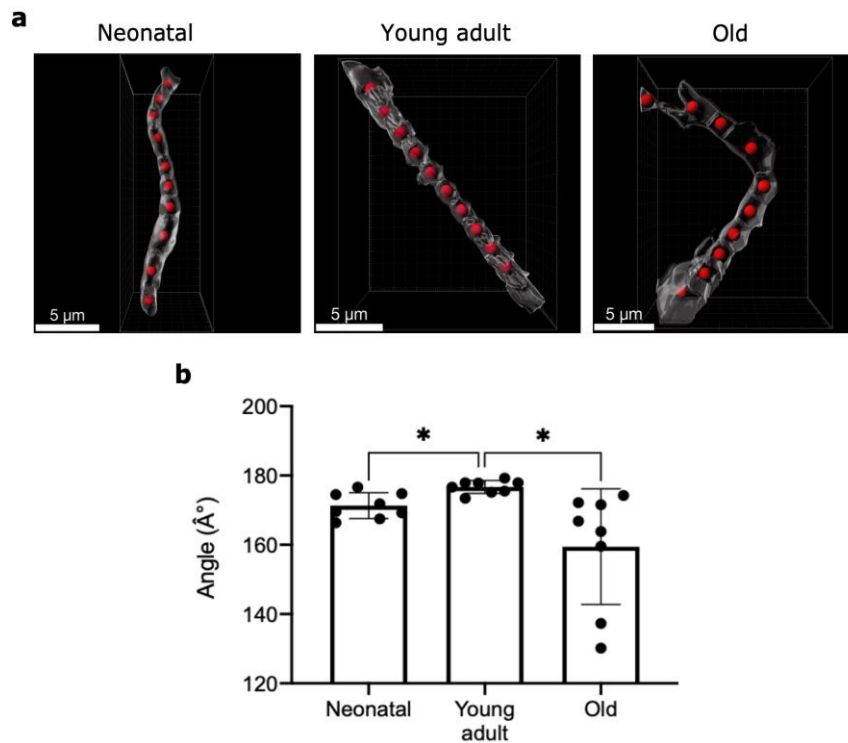


Figure 6: 3D assessment of angular distribution in the isolated myofibril segments. (a) Segments of myofibrils containing 10 A bands are shown for neonatal, young adult and old hearts marked with measurement points in red. (b) Graph showing the angular distribution between the measurement points for all age groups. Scale bar: 5 μm for all images.

Validation of structural differences in all age groups

The TPEF generated autofluorescence signal and histology of the myocardium further validated the differences in overall tissue composition of the three age groups. A striking difference was the cellularity of the neonatal myocardium. The neonatal myocardial cells are generally smaller than the adult CMs and thus displayed a higher nuclear to cytoplasm ratio (Fig. 7).

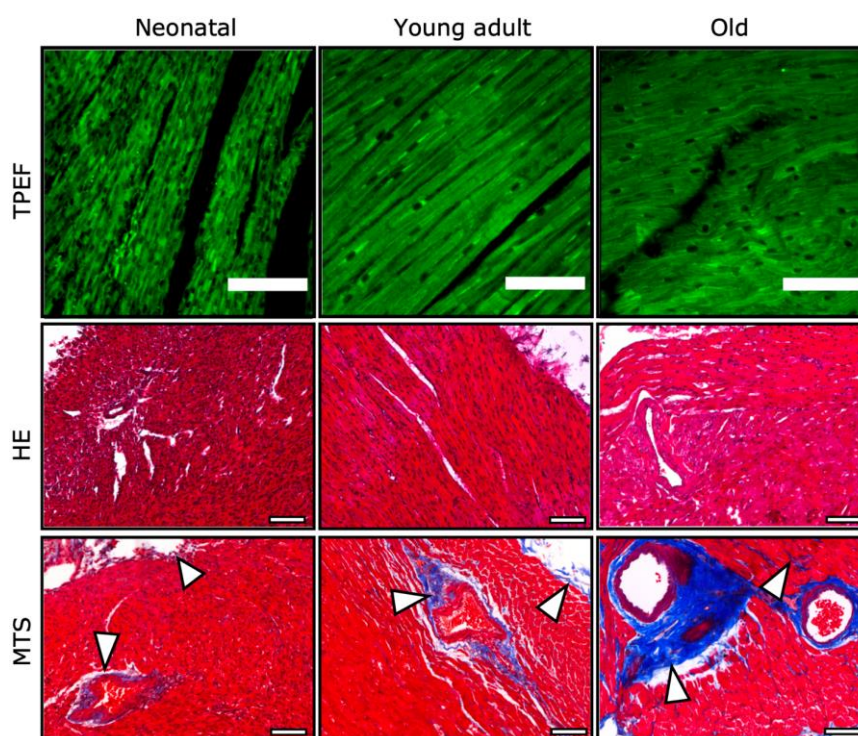


Figure 7: Comparison of neonatal, young adult and old myocardium morphology. TPEF emitted autofluorescence in vibratome sections and Haematoxylin & Eosin (HE) staining in paraffin sections show the overall morphology of the myocardium and the nuclear to cytoplasm ratio. Masson-trichrome stained (MTS) tissue sections present the collagen deposition in blue (shown by white arrowheads) and muscle in red. Scale bar: 100 μ m in all images.

Excess collagen deposition was found in the old marmoset, while in neonatal and adult animals, collagen was mainly present at the epicardial wall and the vicinity of blood vessels (Fig. 7, bottom row). These findings validated that the hyper-cellularity, the overall lack of organization and higher spacing between the myofibrils in the neonatal hearts facilitates the growth and maturation of myocardial cells to sustain the cardiac function throughout the lifespan. Structural disorganization was the main feature observed in old/geriatric hearts which may occur due to excess deposition of connective tissue indicating a pathogenic remodeling process.

Discussion

Our study demonstrates a TPM based label-free imaging approach for a comprehensive assessment of age-related structural differences in the cardiac tissue obtained from non-human primates (NHPs). By successfully segregating the collagen originated SHG as the backscattered signal from myosin emitted SHG, a reliable quantification of connective tissue content was performed in neonatal/newborn (<4 weeks), young adult (1-4 years) and old/geriatric (>10 years) marmosets. Additionally, the total tissue volume (myosin + collagen) which was detected as forward SHG signal was determined in 3D all groups. Myosin emitted SHG was quantified in overview as well as in zoomed-in images to provide vital cues for evaluating age-related structural differences. Our results demonstrate for the first-time significant differences in total tissue volume, myofibril spacing, alignment, curvature and angular distribution in hearts of marmosets of different age groups using a label-free TPM imaging approach.

Imaging intrinsic signals in form of TPEF and SHG provided reliable high-resolution visualization of various structures in marmoset hearts at the cellular and subcellular levels, such as cardiomyocytes, collagen, elastin, nuclei and myosin. In our previous study, the collagen emitted SHG signal was morphologically identified as fibrous structure and myosin by its typical striated pattern [32]. SHG is an anisotropic process that mainly propagates in the direction of the incident light with a minor fraction of backscattered signal. Compared to myosin, collagen is a very strong SH generator at excitation wavelengths above 800 nm [29,32] and our results demonstrate that it provides a suitable quantitative signal in epi-direction as well. Myosin, on the other hand, requires a higher threshold of excitation energy to be detected in the epi-direction. Harnessing these differences, we successfully developed a simple strategy to detect collagen emitted SHG in backward direction with a negligible signal from myosin. However, one limitation involving this approach is that the horizontally oriented collagen fibers scatter bidirectionally while the vertically oriented collagen fibers scatter mostly in the forward direction [29,33]. Since relatively thin tissue slices (50 or 100 μm) were used, this error was minimized [34]. Importantly, the quantification of collagen for all age groups was also performed in epi-direction only. Nonetheless, the detection of collagen fibers with variable

orientation in thicker samples could be optimized by altering the polarization of excitation light and/or by adjusting the sample orientation, as has been previously performed [27,29,34].

Myosin emitted only a weak SHG signal in epi-direction as demonstrated by our results and is highly influenced by the orientation of the myofibrils and semicrystalline order of A bands [32,35]. While our image acquisition settings resulted in optimal SH signal intensity from myosin at the forward detector, it also caused minimal signal saturation from collagen SHG. This can be attributed to the structural assembly of both harmonophores as collagen fibers associate into bundles and generally have a greater diameter than myosin fibers [32,34].

By using this label-free imaging approach, age-related structural differences were found in common marmoset monkeys divided into three groups neonatal, young adult and old/geriatric. This selection of age groups matches with the previously reported aging profile of common marmoset monkeys kept in captivity for both male and female [36]. By using this label-free imaging approach, age-related structural differences were found in common marmoset monkeys. Volumetric analysis showed a substantial increase in collagen at the myocardium with aging. The interplay of various signaling pathways contributes to the maturation, as well as pathological deposition of ECM [13]. Recently, it has been established that fibroblasts are a key constituent in the microenvironment promoting cardiac maturation [37]. The low volume of collagen detected in neonatal hearts is because the fibroblasts increase postnatally until adulthood [39]. Under healthy conditions (i.e., the adult hearts) cardiac fibroblasts regulate ECM content and provide a scaffold for CMs [38]. During aging the fibroblasts undergo fibroblast-to-myofibroblast transition which produces profibrotic factors, driving fibrosis progression. In aged hearts the myofibroblasts mediated attenuation of the matrix-degrading pathways [13,16,39] can contribute to the excessive collagen volume that was observed in the old/geriatric hearts as shown by the 3D analysis. Development of age-related fibrosis has been reported previously in marmosets with minor effect on cardiac functional efficiency [17]. Our approach for the first time provides reliable label-free volumetric quantification of age-related collagen remodeling in NHPs. The collagen volume in old/geriatric animals was found to be increased however, this did not reach significance compared to neonatal and adult mainly.

Our results also revealed an increase in the total tissue volume (myosin + collagen) which was detected as forward SHG at regions of pathological remodeling with aging in marmosets. These findings support the notion that even after cell-cycle withdrawal, a postnatal heart continues to

gain volume by a proportional increase in CM mass and myofibril expansion until early adulthood through a process called physiological or maturational hypertrophy [7,40,41]. This tissue growth and maturation process reduces overall spacing between myofibrils by early adulthood; however, without resulting in significant increase in tissue volume. Conversely, the aged hearts involve apoptosis induced reduction in the number of CM and an overall lower LV mass [17,42,43]. Our 3D analysis, however, showed a significantly higher total volume in the old/geriatric marmoset hearts at the ROIs as compared to the neonatal heart indicating a progressive increase in LV mass at pathological sites. We postulate that the CM loss is compensated by the age-related pathophysiological CM hypertrophy and excessive collagen deposition in the interstitial space potentially caused by arterial stiffening and increased hemodynamic load [44–46].

In the neonatal hearts, lower tissue volume coincides with the higher degree of spacing reflected by increased myofibril length. The myofibril curvature, alignment and angle are also significantly different from the adult and old marmoset hearts. It was further established that neonatal cardiac tissue lacked fully developed ICDs at this developmental stage in marmosets as these could not be visualized in SHG images. This indicates that ICD associated cell adhesions structures including fascia adherens, desmosomes and gap junctions are also not fully expressed in neonates contributing to the structural disassembly. Moreover, it is known that CM integration requires attachment to ECM via focal adhesion structures called costameres which are also not developed in the neonatal hearts [47]. Besides tissue integration, the ICDs and costameres also contribute to CM maturation by harboring vinculin-based actomyosin assembly that is required for sarcomere expansion [7,47]. By early adulthood, the targeted localization of ICD and costameric components to the CM termini does indeed occur, which was evident by the clear banding and improved alignment of myofibrils as observed in young adult marmoset hearts.

In the old/geriatric marmoset hearts, the disorganisation of the myocardium indicates pathological remodeling of the cardiac tissue at several heterogeneously distributed regions of interest. Our results highlight significant age-related alterations in the overall alignment, curvature and angular distribution of the hypercontracted myofibrils. We postulate that the presence of high ECM content and distorted myofibrils are the main contributors to the structural disassembly in the old hearts. Several studies have reported cardiac

hypercontractility caused by hypertrophic cardiomyopathies [48]. Our previous work also showed hypertrophy induced myofibril undulation and hypercontractility using SHG imaging in a cardiac pressure-overload mouse model [30]. In addition to hypertrophy, age-related hypercontractility is linked to cardiac stiffness and abnormalities in cardiac EEC due to Ca^{2+} overload. A recent study reported the expression of the Transient Receptor Potential Vanilloid-4 (TRPV4) – a non-selective cation channel – in aged mice hearts causing an additional sarcolemmal Ca^{2+} influx pathway [49]. This consequently contributes to excessive intracellular Ca^{2+} accumulation provoking cardiac hypercontractility. Our data strongly indicate loss of structural integrity in aged hearts and provide a potential therapeutic target for maintaining cardiac function in elderly patients.

TPEF and histological assessment validated the basic differences in the myocardium in all three-age group. The high nuclear to cytoplasm ratio in the neonatal hearts declines as the CM mature in adult mammalian hearts as observed in TPEF and histological images which mainly occurs via DNA synthesis without nuclear division to make polyploid nuclei [50,51]. Morphologically it was also evident that the nuclei in mature CM are larger in size than neonatal ones which can be attributed to the higher DNA content in adult hearts.

In summary, this study shows that the transition of the cardiac tissue from an immature state in neonatal marmoset hearts to an adult mature one involves an increase in size and gain in structural organization, volume and banding of the myofibrils via the formation of fully developed ICDs and ECM maturation. In old/geriatric marmoset hearts, pathological remodeling of cardiac tissue results in loss of structural organization due to excessive collagen deposition and hypercontractile state of myofibrils. Further, taking into account the cardiovascular similarities shared between marmosets and humans this imaging approach can be applied as a powerful tool for analyzing human cardiac tissue in detail. These findings highlight the unrivalled potential of TPM label-free imaging that can be further applied for monitoring the effects of therapeutic approaches for cardiac regeneration and repair on the structural level. They also provide essential foundations for intravital imaging using TPM of cardiac developmental and pathological remodeling. Advanced understanding of cardiac structural maturation and age-related remodeling can elucidate biophysical and biochemical cues causing abnormal cardiac maturation and aging.

Supplementary Material

Animal data

Table S1: Data for the common marmoset monkeys (*Callithrix jacchus*) including age, weight, and gender

Age group	Age (Years / months or Days)	Weight (g)	Gender
Old	11y / 0m	306	m
	10y / 8m	332	m
	13y / 3m	336	m
Young Adult	1y / 0m	334	m
	2 y / 11m	468	m
	4y / 4m	560	m
Neonatal/newborn	24 days	78	f
	4 days	28.5	m
	6 days	30.5	m

S2: Sample preparation:

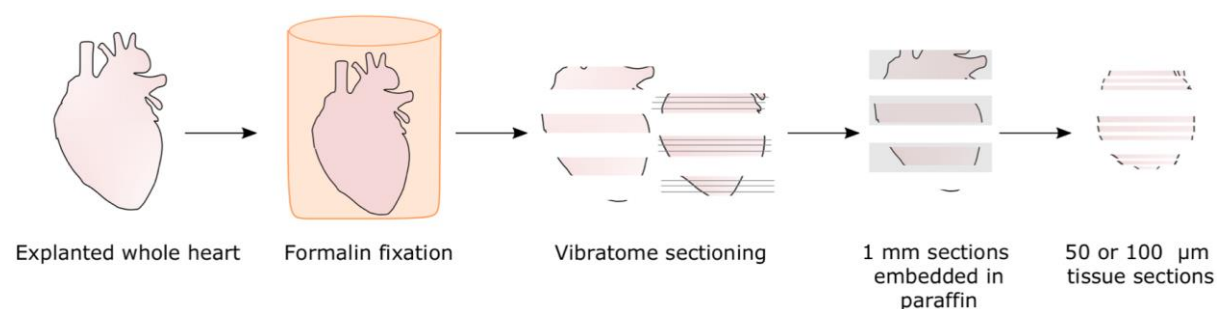


Figure S1: Schematic for sample preparation. Excised hearts were fixed in formalin and sectioned using vibratome into 1mm, 50 and 100 μ m tissue slices. 1mm tissue slices were embedded in paraffin and then section into 2 μ m sections for histology. 50 and 100 μ m sections were used for TPM imaging.

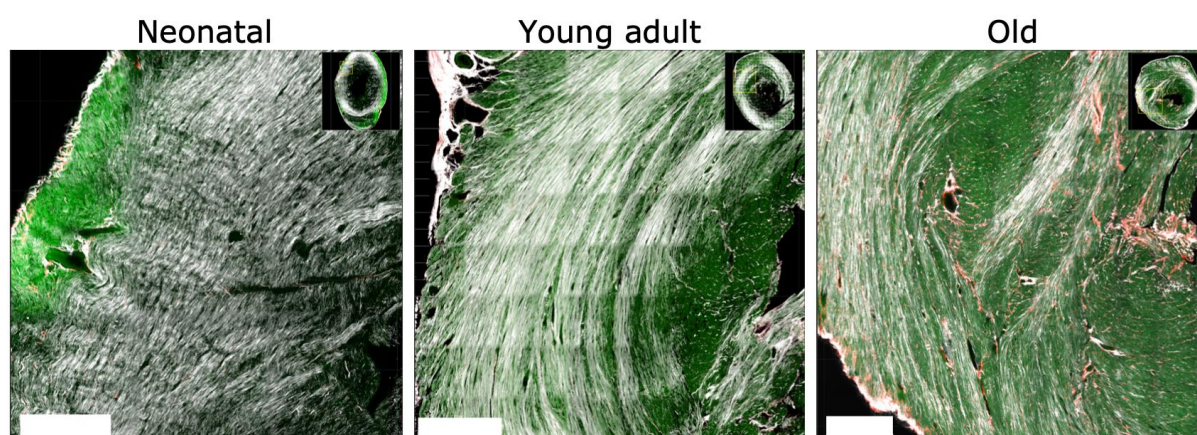
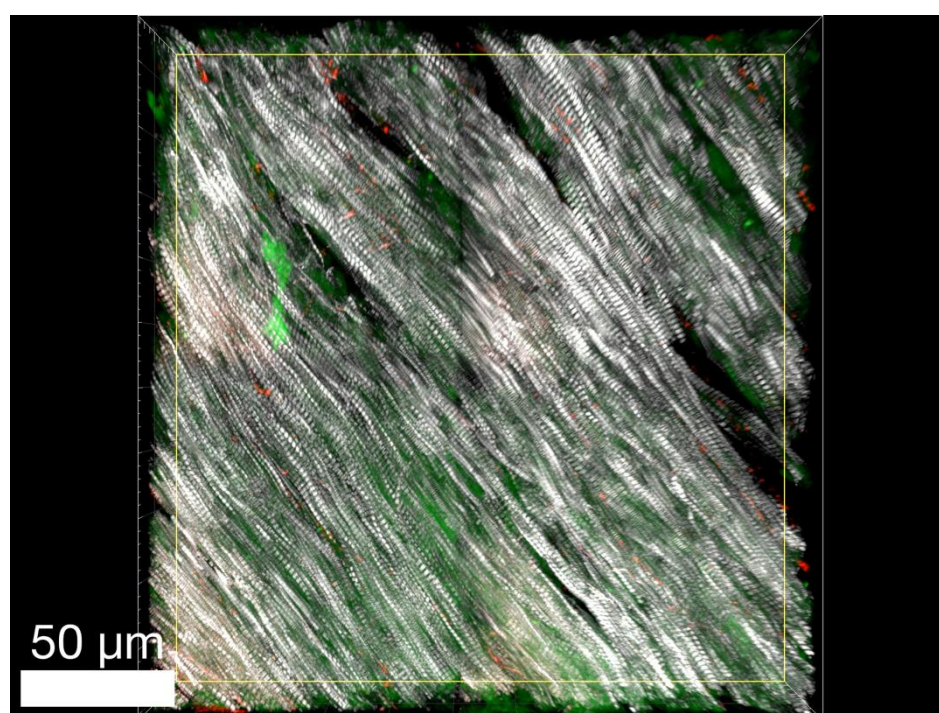
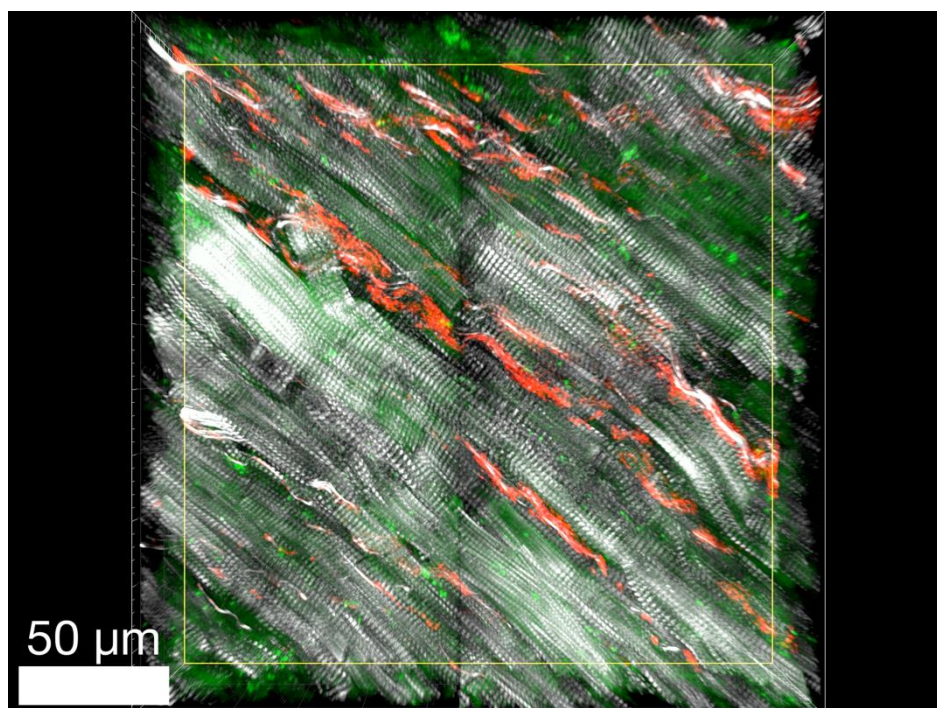
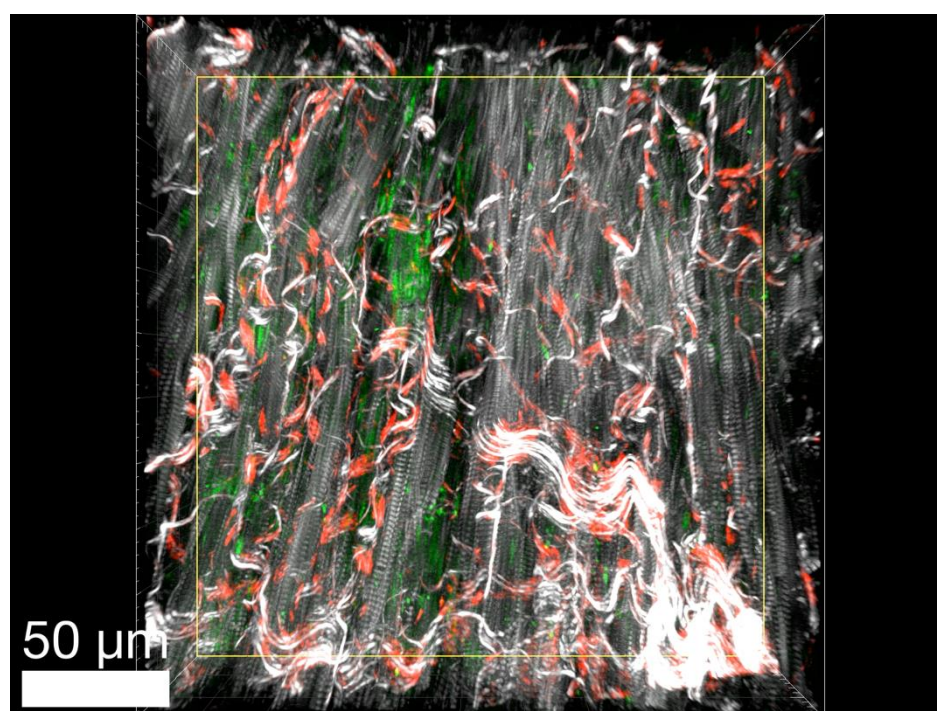
Cardiac morphology in all age groups

Figure S2: Overview of TPM label-free images in different age groups. Representative overview showing cardiac morphology in neonatal, young adult and old hearts for autofluorescence (green), backward SHG (red) and forward SHG (white). Scale bar: 200 μm .

Movie S1: Neonatal heart**Movie S2: Young adult**



Movie S3: Old heart



3D rendering of myofibril segment

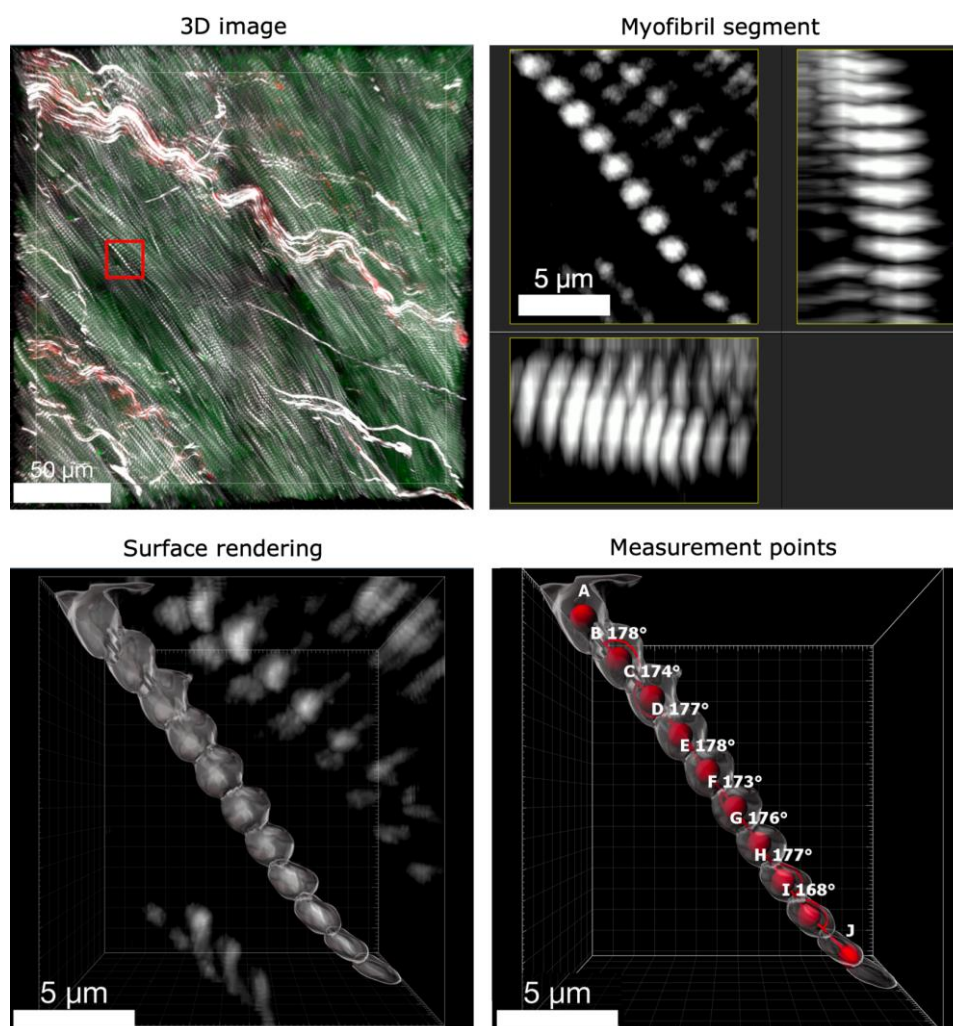


Figure S3: Workflow for 3D surface rendering and angular distribution analysis along single myofibril segments. A segment of single myofibril was cropped from a 3D volume in xy, yz and xz plane to extract ten SHG emitting A bands in an adult heart. 3D Surface rendering was performed on the isolated fragment of the myofibril. A measurement point was set at the center of mass for each A band. Angular distribution was determined between the measurement points.

Reference list

1. G. Maroli and T. Braun, "The long and winding road of cardiomyocyte maturation," *Cardiovascular Research* 117(3), 712–726 (2021).
2. M.-T. Zhao, S. Ye, J. Su, and V. Garg, "Cardiomyocyte Proliferation and Maturation: Two Sides of the Same Coin for Heart Regeneration," *Front. Cell Dev. Biol.* 8, (2020).
3. N. Velayutham, E. J. Agnew, and K. E. Yutzey, "Postnatal cardiac development and regenerative potential in large mammals," *Pediatr Cardiol* 40(7), 1345–1358 (2019).
4. V. Obas and R. S. Vasan, "The aging heart," *Clinical Science* 132(13), 1367–1382 (2018).
5. M. Günthel, P. Barnett, and V. M. Christoffels, "Development, Proliferation, and Growth of the Mammalian Heart," *Mol Ther* 26(7), 1599–1609 (2018).
6. Lakatta Edward G., "Arterial and Cardiac Aging: Major Shareholders in Cardiovascular Disease Enterprises," *Circulation* 107(3), 490–497 (2003).
7. Guo Yuxuan and Pu William T., "Cardiomyocyte Maturation," *Circulation Research* 126(8), 1086–1106 (2020).
8. M. Ponnusamy, P.-F. Li, and K. Wang, "Understanding cardiomyocyte proliferation: an insight into cell cycle activity," *Cell. Mol. Life Sci.* 74(6), 1019–1034 (2017).
9. M. Mollova, K. Bersell, S. Walsh, J. Savla, L. T. Das, S.-Y. Park, L. E. Silberstein, C. G. dos Remedios, D. Graham, S. Colan, and B. Kühn, "Cardiomyocyte proliferation contributes to heart growth in young humans," *PNAS* 110(4), 1446–1451 (2013).
10. O. Bergmann, R. D. Bhardwaj, S. Bernard, S. Zdunek, F. Barnabé-Heider, S. Walsh, J. Zupicich, K. Alkass, B. A. Buchholz, H. Druid, S. Jovinge, and J. Frisén, "Evidence for Cardiomyocyte Renewal in Humans," *Science* 324(5923), 98–102 (2009).
11. M. C. Florio, A. Magenta, S. Beji, E. G. Lakatta, and M. C. Capogrossi, "Aging, MicroRNAs, and Heart Failure," *Current Problems in Cardiology* 45(12), 100406 (2020).
12. B. A. Borlaug, "Evaluation and management of heart failure with preserved ejection fraction," *Nature Reviews Cardiology* 17(9), 559–573 (2020).
13. C. A. Meschiari, O. K. Ero, H. Pan, T. Finkel, and M. L. Lindsey, "The impact of aging on cardiac extracellular matrix," *GeroScience* 39(1), 7–18 (2017).
14. J. A. C. Lima, "The Aging Human Heart," *Circ Cardiovasc Imaging* 10(1), (2017).
15. C.-L. Hung, A. Gonçalves, A. M. Shah, S. Cheng, D. Kitzman, and S. D. Solomon, "Age- and Sex-Related Influences on Left Ventricular Mechanics in Elderly Individuals Free of Prevalent Heart Failure: The ARIC Study (Atherosclerosis Risk in Communities)," *Circ Cardiovasc Imaging* 10(1), (2017).
16. A. Biernacka and N. G. Frangogiannis, "Aging and Cardiac Fibrosis," *Aging Dis* 2(2), 158–173 (2011).
17. A. Moussavi, M. Mietsch, C. Drummer, R. Behr, J. Mylius, and S. Boretius, "Cardiac MRI in common marmosets revealing age-dependency of cardiac function," *Sci Rep* 10, (2020).
18. J. Wu, S. Xia, B. Kalionis, W. Wan, and T. Sun, "The Role of Oxidative Stress and Inflammation in Cardiovascular Aging," *BioMed Research International* 2014, e615312 (2014).
19. L. Lu, J. Guo, Y. Hua, K. Huang, R. Magaye, J. Cornell, D. J. Kelly, C. Reid, D. Liew, Y. Zhou, A. Chen, W. Xiao, Q. Fu, and B. H. Wang, "Cardiac fibrosis in the ageing

- heart: Contributors and mechanisms," *Clinical and Experimental Pharmacology and Physiology* 44(S1), 55–63 (2017).
20. N. G. Frangogiannis, "Cardiac fibrosis: Cell biological mechanisms, molecular pathways and therapeutic opportunities," *Mol Aspects Med* 65, 70–99 (2019).
 21. W. Chen and N. G. Frangogiannis, "The role of inflammatory and fibrogenic pathways in heart failure associated with aging," *Heart Fail Rev* 15(5), 415–422 (2010).
 22. H. A. Feridooni, K. M. Dibb, and S. E. Howlett, "How cardiomyocyte excitation, calcium release and contraction become altered with age," *Journal of Molecular and Cellular Cardiology* 83, 62–72 (2015).
 23. M. Paz Ocaranza, J. A. Riquelme, L. García, J. E. Jalil, M. Chiong, R. A. S. Santos, and S. Lavandero, "Counter-regulatory renin–angiotensin system in cardiovascular disease," *Nature Reviews Cardiology* 17(2), 116–129 (2020).
 24. T. Kohl, V. Westphal, S. W. Hell, and S. E. Lehnart, "Superresolution microscopy in heart — Cardiac nanoscopy," *Journal of Molecular and Cellular Cardiology* 58, 13–21 (2013).
 25. L. Wang, B. Chen, W. Yan, Z. Yang, X. Peng, D. Lin, X. Weng, T. Ye, and J. Qu, "Resolution improvement in STED super-resolution microscopy at low power using a phasor plot approach," *Nanoscale* 10(34), 16252–16260 (2018).
 26. J. Liu, "Two-photon microscopy in pre-clinical and clinical cancer research," *Front. Optoelectron.* 8(2), 141–151 (2015).
 27. V. Parodi, E. Jacchetti, R. Osellame, G. Cerullo, D. Polli, and M. T. Raimondi, "Nonlinear Optical Microscopy: From Fundamentals to Applications in Live Bioimaging," *Front. Bioeng. Biotechnol.* 8, (2020).
 28. P. Friedl, K. Wolf, G. Harms, and U. H. von Andrian, "Biological Second and Third Harmonic Generation Microscopy," *Current Protocols in Cell Biology* 34(1), 4.15.1–4.15.21 (2007).
 29. B. Weigelin, G.-J. Bakker, and P. Friedl, "Third harmonic generation microscopy of cells and tissue organization," *J Cell Sci* 129(2), 245–255 (2016).
 30. J.-D. Nicolas, A. Khan, A. Markus, B. A. Mohamed, K. Toischer, F. Alves, and T. Salditt, "X-ray diffraction and second harmonic imaging reveal new insights into structural alterations caused by pressure-overload in murine hearts," *Scientific Reports* 10(1), 19317 (2020).
 31. E. Wershof, D. Park, D. J. Barry, R. P. Jenkins, A. Rullan, A. Wilkins, K. Schlegelmilch, I. Roxanis, K. I. Anderson, P. A. Bates, and E. Sahai, "A FIJI macro for quantifying pattern in extracellular matrix," *Life Science Alliance* 4(3), (2021).
 32. N. H. Green, R. M. Delaine-Smith, H. J. Askew, R. Byers, G. C. Reilly, and S. J. Matcher, "A new mode of contrast in biological second harmonic generation microscopy," *Scientific Reports* 7(1), (2017).
 33. W. R. Zipfel, R. M. Williams, R. Christiet, A. Y. Nikitin, B. T. Hyman, and W. W. Webb, "Live tissue intrinsic emission microscopy using multiphoton-excited native fluorescence and second harmonic generation," *Proceedings of the National Academy of Sciences of the United States of America* 100(12), 7075–7080 (2003).
 34. X. Chen, O. Nadiarynk, S. Plotnikov, and P. J. Campagnola, "Second harmonic generation microscopy for quantitative analysis of collagen fibrillar structure," *Nat Protoc* 7(4), 654–669 (2012).
 35. C. Greenhalgh, N. Prent, C. Green, R. Cisek, A. Major, B. Stewart, and V. Barzda, "Influence of semicrystalline order on the second-harmonic generation efficiency in the anisotropic bands of myocytes," *Appl. Opt.* 46(10), 1852 (2007).

36. D. H. Abbott, D. K. Barnett, R. J. Colman, M. E. Yamamoto, and N. J. Schultz-Darken, "Aspects of Common Marmoset Basic Biology and Life History Important for Biomedical Research," *Comparative Medicine* 53(4), 339–350 (2003).
37. Y. Wang, F. Yao, L. Wang, Z. Li, Z. Ren, D. Li, M. Zhang, L. Han, S. Wang, B. Zhou, and L. Wang, "Single-cell analysis of murine fibroblasts identifies neonatal to adult switching that regulates cardiomyocyte maturation," *Nat Commun* 11, (2020).
38. Hall Caitlin, Gehmlich Katja, Denning Chris, and Pavlovic Davor, "Complex Relationship Between Cardiac Fibroblasts and Cardiomyocytes in Health and Disease," *Journal of the American Heart Association* 10(5), e019338 (2021).
39. M. D. Tallquist, "Cardiac Fibroblast Diversity," *Annu Rev Physiol* 82, 63–78 (2020).
40. D. Zhang, Y. Li, D. Heims-Waldron, V. Bezzerides, S. Guatimosim, Y. Guo, F. Gu, P. Zhou, Z. Lin, Q. Ma, J. Liu, D.-Z. Wang, and W. T. Pu, "Mitochondrial Cardiomyopathy Caused by Elevated Reactive Oxygen Species and Impaired Cardiomyocyte Proliferation," *Circ Res* 122(1), 74–87 (2018).
41. Y. Guo, B. D. Jardin, P. Zhou, I. Sethi, B. N. Akerberg, C. N. Toepfer, Y. Ai, Y. Li, Q. Ma, S. Guatimosim, Y. Hu, G. Varuzhanyan, N. J. VanDusen, D. Zhang, D. C. Chan, G.-C. Yuan, C. E. Seidman, J. G. Seidman, and W. T. Pu, "Hierarchical and stage-specific regulation of murine cardiomyocyte maturation by serum response factor," *Nature Communications* 9(1), 3837 (2018).
42. G. Olivetti, M. Melissari, J. M. Capasso, and P. Anversa, "Cardiomyopathy of the aging human heart. Myocyte loss and reactive cellular hypertrophy," *Circ Res* 68(6), 1560–1568 (1991).
43. Li Haobo, Hastings Margaret H., Rhee James, Trager Lena E., Roh Jason D., and Rosenzweig Anthony, "Targeting Age-Related Pathways in Heart Failure," *Circulation Research* 126(4), 533–551 (2020).
44. E. G. Lakatta, "Age-associated cardiovascular changes in health: impact on cardiovascular disease in older persons," *Heart Fail Rev* 7(1), 29–49 (2002).
45. M. A. Horn and A. W. Trafford, "Aging and the cardiac collagen matrix: Novel mediators of fibrotic remodelling," *Journal of Molecular and Cellular Cardiology* 93, 175–185 (2016).
46. N. S. V. Singam, C. Fine, and J. L. Fleg, "Cardiac changes associated with vascular aging," *Clinical Cardiology* 43(2), 92–98 (2020).
47. A. M. Samarel, "Costameres, focal adhesions, and cardiomyocyte mechanotransduction," *American Journal of Physiology-Heart and Circulatory Physiology* 289(6), H2291–H2301 (2005).
48. C. V. Tuohy, S. Kaul, H. K. Song, B. Nazer, and S. B. Heitner, "Hypertrophic cardiomyopathy: the future of treatment," *European Journal of Heart Failure* 22(2), 228–240 (2020).
49. A. B. Veteto, D. Peana, M. D. Lambert, K. S. McDonald, and T. L. Domeier, "Transient receptor potential vanilloid-4 contributes to stretch-induced hypercontractility and time-dependent dysfunction in the aged heart," *Cardiovascular Research* 116(11), 1887–1896 (2020).
50. S. P. Bishop, Y. Zhou, Y. Nakada, and J. Zhang, "Changes in Cardiomyocyte Cell Cycle and Hypertrophic Growth During Fetal to Adult in Mammals," *JAHA* 10(2), (2021).
51. E. Karbassi, A. Fenix, S. Marchiano, N. Muraoka, K. Nakamura, X. Yang, and C. E. Murry, "Cardiomyocyte maturation: advances in knowledge and implications for regenerative medicine," *Nat Rev Cardiol* 17(6), 341–359 (2020).

52. A. Dh, B. Dk, C. Rj, Y. Me, and S.-D. Nj, "Aspects of common marmoset basic biology and life history important for biomedical research.," *Comp Med* 53(4), 339–350 (2003).

Acknowledgements

We thank Bärbel Heidrich and Regine Kurse for assistance in sample preparation and Sabine Wolfgramm and Bettina Jeep for providing great technical assistance for histology.

Funding

This work was supported by the Deutsche Forschungsgemeinschaft (DFG, German Research Foundation) under Germany's Excellence Strategy - EXC 2067/1- 39072994.

AK was supported by a seed grant of the Physics-to-Medicine Initiative Göttingen.

Competing interests

The authors declare that they have no competing interests.

Data availability

All data generated or analyzed during this study are included in this published article and its supplementary information files.

Chapter 3 – Simple low dose radiography allows precise lung volume assessment in mice

Amara Khan^{1}, Andrea Markus¹, Thomas Rittmann², Jonas Albers^{1,3}, Frauke Alves^{1,3,4}, Swen Hülsmann^{5,‡} and Christian Dullin^{1,3,‡*}*

Reproduced from *Scientific Reports* **11**, 4163 (2021)

X-ray based lung function (XLF) as a planar method uses dramatically less x-ray dose than computed tomography (CT) but so far lacked the ability to relate its parameters to pulmonary air volume. The purpose of this study was to calibrate the functional constituents of XLF that are biomedically decipherable and directly comparable to that of micro-CT and whole-body plethysmography (WBP). Here, we developed a unique set-up for simultaneous assessment of lung function and volume using XLF, micro-CT and WBP on healthy mice. Our results reveal a strong correlation of lung volumes obtained from radiographic XLF and micro-CT and demonstrate that XLF is superior to WBP in sensitivity and precision to assess lung volumes. Importantly, XLF measurement uses only a fraction of the radiation dose and acquisition time required for CT. Therefore, the redefined XLF approach is a promising tool for preclinical longitudinal studies with a substantial potential of clinical translation.

Introduction

Respiratory diseases account for ~10% of mortality worldwide, which is set to rise due to persistent smoking, pollution and occupational irritants ¹. Depending on the underlying disease, the characteristics of lung dysfunction may involve inadequate oxygen exchange, breath shortening, chronic cough, chest pain and dyspnoea ^{2,3}. To improve our knowledge about the basic mechanisms regarding lung physiology, pathophysiology and treatment strategies, the use of mouse models of lung disease in translational research is inevitable. The pre-clinical assessment of pulmonary function is a valuable tool not only for investigating the pathology of respiratory and allergic diseases but also enables preclinical evaluation of the response to novel therapeutic strategies.

Changes in lung function can be monitored non-invasively in restrained or unrestrained mice by double chamber plethysmography or barometric plethysmography ^{2,4}. Other methods require invasive intubation procedures some of which tend to be terminal ⁵. Of all available techniques, unrestrained whole-body plethysmography (WBP) is extensively used in longitudinal studies due to its ease of use and high data output ^{3,6-8}. However, there is also considerable concern over the validity of plethysmography techniques ⁹⁻¹². The main limitation of this technique is that the functional outcomes rely on the plethysmograph pressure changes, and the relationship between chamber pressure and the lung mechanics might be non-linear. Furthermore, the accurate tidal volume estimates are significantly affected by subtle changes in temperature, pulmonary mechanism and fluctuations in barometric pressure ^{3,10,13}. Plethysmography may also be inconsistent between mouse strains requiring precise selection of the control groups ¹¹.

Recently, the use of lab and synchrotron radiation based micro-computed tomography (micro-CT) has been increasingly used in preclinical studies to assess quantitative parameters including lung volumes, air spaces or lesions and mean lung density ¹⁴⁻¹⁹. These measurements have been performed in an attempt to reflect the structural and functional competence of the lung during disease progression and in response to therapy in numerous animal models of lung diseases, such as cancer, fibrosis, emphysema and transplantation ¹⁴. Not only in clinical routine, but also in preclinical research, dose restrictions are major obstacles. Small-animal models, especially mouse models, are often utilized in preclinical research. Imaging in live

mice for micro-CT based longitudinal lung studies requires a dramatically higher spatial and temporal resolution due to the small size of the mouse and its fast metabolism. Consequently, this limits the use of CT based high-resolution imaging for longitudinal lung studies and also hampers the clinical application of this approach^{20–26}.

Therefore, the development of novel and sophisticated lung function measurement techniques with improved reliability and minimal radiation is fundamentally required. To this end, we recently established a non-invasive lung function method based on planar cinematic x-ray imaging of the chest, namely x-ray-based lung function (XLF) to measure the lung function in preclinical mouse models of allergic airway inflammation (AAI) over time^{27,28}. Using minimal radiation dose and short exposure time, XLF showed significantly higher sensitivity than WBP for reliable assessment of lung function during AAI and response to dexamethasone treatment²⁷. However, previously the functional parameters of XLF were not exactly relatable to commonly used lung function techniques including WBP and micro-CT and none of the XLF parameters represented the lung volume.

In this study, we compared XLF determined end-inspiratory volume (EIV) with the lung volumes from micro-CT and conventional WBP to establish XLF as a biomedically relevant technique. To achieve this, we first designed a unique experimental set-up for performing correlative lung function measurements using XLF, micro-CT and WBP. Using micro-CT as a gold standard approach, XLF was found sensitive and precise to determine lung volumes, as it exhibited a higher degree of correlation with micro-CT than WBP. By successfully correlating two-dimensional (2D) XLF measurements directly with three-dimensional (3D) micro-CT data in healthy mice, we present the refined XLF algorithm as a sensitive and efficient tool for determining lung volume at minimal radiation dose and exposure time.

Materials and Methods

Animal experiment

Eight healthy male C57Bl/6 mice (13 weeks old) were used for *in-vivo* lung function measurements (Table S1). Additional three male mice were used for mechanical ventilation experiments (Table S1). The mice were kept in a temperature and humidity-controlled room with a 12 h light-dark cycle and were fed food and water ad libitum. They were euthanized by cervical dislocation. All animal procedures were performed in compliance with the guidelines of the European Directive (2010/63/EU) and the German ethical laws and were approved by the administration of Lower Saxony, Germany (approval number G15.1747).

Experimental set-up

The experimental set-up was designed to perform either XLF or micro-CT with WBP in parallel (Fig. 1). The custom-made plethysmography chamber (see below) of approximately 14 cm in length and 5 cm in diameter with a capacity of 200 ml was built to fit into the gantry of the *in-vivo* micro-CT system (QuantumFX, PerkinElmer) allowing acquisition of a 20 x 20 mm² FOV for XLF and micro-CT imaging. The mouse was positioned in the WBP chamber, which was then placed on the sample stage inside the micro-CT. The position of mouse and stage was adjusted to have the chest-cavity within the FOV. A piezoelectric sensor (PZT, FT31T-1.3A1-472; KEPO, Ningbo, China) was installed at the door of the micro-CT device to synchronize the data acquisitions for WBP with the acoustic signal from the door interlock system at the beginning and at the end of XLF or micro-CT recording (Supp. Fig. S1).

In-vivo XLF measurement

XLF was performed on unrestrained mice that were isoflurane-anesthetized (~2% isoflurane in 1 l oxygen per min) by acquiring planar cinematic x-ray images of the mice chest cavity using a low-dose *in-vivo* micro-CT as previously described by Dullin *et al.*, 2016²¹ and Markus *et al.*, 2017²². Briefly, mice were placed inside a plastic chamber (Fig. 1) and the breathing frequency of the mice was adjusted manually by changing the isoflurane concentration between 1.5-3% to achieve a breathing frequency of approximately 0.7 Hz. This resulted in a total of 21 breathing cycles recorded in ~34 s scans. XLF measurements were recorded using an x-ray

tube voltage of 90 kVp and a tube current of 100 μ A. The radiographs of the chest movements during the breathing process were sequenced to produce a movie, which later on was parametrized at the lung regions.

Micro-CT imaging

In-vivo 3D micro-CT scans were made immediately after combined XLF and WBP measurements on the isoflurane-anesthetized mice. Mouse lungs were scanned by applying a cardiac gating technique using the following parameters: x-ray tube voltage 90 kVp and tube current 200 μ A. The radiograph projections were taken for the 360° gantry rotation for a total scan time of 4 min 30 s and the entire radiograph was retrospectively gated.

XLF and micro-CT measurements in mechanically ventilated dead mice

Three male mice were euthanized using cervical dislocation and a tracheotomy was performed to ventilate the mice with increasing stroke volumes ranging from 0.5 – 3.0 ml and a fixed stroke rate of ~ 40 stroke/min using a MiniVent ventilator (Type 845, Harvard Apparatus, Holliston, USA). However, due to faster breathing in the ventilated mice, the breathing frequency was approximately one single breathing event per 860 ms. The XLF measurements and micro-CT imaging were performed as described for the *in-vivo* experiments.

Unrestrained whole-body plethysmography

We used a chamber in the so-called flow-through configuration, which utilizes the principle of a pneumotach^{46,47}. In detail, the pressure difference between the recording chamber (220 ml) and a reference chamber (50 ml) was captured by a differential pressure sensor (DPS, Board Mount Pressure Sensor, 0-1" H₂O, 20 mV, 16 VDC supply; Mfr. No: INCH-D-MV, Amphenol Cooperation, Wallingford, CT 06492). Digitization was performed with an analog-digital interface (PowerLab) and LabChart-software (ADInstruments LTD, Oxford, United Kingdom). The connectors on the lid of the chamber were used for isoflurane inlet/outlet and for connecting the DPS. A positive bias flow of 0.4-0.7 l/min was introduced using the anesthesia unit (VisualSonics VS 4112; 50% Air + 50% O₂) to supply the volatile anesthetic isoflurane. The time constant of the pressure decay from the chamber system was adjusted to approximately 40 ms to match commercial chamber systems that we used in earlier papers⁴⁷.

The decay time constant was tested by manually obstructing the air outlet and the measuring the decay of the pressure signal after releasing the obstruction (LabChart Peak Analysis Module).

The raw flow signal was bandpass filtered off-line (0.5 – 20 Hz), to remove movement artifacts, noise and also bias flow, and then integrated for measuring a tidal volume. We used the standard integral settings of the “Integral Channel Calculation module” of the LabChart-software (use of all data points, reset each cycle whereby the integral is reset each time the source signal passes through zero to a positive value). CT induced temperature and humidity inside the plethysmography chamber were adjusted by using a LOG32 data logger (Dostmann electronic GmbH, Wertheim-Reicholzheim, Germany).

WBP temperature and humidity measurements

CT induced temperature and humidity changes inside the plethysmography chamber could not be measured online. We therefore approximated the values for humidity and temperature correction based on separate measurements, that were performed under similar conditions to those used during correlative lung function measurements. In short, the data logger device was placed inside the chamber together with the mouse under isoflurane anesthesia and the temperature and humidity was recorded for ~4 mins. The relative humidity of the air/O₂ mix was below 3%. Relative humidity (rh) inside the chamber dropped during the recording. With the mouse inside the chamber, the rh ranged between 22.5% and 9.4% (mean 16.7%). Considering that the data logger reduces the volume in the chamber, the value inside the chamber without the data logger is expected to be even smaller. The average temperature inside the chamber with the mouse was 27°C. Since the duration of anesthesia was below 15 min, we did not anticipate any significant change in the body temperature (36.5 °C). With an assumed atmospheric pressure of 760 mmHg (1.01308 bar), the volume adjustment factor was 11.7.

WBP data sampling and analysis

Flow signal from the pressure sensor was sampled at 1 kHz, while the PTC signal was sampled at 40 Hz. The intensity of the lung was detected by using the “Plot Z-axis Profile” function of ImageJ software ⁴⁸. Therefore, an ROI was set to the level of the diaphragm in expiration. Data was exported as ACSII and imported to LabChart 8.0 (ADInstruments). For removal of low-

frequency intensity changes resulting from the x-ray tube, “the smoothed” intensity trace (median filter; 101 samples = 100 ms) was subtracted from the raw trace. Processed image data and the WBP data was exported to Axon PCLAMP file format and imported into IGOR Pro 6.37 (Wavemetrics, Lake Oswego, US) for resampling (1 kHz) and reimported into LabChart for final offline analysis. The peak detection module of LabChart was used to identify respiratory parameters including tidal volume (integrated flow), T_{start} and T_{end} (10-90% of peak height) as well as the decay of the signal (τ ; 100 to 0% of peak).

Data quantification and statistical analysis

The data of lung volumes were quantified using *RetrospeCT* (https://gitlab.gwdg.de/thomas.rittmann/retrospective_gating) which includes an iterative GPU-based reconstruction toolbox (tigre, <https://github.com/CERN/TIGRE>). Quantification of XLF measurements were achieved with a custom-built software *xLFinal* <https://github.com/xPITcoding/xLFinal.git>. WBP was performed with an analog-digital interface (PowerLab) and LabChart-software (ADInstruments). For statistical analysis, the paired t-test for same mean implemented in MS Excel 2013 was used with a p-value of 0.05 (*) as margin for statistical significance. To measure correlation, the Pearson correlation coefficient implemented in GraphPad Prism Software version 8 was used (GraphPad Software, La Jolla California USA).

Results

Experimental set-up facilitates correlative lung function measurements

To correlate the XLF parameters directly with WBP and micro-CT, we designed a unique experimental set-up that enabled simultaneous measurements either by combining XLF or micro-CT with WBP. As shown in Figure 1, the custom-made plethysmography chamber was placed into the gantry of the *in-vivo* micro-CT system. The chamber had multiple connectors, which served as isoflurane inlet/outlet and for connecting a differential pressure sensor (DPS; see methods section). Overall, the designed set-up served as an ideal platform to perform correlative lung function.

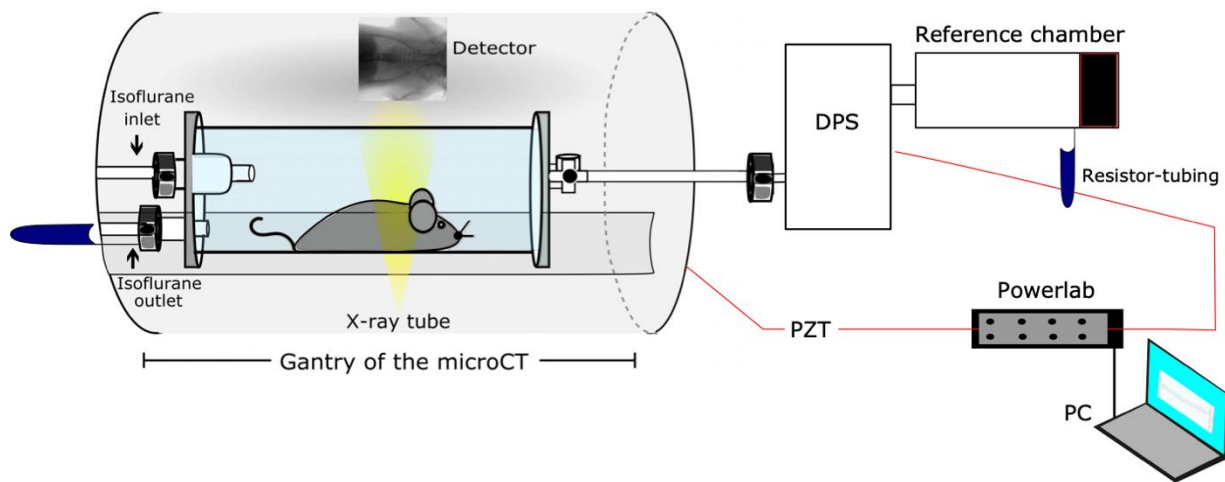


Figure 1: Schematic illustration of the set-up for correlative XLF, WBP and micro-CT measurements. One end of the WBP chamber has an isoflurane inlet/outlet, the other end is connected to the differential pressure sensor (DPS) which in turn is connected to a reference chamber, a Powerlab data acquisition device and a portable computer (PC). The chamber is placed inside the gantry of the micro-CT imaging system on the sample stage. The mouse is positioned inside the chamber such that the chest cavity is within the field of view (FOV). A piezoelectric (PZT) acoustic sensor that transduced the sound of the CT door interlock is used to synchronize data acquisition from WBP with XLF or micro-CT.

Correlating the timing of micro-CT and WBP signal

To perform direct correlation between micro-CT and WBP data we tested and synchronized the timing of signal from each entity. Since the CT-scanner had no signal output to provide information about the timepoint the first image frame was acquired, we had to conceive our own trigger from the CT by installing a piezoelectric sensor to provide an acoustic signal for matching the starting point of CT data acquisition and WBP recording. The peak signals from each method were then synchronized to match the timing and traces of signals recorded. When

comparing the peak of the average x-ray attenuation at the region of interest (ROI) over time (Fig. 2a) and the peak of the WBP volume signal we noticed a significant delay of 27.5 ± 20.0 ms ($p < 0.01$, paired t-test) (Fig. 2b-c). However, taking into consideration the exposure time of the x-ray detector of 33 ms, we assumed that the minimum x-ray attenuation at the lung region and the peak of the WBP lung volume trace coincide as expected (Supp. Fig. S1).

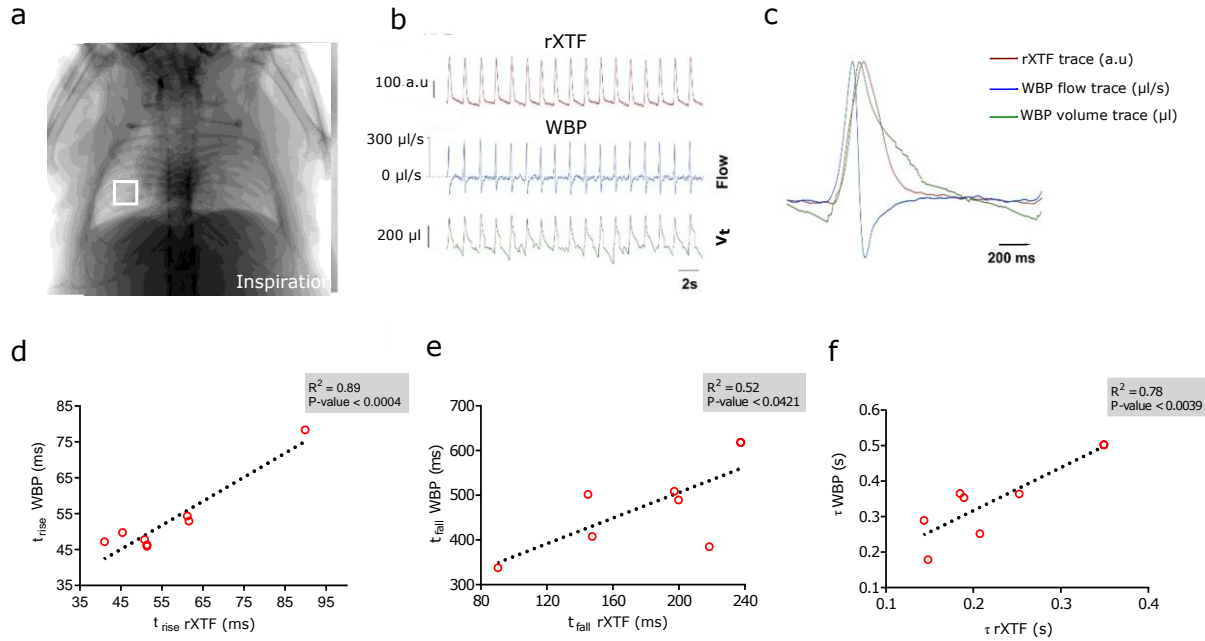


Figure 2: Comparison of traces from relative x-ray transmission function (rXTF) at lung region and WBP. a) XLF-image in inspiration. The white box indicates the region of interest (ROI) that was used to measure changes in intensity of rXTF. b) Data from rXTF and WBP. Red trace: rXTF at the ROI (arbitrary units). Blue trace: band pass filtered (0.5Hz -20Hz) flow trace ($\mu\text{l/s}$) from the WBP. Green trace: WBP Volume trace (V_t , μl) derived from the integral of the flow (reset each cycle). c) Averaged data from b. d-f) Correlation of the time course and signal derived from rXTF and WBP, d) time rise (t_{rise}) of the signal (20%-80%), e) decay of the signals (t_{fall}) (20%-80%) and (f) tau (τ) using a mono-exponential fit (peak to baseline, LabChart 8.0, ADInstruments). P-values and respective coefficients of determination (R^2) from linear regression analysis are shown on the graph.

The rise time (t_{rise}) of the rXTF signal (55.4 ± 16.1 ms) and the WBP volume signal (52.8 ± 8.7 ms) did not differ ($p = 0.0004$, paired t-test) (Fig. 2d). This indicates that WBP can predict the inspiratory phase of the respiratory cycle very precisely. However, while comparing t_{fall} and tau (τ) of the expiratory phase, the two methods revealed significantly different results: t_{fall} 187.1 ± 53.8 ms for rXTF versus 497.4 ± 100.8 ms for WBP ($p < 0.0421$; paired t-test, Fig. 2e) and τ 215.4 ± 65.4 ms for rXTF and 341.3 ± 92.6 ms for WBP ($p < 0.0039$, Fig. 2f). One factor that may account for the difference is the uncertainty regarding the position of the zero-flow point for the end of each respiratory cycle. Moreover, the slower flow for rXTF during

expiration that accounts for this difference, might be a consequence of isoflurane-induced bronchoconstriction ⁵⁹.

Micro-CT based volume measurements

We derived separate volumes ($V_{[\mu CT]}$) for the lung in inspiration and expiration from micro-CT by performing retrospective gating in combination with a modified Feldkamp (FDK) reconstruction algorithm ³⁰. Both steps were implemented in a custom-built software called retrospeCT. We used the FDK algorithm implemented in the TIGRE toolbox (<https://github.com/CERN/TIGRE>) – in contrast to the typically applied version of that algorithm – allows using non-uniformly distributed angular projections. From the angular projections, an ROI line was adjusted to select the representative region of lung expansion near the diaphragm (Fig. 3a). Figure 3b shows an exemplary breathing cycle curve generated by the temporal variations in the x-ray attenuation at this ROI. A moving average filtered curve which presented gradual variations in the trendline was subtracted from the signal to factor out the background. Moreover, the minimum peak distance (expiration points) and the number of frames detected per inhaled phase were adapted to optimize the selection of projections that maintained a consistent data quality for both phases (Fig. 3c). The selection was based on thresholding: Here, the highest value above the inspiration threshold (green line) and the lowest value below the expiration threshold (yellow line) was used for defining end-inspiration and end-expiration frames (Fig 3b).

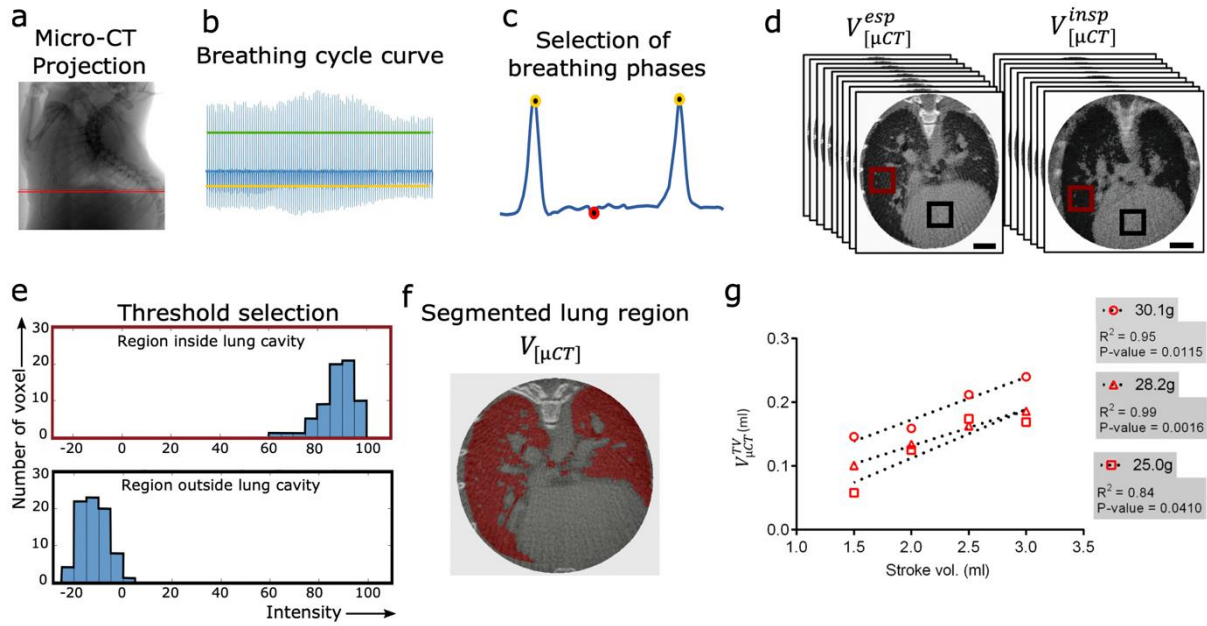


Figure 3: Quantification of 3D lung volumes at expiration and inspiration. (a) The red line marks the exemplary ROI selected near the diaphragm for representing the lung motion in the micro-CT projections. (b) A graph for the lung motion at the ROI is generated where the green and yellow lines show the threshold lines for maxima and minima selection, respectively. (c) A representative single breathing cycle is shown with an exemplary selection of one frame for expiration phase (red circle) and two frames for inspiration phase (yellow circles). (d) Following the selection of multiple breathing phases from the entire breathing curve, the frames from the whole micro-CT projection are sorted to reconstruct two segregated 3D lung volumes for expiration and inspiration. (e) A region inside and outside the lung (red and black squares in d) were selected to generate histograms showing the distribution of grey values for each region. (f) The lung volume ($V_{[\mu CT]}$) (red) is segmented through a region growing method. (g) The calculated tidal volumes from micro-CT ($V_{[\mu CT]}^{TV}$) from the segmented lung region show a strong positive correlation with the increasing stroke volumes used for mechanically ventilating euthanized mice. The weights of the mice, p-values and respective coefficients of determination (R^2) from linear regression analysis are shown on the graph. Scale bars in (d) represent 1 cm.

From the breathing curve, frames at the expiration and inspiration phases were selected resulting in two projection sets with strongly reduced frame numbers (approximately 340 each out of the 8892 frames recorded) and non-equidistant angular spacing (Fig. 3d). Owing to the low number of frames, standard reconstruction algorithms yielded a 3D reconstruction of poor quality. Thus, a modified FDK reconstruction algorithm based on the graphics process unit (GPU) was used for tomographic reconstruction of lung for both the expiration and inspiration set of projections (Fig. 3d and Fig. S2). Still, the resulting 3D data demonstrated a high noise level and a non-uniform background intensity which hindered the segmentation of the lung and thereby a precise volume measurement. To correct the non-uniform background, a slice below

the lung region was subtracted from all other slices. Subsequently, a 3D Gauss-filter was applied to reduce the noise level (Fig. S2). From the resulting filtered volume, the lung at both breathing phases was segmented individually. The lung was first masked to eliminate the area of the surrounding thoracic regions. To select the intensity values that enabled an optimal selection of $V_{[\mu CT]}$, histograms were obtained from manually defined regions inside and outside the lung cavity (Fig. 3e). A region growing algorithm was utilized in which the upper and lower threshold values from the histogram were exploited to select voxels consistent with the intensity of the aerated regions. The gaps within the resulting segmented region were filled by applying a closing operator. Lastly, $V_{[\mu CT]}$ was calculated from the segmented region by simply multiplying the number of segmented voxels with the volume per voxel. Other denser regions such as the mediastinum, consolidation of lung parenchyma and the airway tracts were excluded (Fig. 3f). In principle, $V_{[\mu CT]}$ did not only account for the air spaces within the lung but also for the micro tissue structures including small blood vessels and connective tissue which could not be segmented due to limited resolution of the reconstruction.

For testing the reliability and precision of the described workflow, $V_{[\mu CT]}$ measurements were performed in three dead mice of different age, weights and strains by mechanically ventilating them with increasing stroke volumes (Tables S1 and S2). To achieve this, the tidal volumes from micro-CT ($V_{[\mu CT]}^{TV}$) were determined by calculating the difference between the volume of lung cavity during inspiration and expiration ($V_{[\mu CT]}^{insp} - V_{[\mu CT]}^{exp}$). The fractional increase in $V_{[\mu CT]}^{TV}$ correlated strongly with the applied stroke volumes (Fig. 3g). Unlike the ventilator stroke volume which represents the total ventilation volume, $V_{[\mu CT]}^{TV}$ measures the volume of lung aerated regions and a strong correlation between these parameters signifies that the $V_{[\mu CT]}^{TV}$ indeed reflects the volume of air exchanged. All three mice weighing 30.1 g, 28.2 g and 25.0 g expressed a strong linear positive correlation between both variables with R^2 -values of 0.95, 0.99 and 0.84, respectively (Fig. 3g). However, the relative change between $V_{[\mu CT]}^{TV}$ and the stroke volume did not show an absolute match, which could be attributed to an amount of air leakage, which depends on various factors including the speed of ventilation, increased airway resistance and reduced lung compliance in dead mouse. Nevertheless, the sensitivity of $V_{[\mu CT]}^{TV}$ to the changes in stroke volume warranted the use of this approach as a standard procedure for correlating the lung volumes measured by each method.

Correlation of micro-CT determined volumes with WBP

Using the correlative approach, the *in-vivo* micro-CT measurements were performed in parallel with WBP. For comparing the data obtained from both methods, $V_{[\mu CT]}^{TV}$ was correlated with tidal volume from WBP ($TV_{[WBP]}$). The parameters presented only a weak correlation (correlation coefficient $R^2 = 0.5061$, p-value = 0.0239, Fig. 4).

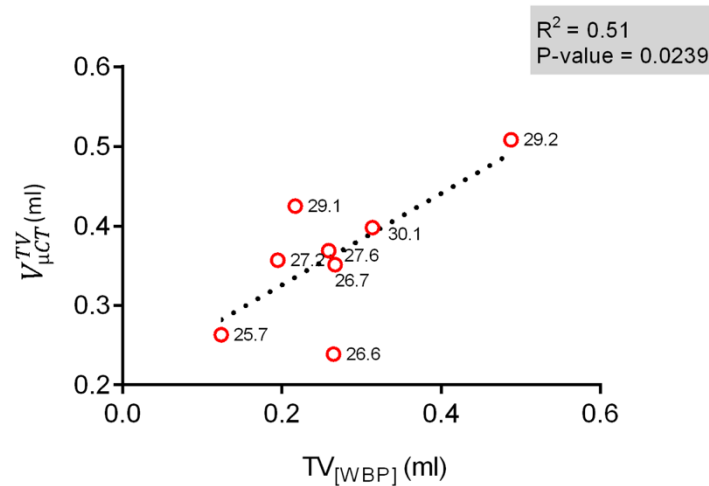


Figure 4: Correlation between lung volumes measured using micro-CT and WBP in living mice. Graph showing a weak positive correlation between $TV_{[WBP]}$ with $V_{[\mu CT]}^{TV}$ ($R^2 = 0.5061$) performed *in-vivo* (n=8) using the correlative set-up. All points are labelled with the respective weights of the mice. The p-values and respective coefficients of determination (R^2) from linear regression analysis is shown on the graph.

Interestingly, both parameters correlated rather poorly ($R^2=0.5061$), probably due to the fundamental differences in volumetric constituents measured by each method. While $V_{[\mu CT]}^{TV}$ quantifies the aerated regions of the lung, $TV_{[WBP]}$ is derived for pressure changes produced by warming and cooling of the inspired air during every single breath^{31,32}. Moreover, the volume is integrated from the calibrated flow signal (Fig. 2). Although band-pass filtering removed the bias flow, the exact zero-flow point for each respiratory cycle remains uncertain due to change of temperature and humidity inside the WBP chamber.

Quantification of advanced XLF parameters

The functional parameters for XLF were measured from the average x-ray transmission at the chest area over time. Previously, we reported the calibration of x-ray transmission over time via the selection of a ROI at left and right lung lobes at the point of maximum contraction, which was normalized by the averaged background intensity selected at a region outside the mouse (Dullin *et al.*, 2016). However, to accomplish adequate background selection, a large FOV is required, which in turn compromises the image resolution at the lung region (Fig. 5a, top panel). Therefore, we now used a modified approach for background correction (Fig. 5a, lower panel). Briefly, an adaptive moving average filter was applied on the x-ray transmission functions $\mathbf{XTF(t)}$, which in the first pass computed the moving average $\mathbf{ma(t)}$, penalised each time point with its absolute distance $\mathbf{d(t)}$ to $\mathbf{ma(t)}$ and in a second pass calculated the adaptive moving average $\mathbf{ama(t)}$ resulting in a baseline of the function that is less affected by the breathing events.

1)

$$ma(t) = \frac{1}{2n} \sum_{t-n}^{t+n} XTF(i)$$

2)

$$d(t) = 1/[|ma(t) - XTF(t)| + 0.1]$$

3)

$$ama(t) = \sum_{t-n}^{t+n} d(i) * XTF(i) / \sum_{t-n}^{t+n} d(i)$$

The exemplary relative x-ray transmission [$rXTF(t)$] shown for two breathing events in Figure 5b, was then calculated as follows:

4)

$$rXTF(t) = XTF(t)/ama(t)$$

The possibility to select a smaller FOV during XLF acquisition by implementing the modified background correction method led to an improved image resolution at the lung region (Fig. 5a, lower panel). This relatively enhanced macroscopic visualization of the lung structures enabled precise selection of the aerated regions at each lung lobe.

Following background correction, the calibrated x-ray transmission over the chest region was used for quantification of *in-vivo* XLF. The functional parameters measured by XLF were determined from the breathing curve (Fig. 5b). The local maxima **I**, which denotes the time points of maximum inspiration (yellow circles, Fig. 5b) were detected. Then the time points of maximum expiration **E** (red circles, Fig. 5b) were identified as the closest local minima before the maxima **I**. To further suppress the effect of noise a moving average filter was applied to define the minima **E**. To split the breathing curve into an active breathing (mainly inspiration) and a passive expiration phase, an intersection point was used at a level function (grey horizontal line, Fig. 5b) resulting in the threshold point rXTF **T** (cyan circle, Fig. 5b). Moreover, this point also separates the background signal and noise from the breathing peaks.

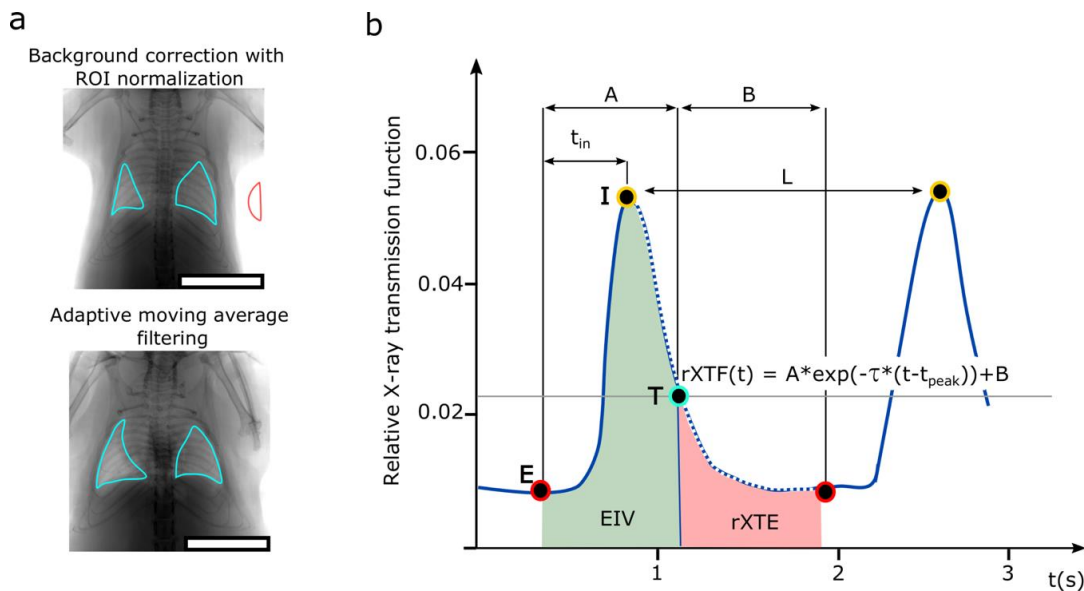


Figure 5: Quantification of advanced XLF parameters from the x-ray transmission over time. (a) A representative radiograph is shown, demonstrating background correction based on the selection of ROI at the lung lobes marked in cyan normalized by selection of the background marked in red (top panel). The modified background correction at ROI is accomplished by applying an adaptive moving average filter which requires a smaller FOV (bottom panel). (b) Two exemplary breathing cycles depicted from the averaged x-ray transmission at the ROI are shown for a healthy mouse over a period of 3 s. The peak intensities representing maximum inhalation **I** are marked by yellow circles while the red circles represent the beginning of a new breathing event and the maximum exhalation phase **E** of the breathing cycle. The breathing curve is split at threshold **T** (marked by a cyan circle and a grey horizontal line) to obtain a breathing (A) and a passive expiration (B) phase. XLF parameters are shown including average inhalation time (t_{in}), average breathing length (L), x-ray-based end-inspiration volume ($EIV_{[XLF]}$), relative X-ray transmission at end-expiration ($rXTE$) and exponential function (τ , calculated in region indicated by blue dotted line). Scale bars in (a) represent 1 cm.

Since quantitative functional parameters in the rXTF are based on the analysis of every single breath, they were measured as an average over the entire recorded data. The inspiration time (t_{in}) was calculated as the average time between the points **E** and **I** for all breathing events recorded. Further, the length of the breathing events (**L**) was calculated as the average distance between the peaks **I** of the rXTF. The first part of the area under the curve (**AUC**) in the interval **E** to **T** was recorded as end-inspiration lung volume ($EIV_{[XLF]}$) while the second part in the interval **T** to **E** denoted the relative X-ray transmission at end-expiration (rXTE). Lastly, to characterize the decay rate τ of the expiration phase (represented by the blue dotted line), which indirectly measures changes in the elastic recoil of the lung, an exponential decay function

$$rXTF(t) = A * \exp\left(-\tau * (t - t_{peak})\right) + B$$

was fitted at the intervals **T** to **E**.

XLF measurements for precise lung volumes

To assess the comparability of XLF based 2D measurements with the lung volumes calculated from 3D projections, we investigated the relationship between the XLF parameters that coincided with the $V_{[\mu CT]}$ (Tables S2 and S3). We, therefore, compared $EIV_{[XLF]}$ which is described by the average AUC in the x-ray transmission function of a breathing event with $V_{[\mu CT]}^{insp}$. Since $EIV_{[XLF]}$ is mostly affected by the total air volume inhaled at the end of the inspiration phase it should be strongly related to the $V_{[\mu CT]}^{insp}$. To analyse the correlation between the two parameters, we again assessed the lung volumes in dead mice that were ventilated with increasing stroke volumes. Since $V_{[\mu CT]}^{insp}$ values have a lower standard error than $V_{[\mu CT]}^{TV}$, they showed an improved correlation with increasing stroke volumes (Supp. Fig. S3) as compared to $V_{[\mu CT]}^{TV}$ (Fig. 3g). $EIV_{[XLF]}$ also exhibited a strong positive correlation with $V_{[\mu CT]}^{insp}$ for all three mice (30.1 g, $R^2 = 0,99$; 28.2 g, $R^2 = 0,99$; and 25.0 g, $R^2 = 0,99$) (Fig. 6a). Importantly, $EIV_{[XLF]}$ also corresponded to the weights of the dead mice, unlike $V_{[\mu CT]}^{insp}$ which was found to be less sensitive to the weights of the mice (Supp. Fig. S3). This is because $EIV_{[XLF]}$ is directly influenced by temporal variations in the x-ray transmission function during air exchange. $EIV_{[XLF]}$ hence quantifies the air volume more precisely than $V_{[\mu CT]}^{insp}$ which determines the volume of the entire aerated lung regions including miniscule soft tissue structures.

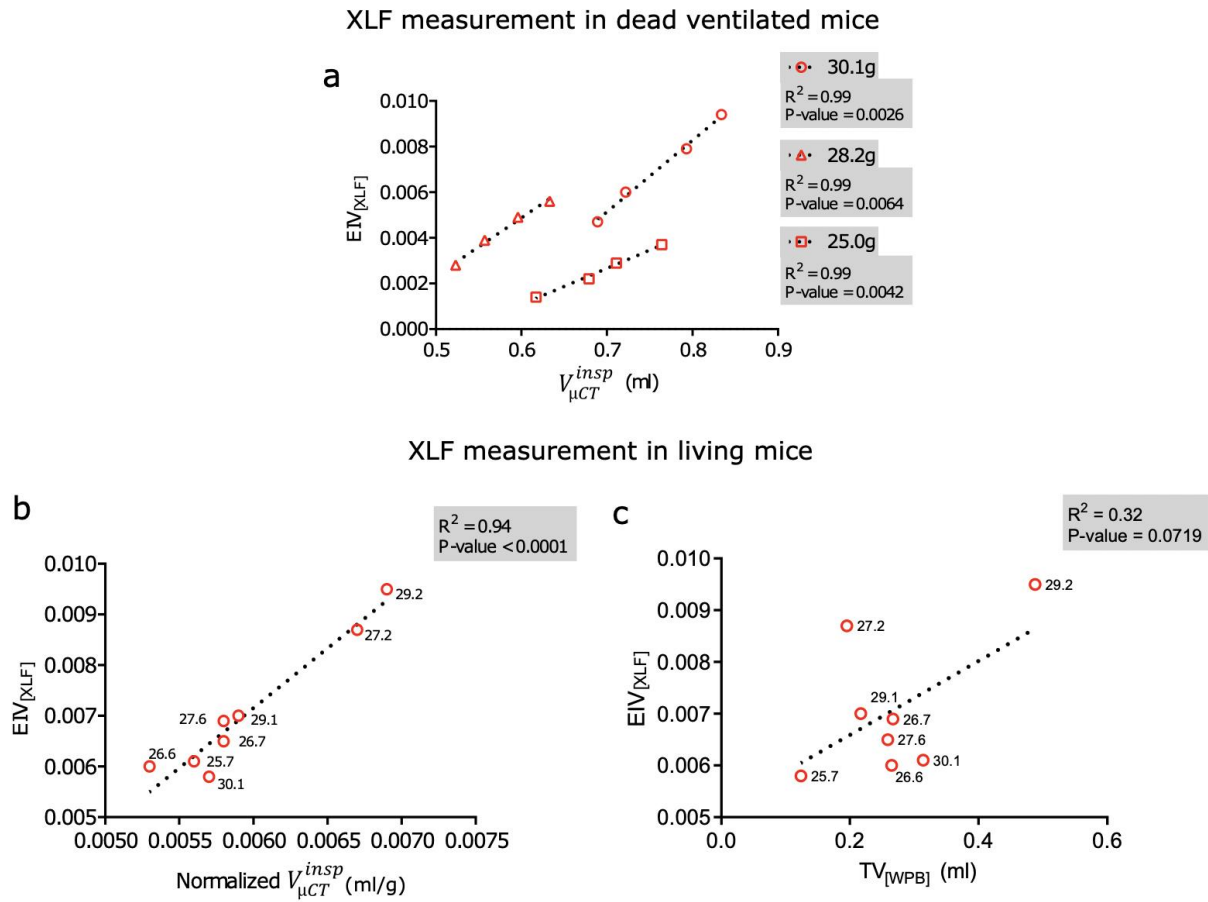


Figure 6: Correlation of XLF measurements with micro-CT and WBP. (a) Graph showing a strong positive correlation between $EIV_{[XLF]}$ with $V_{[\mu CT]}^{insp}$ performed on dead mechanically ventilated mice ($n=3$). (b-c) Graphs showing a strong positive correlation between $EIV_{[XLF]}$ and $V_{[\mu CT]}^{insp}$ ($R^2 = 0.94$) and (c) a weak correlation of $TV_{[WPB]}$ with $EIV_{[XLF]}$ ($R^2 = 0.32$). Data for both b and c is shown for living mice ($n=8$). The respective p-values and coefficients of determination (R^2) from linear regression analysis are shown on the graph. (b-c) All points are labelled with the respective weights of the mice.

Following the calibration of $EIV_{[XLF]}$ in dead mice, we applied this approach in living mice. To establish a direct correlation coefficient between the 2D (XLF) and 3D (micro-CT) datasets in living male mice, which were age and strain matched, the $V_{[\mu CT]}^{insp}$ was normalized with the mouse body mass to the power of 1.5 (Table S3). In living mice, a strong linear positive correlation between $EIV_{[XLF]}$ and normalized $V_{[\mu CT]}^{insp}$ was observed with a correlation coefficient of $R^2 = 0.94$ (Fig. 6b). These findings revealed that lung volumes determined from XLF were precise and comparable to those measured from 3D data acquired by micro-CT. It is noteworthy that the XLF data were recorded in 34 s to determine both lung volume and function with an average

x-ray dose of only 0.17 Gy. In comparison, CT data were acquired in a considerably longer acquisition time of 4.5 min and with a relatively high x-ray dose of approximately 2.7 Gy. This signifies that XLF can perform both lung volume and function measurements in substantially faster acquisition time and by using only a fraction of the x-ray dose that is necessary for CT.

Because tidal volumes cannot be derived from XLF measurements, a direct comparison of XLF and WBP measurements is not possible. Still, a correlation between $EIV_{[XLF]}$ and $TV_{[WBP]}$ was tested which resulted in a weak correlation as expected ($R^2 = 0.32$, Fig. 6c and Table S3). Using $V_{\mu CT}$ as a standard approach, it can be concluded that $EIV_{[XLF]}$ is sensitive and accurate for determining lung volumes at inspiration. Overall, these findings also highlight the difficulties in deriving lung volumes from WBP measurements as compared to XLF.

Discussion

This study presents a refined XLF approach, which enables the determination of lung volumes. This was achieved by using a novel experimental set-up which facilitated correlative assessment of lung volumes in mice using XLF, micro-CT and conventional WBP. To enable the biomedical interpretation of the XLF-acquired parameters as well as their comparison with WBP and CT, XLF parameters described in Dullin *et al.*, 2016 were redefined²⁷. Our results demonstrate that lung volume derived from a simple 2D measurement (XLF) strongly correlates with the volume of the lung determined from micro-CT data.

Semi-automated segmentation of CT images is commonly used to define total lung volume in healthy and diseased mice^{15,19,33–37}, hence we used this method in this study as a benchmark for correlation of lung volumes. However, poor resolution owing to low signal to noise ratio and motion induced image blurring could limit the lung volume quantification using retrospectively gated CT³⁸. Likewise, in the present study due to the comparably large voxel size of 40 μm and motion artefacts, it was not possible to calculate the volume of air only, instead, we measured the entire volume of the aerated regions of the lung. Moreover, changes in the morphology and compliance of the lung can occur at the early post-mortem stage affecting the total ventilation volume reaching the lungs¹⁶. The extent of these post-mortem alterations may even be different in each individual mouse. This explains the lack of perfect correlation between $V_{[\mu CT]}$ and stroke volumes as well as the weights of the dead mice. Other factors such as the relative fast stroke rate of the ventilator (40 strokes/min), leakage at the

tracheal cannula and length and elasticity of the tubes can also contribute to the differences in the total air volume exchanged in mechanically ventilated mice. We used a linear increase in stroke volume which resulted in a perfect correlation with micro-CT lung volume measurements, suggesting a high reliability in $V_{[\mu CT]}$ measurements. Therefore, $V_{[\mu CT]}$ was used as a reference for our correlative approach.

For a direct correlation between the lung volumes obtained from 3D micro-CT and planar XLF, $V_{[\mu CT]}^{insp}$ was normalized by an empirically estimated factor of body mass to the power of 1.5. In the present *in-vivo* study we used mice of the same age, sex and strain; hence it cannot be excluded that additional normalization parameters may be required to compensate for these factors. However, as most mouse studies are typically performed on gender and age matched cohorts, our XLF approach is generally applicable.

Most importantly, the XLF data were recorded with a significantly lower x-ray dose and about 87 percent shorter acquisition time when compared to CT (see results). This signifies that by using only approximately 7% of the x-ray dose used in CT scans, XLF not only measures the lung function more precisely than commonly applied WBP but also determines the lung volume, a parameter that until now could only be reliably assessed by CT. This can serve as a breakthrough for facilitating the use of XLF in longitudinal studies on mouse models of lung disease with repeated lung function measurements without the risk of potential radiation damage to the lung.

XLF-defined lung volume only accounts for air volume at end-inspiration and cannot quantify end-expiration and tidal volumes. This contributed to the poor correlation of $EIV_{[XLF]}$ with $TV_{[WBP]}$. On the other hand, slight breath to breath changes in the humidity and temperature inside the chamber can largely influence the tidal volumes obtained from WBP in small animals^{10,39}. Unfortunately, the humidity and temperature change inside the chamber could not be recorded during correlative lung function measurements as the data logger device can interfere with the x-ray transmission and more importantly changes the posture of the mouse which can affect the breathing pattern. Consequently, we could not determine a correction factor offline (see methods) for the WBP tidal volume which resulted in the rather weak correlation with $V_{[\mu CT]}^{TV}$. Moreover, the standard errors involved in the segmentation of the lung volume at each

inspiratory and expiratory phase both contribute to the resulting $V_{[\mu CT]}^{TV}$ values, therefore reducing its precision and accuracy.

In addition, WBP is complicated to perform in both pre-clinical and clinical use, and can result in significant inconsistencies due to minor technical differences in equipment, handling and surroundings^{40,41}. Henceforth, sophisticated correlative techniques such as presented in this study are required to further test the validity of plethysmography measurements for determining tidal volumes. On the other hand, WBP for preclinical application can be performed in freely moving animals, while XLF requires isoflurane anaesthesia.

In conclusion, we present XLF as a tool for an efficient and reliable assessment of lung function and also lung volumes by successfully correlating radiographic XLF measurements with micro-CT data. Due to the high sensitivity of XLF and the ability to use standard micro-CT equipment or even a simple x-ray tube to perform these studies, XLF can easily be applied in preclinical studies. Most importantly, XLF is performed with minimal x-ray dose and acquisition time and is therefore suitable for longitudinal studies. This also provides a vital basis for clinical translation. X-ray based lung function analysis - especially for studying lung motion - has already been used, but due to x-ray dose limitations has not been routinely applied in the clinic. Fouras *et al.*, 2019 developed a similar approach for low dose x-ray velocimetry for patient setup⁴². However, to date, no clinical data from this system has been published. Our data, showing the use of low x-ray dose for lung function and volume measurements, support the notion that this technique should be further developed for patients. Since the functional and volumetric parameters measured by XLF are designed to reflect airway remodelling contributing to the airflow obstruction, XLF could be used for assessing multiple pulmonary diseases and even enable an early-stage diagnosis in case of pulmonary fibrosis and edema^{43,44}. Ventilation settings which are currently adjusted manually by the operator and by interpreting ventilator-derived parameters could also be regularly monitored by XLF and adjusted to personalized, case-by-case settings⁴⁵. Lastly, XLF may be potentially performed in non-compliant or even unconscious patients, in which e.g., spirometry typically used for lung function measurement, cannot be applied.

Supplementary material

S1: Synchronizing the timing of signals

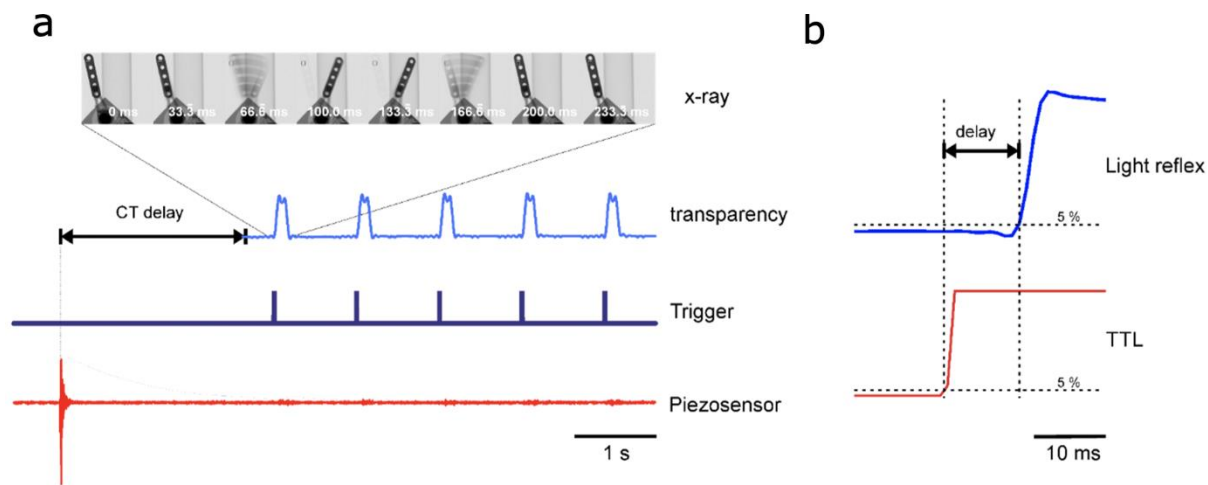


Figure S1: Synchronizing x-ray and WBP based measurements. a) X-ray and whole-body plethysmography (WBP) acquisitions were synchronized using a mechano-acoustical signal from the interlock system of the computed tomography (CT) device that was detected by a piezosensor (PZT) that was placed at the door of the CT (red trace). The delay between this signal and the first image of the radiographic image series was measured by the parallel recording of the CT images and a transistor-transistor logic (TTL) signal (dark blue trace) triggering a custom-made mechanical lever (image series), which was placed inside the CT. The TTL was generated by the Powerlab (8/35) that recorded the piezo signal. b) The response time of the lever to the TTL signal (red trace) was measured by a light reflex (blue trace) that was detected with a Fiberoptometer II (NPI electronic GmbH). For timing the 5% threshold of the signal was used.

The signals from x-ray and WBP measurements were synchronized as shown in Figure 1. The delay (CT-delay in Fig. S1a) from the click to the first image was found to be 3243.3 ± 28.4 ms ($n=4$). Thus, the timing error (< 30 ms) is small then the duration of a single XLF-image (33 ms), allowing us to record the timing of the respiratory signal with sufficient precision during the entire duration of radiographic recording.

S2: Animal data:

The mice used for in-vivo assessment of lung function using the correlative approach were all age, strain and gender (male) matched. This was done to reduce the number of factors that may influence the lung function measurements. The mechanically ventilated dead mice were only gender matched (male) and therefore of different age and strains.

Table S1: Data for the mice including age, body weights and normalized body weights.

Experiment	Mouse	Age (weeks)	Gender	Strain	Body weight (g)	Normalized body weights (g ^{1.5})
In-vivo	1	13	Male	C57BL/6	30.1	165.1
	2	13	Male	C57BL/6	27.6	145.0
	3	13	Male	C57BL/6	29.2	157.8
	4	13	Male	C57BL/6	29.1	157.0
	5	13	Male	C57BL/6	27.2	141.9
	6	13	Male	C57BL/6	25.7	130.2
	7	13	Male	C57BL/6	26.6	137.1
	8	13	Male	C57BL/6	26.7	138.0
Mechanically ventilated dead mice	1	49	Male	BALB/c	30.1	165.1
	2	10	Male	C57BL/6	25.0	125.0
	3	10	Male	C57BL/6	28.2	149.8

S3: XLF, micro-CT and WBP measurements in dead ventilated mice

Table S2: Lung volumes obtained from XLF and micro-CT in mechanically ventilated mice

Mouse	Stroke volume (ml)	XLF		Micro-CT	
		EIV _[XLF]	$V_{[\mu CT]}^{insp}$ (ml)	$LV_{[\mu CT]}^{exp}$ (ml)	
1	1.5	0.0047	0.689	0.543	
	2.0	0.0060	0.722	0.563	
	2.5	0.0079	0.793	0.581	
	3.0	0.0094	0.834	0.594	
Mean \pm SD	-	0.0070 \pm 0.0021	0.7595 \pm 0.0660	0.57025 \pm 0.0222	
2	1.5	0.0014	0.617	0.559	
	2.0	0.0022	0.679	0.554	
	2.5	0.0029	0.711	0.537	
	3.0	0.0037	0.764	0.595	
Mean \pm SD	-	0.0025 \pm 0.0010	0.6928 \pm 0.0615	0.5613 \pm 0.0244	
3	1.5	0.0028	0.523	0.422	
	2.0	0.0039	0.557	0.423	
	2.5	0.0049	0.596	0.433	
	3.0	0.0056	0.633	0.447	
Mean \pm SD	-	0.0043 \pm 0.0012	0.5773 \pm 0.0477	0.4313 \pm 0.0116	

EIV_[XLF] = XLF measured end-inspiratory volume; $V_{[\mu CT]}^{insp}$ = micro-CT measured lung volume at inspiration; $LV_{[\mu CT]}^{exp}$ = micro-CT measured lung volume at expiration

Table S3: Lung volumes obtained from XLF, micro-CT and WBP measurements in living mice

XLF		Micro-CT			WBP	
Mouse	$EIV_{[XLF]}$	$V_{[\mu CT]}^{insp}$ (ml)	Normalized $V_{[\mu CT]}^{insp}$ (ml/g)	$V_{[\mu CT]}^{exp}$ (ml)	$V_{[\mu CT]}^{TV}$ (ml)	$TV_{[WBP]}$ (ml)
1	0.0061	0.921	0.0056	0.523	0.398	0.314
2	0.0065	0.837	0.0058	0.468	0.369	0.259
3	0.0095	1.088	0.0069	0.580	0.508	0.488
4	0.0070	0.932	0.0059	0.507	0.425	0.217
5	0.0087	0.944	0.0067	0.587	0.357	0.195
6	0.0058	0.737	0.0057	0.474	0.263	0.124
7	0.0060	0.725	0.0053	0.486	0.239	0.265
8	0.0069	0.800	0.0058	0.449	0.351	0.267
Mean	0.0071	0.8730	0.0060	0.5092	0.3638	0.2661
(\pm) SD	± 0.001	± 0.122	± 0.001	± 0.051	± 0.086	± 0.106

Mean \pm standard deviation (SD) is shown for all datasets. $EIV_{[XLF]}$ = XLF measured end-inspiratory volume; $V_{[\mu CT]}^{insp}$ = micro-CT measured lung volume at inspiration; $V_{[\mu CT]}^{exp}$ = micro-CT measured lung volume at expiration; $V_{[\mu CT]}^{TV}$ = micro-CT measured tidal volume; $TV_{[WBP]}$ = WBP measured tidal volume.

S4: Comparison of three-dimensional (3D) data reconstructed by using the standard algorithm and modified Feldkamp (FDK) reconstruction

The proprietary retrospective gating software of the device can only be used to remove breathing artifacts (Fig. S2a) but cannot reconstruct the lung in two separate states. To achieve a reconstruction with strongly reduced breathing artifacts the software uses 494 frames out of the 7904 initially acquired. In order to reconstruct the lung in the two states i.e., an end-inspiration and end-expiration, we used custom-made software in combination with 200 projections for each phase. Our software uses a Feldkamp algorithm that can deal with non-uniformly angularly distributed projection data and is implemented in TIGRE. This resulted in reconstruction of images shown in figure S2b, while the FDK reconstruction after the subtraction of a slice outside the lung region and following Gaussian low-pass filtering is displayed in figure S2c. The normalized profile plot (Fig. S2d) at the position indicated by the blue line over the lung region (Fig. S2a-c) shows an apparent shading in the original FDK data, which would not enable segmentation of the lung with a threshold-based algorithm. In contrast to that, the proposed subtraction of a slice outside the lung region and the subsequent Gaussian low pass filtering removes the shading and boosts the contrast to noise ratio from initially about 0.5 to 3. Subsequently, the lung region can be segmented using the threshold indicated by the gray line (Fig. S2d).

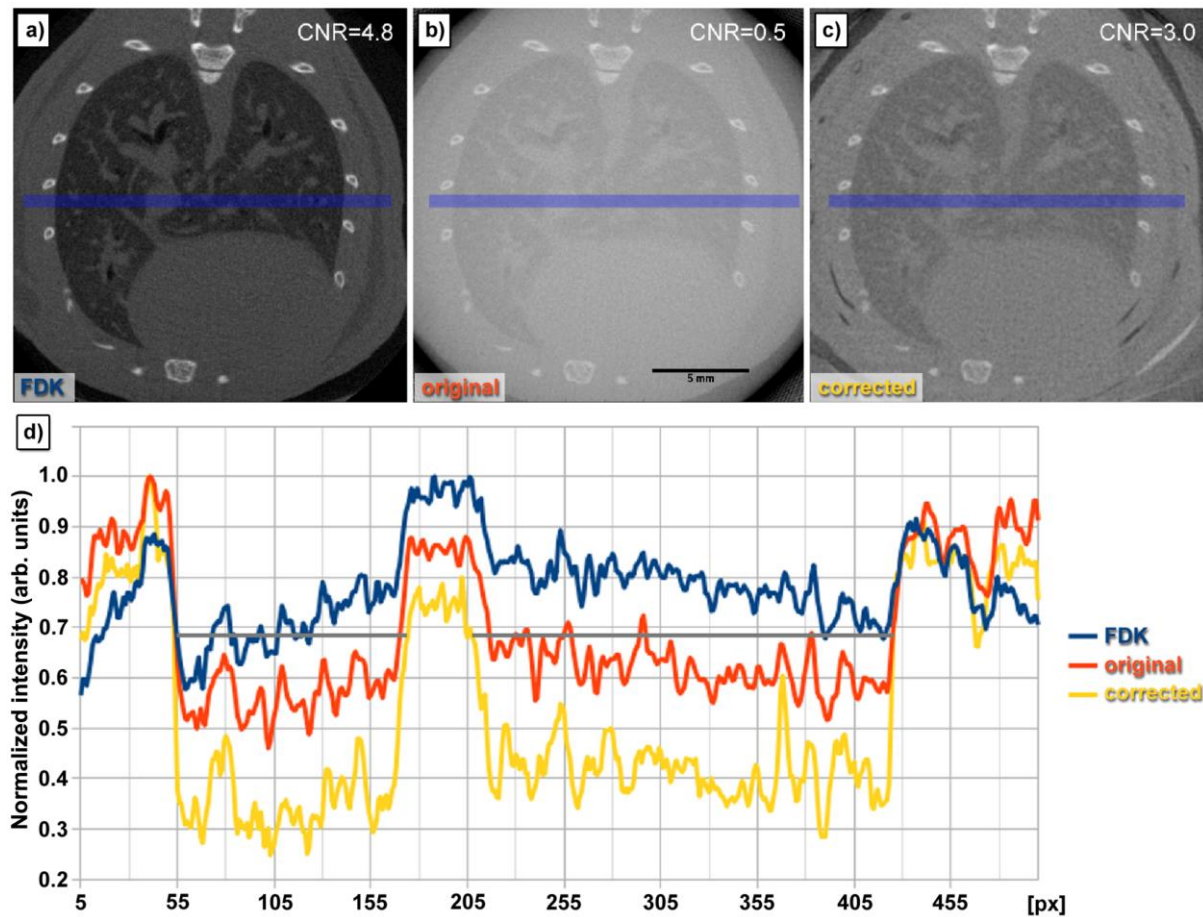


Figure S2: Comparison of micro-CT data reconstructions using standard retrospective gating software, modified FDK algorithm and FDK-reconstruction post filtering. a) Micro-CT reconstruction using the standard device-based algorithm with combined breathing states (inspiration and expiration) b) FDK-reconstructed image without additional correction factors. c) Image reconstruction using the modified FDK algorithm with post-process corrections including shading correction and enhanced contrast-to-noise ratio. d) The normalized profile-plot at the position indicated by the blue line over the lung region in a-c.

S5: Correlation between micro-CT determined lung volumes at inspiration and stroke volumes in dead ventilated mice

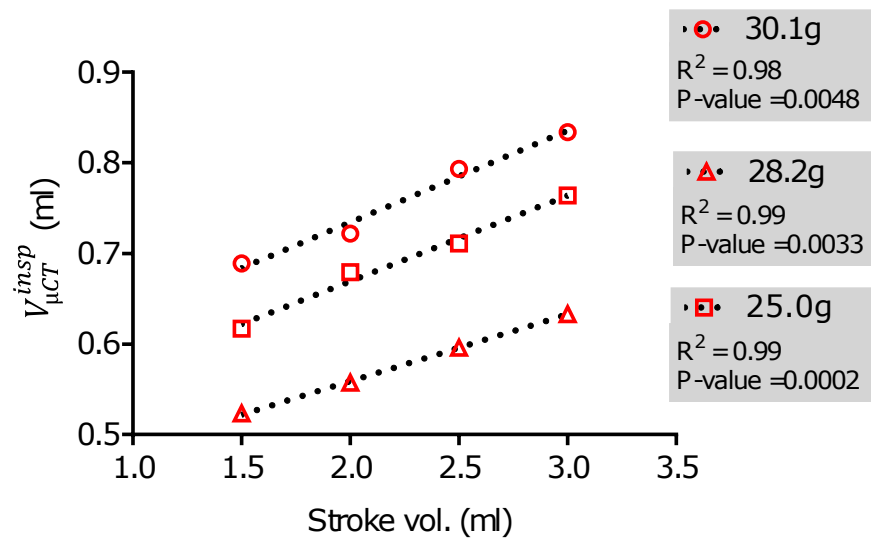


Figure S3: Correlation between $V_{\mu CT}^{insp}$ and stroke volumes applied for ventilating dead mice. Graph showing strong correlation between $V_{\mu CT}^{insp}$ and increasing stroke volume used for ventilating dead mice. The weights of the mice, respective coefficients of determination (R^2) from linear regression analysis and p-values (GraphPad Software) are shown on the graph.

Reference list

1. World Health Organization, World Health Statistics 2008. WHO, Geneva, Switzerland; <https://www.who.int/whosis/whostat/2008/en/> (2008).
2. Hoymann, H. G. Lung Function Measurements in Rodents in Safety Pharmacology Studies. *Front Pharmacol* **3**, (2012).
3. Lim, R. *et al.* Measuring Respiratory Function in Mice Using Unrestrained Whole-body Plethysmography. *JoVE* 51755 (2014) doi:10.3791/51755.
4. Glaab, T., Taube, C., Braun, A. & Mitzner, W. Invasive and noninvasive methods for studying pulmonary function in mice. *Respir Res* **8**, 63 (2007).
5. McGovern, T. K., Robichaud, A., Fereydoonzad, L., Schuessler, T. F. & Martin, J. G. Evaluation of respiratory system mechanics in mice using the forced oscillation technique. *J Vis Exp* e50172 (2013) doi:10.3791/50172.
6. Hamelmann, E., Schwarze, J., Takeda, K. & Oshiba, A. Noninvasive Measurement of Airway Responsiveness in Allergic Mice Using Barometric Plethysmography. **156**, 10 (1997).
7. Vanoirbeek, J. A. J. *et al.* Noninvasive and Invasive Pulmonary Function in Mouse Models of Obstructive and Restrictive Respiratory Diseases. *Am J Respir Cell Mol Biol* **42**, 96–104 (2010).
8. Quindry, J. C., Ballmann, C. G., Epstein, E. E. & Selsby, J. T. Plethysmography measurements of respiratory function in conscious unrestrained mice. *J Physiol Sci* **66**, 157–164 (2016).
9. Mitzner, W. & Tankersley, C. Noninvasive measurement of airway responsiveness in allergic mice using barometric plethysmography. *Am J Respir Crit Care Med* **158**, 340–342 (1998).
10. Lundblad, L. K. A., Irvin, C. G., Adler, A. & Bates, J. H. T. A reevaluation of the validity of unrestrained plethysmography in mice. *Journal of Applied Physiology* **93**, 1198–1207 (2002).
11. Adler, A., Cieslewicz, G. & Irvin, C. G. Unrestrained plethysmography is an unreliable measure of airway responsiveness in BALB/c and C57BL/6 mice. *Journal of Applied Physiology* **97**, 286–292 (2004).
12. Zhang, Q., Lai, K., Xie, J., Chen, G. & Zhong, N. Does unrestrained single-chamber plethysmography provide a valid assessment of airway responsiveness in allergic BALB/c mice? *Respir Res* **10**, 61 (2009).
13. Reynolds, J. S. & Frazer, D. G. Noninvasive pulmonary function screening in spontaneously breathing rodents: An engineering systems perspective. *Pharmacology & Therapeutics* **131**, 359–368 (2011).
14. Vande Velde, G. *et al.* Longitudinal micro-CT provides biomarkers of lung disease that can be used to assess the effect of therapy in preclinical mouse models, and reveal compensatory changes in lung volume. *Dis Model Mech* **9**, 91–98 (2016).

15. Ruscitti, F. *et al.* Longitudinal assessment of bleomycin-induced lung fibrosis by Micro-CT correlates with histological evaluation in mice. *Multidisciplinary Respiratory Medicine* **12**, 8 (2017).
16. Lovric, G. *et al.* Tomographic in vivo microscopy for the study of lung physiology at the alveolar level. *Scientific Reports* **7**, 12545 (2017).
17. Porra, L. *et al.* Quantitative Imaging of Regional Aerosol Deposition, Lung Ventilation and Morphology by Synchrotron Radiation CT. *Sci Rep* **8**, (2018).
18. Dullin, C. *et al.* MÖNCH detector enables fast and low-dose free-propagation phase-contrast computed tomography of in situ mouse lungs. *J Synchrotron Rad* **25**, 565–569 (2018).
19. Ruscitti, F. *et al.* Quantification of Lung Fibrosis in IPF-Like Mouse Model and Pharmacological Response to Treatment by Micro-Computed Tomography. *Front. Pharmacol.* **11**, (2020).
20. Plathow, C. *et al.* Computed Tomography Monitoring of Radiation-Induced Lung Fibrosis in Mice. *Investigative Radiology* **39**, 600–609 (2004).
21. Rivina, L., Davoren, M. & Schiestl, R. H. Radiation-Induced Lung Cancers in Murine Models. *ALC* **03**, 38–44 (2014).
22. Graves, P. R., Siddiqui, F., Anscher, M. S. & Movsas, B. Radiation pulmonary toxicity: from mechanisms to management. *Semin Radiat Oncol* **20**, 201–207 (2010).
23. Iwakawa, M. *et al.* Strain Dependent Differences in a Histological Study of CD44 and Collagen Fibers with an Expression Analysis of Inflammatory Response-related Genes in Irradiated Murine Lung. *JRR* **45**, 423–433 (2004).
24. Granton, P. V. *et al.* A Longitudinal Evaluation of Partial Lung Irradiation in Mice by Using a Dedicated Image-Guided Small Animal Irradiator. *International Journal of Radiation Oncology*Biology*Physics* **90**, 696–704 (2014).
25. Vande Velde, G. *et al.* Longitudinal in vivo microcomputed tomography of mouse lungs: No evidence for radiotoxicity. *Am J Physiol Lung Cell Mol Physiol* **309**, L271–L279 (2015).
26. Berghen, N. *et al.* Radiosafe micro-computed tomography for longitudinal evaluation of murine disease models. *Scientific Reports* **9**, 17598 (2019).
27. Dullin, C. *et al.* X-Ray based Lung Function measurement—a sensitive technique to quantify lung function in allergic airway inflammation mouse models. *Sci Rep* **6**, (2016).
28. Markus, M. A. *et al.* X-ray-based lung function measurement reveals persistent loss of lung tissue elasticity in mice recovered from allergic airway inflammation. *American Journal of Physiology-Lung Cellular and Molecular Physiology* **313**, L763–L771 (2017).
29. Eilers, H. *et al.* Pungent General Anesthetics Activate Transient Receptor Potential-A1 to Produce Hyperalgesia and Neurogenic Bronchoconstriction. *Anesthesiology* **112**, 1452–1463 (2010).
30. Feldkamp, L. A., Davis, L. C. and J. W. Kress. Practical cone-beam algorithm. *J. Opt. Soc. Am. A* **1**, 10.1118/1.1759828 (1984).

31. Drorbaugh, J. E. & Fenn, W. O. A barometric method for measuring ventilation in newborn infants. *Pediatrics* **16**, 81–87 (1955).
32. Bartlett, D. & Tenney, S. M. Control of breathing in experimental anemia. *Respiration Physiology* **10**, 384–395 (1970).
33. Murrie, R. P. *et al.* Real-time in vivo imaging of regional lung function in a mouse model of cystic fibrosis on a laboratory X-ray source. *Scientific Reports* **10**, 447 (2020).
34. Bell, R. D., Rudmann, C., Wood, R. W., Schwarz, E. M. & Rahimi, H. Longitudinal micro-CT as an outcome measure of interstitial lung disease in TNF-transgenic mice. *PLOS ONE* **13**, e0190678 (2018).
35. Gradl, R. *et al.* Visualizing treatment delivery and deposition in mouse lungs using in vivo x-ray imaging. *Journal of Controlled Release* **307**, 282–291 (2019).
36. Gradl, R. *et al.* Dynamic In Vivo Chest X-ray Dark-Field Imaging in Mice. *IEEE Transactions on Medical Imaging* **38**, 649–656 (2019).
37. Backer, J. W. D. *et al.* Study of the Variability in Upper and Lower Airway Morphology in Sprague–Dawley Rats Using Modern Micro-CT Scan-Based Segmentation Techniques. *The Anatomical Record* **292**, 720–727 (2009).
38. Blocker, S. J., Holbrook, M. D., Mowery, Y. M., Sullivan, D. C. & Badea, C. T. The impact of respiratory gating on improving volume measurement of murine lung tumors in micro-CT imaging. *PLoS One* **15**, (2020).
39. Enhorning, G., Schaik, S. van, Lundgren, C. & Vargas, I. Whole-body plethysmography, does it measure tidal volume of small animals? *Can. J. Physiol. Pharmacol.* **76**, 945–951 (1998).
40. Mailhot-Larouche, S. *et al.* Assessment of Respiratory Function in Conscious Mice by Double-chamber Plethysmography. *J Vis Exp* (2018) doi:10.3791/57778.
41. Paton, J. *et al.* Discrepancies between pediatric laboratories in pulmonary function results from healthy children. *Pediatric Pulmonology* **47**, 588–596 (2012).
42. Fouras, A. *et al.* Novel x-ray velocimetry-based quantitative regional lung function analysis to assess risk of radiation-induced pneumonitis and pulmonary fibrosis. *Chest* **156**, A2264–A2265 (2019).
43. Sgalla, G. *et al.* Idiopathic pulmonary fibrosis: pathogenesis and management. *Respiratory Research* **19**, 32 (2018).
44. Assaad, S. Assessment of Pulmonary Edema_ Principles and Practice. *Journal of Cardiothoracic and Vascular Anesthesia* **14** (2018).
45. Silva, P. L. & Rocco, P. R. M. The basics of respiratory mechanics: ventilator-derived parameters. *Ann Transl Med* **6**, (2018).
46. Zhang, B., McDonald, F. B., Cummings, K. J., Frappell, P. B. & Wilson, R. J. A. Novel method for conscious airway resistance and ventilation estimation in neonatal rodents using plethysmography and a mechanical lung. *Respiratory Physiology & Neurobiology* **201**, 75–83 (2014).
47. Hülsmann, S., Mesuret, G., Dannenberg, J., Arnoldt, M. & Niebert, M. GlyT2-Dependent Preservation of MECP2-Expression in Inhibitory Neurons Improves Early Respiratory

- Symptoms but Does Not Rescue Survival in a Mouse Model of Rett Syndrome. *Front Physiol* **7**, (2016).
48. Schindelin, J. *et al.* *Fiji: An open-source platform for biological-image analysis*. vol. 9 (2012).

Acknowledgements

We thank Sarah Garbode and Bärbel Heidrich for assistance during animal experiments.

Funding

AK was supported by a seed grant of the Physics-to-Medicine Initiative Göttingen.

Competing interests

The authors declare that they have no competing interests.

Data availability

All data generated or analyzed during this study are included in this published article and its supplementary information files.

Ethical approval

Ethical permission for animal experiments was granted by the Nieders. Landesamt für Verbraucherschutz und Lebensmittelsicherheit (approval number G15.1747)

Discussion/ Summary of Publications

Comparative label-free imaging approach for assessing cardiac fibrosis and hypertrophy

Myocardial fibrosis is a common pathological process during the course of different cardiovascular diseases with a proven prognostic value in the development of heart failure. The structural alterations in the myocardial architecture caused by fibrosis requires detailed ex-vivo imaging of fibrotic tissue for identification and quantification of structural modification at sub-cellular level.

In chapter 1, I present a unique comparative multi-imaging label-free approach combining second harmonic generation (SHG) imaging and x-ray diffraction to assess cardiac remodeling in a mouse model of pressure overload. To date, SHG imaging is relatively little established to investigate the cardiac structural composition as compared to x-ray diffraction. In fact, most of SHG imaging in previous studies has been mostly applied in isolated cardiomyocytes (Liu et al., 2011; Varga et al., 2020; Yang et al., 2016). Our study is the first to implement SHG imaging for the characterization of structural modulations in entire transverse tissue sections of healthy and disease hearts. Morphologically, the SHG signals from collagen and myosin could be clearly distinguished in cardiac tissue. Furthermore, the assessment of collagen emitted SHG revealed micro- to macro-level (i.e., single fibril to bundles) deposition of collagen in the interstitial space of fibrotic hearts. Profound differences in the tissue architecture of TAC operated hearts were detected when compared to healthy hearts including interstitial and perivascular fibrosis and disruption of surrounding myocardium. By contrast, Yuan et al. found no differences at morphological level but only reported changes in myosin in a cell stretch model (Yuan et al., 2019) when they performed SHG imaging in healthy and TAC operated cardiac tissues. The discrepancy in the observations was due to fundamental differences in their animal model, sample preparation and image acquisition as compared to our work (Yuan et al., 2019). In our study, cardiac tissue sections were obtained from TAC-operated hearts 16 weeks post-surgery while in the work by Yuan et al., 2019 hearts were imaged 4 weeks after TAC surgery. Further, they imaged cryofrozen tissue sections using a relatively small field of view (FOV) while we analyzed formalin fixed samples and performed scanning of entire tissue sections. This highlights that identification of fibrosis incurred micro-

modulations in heart requires scanning over large areas of cardiac tissue sections. Furthermore, in our study SHG imaging showed higher precision in the evaluation of perivascular fibrosis than conventional histology. Interestingly, as shown in our study by the myosin emitted SHG signal in TAC hearts, myofibril hypercontractility (or undulations), which was previously mainly associated with hypertrophic cardiomyopathy (HCM), is also a significant feature of hypertensive hearts. In HCM, hypercontractility is primarily caused by mutations in β -cardiac myosin and myosin-binding protein-C (MyBP-C) (Spudich, 2019) and also via *ACTN2* mutation as shown in a recent study (Prondzynski et al., 2019). We hypothesize that the underlying cause of myofibril hypercontractility due to pressure-overload might be related to the compensatory mechanisms that help to maintain cardiac function. However, the molecular pathways contributing to myofibril hypercontractility due to hypertension still need to be identified.

The findings presented in chapter 1 show that the comparative approach by SHG and x-ray diffraction is ideal to support and validate the data obtained from both imaging modalities. The diffraction maps of transverse sections of cardiac tissue can additionally resolve the specific peak intensity, fiber orientation and filament spacing at each layer of the heart i.e., epicardial, myocardial and endocardial layer. In fibrotic tissue, 2D maps of high filament spacing and a low peak intensity identified the site of fibrotic lesions and an increase in acto-myosin lattice in the surrounding tissue. Additionally, a low anisotropy at fibrotic regions reflects tissue replacement while maintaining only a residual degree of original orientation of the tissue which might help maintain cardiac functioning in diseased hearts. However, regions with an increase in acto-myosin filaments and tissue replacement are known to contribute to anomalies in cardiac conduction which is typically observed in fibrotic hearts (Nguyen et al., 2014; Wada et al., 2013). In comparison to SHG imaging, x-ray diffraction has been extensively implemented on heart to elucidate the micro-level structural arrangement of the acto-myosin lattice. Nicolas et al., performed scanning x-ray diffraction in various types of healthy cardiac cells and tissue including neonatal (rat) and adult (mouse) cardiac cells, induced pluripotent stem cells (iPSC) derived cardiomyocytes, engineered heart muscle (EHM) and cardiac tissue sections (mouse) (Nicolas et al., 2017; J. D. Nicolas et al., 2019). The results from these extensive studies linked the diffraction signal to the underlying actin cortex where highest muscle diffraction peak was observed in cardiac tissue followed by adult cardiomyocytes. In fully developed cardiac tissue and isolated adult cardiomyocytes, a clear mapping of multiple averaged diffraction scattering

patterns was also acquired for orientation and anisotropy (J.-D. Nicolas et al., 2019; Nicolas et al., 2017). However, the highly structured diffraction pattern of classical muscle is not resolved in neonatal cardiomyocytes and EHM due to immature and underdeveloped structures (J. D. Nicolas et al., 2019).

In our study, the regions in the TAC-operated cardiac tissue slices lacking acto-myosin lattice diffraction signal and SHG signal from both myosin and collagen were initially obscure. Upon two-photon excitation fluorescence (TPEF) imaging of DRAQ5 stained nuclei we observed that such regions have high infiltration of immune cells and IHC revealed presence of activated myofibroblasts signifying an active fibrosis process at these regions. The infiltration of immune cells is a known phenomenon that occurs in early stages of fibrosis progression (Bacmeister et al., 2019). Thus, the combined use of x-ray diffraction and SHG enables detecting an early onset of fibrosis with immune-cell infiltration and also end-stage fibrosis with ECM turnover and collagen deposition accompanied by myofibril disruption.

The results from both imaging modalities signify that the adverse effects of fibrosis on tissue structure spread beyond the fibrotic lesions to the surrounding myocardium, in particular the myofibril distortion and increased acto-myosin interfilament spacing, as presented in chapter 1. These new insights into cardiac remodeling suggest that a range of other molecular and structural targets for early detection of fibrosis induced tissue remodeling could be investigated. For instance, the analysis of hypercontractility of myofibrils in surrounding tissue, could be performed in addition to assessing elastic stiffness and strain rate of fibrotic lesions by non-invasive functional assessment using speckle tracking-echocardiography. So far, most of the in-vivo diagnostic techniques are focused on detection of fibrotic lesions by homing probes to sites of fibrosis and inflammation (Baues et al., 2017; Hassan et al., 2020; Ziegler et al., 2016). The results of our ex-vivo imaging approach, revealing disruption of myofibrils around the fibrotic regions and increase in overall filament spacing, highlight that the scope for detecting fibrosis induced tissue remodeling can now be extended to evaluate and quantify orientation, spacing and morphology of myofibrils. For instance, x-ray diffraction and/or more readily available SHG imaging could be applied to detect micro-level remodeling not only at fibrotic lesions but also at the surrounding myocardium in endomyocardial biopsies (EMB). In this way, the effects of non-representation of pathological tissue, discrepancies in interpretation, complex sample preparation and staining procedures can be reduced.

Age-related divergent remodeling of the cardiac muscle and ECM

Next, we applied a modified and advanced TPM approach to augment the label-free imaging approach for assessing cardiac maturation and age-related fibrosis in non-human primates (NHP) as shown in chapter 2. By successfully segregating the collagen originated SHG as the backscattered signal from myosin emitted SHG, a reliable quantification of connective tissue content was performed in hearts of neonatal/newborn (<4 weeks), young adult (1-4 years) and old/geriatric (>10 years) marmosets. Additionally, the total tissue volume (myosin + collagen), which was detected as forward SHG signal, was determined in 3D for all age groups. Myosin emitted SHG was quantified in overview as well as in zoomed-in images to provide vital cues for evaluating age-related structural differences in the myocardium. Our results demonstrate for the first time significant differences in total tissue volume, myofibril spacing, alignment, curvature and angular distribution in hearts of marmosets of different age groups using a label-free TPM imaging approach.

First, to investigate age-related cardiac remodeling, we acquired and defined intrinsic autofluorescence signals from the myocardium. At the extracellular level, autofluorescence is mainly generated by elastin and blood cells and at the intracellular level it arises from various mitochondrial proteins while the nuclei appear dark. In accordance with stained histological slices, TPEF label-free images reveal a high nuclear-to-cytoplasm ratio in neonatal marmoset hearts which declines as the cardiomyocytes mature in the adult hearts as presented in chapter 2. As shown by others, this decline in nuclear density from neonatal to adult stage mainly occurs via DNA synthesis without nuclear division to make polyploid nuclei (Bishop et al., 2021; Karbassi et al., 2020). Our findings demonstrate the characteristics of TPEF emitted autofluorescence in cardiac tissue for elucidating nuclear density and presence of connective tissue components (i.e., elastin) which offers versatile applications in tissue engineering and developmental studies to reflect tissue maturity. TPEF has been applied by others for imaging live cells and tissue interactions (Benninger et al., 2008), in developmental biology (Abu-Siniyeh and Al-Zyoud, 2020) and for understanding the tumor micro-environment (Williams et al., 2010).

The SHG signal intensity from myosin tends to be weaker than that of collagen as observed in both of our studies. This is mainly due to fundamental differences in the structural assembly of both harmonophores and the dependence of myosin on the orientation of the myofibrils and

semicrystalline order of A bands (Greenhalgh et al., 2007). This poses a real challenge to image both harmonophores in the same frame with adequate quantifiable intensities. To overcome this and to segregate the SHG signals from collagen and myosin we simply acquired the SHG signals bidirectionally. SHG being an anisotropic process, propagates in forward direction with minimal backscattered signal. Hence, the intensity of myosin is optimal in forward direction while collagen emits ideal signal intensity in epi-direction without causing signal saturation, as shown in chapter 2. The image acquisition settings are also critical for obtaining signal intensities. In our TPM experimental design we managed to execute simultaneous bidirectional acquisition by applying the same excitation/emission wavelengths. Furthermore, by collecting backscattered signals via the objective lens and forward signals through the condenser lens we were able to use minimal illumination power to avoid tissue damage, especially during the 3D imaging. Since TPM enables high imaging depth, we performed volumetric assessment of collagen and myosin in relatively transparent (50 – 100 μm) slices which was found to be the optimum thickness of cardiac tissue slices to maintain a constant SHG signal intensity throughout the acquired volume (particularly the z-stacks).

One of the main findings from our study is the significant structural modulation that takes place during cardiac maturation and age-related pathological remodeling in marmosets. Our volumetric assessment revealed a relative increase in collagen volume with age which can be in part attributed to the number of fibroblasts that increases postnatally until adulthood (Banerjee et al., 2007; Hall Caitlin et al., 2021). Varying populations of cardiac fibroblasts in postnatal heart promote cardiac organogenesis and ECM maturation, and during the postnatal period, ECM remodeling is active which is promoted by the presence of periostin-expressing cardiac fibroblasts (Hortells et al., 2020). However, previous work has shown that in adult hearts the fibroblasts become quiescent, and the ECM is fully developed to provide a scaffold for maintaining tissue structure and dynamics (Hall Caitlin et al., 2021). My finding of substantially high collagen volume in geriatric marmoset hearts indicates the development of age-related interstitial and perivascular fibrosis. This signifies the pathological activation and transdifferentiation of fibroblasts into myofibroblasts by old age. The presence of periostin-expressing cardiac fibroblasts in aged hearts, in absence of an underlying pathology, also promotes the infiltration of inflammatory cells and fibrosis progression (Landry et al., 2017; Li et al., 2014). Evolving evidence suggests that activation of several distinct signaling pathways may participate in age-associated fibrotic cardiac remodeling. Reactive oxygen

species (ROS) (Checa and Aran, 2020), fibroblast progenitors (Trial and Cieslik, 2018), transforming growth factor (TGF)- β activation (Bujak and Frangogiannis, 2007), chemokine-mediated recruitment of immune cells (Meschiari et al., 2017) and angiotensin II signaling (Lu et al., 2017) mediate interstitial and perivascular fibrosis in the aged hearts. Impaired collagen degradation may play a more critical role than increased *de novo* synthesis in the pathogenesis of aging-associated fibrosis (Lu et al., 2017).

By investigating the impact of ECM and the combined volume of collagen and myosin (total tissue volume) on the structural organization of myofibril, parameters such as myofibril alignment, curvature, angulation and spacing at sub-cellular level were measured for the first time in cardiac tissue. In neonatal marmoset cardiac tissue, a loosely packed structure with no proper adhesion between the myofibrils contributes to the overall low total tissue volume. This structural composition in neonatal hearts was further attributed to the absence of fully developed intercalated disks (ICDs) as shown in our SHG images. This correlates to the understanding that the spatiotemporal movement of ICDs associated proteins including fascia adherens, desmosomes and gap junctions from the lateral side of the myocytes to the cell termini does not occur at this stage (Guo Yuxuan and Pu William T., 2020). This finding is in line with the human developmental process of cardiomyocytes in which the targeted localization of adherens junction proteins (N-cadherin) to the ICDs occurs at about 10.5 months of age (Vreeker et al., 2014). In rodents however, the ICDs develop as early as postnatal day three (Bishop et al., 2021) which further emphasizes the relevance of using NHP as a model for investigating cardiac aging. In our study the myofibril misalignment and absence of adhesion between myofibrils can be related to the low volume of immature ECM components since cardiomyocyte integration requires attachment to the ECM via focal adhesion structures, the costameres, which are also not developed in the neonatal hearts (Guo Yuxuan and Pu William T., 2020). ICDs and costameres also contribute to tissue integration as well as cardiomyocyte maturation by harboring the vinculin-based actomyosin assembly that is required for sarcomere expansion (Chopra et al., 2018). In comparison, in the young adult marmosets with an age range of 2 – 4 years, a fine arrangement of well aligned myofibrils as well as fully developed ICDs and ECM are present as clearly visible by our SHG imaging approach.

An aged heart begins to display signs of pathological tissue remodeling with the appearance of hypercontracted and distorted myofibrils as shown in our SHG images. In old/geriatric hearts, despite the apoptosis induced reduction in the number of cardiomyocyte and a lower LV mass in the whole hearts in-vivo, we observed the highest total tissue volume at the ROI. This can be mainly attributed to the lower spacing between hypertrophic myofibrils and excessive ECM deposition which adds to the high tissue volume at the pathological sites. Unlike hypertensive hearts, in which the underlying cause of myofibril hypercontractility is unidentified, in aged hearts it can be primarily attributed to alteration in excitation-contraction coupling (ECC). Aging is associated with various modifications in ECC components including i) the decline in expression and activity of sarco/endoplasmic reticulum Ca^{2+} -ATPase (SERCA2a) which results in poor Ca^{2+} transient decay rates and concomitantly weakens the cardiomyocyte relaxation rate and ii) the increased activity of ryanodine receptor (RyR) during diastole contributing to increases in resting Ca^{2+} ions. These age-related modifications have been shown to promote cellular Ca^{2+} overload-mediated cardiac dysfunction (Hano et al., 1995; Xu and Narayanan, 1998; Fares and Howlett, 2010). A recent study reported the expression of the Transient Receptor Potential Vanilloid-4 (TRPV4), which is a non-selective cation channel in aged mice hearts causing an additional sarcolemmal Ca^{2+} influx pathway, which contributes to excessive intracellular Ca^{2+} accumulation provoking cardiac hypercontractility (Veteto et al., 2020). Receptors such as TRPV4 can serve as an alternative target for designing PET and SPECT tracers for identifying Ca^{2+} overload-induced cardiac dysfunction in-vivo, in addition to targeting biomarkers specific to fibrosis and/or inflammation in old patients. Owing to the comparable lifespan in human and NHP aging, our findings offer clinically relevant data therefore it is of great value to assess hypercontractility older patients.

In conclusion, our label-free high-resolution TPM approach enables visualization and quantification of subcellular structural features for understanding vital age-related morphological alterations in the marmoset heart. These findings highlight the unrivalled potential of TPM label-free imaging that could be further applied for investigating the effects of therapeutic approaches for cardiac regeneration and repair on the structural level in pre-clinical models.

Future perspectives – Label-free imaging as next-generation diagnostic tool for pre-clinical and clinical application

In contrast to histology and immunohistochemistry which only provides 2D data, our TPM imaging approach could provide label-free, volumetric, high-resolution information on clinical samples including whole biopsies. For instance, it can be readily clinically applied for assessing EMB in 2D and 3D. EMB are – according to the specific guidelines from the European Society of Cardiology and American Heart Association, the American College of Cardiology – advised to be used for different diagnostic purpose, such as monitoring cardiac allograft rejection or identifying in the patients an unexplained new-onset of heart failure with new ventricular arrhythmias and a dilated left ventricle, or in conditions when the patient fails to respond to the standard treatment within 1–2 weeks (Cooper et al., 2007; Mewton et al., 2011).

The comprehensive SHG data provided by our studies on cardiac tissue have versatile implications for pre-clinical applications, such as intravital TPM and SHG imaging of the heart that could discern details of micro-fibrotic lesions and myofibril arrangement. Recently, a proof-of-concept study was performed in adult CAG/GFP transgenic rats for in-vivo intravital imaging of cardiac ischemia/reperfusion (I/R) (Matsuura et al., 2018a). This study successfully observed myocardial subcellular dynamics, mitochondrial distribution, I/R injury-induced suppression of the contraction/relaxation cycle and leukocyte accumulation in cardiac tissue (Matsuura et al., 2018b). The visualization of various cardiac structures including the myocardium, capillaries and mitochondrial membranes relied upon the use of fluorescent dyes in this study. Photobleaching and phototoxicity of the fluorescent dyes hinder longitudinal assessments as well as the quantification of signal intensity in a time-dependent manner. However, since TPM demonstrates minimal photobleaching and photodamage restricted to the volume of the focal plane as compared to other microscopy techniques, imaging intrinsic signals in form of SHG and TPEF can largely overcome these drawbacks. Both of our studies provide detailed descriptions of acquisition and identification of cardiac structures for implementing label-free TPM for intravital imaging. A detailed understanding of the distinction between forward and backscattered SHG signals in cardiac tissue is important for intravital microscopy, which is performed on high-scattering opaque organs and requires signal acquisition in epi-direction. This can pose a challenge for imaging and quantifying collagen

and myosin emitted SHG in whole hearts as backward signal in a single frame. Therefore, we expect that morphological distinction between the two harmonophores highlighted in chapter 1 can be an advantage for the use of TPM based intravital imaging of beating hearts.

In future, the most promising application of our imaging approach might be in the field of two-photon endoscopy which is feasible for preclinical and clinical diagnostics. Interestingly, label-free imaging using TPM micro-endoscopy has been already performed successfully in a mouse model of unilateral urethral obstruction (Ducourthial et al., 2015). In-vivo 3D imaging enabled detection of significant signals from the tubules up to 300 μm below the kidney outer surface. The results further showed a higher degree of collagen at the capsular surface and enlargement of the renal capsule in fibrotic kidney when compared to the healthy one (Ducourthial et al., 2015). Such an approach enables high-resolution, in-vivo visualization of ECM with increased specificity that is so far not accomplished by current non-invasive pre-clinical imaging techniques.

TPM endoscopy in clinical studies is focused on two main research areas: 1) in-vivo TPM dermatological imaging, and 2) in-vivo TPM endoscopy of deeper tissue regions (Perry et al., 2012). TPM endoscopy for dermatological imaging identified distinct features of ascending melanocytes such as architectural disarray of epidermis, the presence of dendritic and pleomorphic cells and poorly defined keratinocyte cell borders, which can differentiate between cancerous skin tissues from healthy human skins with accuracy (Dimitrow et al., 2009; Paoli et al., 2009). TPM micro-endoscopy of deep tissue is mainly applied by two means – intracorporeal and intracavitary endoscopy. Intracorporeal endoscopy employs needle-like lenses to penetrate areas near the body surface while intracavitary endoscopy uses lenses attached to a flexible fiberoptic probe that enables deeper intracavity imaging (Liu, 2015). TPM endoscopy can help replace more invasive or surgical biopsy-based methods to detect fibrosis in multiple organs including heart, however, its use is largely hindered by technological obstacles. One example is the difficulty of incorporating femtosecond pulse rate laser source within the optical fiber (Fu and Gu, 2007). Recent efforts for overcoming these technical challenges, such as the use of gradient-index (GRIN) lenses and units based on microelectromechanical systems (MEMS), have substantially improved clinical application of TPM endoscopy (Chien et al., 2020; Qiu and Piyawattanamatha, 2017). With minimal invasion, GRIN lens-based endoscopes with a 350 μm diameter successfully facilitated visualizing

individual sarcomeres in passive and activate skeletal muscle revealing contractile dynamics with millisecond-scale resolution in human subjects (Llewellyn et al., 2008). Intravital or TPM endoscopy in beating hearts, however, involves additional challenges due to motion artifacts. Vinegoni et al. performed TPM and confocal based intravital imaging of beating hearts in a proof-of-concept study and presented a motion artifact removal protocol (Vinegoni et al., 2015). They showed that by using mechanical tissue stabilization and by applying cardiorespiratory gating, periodic reproducibility in the images can be achieved to minimize motion induced artefacts (Vinegoni et al., 2015). Additionally, the use of suitable post processing computational algorithms and software to acquire the timing of signal from the microscope, the electrocardiogram (ECG) and the ventilator waveform, can further correct the motion artefacts (Vinegoni et al., 2015). Thus, both TPM based intravital microscopy and endoscopy have the potential to be used in animal models and humans as next-generation cardiac diagnostic tools which can be combined with various functional imaging techniques such as CCT, CMR and echocardiography (Matsuura et al., 2018a).

New mode of lung function assessment using advanced XLF

Techniques to reliably assess lung function particularly in pre-clinical animal models are inefficient and underdeveloped. In chapter 3, we report an advanced x-ray based lung function (XLF) approach that measures various functional parameters including inspiration time (t_{in}), length of the breathing events (L), decay rate (τ) of the expiration phase as well as lung volume from simple low dose radiographic images of the chest in living mice. The XLF algorithm described in a previous study from Dullin et al. was used as basis and was redefined to achieve functional parameters that are comparable to whole body plethysmography (WBP) and micro-CT and are biomedically interpretable. We show that XLF measured lung volumes reveal higher precision and sensitivity when compared to WBP.

To enhance the quality of x-ray radiographic images, a relatively small FOV was used which is optimal for in-vivo lung imaging using a benchtop micro-CT system for XLF and for micro-CT measured lung volumes (Ruscitti et al., 2020, 2017; Vande Velde et al., 2016, 2015). In the next critical step, we succeeded to synchronize the timing of signals acquired from WBP, XLF and micro-CT. Since micro-CT lacks a signal output to provide information about the timepoint to acquire the first image frame, we conceived our own trigger from the CT via installation of a piezoelectric sensor. This provides an acoustic signal for matching the starting point of CT data acquisition and WBP recording. Further experiments by us demonstrate that this unique yet simple experimental design is feasible for future studies to perform non-invasive multimodal lung function assessment in various small animal models of lung disease including lung fibrosis to measure lung volumes, decay rates and inspiration (see appendix).

In our approach micro-CT measured lung volume is used as a gold-standard for correlation of lung volumes acquired from XLF and WBP. Semi-automated segmentation of CT images is commonly applied to determine total lung volume (Backer et al., 2009; Ruscitti et al., 2020; Vande Velde et al., 2016) in pre-clinical studies and offers higher sensitivity in comparison to plethysmography. We developed an efficacious pipeline for extracting segregated lung volumes for inhalation ($V_{[\mu CT]}^{insp}$) and expiration phases ($V_{[\mu CT]}^{exp}$) and the difference between the two breathing phases ($V_{[\mu CT]}^{insp} - V_{[\mu CT]}^{exp}$) resulted in tidal volume ($V_{[\mu CT]}^{TV}$). A strong correlation between $V_{[\mu CT]}^{TV}$ and stroke volume used for ventilating dead mice warranted the use of our micro-CT approach to determine lung volumes as a benchmark. However, the lab based micro-

CT systems have poor resolution due to low signal-to-noise-ratio and motion induced image blurring which results in delineation of lung aerated regions that include minute soft tissue structures instead of absolute air volume. To further enhance the spatial resolution towards micrometer scale, in-vivo lung imaging can be performed at third-generation synchrotrons (SR) (Lovric et al., 2017) for accurate measurement of air volume excluding meniscal soft tissue structures. SR based micro-CT – owing to sufficient electron flux and highly coherent x-rays – is markedly higher in sensitivity to soft tissue micro-architecture when compared with lab-based CT (Lovric et al., 2017). However, high radiation dose and long acquisition time are the main limiting factors for routine application of micro-CT techniques for longitudinal pre-clinical studies and clinical translation. By contrast, radiographic XLF measurements as established by us, uses only 7% of the radiation dose required for micro-CT as well as significantly shorter acquisition times. Importantly, a strong correlation between end-inspiratory volume ($EIV_{[XLF]}$) and $V_{[\mu CT]}^{insp}$ signified the sensitivity and precision of XLF measured lung volumes. Corroborating the findings from Dullin et al., this imaging approach provides longitudinal non-invasive assessment that could be applied for assessing fibrosis progression and response to therapy (see appendix). Moreover, the integration of this imaging technique in experimental research can greatly reduce the number of animals required and by precisely staging fibrosis could also help lessen the distress caused by severe fibrosis.

$EIV_{[XLF]}$ values had to be normalized with empirically driven estimation factor since XLF is sensitive to mouse body weights. The effects of gender and strain on XLF measurements were not assessed in our study which might require further normalization. Nonetheless, as most pre-clinical studies are typically performed on gender and strain matched cohorts, the XLF approach is generally feasible. One main limitation involving XLF is that it can only quantify air volume at end-inspiration ($EIV_{[XLF]}$) but cannot determine end-expiration and tidal volumes. This might contribute to the poor correlation between $EIV_{[XLF]}$ and WBP measured tidal volumes ($TV_{[WBP]}$). However, as opposed to $EIV_{[XLF]}$ which strongly correlated with $V_{[\mu CT]}^{insp}$, $TV_{[WBP]}$ versus $V_{[\mu CT]}^{TV}$ showed a poor correlation. This is mainly because of inaccuracies in WBP measurements which occur due to the slight changes in humidity and temperature at each breath inside the chamber, influencing the quantification of $TV_{[WBP]}$ (Enhörning et al., 1998; Hülsmann et al., 2021; Lundblad et al., 2002).

We present XLF as an efficient and advanced tool for lung function assessment by successfully correlating XLF based radiographic data with micro-CT measurements. Due to the high sensitivity, fast acquisition time and use of low radiation dose, XLF measurements are highly suitable for longitudinal studies and the implementation in preclinical research.

Future perspective – Advanced XLF approach as next generation diagnostic tool for measuring lung function

Current methods for pre-clinical lung function measurements provide readouts of lung mechanics by testing airway resistance and compliance using devices such as the flexiVent small animal ventilator (Scireq, Canada) which generally requires orotracheal intubation or tracheostomy and subsequent euthanasia (Bonnardel et al., 2019). They also need post-mortem analysis of the lung tissue using histological or biochemical tests to detect and localise disease. XLF, on the other hand, offers a reliable and sensitive non-invasive alternative for longitudinal assessment of lung function for diagnostics during the course of the disease as well as for monitoring the response to novel therapeutics. Importantly, XLF is a simple technique which requires standard micro-CT equipment or even a simple x-ray tube making it easily feasible for routine pre-clinical application as opposed to MRI imaging which requires complex handling, data processing and expensive equipment.

For patient application, 4D x-ray based real-time imaging of lung motion and airflow to determine global and localized functional deficits are under development, however, to date no clinical equipment is available (Fouras et al., 2019; Murrie et al., 2020). These studies highlight the potential and demand of x-ray based pulmonary functional imaging in clinical settings. The routine clinical use of x-ray based lung functional analysis is mainly limited due to the use of high x-ray doses. In this context, XLF is a promising tool to overcome this hurdle, since it is a fast radiographic measurement which could be performed at clinically approved radiation doses. The XLF measured functional and volumetric parameters are designed to reflect airway remodeling causing obstruction of airflow which offer the assessment of multiple pulmonary disorders such as pulmonary edema, particularly it may provide early diagnosis of lung fibrosis. It can be envisaged that XLF can be potentially performed in non-compliant or even unconscious patients, in which other techniques such as spirometry typically used for lung function measurement, cannot be applied. Lastly, the ventilator settings that are currently

adjusted by the lung and chest wall mechanics of the patient and/or the operator, can result in ventilator induced lung injury if not regularly supervised (Silva and Rocco, 2018). This could be monitored and adjusted using XLF.

Conclusion

This thesis provides new tools and perspectives for imaging based assessment of cardiac and lung fibrosis. Distinct limitations are involved in the current diagnostics of fibrosis in each organ wherein early assessment of cardiac fibrosis essentially requires visualization and characterization of sub-cellular structural remodeling while early detection of lung fibrosis is hindered by lack of sensitive and reliable functional imaging techniques.

To this end, the comprehensive evaluation and quantification of cardiac structures using label-free TPM and x-ray diffraction imaging provided unprecedented characterization of pathological alterations in cardiac tissue obtained from a mouse model of pressure-overload. In the first study, SHG imaging of healthy cardiac tissue provided detailed morphological differences between myosin and collagen where both harmonophores were imaged in a single frame which was not performed at this resolution in any previous work. SHG emission enabled specific imaging of collagen deposition from single collagen fibrils to large regions of interstitial and perivascular fibrosis. Using SHG imaging, my work for the first time identified the detrimental impact of fibrosis and hypertrophy on the myocardium including the hypercontractility (or undulation) of myofibrils. These findings were corroborated with x-ray diffraction which revealed a low anisotropy and peak intensity with a larger acto-myosin filament spacing at the sites of tissue remodeling. Overall, this unique comparative imaging approach revealed that the effects of fibrosis and hypertrophy spread beyond fibrotic regions and induce micro-modulations in the surrounding myocardium. This provides new potential imaging biomarkers for diagnostics that may allow early intervention to control fibrosis related cardiac dysfunction. The results from this study can be translated to clinical application such as for 3D, label-free and high-resolution imaging of EMB to obtain additional information of prognostic or diagnostic value in cardiac disease.

For imaging age-associated cardiac maturation and fibrosis in NHP, the TPM approach was modified and demonstrate that it enables i) acquisition of TPEF in addition to SHG signal, ii) segregation of collagen and myosin SHG emission and iii) performing 3D imaging. The combination of SHG and TPEF imaging enables visualization of versatile intracellular and extracellular cardiac tissue structures which we expect to be used in TPM based in-vivo cardiac imaging in the future. We devised a simple yet effective experimental design to segregate SHG

emission from collagen as backscattered signal and combined collagen and myosin emitted SHG as forward transmitted signal. Using this strategy, high-resolution 2D and 3D images are acquired without any tissue damage for reliably quantifying spatial composition of myofibrils. Furthermore, it allows to perform volumetric assessment of collagen and total tissue volume (myosin + collagen) in cardiac tissue. Our findings using volumetric analysis showed a progressive increase in collagen and total tissue volume (myosin + collagen) with aging which was related to various age specific structural hallmarks identified by SHG imaging such as myofibril adhesion and ECM content. These findings not only highlight the importance of TPM label free imaging for investigating cardiac fibrosis, but also show its potential to understand cardiac regeneration processes and monitoring cardiac repair in response to treatment. By applying semi-automated analysis significant differences were revealed for the first time in total tissue volume, myofibril length, alignment, curvature and angulation in all three age groups. Our promising results encourage further development of TPM based label-free intravital microscopy and endoscopy for early and reliable detection of cardiac fibrosis.

In comparison to myocardial fibrosis which requires detailed sub-cellular evaluation, the current diagnosis of lung fibrosis lacks reliable non-invasive pre-clinical functional assessment. We developed an advanced radiographic XLF approach for an efficient measurement of both lung function and volume. This was achieved by using a unique set-up for direct correlation of XLF measured lung volumes with WBP and micro-CT. The strong positive correlation between lung volumes from XLF and micro-CT measurements revealed XLF as a more reliable and sensitive technique than WBP which showed a poor correlation with micro-CT based lung volumes. Overall, radiographic low dose XLF measurement allows short acquisition times, longitudinal and non-invasive analysis of functional and volumetric parameters in mice that can be implemented for the evaluation of a variety of disease related mouse models. These advantages highlight the substantial potential of XLF for clinical translation. It is also expected that this novel and biomedically relevant XLF imaging technique will improve the assessment of airway remodeling and tissue stiffness in fibrotic lungs in small animal models. Moreover, it can be potentially applied for longitudinally monitoring the response to treatment with antifibrotic compounds in mouse model of lung fibrosis in future studies.

Appendix

Introduction

Proof of concept for the assessment of lung fibrosis and treatment response using XLF

Idiopathic pulmonary fibrosis (IPF) is a chronic progressive, incurable, and debilitating disease with a median survival of 3–4 years (Lederer and Martinez, 2018; Richeldi et al., 2017). The pathogenesis of IPF is associated with multiple fibrogenic pathways including fibroblast proliferation, alveolar epithelial cell injury, abnormal accumulation of extracellular matrix (ECM) proteins, and development of irreversible interstitial fibrosis (Richeldi et al., 2017; Sgalla et al., 2018). To date, there is no curable treatment for IPF. Nintedanib is one of two anti-fibrotic therapeutics available for the treatment of IPF which has been approved since 2014 (Wongkarnjana et al., 2019). Along with pirfenidone and other antacid medications, nintedanib is now recommended for the treatment of IPF by international clinical guidelines (Wuyts et al., 2020). Nintedanib is an oral tyrosine kinase inhibitor that acts as an ATP-competitive inhibitor of fibroblast growth factor receptor (FGFR)-1, vascular endothelial growth factor receptor (VEGFR)-2 and platelet-derived growth factor receptor (PDGFR)- α and β . The inhibition of (FGFR)-1, (VEGFR)-2 and (PDGFR)- α and β leads to blockage of autophosphorylation of these receptors and inhibition of signaling cascades such as the activation of lung fibroblasts, which play a significant role in the pathogenesis of IPF (Wollin et al., 2015). Furthermore, nintedanib via inhibition of (FGFR)-1 and (VEGFR)-2 promotes anti-angiogenesis which plays a key role in limiting excessive deposition of ECM and reducing small vessel density in fibroblastic foci. Uncontrolled angiogenesis in such transitional zones would result in a higher degree of fibrosis with abnormal microvascular structures. Further, in-vitro and in-vivo pre-clinical studies show nintedanib mediated downregulation of transforming growth factor (TGF)- β 1 expression, interleukin (IL)-1 β , IL-6, CXCL1/KC and tissue inhibitors of metalloproteinases, highlighting its ability as both anti-fibrotic and anti-inflammatory agent (Sheu et al., 2019; Wollin et al., 2014). However, further studies are required to confirm these findings. Nonetheless, the proven antifibrotic and anti-angiogenesis properties makes nintedanib an appealing treatment for IPF. Clinically, nintedanib significantly slows the disease progression as shown by an improved annual rate of forced vital capacity (FVC) in IPF patients

as well as reduced risk of acute aggravation, irrespective of disease severity (Wongkarnjana et al., 2019).

To test the ability of advanced x-ray based lung function (XLF) for longitudinal and sensitive assessment of lung fibrosis as well as treatment response, we performed combined XLF and micro-CT measurements in a bleomycin induced mouse model of lung fibrosis and monitored the response to nintedanib treatment using a similar approach as described in chapter 3.

Materials and Methods

Animal model of bleomycin induced lung fibrosis

Male C57Bl/6 mice (12 weeks old) purchased from Charles River Laboratories were used to generate the bleomycin induced pulmonary fibrosis. Mice were fed food and water ad libitum. All animal in-vivo procedures were performed in compliance with the guidelines of European (2010/63/EU) and German ethical laws and were approved by the administration of Lower Saxony, Germany (approval number G15.1747).

Experimental set-up

Mice were randomly divided into three groups: healthy (n = 3), untreated (n = 3) and treated (n = 4). On day 0, baseline XLF and micro-CT measurements were performed in all groups. After baseline measurements, mice belonging to the untreated and treated group were intratracheally (i.t.) administered with a single dose of 50 µl of 1.5 mg/kg bleomycin dissolved in NaCl at day 0 (BLEO-cell, STADA Pharma, GmbH) and the healthy group did not receive any i.t. treatment. On day 7, XLF and microCT were performed in all groups (i.e., 1 week after induction of fibrosis in treated and untreated groups). From day 7 onwards the treated group received a daily oral administration of the anti-fibrotic therapeutic agent, nintedanib until day 21 while untreated group received saline as vehicle. Nintedanib was dissolved in 1% of tween 80 in milliQ water at 6 mg/ml and administered at 60 mg/ kg by oral gavage. XLF and micro-CT was performed in all groups on day 14 and day 21. After XLF and micro-CT measurements mice were sacrificed for explanting the lungs for histology on day 21. (Figure 7).

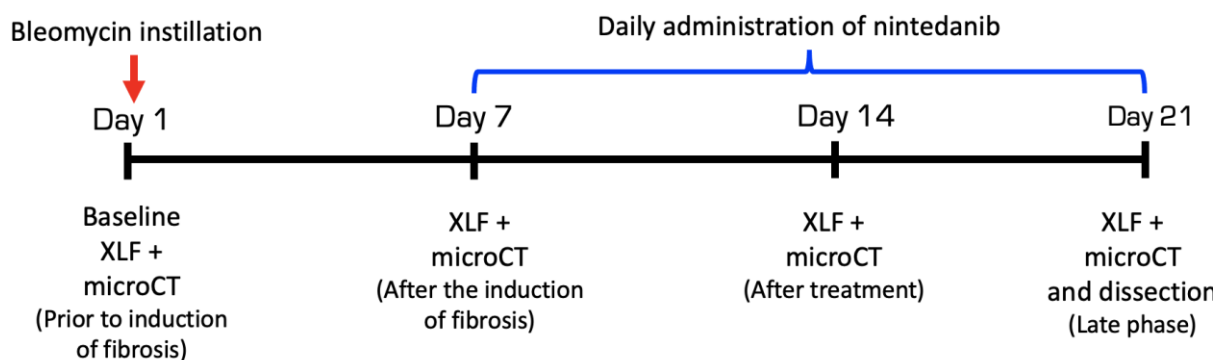


Figure 8: Experimental timeline of bleomycin induced lung fibrosis and treatment with nintedanib. Bleomycin instillation and nintedanib treatment as well as the time points of XLF and micro-CT measurements are shown for the respective days.

Micro-CT and x-ray based lung function measurements

Micro-CT and XLF measurements were performed as described in chapter 3 of this thesis.

Histological staining

The explanted lungs were inflated with a cannula through the trachea by gentle infusion with 4% paraformaldehyde, fixed for 24 h and embedded in paraffin. The paraffin-embedded lungs were cut into 2 μm sections. The sections were deparaffinized and dehydrated followed by Masson's Trichrome staining (MTS) as described before (Foot, 1933).

Results

To test the sensitivity of XLF for the assessment of lung fibrosis as well as to monitor the response to anti-fibrotic treatment using nintedanib, we performed XLF in combination with micro-CT. In healthy mice the mouse body weights remained relatively constant while the untreated and treated groups showed a decrease in body weights until day 14. However, on day 21 the nintedanib treated mice gained weight indicating signs of recovery whereas the untreated group demonstrated a loss in weight.

The baseline measurements for all groups showed similar values for micro-CT acquired lung volumes at inspiration ($V_{[\mu\text{CT}]}^{\text{insp}}$), XLF measured end-inspiratory volume ($\text{EIV}_{[\text{XLF}]}$) and decay rates at expiration (Figure 8). One week after the instillation of bleomycin, the untreated and treated groups reveal a reduction in body weights and also a strong decline in $\text{EIV}_{[\text{XLF}]}$ and

$V_{[\mu CT]}^{insp}$, whereas the healthy group had only minor changes in these parameters. On day 14, the nintedanib treated mice exhibited an increase in both $EIV_{[XLF]}$ and $V_{[\mu CT]}^{insp}$ which indicated recovery from fibrosis in these mice. In comparison, the untreated mice had a persistently low $EIV_{[XLF]}$ and $V_{[\mu CT]}^{insp}$ at day 14. However, $EIV_{[XLF]}$ did not perfectly match the $V_{[\mu CT]}^{insp}$ in the untreated group at day 14 whereby the $V_{[\mu CT]}^{insp}$ showed a higher reduction in the lung volume (Figure 8). The healthy group also showed a decline in $EIV_{[XLF]}$ and $V_{[\mu CT]}^{insp}$ at day 14 which was unexpected. At day 21, despite differences in weight distribution, the healthy and nintedanib treated groups displayed comparable $EIV_{[XLF]}$ and $V_{[\mu CT]}^{insp}$, whereas the untreated fibrotic group showed the lowest lung volumes (Figure 8).

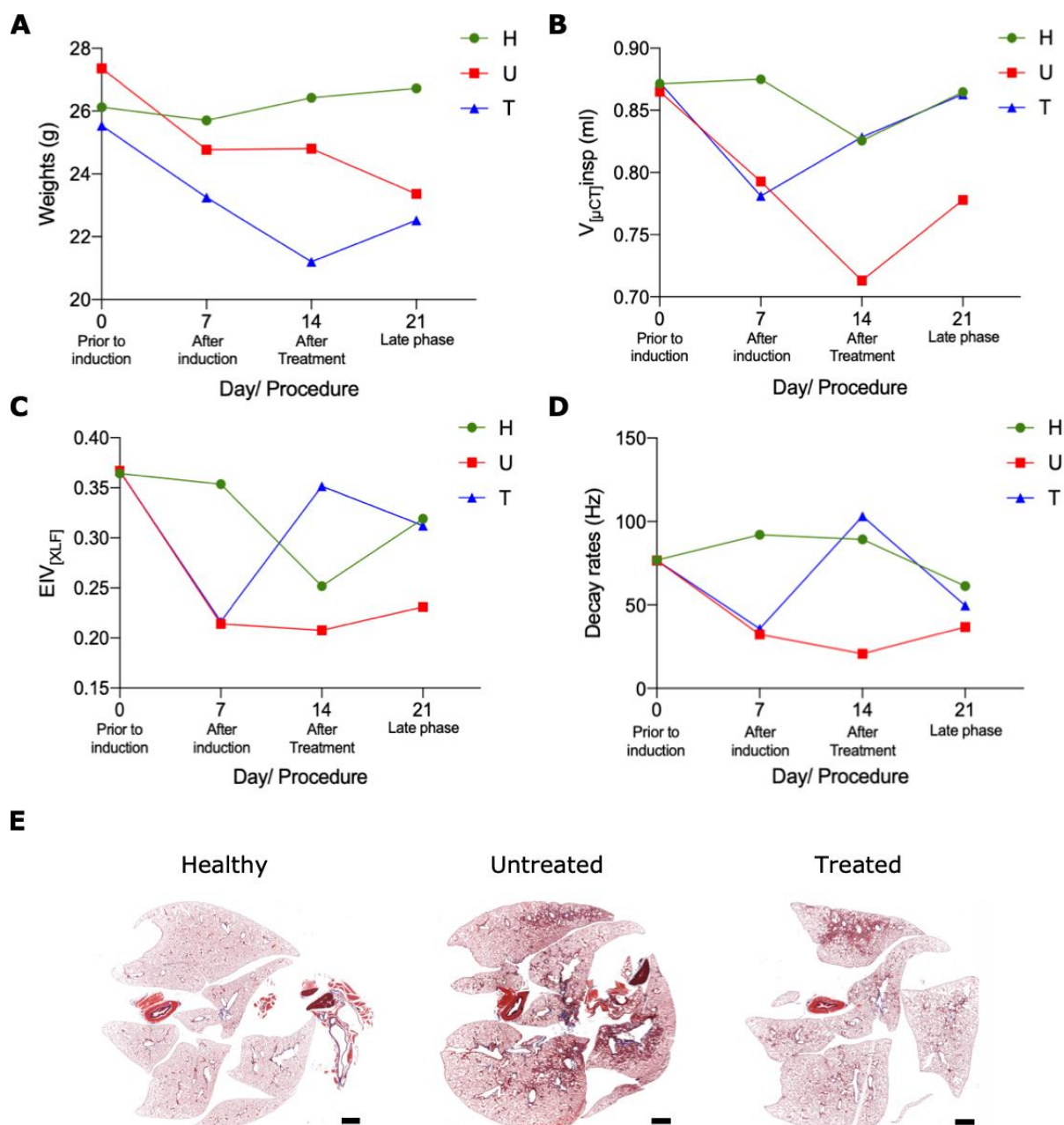


Figure 9: Micro-CT, XLF and histological assessment of healthy, untreated fibrotic and nintedanib treated mice. Graphs showing A) the weight distribution B) $V_{[\mu CT]}^{insp}$ C) $EIV_{[XLF]}$ and D) decay rates for healthy, untreated fibrotic and nintedanib treated mice for day 0 (without induction), day 7 (after bleomycin instillation and fibrosis induction in untreated and treated groups), day 14 (after treatment with nintedanib in the treated group only) and day 21 (late phase). (E) Representative MTS stainings of a paraffin slice from lungs of each group.

In addition to the volumetric measurements, XLF can also assess functional parameters such as the decay rate (τ) of the expiration phase, which reflects the elasticity of the lung tissue. In untreated mice, due to the presence of stiff fibrotic tissue, there was a decline in decay rate on

day 7 and 14. The decay rate in untreated mice by day 21 showed an increase suggesting an improvement in lung function, possibly due to initial resolution of fibrosis. In the treated group a decline in decay rate was only observed on day 7 before the application of nintedanib. However, a stark improvement in this group was observed one week after the nintedanib treatment i.e., on day 14. On day 21, the decay rate in the treated group showed a decline which slightly corresponded to the trend observed in the healthy group. In the healthy group, the decay rate did not demonstrate as many variations as the untreated and treated group. These slight alterations in the decay rates of the healthy group can be related to the effects of anesthesia.

The Masson trichome staining of the lung tissue validated these findings which revealed an evident heterogeneity in the distribution of fibrosis among various lung lobes in the untreated group. The nintedanib treated group showed minimal fibrosis deposition at a single lobe only.

Discussion and conclusion

This proof-of-concept investigation demonstrated that XLF enables the assessment of fibrosis which showed a decline in both lung volume ($EIV_{[XLF]}$) and compliance (decay rate) in the fibrotic mice. Furthermore, by exhibiting an improvement in both parameters, i.e. $EIV_{[XLF]}$ and decay rate, XLF can longitudinally and non-invasively monitor the response to nintedanib treatment.

As described in the study reported in chapter 3, micro-CT measurements were used as a gold-standard for measuring lung volumes. Our preliminary results demonstrated that in all groups the $EIV_{[XLF]}$ and $V_{[\mu CT]}^{insp}$ points correspond closely at the early phase (day 7) highlighting the sensitivity of XLF measurements to assess induction of fibrosis. It is known from previous work that intra-tracheal administration of bleomycin results in faster progression of fibrosis which decreases the gas-exchange capacity of the lung (Ruscitti et al., 2020, 2017). Furthermore, clinical studies also show a low air volume in IPF patients which is diagnosed by a reduced forced vital capacity (Casan Clarà et al., 2016). This is in line with our results, which show lower lung volumes in fibrotic mice. After the treatment with nintedanib, both $EIV_{[XLF]}$ and $V_{[\mu CT]}^{insp}$ follow a similar trend and reveal an increase in the lung volumes of the treated group. Our results further show that over time $EIV_{[XLF]}$ and $V_{[\mu CT]}^{insp}$ of the treated group corresponds to the healthy group. This finding was strengthened by ex-vivo histological assessment showing

that the nintedanib treated group had moderate fibrosis lesions in comparison to the untreated group which had multiple heterogeneously distributed fibrotic lesions in various lobes. Ruscitti et al. reported the inhibitory effects of nintedanib treatment on fibrotic progression for maintaining a higher degree of aerated lung regions, whereas the untreated mice showed a substantial decrease in aerated regions in the fibrotic lungs (Ruscitti et al., 2020).

Besides lung volumes, XLF measurements also provide functional parameters. We assess the decay rate of the expiratory phase that reflects upon lung compliance and elasticity. During the early phase prior to treatment, bleomycin treated mice show a decrease in decay rate indicating the development of fibrosis and the presence of a stiffer parenchyma. Villetti et al., by correlating micro-CT and histology showed that bleomycin induced severe fibrosis development occur as early as day seven (Villetti et al., 2016). Nintedanib treatment improves lung elasticity as indicated by our results which show an increase in decay rate for day 14. Our results also show that at day 21 the decay rate in untreated fibrotic mice tend to improve, which highlights that fibrosis in bleomycin treated mice is self-resolving. It is known for the bleomycin model that the initial inflammatory phase is followed by a peak fibrotic response which is resolved over time (B. Moore et al., 2013; Ruscitti et al., 2017).

The discrepancy in the $EIV_{[XLF]}$ and $V_{[\mu CT]}^{insp}$ values at day 14 for the untreated group and healthy mice can be due to multiple reasons including the sensitivity of XLF measurements to the mouse body weights, the image quality of micro-CT reconstructions for delineating aerated lung volumes and mainly the small sample size. Nonetheless, the overall trend of $EIV_{[XLF]}$ and $V_{[\mu CT]}^{insp}$ is comparable for all groups as presented by these preliminary findings which highlight the potential of XLF for assessment of lung fibrosis with and without treatment. Future investigations with more animals are required to confirm and also improve these findings. In conclusion, this overview demonstrates the ability of XLF to perform a functional and volumetric assessment of lung fibrosis progression and to evaluate the response to treatment. Our findings substantiate XLF as a sensitive, simple and reliable tool for the diagnosis, monitoring and treatment assessment of preclinical lung diseases.

Bibliography

- Abu-Siniyeh, A., Al-Zyoud, W., 2020. Highlights on selected microscopy techniques to study zebrafish developmental biology. *Laboratory Animal Research* 36, 12. <https://doi.org/10.1186/s42826-020-00044-2>
- Adamson, E.B., Ludwig, K.D., Mummy, D.G., Fain, S.B., 2017. Magnetic Resonance Imaging with Hyperpolarized Agents: Methods and Applications. *Phys Med Biol* 62, R81–R123. <https://doi.org/10.1088/1361-6560/aa6be8>
- Adler, A., Cieslewicz, G., Irvin, C.G., 2004. Unrestrained plethysmography is an unreliable measure of airway responsiveness in BALB/c and C57BL/6 mice. *Journal of Applied Physiology* 97, 286–292. <https://doi.org/10.1152/japplphysiol.00821.2003>
- Ahmed, T., Goyal, A., 2021. Endomyocardial Biopsy, in: StatPearls. StatPearls Publishing, Treasure Island (FL).
- Ashton, J.R., Befera, N., Clark, D., Qi, Y., Mao, L., Rockman, H.A., Johnson, G.A., Badea, C.T., 2014. Anatomical and functional imaging of myocardial infarction in mice using micro-CT and eXIA 160 contrast agent. *Contrast Media & Molecular Imaging* 9, 161–168. <https://doi.org/10.1002/cmml.1557>
- B. Moore, B., Lawson, W.E., Oury, T.D., Sisson, T.H., Raghavendran, K., Hogaboam, C.M., 2013. Animal Models of Fibrotic Lung Disease. *Am J Respir Cell Mol Biol* 49, 167–179. <https://doi.org/10.1165/rcmb.2013-0094TR>
- Backer, J.W.D., Vos, W.G., Burnell, P., Verhulst, S.L., Salmon, P., Clerck, N.D., Backer, W.D., 2009. Study of the Variability in Upper and Lower Airway Morphology in Sprague–Dawley Rats Using Modern Micro-CT Scan-Based Segmentation Techniques. *The Anatomical Record* 292, 720–727. <https://doi.org/10.1002/ar.20877>
- Bacmeister, L., Schwarzl, M., Warnke, S., Stoffers, B., Blankenberg, S., Westermann, D., Lindner, D., 2019. Inflammation and fibrosis in murine models of heart failure. Dr. Dietrich Steinkopff Verlag GmbH and Co. KG. <https://doi.org/10.1007/s00395-019-0722-5>
- Banerjee, I., Fuseler, J.W., Price, R.L., Borg, T.K., Baudino, T.A., 2007. Determination of cell types and numbers during cardiac development in the neonatal and adult rat and mouse. *American Journal of Physiology-Heart and Circulatory Physiology* 293, H1883–H1891. <https://doi.org/10.1152/ajpheart.00514.2007>
- Baues, M., Dasgupta, A., Ehling, J., Prakash, J., Boor, P., Tacke, F., Kiessling, F., Lammers, T., 2017. Fibrosis imaging: Current concepts and future directions. *Adv Drug Deliv Rev* 121, 9–26. <https://doi.org/10.1016/j.addr.2017.10.013>
- Benninger, R.K.P., Hao, M., Piston, D.W., 2008. Multi-photon excitation imaging of dynamic processes in living cells and tissues, in: *Reviews of Physiology Biochemistry and Pharmacology, Reviews of Physiology, Biochemistry and Pharmacology*. Springer, Berlin, Heidelberg, pp. 71–92. https://doi.org/10.1007/112_2008_801
- Bishop, S.P., Zhou, Y., Nakada, Y., Zhang, J., 2021. Changes in Cardiomyocyte Cell Cycle and Hypertrophic Growth During Fetal to Adult in Mammals. *JAHA* 10. <https://doi.org/10.1161/JAHA.120.017839>
- Bonnardel, E., Prevel, R., Campagnac, M., Dubreuil, M., Marthan, R., Berger, P., Dupin, I., 2019. Determination of reliable lung function parameters in intubated mice. *Respiratory Research* 20, 211. <https://doi.org/10.1186/s12931-019-1177-9>

- Bujak, M., Frangogiannis, N.G., 2007. The role of TGF- β signaling in myocardial infarction and cardiac remodeling. *Cardiovascular Research* 74, 184–195. <https://doi.org/10.1016/j.cardiores.2006.10.002>
- Casan Clarà, P., Martínez González, C., Ancochea, J., 2016. Lung Function Testing in Idiopathic Pulmonary Fibrosis: More Than Just Spirometry? *Arch Bronconeumol* 52, 457–458. <https://doi.org/10.1016/j.arbr.2016.07.009>
- Cazorla, O., Wu, Y., Irving, T.C., Granzier, H., 2001. Titin-based modulation of calcium sensitivity of active tension in mouse skinned cardiac myocytes. *Circ Res* 88, 1028–1035. <https://doi.org/10.1161/hh1001.090876>
- Checa, J., Aran, J.M., 2020. <p>Reactive Oxygen Species: Drivers of Physiological and Pathological Processes</p>. *JIR* 13, 1057–1073. <https://doi.org/10.2147/JIR.S275595>
- Chen, D.L., Schiebler, M.L., Goo, J.M., van Beek, E.J.R., 2017. PET imaging approaches for inflammatory lung diseases: Current concepts and future directions. *Eur J Radiol* 86, 371–376. <https://doi.org/10.1016/j.ejrad.2016.09.014>
- Chien, Y.-F., Lin, J.-Y., Yeh, P.-T., Hsu, K.-J., Tsai, Y.-H., Chen, S.-K., Chu, S.-W., 2020. Dual GRIN lens two-photon endoscopy for high-speed volumetric and deep brain imaging. *bioRxiv* 2020.09.19.304675. <https://doi.org/10.1101/2020.09.19.304675>
- Chinwalla, A.T., Cook, L.L., Delehaunty, K.D., Fewell, G.A., Fulton, L.A., Fulton, R.S., Graves, T.A., Hillier, L.W., Mardis, E.R., McPherson, J.D., Miner, T.L., Nash, W.E., Nelson, J.O., Nhan, M.N., Pepin, K.H., Pohl, C.S., Ponce, T.C., Schultz, B., Thompson, J., Trevaskis, E., Waterston, R.H., Wendl, M.C., Wilson, R.K., Yang, S.-P., An, P., Berry, E., Birren, B., Bloom, T., Brown, D.G., Butler, J., Daly, M., David, R., Deri, J., Dodge, S., Foley, K., Gage, D., Gnerre, S., Holzer, T., Jaffe, D.B., Kamal, M., Karlsson, E.K., Kells, C., Kirby, A., Kulbokas, E.J., Lander, E.S., Landers, T., Leger, J.P., Levine, R., Lindblad-Toh, K., Mauceli, E., Mayer, J.H., McCarthy, M., Meldrim, J., Meldrim, J., Mesirov, J.P., Nicol, R., Nusbaum, C., Seaman, S., Sharpe, T., Sheridan, A., Singer, J.B., Santos, R., Spencer, B., Stange-Thomann, N., Vinson, J.P., Wade, C.M., Wierzbowski, J., Wyman, D., Zody, M.C., Birney, E., Goldman, N., Kasprzyk, A., Mongin, E., Rust, A.G., Slater, G., Stabenau, A., Ureta-Vidal, A., Whelan, S., Ainscough, R., Attwood, J., Bailey, J., Barlow, K., Beck, S., Burton, J., Clamp, M., Clee, C., Coulson, A., Cuff, J., Curwen, V., Cutts, T., Davies, J., Eyra, E., Grafham, D., Gregory, S., Hubbard, T., Hunt, A., Jones, M., Joy, A., Leonard, S., Lloyd, C., Matthews, L., McLaren, S., McLay, K., Meredith, B., Mullikin, J.C., Ning, Z., Oliver, K., Overton-Larty, E., Plumb, R., Potter, S., Quail, M., Rogers, J., Scott, C., Searle, S., Shownkeen, R., Sims, S., Wall, M., West, A.P., Willey, D., Williams, S., Abril, J.F., Guigó, R., Parra, G., Agarwal, P., Agarwala, R., Church, D.M., Hlavina, W., Maglott, D.R., Sapozhnikov, V., Alexandersson, M., Pachter, L., Antonarakis, S.E., Dermitzakis, E.T., Reymond, A., Ucla, C., Baertsch, R., Diekhans, M., Furey, T.S., Hinrichs, A., Hsu, F., Karolchik, D., Kent, W.J., Roskin, K.M., Schwartz, M.S., Sugnet, C., Weber, R.J., Bork, P., Letunic, I., Suyama, M., Torrents, D., Zdobnov, E.M., Botcherby, M., Brown, S.D., Campbell, R.D., Jackson, I., Bray, N., Couronne, O., Dubchak, I., Poliakov, A., Rubin, E.M., Brent, M.R., Flicek, P., Keibler, E., Korf, I., Batalov, S., Bult, C., Frankel, W.N., Carninci, P., Hayashizaki, Y., Kawai, J., Okazaki, Y., Cawley, S., Kulp, D., Wheeler, R., Chiaromonte, F., Collins, F.S., Felsenfeld, A., Guyer, M., Peterson, J., Wetterstrand, K., Copley, R.R., Mott, R., Dewey, C., Dickens, N.J., Emes, R.D., Goodstadt, L., Ponting, C.P., Winter, E., Dunn, D.M., von Niederhausern, A.C., Weiss, R.B., Eddy, S.R., Johnson, L.S., Jones, T.A., Elnitski, L., Kolbe, D.L., Eswara, P., Miller, W., O'Connor, M.J.,

- Schwartz, S., Gibbs, R.A., Muzny, D.M., Glusman, G., Smit, A., Green, E.D., Hardison, R.C., Yang, S., Haussler, D., Hua, A., Roe, B.A., Kucherlapati, R.S., Montgomery, K.T., Li, J., Li, M., Lucas, S., Ma, B., McCombie, W.R., Morgan, M., Pevzner, P., Tesler, G., Schultz, J., Smith, D.R., Tromp, J., Worley, K.C., Lander, E.S., Abril, J.F., Agarwal, P., Alexandersson, M., Antonarakis, S.E., Baertsch, R., Berry, E., Birney, E., Bork, P., Bray, N., Brent, M.R., Brown, D.G., Butler, J., Bult, C., Chiaromonte, F., Chinwalla, A.T., Church, D.M., Clamp, M., Collins, F.S., Copley, R.R., Couronne, O., Cawley, S., Cuff, J., Curwen, V., Cutts, T., Daly, M., Dermitzakis, E.T., Dewey, C., Mouse Genome Sequencing Consortium, Genome Sequencing Center:, Whitehead Institute/MIT Center for Genome Research:, European Bioinformatics Institute:, Wellcome Trust Sanger Institute, Research Group in Biomedical Informatics, Bioinformatics, National Center for Biotechnology Information, Department of Mathematics, Division of Medical Genetics, Center for Biomolecular Science and Engineering, EMBL, UK MRC Mouse Sequencing Consortium, Lawrence Berkeley National Laboratory, Department of Computer Science, School of Computer Science, The Jackson Laboratory, Laboratory for Genome Exploration, Affymetrix Inc., Departments of Statistics and Health Evaluation Sciences, National Human Genome Research Institute, Wellcome Trust Centre for Human Genetics, Department of Electrical Engineering, Department of Human Anatomy and Genetics, Department of Human Genetics, Howard Hughes Medical Institute and Department of Genetics, Departments of Biochemistry and Molecular Biology and Computer Science and Engineering, Department of Computer Science and Engineering, Baylor College of Medicine, The Institute for Systems Biology, Department of Biochemistry and Molecular Biology, Howard Hughes Medical Institute, Department of Chemistry and Biochemistry, Departments of Genetics and Medicine and Harvard-Partners Center for Genetics and Genomics, Department of Statistics, US DOE Joint Genome Institute, Cold Spring Harbor Laboratory, Wellcome Trust, Max Planck Institute for Molecular Genetics, Genome Therapeutics Corporation, Bioinformatics Solutions Inc., Department of Molecular and Human Genetics, Department of Biology, Members of the Mouse Genome Analysis Group, 2002. Initial sequencing and comparative analysis of the mouse genome. *Nature* 420, 520–562. <https://doi.org/10.1038/nature01262>
- Chopra, A., Kutys, M.L., Zhang, K., Polacheck, W.J., Sheng, C.C., Luu, R.J., Eyckmans, J., Hinson, J.T., Seidman, J.G., Seidman, C.E., Chen, C.S., 2018. Force generation via β -cardiac myosin, titin, and α -actinin drives cardiac sarcomere assembly from cell-matrix adhesions. *Dev Cell* 44, 87–96.e5. <https://doi.org/10.1016/j.devcel.2017.12.012>
- Cooper, L.T., Baughman, K.L., Feldman, A.M., Frustaci, A., Jessup, M., Kuhl, U., Levine, G.N., Narula, J., Starling, R.C., Towbin, J., Virmani, R., American Heart Association, American College of Cardiology, European Society of Cardiology, Heart Failure Society of America, Heart Failure Association of the European Society of Cardiology, 2007. The role of endomyocardial biopsy in the management of cardiovascular disease: a scientific statement from the American Heart Association, the American College of Cardiology, and the European Society of Cardiology. Endorsed by the Heart Failure Society of America and the Heart Failure Association of the European Society of Cardiology. *J Am Coll Cardiol* 50, 1914–1931. <https://doi.org/10.1016/j.jacc.2007.09.008>

- Darby, I.A., Hewitson, T.D., 2007. Fibroblast Differentiation in Wound Healing and Fibrosis, in: *International Review of Cytology*. Academic Press, pp. 143–179.
[https://doi.org/10.1016/S0074-7696\(07\)57004-X](https://doi.org/10.1016/S0074-7696(07)57004-X)
- Denk, W., Strickler, J.H., Webb, W.W., 1990. Two-photon laser scanning fluorescence microscopy. *Science* 248, 73–76. <https://doi.org/10.1126/science.2321027>
- Dewey, M., Siebes, M., Kachelrieß, M., Kofoed, K.F., Maurovich-Horvat, P., Nikolaou, K., Bai, W., Kofler, A., Manka, R., Kozerke, S., Chiribiri, A., Schaeffter, T., Michallek, F., Bengel, F., Nekolla, S., Knaapen, P., Lubberink, M., Senior, R., Tang, M.-X., Piek, J.J., van de Hoef, T., Martens, J., Schreiber, L., 2020. Clinical quantitative cardiac imaging for the assessment of myocardial ischaemia. *Nature Reviews Cardiology* 17, 427–450. <https://doi.org/10.1038/s41569-020-0341-8>
- Dimitrow, E., Ziemer, M., Koehler, M.J., Norgauer, J., König, K., Elsner, P., Kaatz, M., 2009. Sensitivity and Specificity of Multiphoton Laser Tomography for In Vivo and Ex Vivo Diagnosis of Malignant Melanoma. *J Invest Dermatol* 129, 1752–1758.
<https://doi.org/10.1038/jid.2008.439>
- Distler, J.H.W., Györfi, A.-H., Ramanujam, M., Whitfield, M.L., Königshoff, M., Lafyatis, R., 2019. Shared and distinct mechanisms of fibrosis. *Nature Reviews Rheumatology* 15, 705–730. <https://doi.org/10.1038/s41584-019-0322-7>
- Ducourthial, G., Leclerc, P., Mansuryan, T., Fabert, M., Brevier, J., Habert, R., Braud, F., Batrin, R., Vever-Bizet, C., Bourg-Heckly, G., Thiberville, L., Druilhe, A., Kudlinski, A., Louradour, F., 2015. Development of a real-time flexible multiphoton microendoscope for label-free imaging in a live animal. *Scientific Reports* 5, 18303.
<https://doi.org/10.1038/srep18303>
- Dullin, C., Markus, M.A., Larsson, E., Tromba, G., Hülsmann, S., Alves, F., 2016. X-Ray based Lung Function measurement—a sensitive technique to quantify lung function in allergic airway inflammation mouse models. *Sci Rep* 6.
<https://doi.org/10.1038/srep36297>
- Enhörning, G., Schaik, S. van, Lundgren, C., Vargas, I., 1998. Whole-body plethysmography, does it measure tidal volume of small animals? *Can. J. Physiol. Pharmacol.* 76, 945–951. <https://doi.org/10.1139/y99-002>
- Everett, R.J., Stirrat, C.G., Semple, S.I.R., Newby, D.E., Dweck, M.R., Mirsadraee, S., 2016. Assessment of myocardial fibrosis with T1 mapping MRI. *Clinical Radiology* 71, 768–778. <https://doi.org/10.1016/j.crad.2016.02.013>
- Fares, E., Howlett, S.E., 2010. Effect of age on cardiac excitation–contraction coupling. *Clinical and Experimental Pharmacology and Physiology* 37, 1–7.
<https://doi.org/10.1111/j.1440-1681.2009.05276.x>
- Foot, N.C., 1933. The Masson Trichrome Staining Methods in Routine Laboratory Use. *Stain Technology* 8, 101–110. <https://doi.org/10.3109/10520293309116112>
- Fouras, A., Shiao, S., Wenger, D., Winnett, A., Doshi, C., Carnibella, R., Shah, P., Jamison, R., DeMarco, J., Martin, C., Dusting, J., Vij, N., Fouras, A., 2019. NOVEL X-RAY VELOCIMETRY-BASED QUANTITATIVE REGIONAL LUNG FUNCTION ANALYSIS TO ASSESS RISK OF RADIATION-INDUCED PNEUMONITIS AND PULMONARY FIBROSIS. *Chest* 156, A2264–A2265.
<https://doi.org/10.1016/j.chest.2019.08.315>
- Frangogiannis, N.G., 2019. Cardiac fibrosis: Cell biological mechanisms, molecular pathways and therapeutic opportunities. *Mol Aspects Med* 65, 70–99.
<https://doi.org/10.1016/j.mam.2018.07.001>

- Friedl, P., Wolf, K., Harms, G., Andrian, U.H. von, 2007. Biological Second and Third Harmonic Generation Microscopy. *Current Protocols in Cell Biology* 34, 4.15.1-4.15.21. <https://doi.org/10.1002/0471143030.cb0415s34>
- Friedman, S.L., Sheppard, D., Duffield, J.S., Violette, S., 2013. Therapy for Fibrotic Diseases: Nearing the Starting Line. *Science Translational Medicine* 5, 167sr1-167sr1. <https://doi.org/10.1126/scitranslmed.3004700>
- Fu, L., Gu, M., 2007. Fibre-optic nonlinear optical microscopy and endoscopy. *Journal of Microscopy* 226, 195–206. <https://doi.org/10.1111/j.1365-2818.2007.01777.x>
- Gammon, S.T., Foje, N., Brewer, E.M., Owers, E., Downs, C.A., Budde, M.D., Leevy, W.M., Helms, M.N., 2014. Preclinical anatomical, molecular, and functional imaging of the lung with multiple modalities. *American Journal of Physiology-Lung Cellular and Molecular Physiology* 306, L897–L914. <https://doi.org/10.1152/ajplung.00007.2014>
- Green, N.H., Delaine-Smith, R.M., Askew, H.J., Byers, R., Reilly, G.C., Matcher, S.J., 2017. A new mode of contrast in biological second harmonic generation microscopy. *Scientific Reports* 7. <https://doi.org/10.1038/s41598-017-13752-y>
- Greenhalgh, C., Prent, N., Green, C., Cisek, R., Major, A., Stewart, B., Barzda, V., 2007. Influence of semicrystalline order on the second-harmonic generation efficiency in the anisotropic bands of myocytes. *Appl. Opt.* 46, 1852. <https://doi.org/10.1364/AO.46.001852>
- Guo Yuxuan, Pu William T., 2020. Cardiomyocyte Maturation. *Circulation Research* 126, 1086–1106. <https://doi.org/10.1161/CIRCRESAHA.119.315862>
- Gyöngyösi, M., Winkler, J., Ramos, I., Do, Q.-T., Firat, H., McDonald, K., González, A., Thum, T., Díez, J., Jaisser, F., Pizard, A., Zannad, F., 2017. Myocardial fibrosis: biomedical research from bench to bedside. *European Journal of Heart Failure* 19, 177–191. <https://doi.org/10.1002/ejhf.696>
- Haaf, P., Garg, P., Messroghli, D.R., Broadbent, D.A., Greenwood, J.P., Plein, S., 2016. Cardiac T1 Mapping and Extracellular Volume (ECV) in clinical practice: a comprehensive review. *Journal of Cardiovascular Magnetic Resonance* 18, 89. <https://doi.org/10.1186/s12968-016-0308-4>
- Hall Caitlin, Gehmlich Katja, Denning Chris, Pavlovic Davor, 2021. Complex Relationship Between Cardiac Fibroblasts and Cardiomyocytes in Health and Disease. *Journal of the American Heart Association* 10, e019338. <https://doi.org/10.1161/JAHA.120.019338>
- Hano, O., Bogdanov, K.Y., Sakai, M., Danziger, R.G., Spurgeon, H.A., Lakatta, E.G., 1995. Reduced threshold for myocardial cell calcium intolerance in the rat heart with aging. *American Journal of Physiology-Heart and Circulatory Physiology* 269, H1607–H1612. <https://doi.org/10.1152/ajpheart.1995.269.5.H1607>
- Haselgrove, J.C., Huxley, H.E., 1973. X-ray evidence for radial cross-bridge movement and for the sliding filament model in actively contracting skeletal muscle. *Journal of Molecular Biology* 77, 549–568. [https://doi.org/10.1016/0022-2836\(73\)90222-2](https://doi.org/10.1016/0022-2836(73)90222-2)
- Hassan, S., Barrett, C.J., Crossman, D.J., 2020. Imaging tools for assessment of myocardial fibrosis in humans: the need for greater detail. *Biophys Rev* 12, 969–987. <https://doi.org/10.1007/s12551-020-00738-w>
- Henderson, N.C., Rieder, F., Wynn, T.A., 2020. Fibrosis: from mechanisms to medicines. *Nature* 587, 555–566. <https://doi.org/10.1038/s41586-020-2938-9>
- Horowitz, J.C., Thannickal, V.J., 2018. Mechanisms for the Resolution of Organ Fibrosis. *Physiology* 34, 43–55. <https://doi.org/10.1152/physiol.00033.2018>

- Hortells, L., Valiente-Alandi, I., Thomas, Z.M., Agnew, E.J., Schnell, D.J., York, A.J., Vagnozzi, R.J., Meyer, E.C., Molkentin, J.D., Yutzey, K.E., 2020. A specialized population of Periostin-expressing cardiac fibroblasts contributes to postnatal cardiomyocyte maturation and innervation. *PNAS* 117, 21469–21479. <https://doi.org/10.1073/pnas.2009119117>
- Hülsmann, S., Khan, A., Hagos, L., Hindermann, M., Nägel, T., Dullin, C., 2021. Whole-body plethysmography revisited. *bioRxiv* 2021.02.24.432470. <https://doi.org/10.1101/2021.02.24.432470>
- Huxley, H.E., Brown, W., Holmes, K.C., 1965. Constancy of axial spacings in frog sartorius muscle during contraction. *Nature* 206, 1358. <https://doi.org/10.1038/2061358a0>
- Ivankovic, I., Déan-Ben, X.L., Haas, H., Kimm, M.A., Wildgruber, M., Razansky, D., 2020. Volumetric Optoacoustic Tomography Differentiates Myocardial Remodelling. *Mol Imaging Biol* 22, 1235–1243. <https://doi.org/10.1007/s11307-020-01498-5>
- Karlas, A., Fasoula, N.-A., Paul-Yuan, K., Reber, J., Kallmayer, M., Bozhko, D., Seeger, M., Eckstein, H.-H., Wildgruber, M., Ntziachristos, V., 2019. Cardiovascular optoacoustics: From mice to men – A review. *Photoacoustics* 14, 19–30. <https://doi.org/10.1016/j.pacs.2019.03.001>
- Karsdal, M.A., Nielsen, S.H., Leeming, D.J., Langholm, L.L., Nielsen, M.J., Manon-Jensen, T., Siebuhr, A., Gudmann, N.S., Rønnow, S., Sand, J.M., Daniels, S.J., Mortensen, J.H., Schuppan, D., 2017. The good and the bad collagens of fibrosis – Their role in signaling and organ function. *Advanced Drug Delivery Reviews, Fibroblasts and extracellular matrix: Targeting and therapeutic tools in fibrosis and cancer* 121, 43–56. <https://doi.org/10.1016/j.addr.2017.07.014>
- Kellman, P., Arai, A.E., McVeigh, E.R., Aletras, A.H., 2002. Phase-Sensitive Inversion Recovery for Detecting Myocardial Infarction Using Gadolinium-Delayed Hyperenhancement. *Magn Reson Med* 47, 372–383.
- Kohl, T., Westphal, V., Hell, S.W., Lehnart, S.E., 2013. Superresolution microscopy in heart — Cardiac nanoscopy. *Journal of Molecular and Cellular Cardiology, Calcium Signaling in Heart* 58, 13–21. <https://doi.org/10.1016/j.yjmcc.2012.11.016>
- Konhilas, J.P., Irving, T.C., de Tombe, P.P., 2002. Myofilament calcium sensitivity in skinned rat cardiac trabeculae: role of interfilament spacing. *Circ Res* 90, 59–65. <https://doi.org/10.1161/hh0102.102269>
- Kruger, S.J., Nagle, S.K., Couch, M.J., Ohno, Y., Albert, M., Fain, S.B., 2016. Functional Imaging of the Lungs with Gas Agents. *J Magn Reson Imaging* 43, 295–315. <https://doi.org/10.1002/jmri.25002>
- Landry, N.M., Cohen, S., Dixon, I.M.C., 2017. Periostin in cardiovascular disease and development: a tale of two distinct roles. *Basic Res Cardiol* 113, 1. <https://doi.org/10.1007/s00395-017-0659-5>
- Lederer, D.J., Martinez, F.J., 2018. Idiopathic Pulmonary Fibrosis. *New England Journal of Medicine*. <https://doi.org/10.1056/NEJMr1705751>
- Li, Q., Liu, X., Wei, J., 2014. Ageing related periostin expression increase from cardiac fibroblasts promotes cardiomyocytes senescent. *Biochemical and Biophysical Research Communications* 452, 497–502. <https://doi.org/10.1016/j.bbrc.2014.08.109>
- Lim, R., Zavou, M.J., Milton, P.-L., Chan, S.T., Tan, J.L., Dickinson, H., Murphy, S.V., Jenkin, G., Wallace, E.M., 2014. Measuring Respiratory Function in Mice Using Unrestrained Whole-body Plethysmography. *JoVE* 51755. <https://doi.org/10.3791/51755>

- Lima, J.A.C., 2017. The Aging Human Heart. *Circ Cardiovasc Imaging* 10. <https://doi.org/10.1161/CIRCIMAGING.116.005899>
- Liu, H., Qin, W., Shao, Y., Ma, Z., Ye, T., Borg, T., Gao, B.Z., 2011. Myofibrillogenesis in live neonatal cardiomyocytes observed with hybrid two-photon excitation fluorescence-second harmonic generation microscopy. *J Biomed Opt* 16. <https://doi.org/10.1117/1.3662457>
- Liu, J., 2015. Two-photon microscopy in pre-clinical and clinical cancer research. *Front. Optoelectron.* 8, 141–151. <https://doi.org/10.1007/s12200-014-0415-5>
- Llewellyn, M.E., Barretto, R.P.J., Delp, S.L., Schnitzer, M.J., 2008. Minimally invasive high-speed imaging of sarcomere contractile dynamics in mice and humans. *Nature* 454, 784–788. <https://doi.org/10.1038/nature07104>
- Lonzezzetti, L., Zanon, M., Pacini, G.S., Altmayer, S., Oliveira, D.M. de, Rubin, A.S., Gazzoni, F.F., Barros, M.C., Hochegger, B., 2019. Magnetic resonance imaging of interstitial lung diseases: A state-of-the-art review. *Respiratory Medicine* 155, 79–85. <https://doi.org/10.1016/j.rmed.2019.07.006>
- Lopez, A.L., Larina, I.V., 2019. Second harmonic generation microscopy of early embryonic mouse hearts. *Biomedical Optics Express* 10, 2898. <https://doi.org/10.1364/boe.10.002898>
- Lovric, G., Mokso, R., Arcadu, F., Vogiatzis Oikonomidis, I., Schittny, J.C., Roth-Kleiner, M., Stampanoni, M., 2017. Tomographic in vivo microscopy for the study of lung physiology at the alveolar level. *Scientific Reports* 7, 12545. <https://doi.org/10.1038/s41598-017-12886-3>
- Lu, L., Guo, J., Hua, Y., Huang, K., Magaye, R., Cornell, J., Kelly, D.J., Reid, C., Liew, D., Zhou, Y., Chen, A., Xiao, W., Fu, Q., Wang, B.H., 2017. Cardiac fibrosis in the ageing heart: Contributors and mechanisms. *Clinical and Experimental Pharmacology and Physiology* 44, 55–63. <https://doi.org/10.1111/1440-1681.12753>
- Lundblad, L.K.A., Irvin, C.G., Adler, A., Bates, J.H.T., 2002. A reevaluation of the validity of unrestrained plethysmography in mice. *Journal of Applied Physiology* 93, 1198–1207. <https://doi.org/10.1152/japplphysiol.00080.2002>
- Lynch, J.P., Belperio, J.A., 2011. Idiopathic Pulmonary Fibrosis. *Diffuse Lung Disease* 171–194. https://doi.org/10.1007/978-1-4419-9771-5_10
- Ma, Z.-G., Yuan, Y.-P., Wu, H.-M., Zhang, X., Tang, Q.-Z., 2018. Cardiac fibrosis: new insights into the pathogenesis. *Int. J. Biol. Sci.* 14, 1645–1657. <https://doi.org/10.7150/ijbs.28103>
- Markus, M.A., Borowik, S., Reichardt, M., Tromba, G., Alves, F., Dullin, C., 2017. X-ray-based lung function measurement reveals persistent loss of lung tissue elasticity in mice recovered from allergic airway inflammation. *Am J Physiol Lung Cell Mol Physiol* 313, L763–L771. <https://doi.org/10.1152/ajplung.00136.2017>
- Mathieson, J.R., Mayo, J.R., Staples, C.A., Müller, N.L., 1989. Chronic diffuse infiltrative lung disease: comparison of diagnostic accuracy of CT and chest radiography. *Radiology* 171, 111–116. <https://doi.org/10.1148/radiology.171.1.2928513>
- Matsubara, I., Maughan, D.W., Saeki, Y., Yagi, N., 1989. Cross-bridge movement in rat cardiac muscle as a function of calcium concentration. *J Physiol* 417, 555–565.
- Matsubara, I., Suga, H., Yagi, N., 1977. An X-ray diffraction study of the cross-circulated canine heart. *J Physiol* 270, 311–320.
- Matsubara, I., Yagi, N., Endoh, M., 1978. Behaviour of myosin projections during the staircase phenomenon of heart muscle. *Nature* 273, 67–67. <https://doi.org/10.1038/273067a0>

- Matsuura, R., Miyagawa, S., Fukushima, S., Goto, T., Harada, A., Shimozaki, Y., Yamaki, K., Sanami, S., Kikuta, J., Ishii, M., Sawa, Y., 2018a. Intravital imaging with two-photon microscopy reveals cellular dynamics in the ischemia-reperfused rat heart. *Sci Rep* 8. <https://doi.org/10.1038/s41598-018-34295-w>
- Matsuura, R., Miyagawa, S., Fukushima, S., Goto, T., Harada, A., Shimozaki, Y., Yamaki, K., Sanami, S., Kikuta, J., Ishii, M., Sawa, Y., 2018b. Intravital imaging with two-photon microscopy reveals cellular dynamics in the ischemia-reperfused rat heart. *Scientific Reports* 8, 15991. <https://doi.org/10.1038/s41598-018-34295-w>
- McGovern, T.K., Robichaud, A., Fereydoonzad, L., Schuessler, T.F., Martin, J.G., 2013. Evaluation of respiratory system mechanics in mice using the forced oscillation technique. *J Vis Exp* e50172. <https://doi.org/10.3791/50172>
- Meschiari, C.A., Ero, O.K., Pan, H., Finkel, T., Lindsey, M.L., 2017. The impact of aging on cardiac extracellular matrix. *GeroScience* 39, 7–18. <https://doi.org/10.1007/s11357-017-9959-9>
- Mewton, N., Liu, C.Y., Croisille, P., Bluemke, D., Lima, J.A.C., 2011. Assessment of myocardial fibrosis with cardiovascular magnetic resonance. *J Am Coll Cardiol* 57, 891–903. <https://doi.org/10.1016/j.jacc.2010.11.013>
- Miller, G.W., Mugler, J.P., Sá, R.C., Altes, T.A., Prisk, G.K., Hopkins, S.R., 2014. Advances in functional and structural imaging of the human lung using proton MRI. *NMR in Biomedicine* 27, 1542–1556. <https://doi.org/10.1002/nbm.3156>
- Moharram, M.A., Lamberts, R.R., Whalley, G., Williams, M.J.A., Coffey, S., 2019. Myocardial tissue characterisation using echocardiographic deformation imaging. *Cardiovasc Ultrasound* 17. <https://doi.org/10.1186/s12947-019-0176-9>
- Mollova, M., Bersell, K., Walsh, S., Savla, J., Das, L.T., Park, S.-Y., Silberstein, L.E., Remedios, C.G. dos, Graham, D., Colan, S., Kühn, B., 2013. Cardiomyocyte proliferation contributes to heart growth in young humans. *PNAS* 110, 1446–1451. <https://doi.org/10.1073/pnas.1214608110>
- Montesi, S.B., Désogère, P., Fuchs, B.C., Caravan, P., 2019 Molecular imaging of fibrosis: recent advances and future directions. *J Clin Invest* 129, 24–33. <https://doi.org/10.1172/JCI122132>
- Moussavi, A., Mietsch, M., Drummer, C., Behr, R., Mylius, J., Boretius, S., 2020. Cardiac MRI in common marmosets revealing age-dependency of cardiac function. *Sci Rep* 10. <https://doi.org/10.1038/s41598-020-67157-5>
- Murrie, R.P., Werdiger, F., Donnelley, M., Lin, Y., Carnibella, R.P., Samarage, C.R., Pinar, I., Preissner, M., Wang, J., Li, J., Morgan, K.S., Parsons, D.W., Dubsky, S., Fouras, A., 2020. Real-time in vivo imaging of regional lung function in a mouse model of cystic fibrosis on a laboratory X-ray source. *Sci Rep* 10. <https://doi.org/10.1038/s41598-019-57376-w>
- Nguyen, T.P., Qu, Z., Weiss, J.N., 2014. Cardiac Fibrosis and Arrhythmogenesis: The Road to Repair is Paved with Perils. *J Mol Cell Cardiol* 0, 83–91. <https://doi.org/10.1016/j.yjmcc.2013.10.018>
- Nicolas, J.-D., Aeffner, S., Salditt, T., 2019. Radiation damage studies in cardiac muscle cells and tissue using microfocused X-ray beams: experiment and simulation. *J Synchrotron Rad* 26, 980–990. <https://doi.org/10.1107/S1600577519006817>
- Nicolas, J.D., Bernhardt, M., Markus, A., Alves, F., Burghammer, M., Salditt, T., 2017. Scanning X-ray diffraction on cardiac tissue: Automatized data analysis and processing. *Journal of Synchrotron Radiation* 24, 1163–1172. <https://doi.org/10.1107/S1600577517011936>

- Nicolas, J.D., Bernhardt, M., Schlick, S.F., Tiburcy, M., Zimmermann, W.H., Khan, A., Markus, A., Alves, F., Toischer, K., Salditt, T., 2019. X-ray diffraction imaging of cardiac cells and tissue. *Progress in Biophysics and Molecular Biology* 144, 151–165. <https://doi.org/10.1016/j.pbiomolbio.2018.05.012>
- Obas, V., Vasan, R.S., 2018. The aging heart. *Clinical Science* 132, 1367–1382. <https://doi.org/10.1042/CS20171156>
- Paoli, J., Smedh, M., Ericson, M.B., 2009. Multiphoton laser scanning microscopy--a novel diagnostic method for superficial skin cancers. *Semin Cutan Med Surg* 28, 190–195. <https://doi.org/10.1016/j.sder.2009.06.007>
- Patel, M.C., Levin, D.C., Parker, L., Rao, V.M., 2015. Have CT and MR Angiography Replaced Catheter Angiography in Diagnosing Peripheral Arterial Disease? *Journal of the American College of Radiology* 12, 909–914. <https://doi.org/10.1016/j.jacr.2015.04.020>
- Patten, R.D., Hall-Porter, M.R., 2009. Small Animal Models of Heart Failure: Development of Novel Therapies, Past and Present. *Circ Heart Fail* 2, 138–144. <https://doi.org/10.1161/CIRCHEARTFAILURE.108.839761>
- Perry, S.W., Burke, R.M., Brown, E.B., 2012. Two-Photon and Second Harmonic Microscopy in Clinical and Translational Cancer Research. *Ann Biomed Eng* 40, 277–291. <https://doi.org/10.1007/s10439-012-0512-9>
- Plotnikov, S.V., Millard, A.C., Campagnola, P.J., Mohler, W.A., 2006. Characterization of the Myosin-Based Source for Second-Harmonic Generation from Muscle Sarcomeres. *Biophysical Journal* 90, 693–703. <https://doi.org/10.1529/biophysj.105.071555>
- Prondzynski, M., Lemoine, M.D., Zech, A.T., Horváth, A., Di Mauro, V., Koivumäki, J.T., Kresin, N., Busch, J., Krause, T., Krämer, E., Schlossarek, S., Spohn, M., Friedrich, F.W., Münch, J., Laufer, S.D., Redwood, C., Volk, A.E., Hansen, A., Mearini, G., Catalucci, D., Meyer, C., Christ, T., Patten, M., Eschenhagen, T., Carrier, L., 2019. Disease modeling of a mutation in α -actinin 2 guides clinical therapy in hypertrophic cardiomyopathy. *EMBO Molecular Medicine* 11, e11115. <https://doi.org/10.15252/emmm.201911115>
- Qiu, Z., Piyawattanamatha, W., 2017. New Endoscopic Imaging Technology Based on MEMS Sensors and Actuators. *Micromachines (Basel)* 8. <https://doi.org/10.3390/mi8070210>
- Richeldi, L., Collard, H.R., Jones, M.G., 2017. Idiopathic pulmonary fibrosis. *Lancet* 389, 1941–1952. [https://doi.org/10.1016/S0140-6736\(17\)30866-8](https://doi.org/10.1016/S0140-6736(17)30866-8)
- Rockey, D.C., Bell, P.D., Hill, J.A., 2015. Fibrosis--a common pathway to organ injury and failure. *N Engl J Med* 372, 1138–1149. <https://doi.org/10.1056/NEJMr1300575>
- Rubart Michael, 2004. Two-Photon Microscopy of Cells and Tissue. *Circulation Research* 95, 1154–1166. <https://doi.org/10.1161/01.RES.0000150593.30324.42>
- Ruscitti, F., Ravanetti, F., Bertani, V., Ragionieri, L., Mecozzi, L., Sverzellati, N., Silva, M., Ruffini, L., Menozzi, V., Civelli, M., Villetti, G., Stellari, F.F., 2020. Quantification of Lung Fibrosis in IPF-Like Mouse Model and Pharmacological Response to Treatment by Micro-Computed Tomography. *Front. Pharmacol.* 11. <https://doi.org/10.3389/fphar.2020.01117>
- Ruscitti, F., Ravanetti, F., Essers, J., Ridwan, Y., Belenkov, S., Vos, W., Ferreira, F., KleinJan, A., van Heijningen, P., Van Holsbeke, C., Cacchioli, A., Villetti, G., Stellari, F.F., 2017. Longitudinal assessment of bleomycin-induced lung fibrosis by Micro-CT correlates with histological evaluation in mice. *Multidiscip Respir Med* 12, 8. <https://doi.org/10.1186/s40248-017-0089-0>

- Sado, D.M., Flett, A.S., Moon, J.C., 2011. Novel imaging techniques for diffuse myocardial fibrosis. *Future Cardiology* 7, 643–650. <https://doi.org/10.2217/fca.11.45>
- Sgalla, G., Iovene, B., Calvello, M., Ori, M., Varone, F., Richeldi, L., 2018. Idiopathic pulmonary fibrosis: pathogenesis and management. *Respiratory Research* 19, 32. <https://doi.org/10.1186/s12931-018-0730-2>
- Sheu, C.-C., Chang, W.-A., Tsai, M.-J., Liao, S.-H., Chong, I.-W., Kuo, P.-L., 2019. Gene Expression Changes Associated with Nintedanib Treatment in Idiopathic Pulmonary Fibrosis Fibroblasts: A Next-Generation Sequencing and Bioinformatics Study. *J Clin Med* 8. <https://doi.org/10.3390/jcm8030308>
- Shirai Mikiyasu, Schwenke Daryl O., Tsuchimochi Hirotugu, Umetani Keiji, Yagi Naoto, Pearson James T., 2013. Synchrotron Radiation Imaging for Advancing Our Understanding of Cardiovascular Function. *Circulation Research* 112, 209–221. <https://doi.org/10.1161/CIRCRESAHA.111.300096>
- Sibley, C.T., Noureldin, R.A., Gai, N., Nacif, M.S., Liu, S., Turkbey, E.B., Mudd, J.O., van der Geest, R.J., Lima, J.A.C., Halushka, M.K., Bluemke, D.A., 2012. T1 Mapping in Cardiomyopathy at Cardiac MR: Comparison with Endomyocardial Biopsy. *Radiology* 265, 724–732. <https://doi.org/10.1148/radiol.12112721>
- Silva, P.L., Rocco, P.R.M., 2018. The basics of respiratory mechanics: ventilator-derived parameters. *Ann Transl Med* 6. <https://doi.org/10.21037/atm.2018.06.06>
- Spudich, J.A., 2019. Three perspectives on the molecular basis of hypercontractility caused by hypertrophic cardiomyopathy mutations. *Pflugers Arch - Eur J Physiol* 471, 701–717. <https://doi.org/10.1007/s00424-019-02259-2>
- Suzuki, Y., Yeung, A.C., Ikeno, F., 2009. The Pre-Clinical Animal Model in the Translational Research of Interventional Cardiology. *JACC: Cardiovascular Interventions* 2, 373–383. <https://doi.org/10.1016/j.jcin.2009.03.004>
- Tardif, S.D., Mansfield, K.G., Ratnam, R., Ross, C.N., Ziegler, T.E., 2011. The Marmoset as a Model of Aging and Age-Related Diseases. *ILAR J* 52, 54–65.
- Thannickal, V.J., Toews, G.B., White, E.S., Lynch III, J.P., Martinez, F.J., 2004. Mechanisms of Pulmonary Fibrosis. *Annu. Rev. Med.* 55, 395–417. <https://doi.org/10.1146/annurev.med.55.091902.103810>
- Thannickal, V.J., Zhou, Y., Gaggar, A., Duncan, S.R., 2014. Fibrosis: ultimate and proximate causes. *J Clin Invest* 124, 4673–4677. <https://doi.org/10.1172/JCI74368>
- Theilmann, R.J., Arai, T.J., Samiee, A., Dubowitz, D.J., Hopkins, S.R., Buxton, R.B., Prisk, G.K., 2009. Quantitative MRI measurement of lung density must account for the change in T(2) (*) with lung inflation. *J Magn Reson Imaging* 30, 527–534. <https://doi.org/10.1002/jmri.21866>
- Toh, R., Shinohara, M., Takaya, T., Yamashita, T., Masuda, S., Kawashima, S., Yokoyama, M., Yagi, N., 2006. An X-Ray Diffraction Study on Mouse Cardiac Cross-Bridge Function In Vivo: Effects of Adrenergic β -Stimulation. *Biophysical Journal* 90, 1723–1728. <https://doi.org/10.1529/biophysj.105.074062>
- Travers, J.G., Kamal, F.A., Robbins, J., Yutzey, K.E., Blaxall, B.C., 2016. Cardiac Fibrosis: The Fibroblast Awakens. *Circ Res* 118, 1021–1040. <https://doi.org/10.1161/CIRCRESAHA.115.306565>
- Trial, J., Cieslik, K.A., 2018. Changes in cardiac resident fibroblast physiology and phenotype in aging. *American Journal of Physiology-Heart and Circulatory Physiology* 315, H745–H755. <https://doi.org/10.1152/ajpheart.00237.2018>
- Vande Velde, G., De Langhe, E., Poelmans, J., Bruyndonckx, P., d'Agostino, E., Verbeken, E., Bogaerts, R., Lories, R., Himmelreich, U., 2015. Longitudinal in vivo

- microcomputed tomography of mouse lungs: No evidence for radiotoxicity. *Am J Physiol Lung Cell Mol Physiol* 309, L271–L279.
<https://doi.org/10.1152/ajplung.00098.2015>
- Vande Velde, G., Poelmans, J., De Langhe, E., Hillen, A., Vanoirbeek, J., Himmelreich, U., Lories, R.J., 2016. Longitudinal micro-CT provides biomarkers of lung disease that can be used to assess the effect of therapy in preclinical mouse models, and reveal compensatory changes in lung volume. *Dis Model Mech* 9, 91–98.
<https://doi.org/10.1242/dmm.020321>
- Varga, B., Meli, A.C., Radoslavova, S., Panel, M., Lacampagne, A., Gergely, C., Cazorla, O., Cloître, T., 2020. Internal structure and remodeling in dystrophin-deficient cardiomyocytes using second harmonic generation. *Nanomedicine: Nanotechnology, Biology and Medicine* 30, 102295. <https://doi.org/10.1016/j.nano.2020.102295>
- Velayutham, N., Agnew, E.J., Yutzey, K.E., 2019. Postnatal cardiac development and regenerative potential in large mammals. *Pediatr Cardiol* 40, 1345–1358.
<https://doi.org/10.1007/s00246-019-02163-7>
- Velde, G.V., De Langhe, E., Poelmans, J., Dresselaers, T., Lories, R.J., Himmelreich, U., 2014. Magnetic Resonance Imaging for Noninvasive Assessment of Lung Fibrosis Onset and Progression: Cross-Validation and Comparison of Different Magnetic Resonance Imaging Protocols With Micro-Computed Tomography and Histology in the Bleomycin-Induced Mouse Model. *Investigative Radiology* 49, 691–698.
<https://doi.org/10.1097/RLI.0000000000000071>
- Veldhoen, S., Weng, A.M., Knapp, J., Kunz, A.S., Stäb, D., Wirth, C., Segerer, F., Hebestreit, H., Malzahn, U., Köstler, H., Bley, T.A., 2017. Self-gated Non-Contrast-enhanced Functional Lung MR Imaging for Quantitative Ventilation Assessment in Patients with Cystic Fibrosis. *Radiology* 283, 242–251.
<https://doi.org/10.1148/radiol.2016160355>
- Veteto, A.B., Peana, D., Lambert, M.D., McDonald, K.S., Domeier, T.L., 2020. Transient receptor potential vanilloid-4 contributes to stretch-induced hypercontractility and time-dependent dysfunction in the aged heart. *Cardiovascular Research* 116, 1887–1896. <https://doi.org/10.1093/cvr/cvz287>
- Villetti, G., Ridwan, Y., Belenkov, S., Essers, J., Ruscitti, F., Ravenetti, F., Heiningen, P.V., Wos, W., Holsbeke, C.V., Civelli, M., Stellari, F., 2016. Longitudinal assessment of lung fibrosis by micro CT correlates with histological evaluation in bleomycin-induced mice. *European Respiratory Journal* 48.
<https://doi.org/10.1183/13993003.congress-2016.OA3505>
- Vinegoni, C., Aguirre, A.D., Lee, S., Weissleder, R., 2015. Imaging the beating heart in the mouse using intravital microscopy techniques. *Nat Protoc* 10, 1802–1819.
<https://doi.org/10.1038/nprot.2015.119>
- Vreeker, A., van Stuijvenberg, L., Hund, T.J., Mohler, P.J., Nikkels, P.G.J., van Veen, T.A.B., 2014. Assembly of the Cardiac Intercalated Disk during Pre- and Postnatal Development of the Human Heart. *PLoS One* 9.
<https://doi.org/10.1371/journal.pone.0094722>
- Wada, Y., Aiba, T., Matsuyama, T., Kanzaki, H., Anzai, T., Ishihara, M., Yasuda, S., Ogawa, H., Ishibashi-Ueda, H., Shimizu, W., 2013. Clinical significance of tissue fibrosis and conduction abnormality in long-term prognosis in hypertrophic cardiomyopathy. *European Heart Journal* 34. <https://doi.org/10.1093/eurheartj/ehs309.P4228>

- Wang, B.-G., König, K., Halbhuber, K.-J., 2010. Two-photon microscopy of deep intravital tissues and its merits in clinical research. *J Microsc* 238, 1–20. <https://doi.org/10.1111/j.1365-2818.2009.03330.x>
- Wang, L., Chen, B., Yan, W., Yang, Z., Peng, X., Lin, D., Weng, X., Ye, T., Qu, J., 2018. Resolution improvement in STED super-resolution microscopy at low power using a phasor plot approach. *Nanoscale* 10, 16252–16260. <https://doi.org/10.1039/C8NR03584A>
- Weigel, B., Bakker, G.-J., Friedl, P., 2016. Third harmonic generation microscopy of cells and tissue organization. *J Cell Sci* 129, 245–255. <https://doi.org/10.1242/jcs.152272>
- Williams, R.M., Flesken-Nikitin, A., Ellenson, L.H., Connolly, D.C., Hamilton, T.C., Nikitin, A.Y., Zipfel, W.R., 2010. Strategies for High-Resolution Imaging of Epithelial Ovarian Cancer by Laparoscopic Nonlinear Microscopy. *Transl Oncol* 3, 181–194.
- Wollin, L., Maillet, I., Quesniaux, V., Holweg, A., Ryffel, B., 2014. Antifibrotic and anti-inflammatory activity of the tyrosine kinase inhibitor nintedanib in experimental models of lung fibrosis. *J Pharmacol Exp Ther* 349, 209–220. <https://doi.org/10.1124/jpet.113.208223>
- Wollin, L., Wex, E., Pautsch, A., Schnapp, G., Hostettler, K.E., Stowasser, S., Kolb, M., 2015. Mode of action of nintedanib in the treatment of idiopathic pulmonary fibrosis. *European Respiratory Journal*. <https://doi.org/10.1183/09031936.00174914>
- Wongkarnjana, A., Yanagihara, T., Kolb, M.R., 2019. Treatment of idiopathic pulmonary fibrosis with Nintedanib: an update. *Expert Rev Respir Med* 13, 1139–1146. <https://doi.org/10.1080/17476348.2019.1673733>
- Wu, Z., Rademakers, T., Kiessling, F., Vogt, M., Westein, E., Weber, C., Megens, R.T.A., van Zandvoort, M., 2017. Multi-photon microscopy in cardiovascular research. *Methods* 130, 79–89. <https://doi.org/10.1016/j.ymeth.2017.04.013>
- Wuyts, W.A., Wijsenbeek, M., Bondue, B., Bouros, D., Bresser, P., Robalo Cordeiro, C., Hilberg, O., Magnusson, J., Manali, E.D., Morais, A., Papiris, S., Shaker, S., Veltkamp, M., Bendstrup, E., 2020. Idiopathic Pulmonary Fibrosis: Best Practice in Monitoring and Managing a Relentless Fibrotic Disease. *RES* 99, 73–82. <https://doi.org/10.1159/000504763>
- Wynn, T., 2008. Cellular and molecular mechanisms of fibrosis. *J Pathol* 214, 199–210. <https://doi.org/10.1002/path.2277>
- Wynn, T.A., Ramalingam, T.R., 2012. Mechanisms of fibrosis: therapeutic translation for fibrotic disease. *Nature Medicine* 18, 1028–1040. <https://doi.org/10.1038/nm.2807>
- Xu, A., Narayanan, N., 1998. Effects of aging on sarcoplasmic reticulum Ca²⁺-cycling proteins and their phosphorylation in rat myocardium. *American Journal of Physiology-Heart and Circulatory Physiology* 275, H2087–H2094. <https://doi.org/10.1152/ajpheart.1998.275.6.H2087>
- Yagi, N., Shimizu, J., Mohri, S., Araki, J., Nakamura, K., Okuyama, H., Toyota, H., Morimoto, T., Morizane, Y., Kurusu, M., Miura, T., Hashimoto, K., Tsujioka, K., Suga, H., Kajiyama, F., 2004. X-ray Diffraction from a Left Ventricular Wall of Rat Heart. *Biophysical Journal* 86, 2286–2294. [https://doi.org/10.1016/S0006-3495\(04\)74286-1](https://doi.org/10.1016/S0006-3495(04)74286-1)
- Yamada, A., Kitagawa, K., Nakamura, S., Takafuji, M., Goto, Y., Okamoto, R., Dohi, K., Sakuma, H., 2020. Quantification of extracellular volume fraction by cardiac computed tomography for noninvasive assessment of myocardial fibrosis in hemodialysis patients. *Scientific Reports* 10, 15367. <https://doi.org/10.1038/s41598-020-72417-5>

- Yang, H., Schmidt, L.P., Wang, Z., Yang, X., Shao, Y., Borg, T.K., Markwald, R., Runyan, R., Gao, B.Z., 2016. Dynamic Myofibrillar Remodeling in Live Cardiomyocytes under Static Stretch. *Sci Rep* 6. <https://doi.org/10.1038/srep20674>
- Yuan, C., Wang, Z., Borg, T.K., Ye, T., Baicu, C., Bradshaw, A., Zile, M., Runyan, R.B., Shao, Y., Gao, B.Z., 2019. Changes in the crystallographic structures of cardiac myosin filaments detected by polarization-dependent second harmonic generation microscopy.
- Zeisberg, M., Kalluri, R., 2013. Cellular Mechanisms of Tissue Fibrosis. 1. Common and organ-specific mechanisms associated with tissue fibrosis. *Am J Physiol Cell Physiol* 304, C216–C225. <https://doi.org/10.1152/ajpcell.00328.2012>
- Zhang, Q., Lai, K., Xie, J., Chen, G., Zhong, N., 2009. Does unrestrained single-chamber plethysmography provide a valid assessment of airway responsiveness in allergic BALB/c mice? *Respir Res* 10, 61. <https://doi.org/10.1186/1465-9921-10-61>
- Zhou, Y., Chen, H., Ambalavanan, N., Liu, G., Antony, V.B., Ding, Q., Nath, H., Eary, J.F., Thannickal, V.J., 2015. Noninvasive Imaging of Experimental Lung Fibrosis. *Am J Respir Cell Mol Biol* 53, 8–13. <https://doi.org/10.1165/rcmb.2015-0032TR>
- Ziegler, M., Alt, K., Paterson, B.M., Kanellakis, P., Bobik, A., Donnelly, P.S., Hagemeyer, C.E., Peter, K., 2016. Highly Sensitive Detection of Minimal Cardiac Ischemia using Positron Emission Tomography Imaging of Activated Platelets. *Scientific Reports* 6, 38161. <https://doi.org/10.1038/srep38161>
- Zipfel, W.R., Williams, R.M., Christiet, R., Nikitin, A.Y., Hyman, B.T., Webb, W.W., 2003. Live tissue intrinsic emission microscopy using multiphoton-excited native fluorescence and second harmonic generation. *Proceedings of the National Academy of Sciences of the United States of America* 100, 7075–7080. <https://doi.org/10.1073/pnas.0832308100>

Acknowledgments

This work would not have been possible without support from many people and intensive collaboration. Foremost I would like to thank Prof. Dr. Frauke Alves for her inspiration, constant guidance and endless support. You have been a great source of motivation and help throughout these years and without it I would not have been able to accomplish as much as I did. I am glad that I could work with you and learn from you!

I also thank my thesis committee members Prof. Dr. Elisabeth Zeisberg for her detailed feedback on translational aspects of heart fibrosis and Prof. Dr. Ralph Dressel for providing his expertise in the role of inflammation in cardiac fibrosis during the committee meetings. I am also thankful to additional members of examination committee Prof. Dr. Herbeutus Jarry, Prof. Tim Salditt and Prof. Dr. Thomas Meyer for reviewing this thesis.

Within AG Alves, I am most indebted to Dr. Andrea Markus for her generous supervision and support, who joined and helped me for many experiments and Dr. Christian Dullin for making the lung imaging experiments possible. The same can be said about Dr. Fernanda Ramos Gomes who was invaluable source of help for the two-photon microscopy experiments. You all took an active interest in my projects, offered your expertise to help develop the imaging techniques and assisted me with complex data analysis. I thank all three of you for always keeping your door open for discussions and making it a great journey by supporting every step of it! All this work was made much easier and smooth by generous technical assistance from Bärbel Heidrich, Bettina Jeep, Sabine Wolfgramm, Sarah Garbode and Regine Kruse who were always so kind to lend their time to my experiments. I cannot express enough gratitude for all the members of AG Alves specially Andrea, Fernanda, Bärbel, Regine and Dr. Joanna Napp with whom I shared the office for being there during the stressful moments and for all the insightful conversations. I also owe thanks to all my fellow students from AG Alves (Jonas, Oliver, Jakub, Angelika, Nathalia, Myrto, Daniele, Bharti and Garyfallia) and my lab rotation students for making this an exciting journey by keeping my spirits always high and by building a great working environment.

During my doctoral studies we worked in interdisciplinary collaboration with other groups at the Göttingen Campus which was met with great enthusiasm, and I am very happy to have

received great assistance in return. Most part of the cardiac fibrosis studies was performed in collaboration with Prof. Tim Salditt who provided invaluable support for experimental design and data analysis. Beyond scientific work, Prof. Salditt has been a great mentor who provided helpful career related advice and it has always been a pleasure to work and learn from him. From Prof. Salditt's group, I would also like to extend profound gratitude to Dr. Jan David Nicolas for the x-ray diffraction experiments and helping with initial SHG data interpretation and to Marius Reichardt with whom I closely worked together on various cardiac fibrosis projects. I was always delighted to meet, have discussions and exchange physics and biomedical ideas with them. I am also grateful to Prof. Dr. Karl Toischer and Dr. Belal Mohammad for generously providing samples from different mouse models of cardiac fibrosis. I would like to thank Prof. Swen Hülsmann for his much needed help in providing important expertise for the lung function measurements and data analysis and for always creating an engaging and intriguing work environment during the experiments and meetings. Our recent collaboration with Prof. Dr. Rabea Hinkel from the German Primate Center (DPZ) offered new and exciting possibilities. Therefore, I would like to extend my whole-hearted gratitude to Prof. Hinkel and Dr. Matthias Mietsch for timely provision of the valuable marmoset samples. I am also thankful to Dr. Miso Mitkovski and Heiko Röhse from the Light Microscopy Facility (LMF) at the MPI-EM for providing basic training and technical help during TPM microscopy experiments.

Last but not the least, I would like to thank my beloved parents who are my forever support system and strength and I owe them a debt greater than they think they deserve. I also owe a lot to my sisters and my brother for being great role models, partners in crime, expectational listeners and for always being there for me under all circumstances. I would like to thank all my friends from Göttingen and beyond for their unconditional support, motivation and for keeping me happy through thick and thin by their pleasant company.

